Synthesis by spray flash evaporation of pure oxides, oxide mixtures and mixed oxides : photocatalytic and pyrotechnic applications

Denis Horst Prüssing

UNIVERSITÉ DE STRASBOURG

ÉCOLE DOCTORALE Physique et Chimie-Physique

Nanomatériaux pour des Systèmes Sous Sollicitations Extrêmes (NS3E)

UMR3208 ISL/CNRS/Unistra

THÈSE présentée par :

Denis Horst PRÜSSING

Soutenue le : **28 Janvier 2021**

pour obtenir le grade de : **Docteur de l'université de Strasbourg**

Discipline/ Spécialité : Science des matériaux

Synthèse par nébulisation flash de spray d'oxydes purs, de mélanges d'oxydes et d'oxydes mixtes – Applications photocatalytiques et pyrotechniques

THÈSE dirigée par :

M. COMET Marc	Docteur HDR, Université de Strasbourg
Mme. KELLER Valérie	Docteur HDR, Directeur des Recherches, Université de Strasbourg

RAPPORTEURS :

Mme. MILLOT Nadine	Professeur, Université de Bourgogne
M. SANTINACCI Lionel	Docteur HDR, Chargé des Recherches, CNRS

AUTRES MEMBRES DU JURY :

M. GILLARD Philippe	Professeur, Université d'Orléans
Mme. POURROY Geneviève	Docteur HDR, Directeur des Recherches, CNRS
M. GADIOU Roger	Professeur, Université de Haute-Alsace

ACKNOWLEDGMENTS

I would like to thank the jury members to have accepted to be part of the defence of this thesis and to evaluate my work. I would like to express my gratitude to Mme. Professor Nadine MILLOT and M. Doctor Lionel SANTINACCI for accepting the role of reports of my thesis, to Mme. Doctor Geneviève Pourroy, to M. Professor Philippe GILLAR and M. Professor Roger GADIOU for taking the role as examiners.

I would like to thank Doctor Denis SPITZER, Director of the laboratory Nanomatériaux pour les Systèmes Sous Sollicitations Extrêmes (NS3E) (UMR 3208 CNRS/ISL/Unistra) for giving me the chance to do this work.

I would like to thank Doctor Marc COMET and Doctor Valérie KELLER, my thesis directors for their support, their help, their guidance and patience along this time and to show me the exciting and always changing world of the research.

To the friends that helped me and supported me, Cristina, Juan, Largo, Javi, Guille, Irene, Migue, Dani, Pablo, Phillip, Denis, Geri, but also to the friend that I made in the while I was here, Laura, Manuel, Manita, Giuseppe, Gabrielle, Javi, Hrvoje, Jonathan and Victor. To all the people with which I passed a wonderful time.

I also would like to thank all the other researchers, engineers, technicians, doctorates and post-doctorates that helped me to keep on: Vincent PICHOT, Pierre AGOSTINI, Laurent SCHLUR, Emeline LOBRY, Pierre GIBOT, Kyung-Tae HAN, Yan BUSBY, Guillaume THOMAS, Michael SCHÄFER, Mazheva GUILLEVIC, Lorenz KRÖNER, Vincent CHARLOT, Jean-Edouard BERTHE, Guillaume GALLAND, Virginie GOETZ, Cedric SCHWARTZ, Jakob HÜBNER, Bastien LALLEMAND, Franck OUDOT, Etienne BIEBER, Loic BERNARD, Silke BRAUN, Bernd WANDERS, Andreas KLAVZAR, Roman WÖLBING and Stefan NAU.

But also all the other colleagues of the ISL which I didn't cite but that I had the pleasure to work with, thank you.

I would like to dedicate this work to my family. To my father who taught me science, to my mother who taught me passion, to my brother who taught me patience and to my grandparents who taught me love.

RÉSUMÉ

Le **premier chapitre** traite des voies classiques utilisées pour la synthèse des nanomatériaux et des propriétés qui en découlent. Le cadre de cette étude est basé sur plusieurs points. Premièrement, l'identification des précurseurs qui peuvent être utilisés ainsi que les conditions expérimentales qui doivent être appliquées dans le processus SFS pour obtenir les matériaux désirés. Deuxièmement, comprendre le fonctionnement des méthodes de synthèse classiques, afin de pouvoir les comparer avec le procédé SFS. Cela se fera essentiellement par le biais des matériaux produits par ces différentes techniques. Et enfin, présenter le procédé SFE.

L'oxyde de titane est l'un des nanomatériaux les plus étudiés. Il est notamment utilisé dan des dispositifs biomédicaux, des cosmétiques et des pigments ou des additifs pour les couleurs. À l'échelle nanométrique, il a un large éventail d'applications dans les domaines de l'énergie, des capteurs et de la photocatalyse, ce qui se justifie par ses propriétés optiques, diélectriques et catalytiques. Ce semi-conducteur présente certains avantages par rapport à d'autres ayant des propriétés similaires, comme des coûts de production relativement faibles et une bonne stabilité chimique et thermique.

L'oxyde de titane est principalement utilisé comme pigment blanc pour différents types de produits, mais aussi comme matériau de remplissage dans l'industrie du papier et du plastique. Les caractéristiques du titane en font un excellent candidat pour la dégradation de substances polluantes par photocatalyse. Les poudres submicrométriques d'oxyde de titane produites dans le cadre de la thèse ont été utilisées pour produire de l'hydrogène par photoreformatioge du méthanol. Le mécanisme photocatalytique dépend de la création et de la recombinaison de paires électron-trou. Les électrons qui reçoivent la quantité d'énergie nécessaire des photons sautent de la bande de valence occupée à la bande de conduction inoccupée. Il a été constaté, en comparant les trois phases, que l'anatase est la modification la plus active, du point de vue photoréactif. Plus les particules sont petites, plus le rapport surface/volume est élevé, et meilleures sont les interactions entre l'oxyde et le réactif. De plus, la profondeur de pénétration des photons dans les cristaux est directement affectée par le taux de photons qui sont réfléchis à la surface des particules.

La production d'hydrogène à partir d'eau et de méthanol est une alternative intéressante pour l'avenir. Cette voie de production d'hydrogène est intéressante comme solution de substitution à partir de combustibles fossiles, car le méthanol peut être obtenu à partir de sources biologiques renouvelables. L'utilisation de l'hydrogène

comme carburant propre est une solution prometteuse qui est étudiée pour la production d'énergie durable. L'oxyde de titane a un faible pouvoir oxydant dans les compositions aluminothermiques. Dans le domaine de la pyrotechnie, les compositions Al/TiO_2 brûlent lentement et l'auto-propagation de la réaction est difficile.

L'oxyde de bismuth est utilisé pour de nombreuses applications comme la production de papiers et de polymères ignifuges, ou comme substitut du tétroxyde de plomb (Pb_3O_4) pour la production d'un effet pyrotechnique mis en œuvre dans les feux d'artifice connu sous le nom « d'œuf de dragon ». Ce matériau sert également à préparer des céramiques en fonte émaillée. Utilisé comme pigment dans l'industrie du verre et de la porcelaine, il permet de remplacer l'oxyde de plomb. Néanmoins, il trouve principalement son utilisation dans le domaine des applications électrochimiques. Les propriétés électriques de l'oxyde de bismuth, comme sa conductivité, permettent d'utiliser ce matériau comme électrode. Elles peuvent également être mises `profit dans des dispositifs de détection de fumée, capables de fonctionner à des températures élevées, ou dan des piles à combustible à oxyde solide qui fonctionnent grâce à la conductivité ionique élevée de la phase δ- Bi_2O_3 à température élevée.

Les titanates de bismuth, $Bi_xTi_yO_z$, sont une famille de composés formés en alternant des couches de type pérovskite et des couches de $(Bi_2O_2)^{2+}$. La famille des titanates de bismuth est un groupe intéressants de matériaux en raison de leurs propriétés électriques et optiques. L'un d'entre eux, le $Bi_4Ti_3O_{12}$, est un matériau ferroélectrique qui a des propriétés piézoélectriques et une température de Curie élevée (675°C), ce qui le rend utile pour les composants piézoélectriques à haute température, les dispositifs de stockage de mémoire ou les dispositifs de blindage optique. Un autre membre bien étudié de cette famille est le $Bi_{12}TiO_{20}$. Ces cristaux ont des propriétés électroniques, optiques et photoconductrices singulières. Cet ensemble original de caractéristiques confère au matériau des propriétés photoréfractives. L'indice de réfraction de ce matériau peut changer de manière réversible sous l'effet de la lumière. Cette caractéristique ouvre des applications potentielles comme les supports d'enregistrement réversibles pour l'holographie en temps réel ou les applications de traitement d'images.

L'oxyde de cuivre a des propriétés intéressantes en tant que semi-conducteur de type p. De ce fait, il est utilisé pour de nombreuses applications comme la détection de gaz, la catalyse et les applications photovoltaïques. En catalyse, l'oxyde de cuivre a été

utilisé soit comme catalyseur direct, soit comme support pour la dégradation de l'oxyde nitreux par l'ammoniac et l'oxydation du monoxyde de carbone, des hydrocarbures et du phénol dans l'eau supercritique. Le cuivre nanométrique présente des propriétés antimicrobiennes à large spectre. L'oxyde de cuivre est utilisé comme oxydant dans les compositions aluminothermiques pour lesquelles il constitue l'un des oxydes les plus réactifs. Ses propriétés oxydantes découlent de la libération d'oxygène par la décomposition thermique de l'oxyde cuivrique (CuO) en oxyde cuivreux (Cu_2O).

Il existe différents types de combinaisons de nanomatériaux d'oxyde de cuivre et d'oxyde de titane. Les méthodes de préparation de composites Cu_2O/TiO_2 ont été rapportées par plusieurs auteurs. Ce matériau est utilisé comme photocatalyseur pour la production d'hydrogène. C'est un matériau intéressant en raison de la jonction d'un semi-conducteur de type p (Cu_2O) et d'un semi-conducteur de type n (TiO_2) qui peut absorber une plus grande partie du rayonnement du spectre solaire et assurer une meilleure séparation des porteurs de charge.

La production d'oxyde de titane a été étudiée de plusieurs manières au cours de l'histoire récente de la science des matériaux. Il existe des précurseurs organiques et inorganiques de cet oxyde. Les voies les plus courantes pour l'obtenir sont basées sur l'hydrolyse ou la précipitation de sels de Ti(IV), comme $TiOSO_4$, $Ti(SO_4)_2$ et $TiCl_4$. Cependant, le contre-anion du sel est généralement présent dans le produit. Le produit obtenu dépend fortement des conditions de réaction, ce qui signifie que des paramètres spécifiques doivent être trouvés pour chaque procédé de synthèse. Les alcoolates sont une autre famille de précurseurs organiques, qui présent l'avantage d'être faciles à manipules et que ne contiennent pas d'éléments susceptiles de contaminer le matériau produit. Les alcoolates de titane sont des composés organométalliques de formule générale $Ti(OR)_n$, où R est un groupe alkyle. Dans le cas de l'isopropanolate de titane, les principaux produits de décomposition sont le propène, le propanol et l'eau. Ces produits sont intéressants d'un point de vue technique pour le système de synthèse par vaporisation flash car ils n'ont pas d'effet corrosif sur les différentes parties constituant l'appareil de SFS et sont faciles à évaporer. En l'absence de catalyseur, le mécanisme de réaction consiste en une hydrolyse et une condensation. Ces réactions ont un cheminement très complexe, qui dépend fortement des conditions dans lesquelles est réalisée la réaction. Le précurseur utilisé, le pH du milieu, la température et l'atmosphère dans laquelle est réalisée la réaction ont une importance capitale. La modification de ces conditions

influe directement sur les propriétés du produit, notamment sur le phase obtenue, anatase ou rutile.

Afin de produire du TiO_2 nanostructuré, sous une forme bien définie, de multiples méthodes de production ont été étudiées au cours des dernières décennies. Citons, par exemple le procéde sol-gel, les synthèses hydrothermales et solvothermales, ou encore le dépôt chimique et physique en phase vapeur. La procédé sol-gel est couramment utilisé pour préparer diverses céramiques à base d'oxydes métalliques. La préparation par le procédé sol-gel d'oxyde de titane est basée sur l'hydrolyse d'un précurseur, suivie d'une étape de condensation. Après mûrissement, le gel est séché avant d'être calciné. Dans la méthode hydrothermale, la réaction a lieu dans une solution aqueuse, dont température et la pression sont contrôlés. La simplicité de cette technique et le faible coût des équipements en font une méthode de synthèse industrielle largement utilisée pour élaborer des particules nanométriques. La méthode solvothermale, qui est analogue à la méthode hydrothermale mais qui repose sur l'usage de solvants non aqueux, est également un procédé de synthèse courant pour l'oxyde de titane. Par rapport à la méthode hydrothermale, une plus grande variété de solvants et leurs combinaisons peuvent être utilisés. Cela permet de produire des particules de différents tailles avec des morphologies plus variées. Le principe du dépôt chimique en phase vapeur réside dans la solidification d'une vapeur qui est produite par une réaction chimique. Si aucune réaction chimique n'intervient dans la production de la matière, on parle alors de dépôt physique en phase vapeur. La solidification de la matière se produit généralement sur une surface chauffée, pour former un revêtement ayant la forme d'un film d'une poudre ou de monocristaux. Il convient également de mentionner la pyrolyse à la flamme, qui est largement utilisée pour la production de matériaux en aérosol comme la silice pyrogénée nanométrique. La pyrolyse par pulvérisation à la flamme requiert une alimentation liquide ou gazeuse pour alimenter la réaction. Cette technique est utilisée pour produire l'oxyde de titane nanostructuré utilisé comme référence (Degussa P25). Des nanoparticules d'oxyde de titane ont été produites avec succès, de manière continue, par synthèse hydrothermale impliquant de l'eau à l'état supercritique.

Les propriétés des semi-conducteurs peuvent être modifiées en introduisant intentionnellement des impuretés dans le réseau cristallin, c'est ce qu'on appelle le dopage. La modification de la composition chimique et de l'arrangement des atomes entraîne des changements dans les propriétés électroniques, optiques et magnétiques

du semi-conducteur. Par conséquent, de nouveaux matériaux sont disponibles pour des applications telles que les lasers, la bio-imagerie et les cellules solaires. L'introduction de métaux dans la matrice d'oxyde de titane d'un point de vue photocatalytique est très intéressante. L'oxyde de titane est utilisé comme photocatalyseur pour dégrader des polluants, pour réduire le CO_2 ou produire de l'hydrogène par scission de la molécule d'eau. Cependant, l'oxyde de titane a un rendement quantique très faible et une large bande interdite, ce qui limite son utilisation dans les applications fonctionnant avec la lumière solaire. L'introduction d'un métal diminue le taux de recombinaison électron-trou et favorise le transfert d'électrons.

En ce que concerne la synthèse des nanoparticules d'oxyde de bismuth, d'autres techniques ont été utilisées. Parmi lesquelles : la synthèse sol-gel, la calcination des composés intermédiaires, la synthèse par combustion ou l'ablation au laser femtoseconde.

Il existe différents oxydes mixtes définis par le rapport molaire entre l'oxyde de bismuth et l'oxyde de titane. Les phases de titanate de bismuth les plus courantes sont $Bi_{12}TiO_{20}$, $Bi_4Ti_3O_{12}$ et $Bi_2Ti_2O_7$. Par le procédé hydrothermal, on peut obtenir des poudres de taille nanométrique de $Bi_{12}TiO_{20}$. Le $Bi_{12}TiO_{20}$ a également été produit par coprécipitation. La méthode classique de préparation de $Bi_4Ti_3O_{12}$ est basée sur la réaction à l'état solide de Bi_2O_3 avec TiO_2 à des températures élevées (1000-1200°C). Le procède sol-gel a également été utilisé avec succès pour la production de $Bi_4Ti_3O_{12}$. Un procédé connu sous le nom de décompositions métallo-organiques a été utilisé pour obtenir des poudres de $Bi_4Ti_3O_{12}$ à l'échelle nanométrique. De la poudre de $Bi_4Ti_3O_{12}$ a également été synthétisée à basse température par un procédé hydrothermal. Du titanate de bismuth $Bi_2Ti_2O_7$ a été produit par synthèse solvothermique.

Des nanoparticules d'oxyde de cuivre peuvent être préparées par le procédé sol-gel. La taille moyenne des particules (3 à 9 nm) varie en fonction de la température de synthèse. Une approche différente pour la synthèse des nanoparticules de CuO est la décomposition thermique directe. La synthèse par précipitation chimique est également couramment utilisée pour la préparation de ces particules. Des nanoparticules d'oxyde de cuivre de morphologies différentes peuvent être obtenues par la méthode sonochimique.

Du mélange d'oxydes cuivre et de titane a été produit par un procédé d'imprégnation humide. Le procédé de réduction par micro-ondes utilise de l'acétate de cuivre pour mettre des nanoparticules d'oxyde de cuivre sur la surface des particules d'oxyde de titane du commerce. Des couches minces de CuO_x/TiO_2 ont été préparées par pulvérisation magnétron réactive RF.

Le **deuxième chapitre** est consacré à la description des techniques et des méthodes utilisées pour préparer et analyser les matériaux étudiés dans la thèse. Les modifications du système original d'évaporation flash de spray (SFE) pour obtenir un procédé capable de synthétiser des nanomatériaux (SFS) seront décrites dans ce chapitre. Les protocoles de synthèse mis en œuvre pour produire les différents matériaux ainsi que les paramètres du procédé seront également détaillés.

L'évaporation flash de spray (SFE) est un procédé capable de produire des particules organiques submicrométriques ou nanométriques de manière simple. Cette méthode a été développée et brevetée par le laboratoire NS3E (Nanomatériaux pour les Systèmes Sous Sollicitations Extrêmes, UMR 3208 ISL-CNRS-UNISTRA) pour répondre à la demande d'une méthode de production à l'échelle industrielle de particules nanométriques. Le procédé d'évaporation flash de spray (SFE) est capable de produire des nanoparticules, il a été développé et breveté par le laboratoire NS3E. La finalité de cette technique est de produire des nanoparticules à l'échelle industrielle d'une manière simple et facile. Le procédé SFE est basé sur la cristallisation de molécules organiques dissoutes dans un solvant organique. Cette cristallisation est en pulvérisant sous vide la solution pressurisée et surchauffée. La chute brutale de pression provoque l'évaporation rapide du solvant et l'abaissement de la température. La solution dont sont composées les gouttelettes devient alors sursaturée, ce qui détermine la cristallisation du soluté. La croissance des particules formées est, ensuite interrompue par l'évaporation totale du solvant. Cependant, le procédé SFE, qui repose sur des phénomènes purement physiques, être utilisé pour la synthèse de nouveaux composés. Le SFS (Spray Flash Synthesis) permet de synthétiser des matériaux de taille nanométrique et submicronique par des réactions chimiques. Dans ce travail, le SFS a été utilisé pour produire des poudres céramiques simples comme l'oxyde de titane ou l'oxyde de cuivre, mais aussi des oxydes mixtes plus complexes, comme les titanates de bismuth. Il a également été utilisé pour incoporer un métal dans des nanoparticules d'oxyde.

Plusieurs modifications ont été apportées à la configuration d'origine de l'appareil de SFE le transformer en système de SFS. Ces modifications ont permis de créer des conditions de réaction stables afin que la réaction puisse avoir lieu, et de contrôler précisément les paramètres pour éviter des fluctuations indésirables tout au long du processus de synthèse.

Pour éviter le démarrage de la réaction dans les cuves, les liquides contenant les réactifs sont placés dans deux réservoirs différents. Les solutions contenant les réactifs sont mélangées juste avant d'être nébulisées dans la chambre sous vide. Un réservoir contenant du solvant pur est également mis en œuvre afin d'alimenter l'installation de sans injecter de réactifs.

Pour assurer la reproductibilité de la composition et l'homogénéité des matériaux obtenus, il est indispensable de maintenir le flux des deux réactifs, qui sont introduits dans la chambre, à un taux constant et calibré pendant tout le processus de synthèse. Ceci est crucial pour assurer les conditions stables, nécessaire au bon déroulement de la réaction chimique. D'autre part, le débit a été diminué de manière à ce que la pompe à vide puisse maintenir une pression constante à l'intérieur de la chambre. Le débit est contrôlé en limitant le débit des fluides alimentant la chambre à l'aide d'une vanne de précision montée sur chaque voie d'alimentation. Ce dispositif permet de contrôler très précisément de faibles débits.

Le système de récupération des versions antérieures du procédé SFE mettait en œuvre des cyclones. Ce mode de récupération utilise la force centrifuge des particules pour les extraire du flux gazeux dans lequel elles sont dispersées. Néanmoins, l'efficacité du dispositif dépend de plusieurs variables indépendantes comme la taille des particules ou la charge électrostatique. Pour éviter cela, une approche différente a été utilisée pour permettre l'extraction des particules du flux de gaz. Pour ce faire, un filtre cylindrique en acier inoxydable a été utilisé. Ce filtre est situé au fond de la chambre de cristallisation, à l'intérieur d'un cylindre solide de plus grand diamètre. De cette façon, les vapeurs sont forcées de le traverser pour sortir du système. Lorsque le gaz passe à travers le filtre, les particules sont retenues à l'intérieur du cylindre.

En raison de sa pression de vapeur plus élevée, l'eau se condense plus facilement que les autres solvants présents dans la chambre pendant le processus. Cette condensation a lieu sur les parois de la chambre, qui sont les parties du système à la température la plus basse. Le chauffage du corps principal du système est effectué à l'aide d'un pistolet thermique placé à une distance rapprochée. Un élément de chauffage additionel, de type ceinture chauffante à gaine de silicone a été placé autour du tube en acier qui conduit le flux de la chambre dans le filtre.

Le matériau choisi pour fabriquer les joints servant à étanchéifier les différentes parties du corps principal, c'est-à-dire la chambre du SFS, doit résister à des sollicitations

thermiques dynamiques et à des composés chimiques agressifs. Le matériau choisi est un caoutchouc nitrile-butadiène lié à des fibres aramides. Les joints fabriqués dans cette matière ont été utilisés entre la chambre et le couvercle, entre le support de buse à buse, entre le support de buse et le tube chauffant, entre le tube chauffant et le couvercle et entre le couvercle et le tube d'alimentation.

En général, toutes les synthèses réalisées par SFS suivent les étapes qui sont décrites ci-dessous. Un premier exemple de synthèse sera décrit en détail. Suivront des protocoles de synthèse où seules les différences importantes sont mises en évidence. Les deux solutions sont d'abord transvasées dans des réservoirs séparés. Tous les réservoirs sont mis sous pression, ceux qui contiennent les solutions de précurseurs ainsi que celui qui contenaient l'isopropanol pur. Le pistolet chauffant et la bande chauffante du filtre sont mis en marche avant la synthèse pour préchauffer le système, afin d'éviter les fluctuations dues par exemple à la condensation du spray. La phase de préchauffage a pour finalité de mettre le système dans des conditions de travail avant de démarrer la synthèse. Pour ce faire, on utilise le même solvant que celui qui est utilisé pour la préparation des solutions, mais sans soluté. Pendant la partie principale du processus, la buse doit être maintenue à température constante. Lorsque la pression à l'intérieur de la chambre et la température de la buse atteignent la valeur souhaitée, la phase de synthèse commence, en interrompant l'alimentation en isopropanol, et en activant l'injection des solutions contenant les réactifs dans la chambre.

Les techniques d'analyse qui ont été utilisées pour caractériser les matériux synthétisés par le procédé SFS ont d'abord été décrites de manière générale. Leur utilisation spécifique dans le cadre de ces recherches a ensuite été discutée. D'un point de vue structural et morphologique, les échantillons ont été analysés par analyse thermogravimétrique (ATG), calorimétrie différentielle à balayage (DSC), spectroscopie infrarouge à transformée de Fourier (FTIR) et spectroscopie Raman, diffraction des rayons X sur poudre, microscopie électronique à balayage (MEB) et microscopie électronique à transmission (MET), mesures de la surface spécifique et de la porosité par absorption d'azote et de mercure, respectivement.

Les compositions pyrotechniques ont été formulées à partir de certains des matériaux synthétisés par le procédé SFS. La méthode de préparation de ces matériaux énergétiques, ainsi que les techniques utilisées pour déterminer leur sensibilité, leur

chaleur d'explosion et pour caractériser leur combustion sont également décrits. Ce chapitre décrit également les dispositifs expérimentaux utilisés pour étudier l'activité photocatalytique de plusieurs matériaux synthétisés par le procédé SFS et les techniques mises en œuvre pour caractériser ces propriétés.

Le **troisième chapitre** détaille les propriétés et les caractéristiques des matériaux préparés par le système SFS. Les matériaux produits sont TiO_2, $Ag@TiO_2$, CuO, $Bi_xTi_yO_z$ et CuO/TiO_2. Les matériaux qui sont décrits ici ont été analysés de différents points de vue. L'accent a été mis sur la morphologie, la distribution en taille des particules et la structure cristalline. L'oxyde de titane a été synthétisé selon trois rapports molaires TTIP/H_2O : 1/1, 1/2 et 1/4. Toutes les poudres d'oxyde de titane produites par SFS sont constituées de particules sphériques de taille submicronique qui sont agglomérées en groupes de plusieurs unités.

Pour un rapport molaire TTIP/H_2O égal à 1/1, les particules sont denses, de composition homogène, totalement amorphes et associées en agglomérats de quelques dizaines d'unités. Pour le rapport molaire 1:2, qui est la valeur stoechiométrique de la réaction chimique, présentent des caractéristiques similaires. Il en va de même pour le rapport molaire 1:4, pour lequel les particules ont néanmoins une morphologie sphérique mieux définie. La composition chimique des nanoparticules produites est d'environ 40 % de composés organiques et 60 % d'oxyde de titane. Cette composition est la même pour tous les cas étudiés. L'hydrolyse n'élimine pas totalement les groupes isopropanolates car la charge partielle des radicaux organiques devient plus positive lorsqu'ils réagissent avec l'eau. Par conséquent, une augmentation de la proportion d'eau n'augmente pas le degré d'hydrolyse. Cela signifie que le taux d'hydrolyse est constant pour tous les systèmes étudiés.

La réaction chimique commence dès que les deux réactifs entrent en contact. Un groupe isopropyle est remplacé par un groupe hydroxyle et une molécule de 2-propanol quitte le système. Ensuite, ce groupe hydroxyle réagit avec un autre groupe hydroxyle d'une autre molécule TTIP formant le réseau de titane et laissant une molécule d'eau comme sous-produit. Cette molécule d'eau relance la boucle, déclenchant la réaction en chaîne qui formera finalement les particules de titane.

Une valeur minimale de la vitesse d'hydrolyse du $Ti(OR)_4$ est estimée à $kh= 10^{-3}\ M^{-1}\ s^{-1}$. En tenant compte de cette valeur et du fait que la vitesse d'hydrolyse et les taux de condensation sont du même ordre pour le TTIP dans l'isopropanol, on peut dire que la majeure partie de la réaction a lieu dans les gouttelettes, où la concentration augmente très rapidement en raison de l'évaporation du solvant. Cela accélère à la fois l'hydrolyse et la condensation, ce qui conduit à la formation de particules. Les

conditions de pulvérisation mises en œuvre dans les procédé SFS, forcent le solvant à s'évaporer, ce qui accélère la réaction chimique et conduit à la formation de matière amorphe. C'est ce qui est observé dans le cas de l'oxyde de titane: le produit d' hydrolyse du TTIP se forme (nucléation) sans avoir le temps de former un réseau ordonné (condensation forcée). En conséquence, les particules formées sont amorphes, car les amas n'ont pas pu s'organiser en un réseau périodique ordonné.

Les particules qui sont synthétisées par le procédé SFS conservent la morphologie de la goutte-mère, mais ont une taille plus petite (réplication). La géométrie la plus stable pour un liquide non contraint est la sphère, car la tension superficielle sous cette forme est minimale. Par conséquent, la forme sphérique des particules provient de la forme sphérique des gouttelettes. En réalité, chaque gouttelette donne naissance à une particule.

L'influence de la calcination sur la morphologie et la taille des particules des nanomatériaux est similaire dans tous les cas étudiés. La forme sphérique des nanoparticules est conservée après le traitement thermique. La calcination des poudres produites par le procédé SFS assure l'oxydation de la fraction organique des particules et fournit suffisamment d'énergie pour induire la réorganisation du réseau de titane. Le traitement thermique produit également une porosité interne dans les particules qui a été observée par microscopie électronique en transmission, et attribuée à la formation de cristaux. La calcination transforme les poudres amorphes synthétisées par le procédé SFS en un phase cristalline unique, l'anatase.

La surface des particules est affectée par le frittage de la matière, ce qui produit une perte de surface spécifique. En conséquence, les particules ne présentent que peu ou pas de porosité de surface. Les isothermes d'adsorption/désorption effectuées sur les trois matériaux présentent une forme de type IV, caractéristique de particules qui forment des agrégats sans surface microporeuse. Cependant, l'analyse de la densité des particules réalisée en comparant la surface théorique à la surface mesurée a montré qu'elles étaient poreuses. Cela peut s'expliquer par la présence d'une porosité interne fermée dans les particules.

L'introduction d'argent dans les particules de titane a été étudiée pour le TiO_2 préparé à partir du rapport molaire 1:2. Les poudres d'oxyde de titane chargées d'argent produites par le SFS sont constituées de particules sphériques de taille submicronique qui sont agglomérées en groupes de plusieurs unités. Ces particules sont denses, de

composition homogène et totalement amorphes, comme le sont les particules obtenues par hydrolyse du TTIP en l'absence d'argent. Cependant, les particules à la différence de ces dernières, Ag@TiO_2 comportent ont des nanoparticules d'argent à leur surface. Ces nanoparticules d'argent sont des sphères irrégulières fixées à la surface de l'oxyde de titane. La présence des particules d'argent à la surface des sphères de titane peut s'expliquer par la différence de rayon des ions constituant les particules. Les ions d'argent migrent hors de la matrice d'ions de titane tandis que la particule se forme.

Les sphères de titane qui supportent les nanoparticules d'oxyde d'argent sont affectées par le traitement thermique de la même manière que dans le cas du matériau vierge. Le matériau obtenu après calcination est une poudre fine et libre de couleur grisâtre. Les particules composites sont recouvertes par des particules d'argent en forme de bâtonnets. La présence d'argent augmente la taille des particules de TiO_2, ce qui s'explique par le fait que plus il y a de matière dans une gouttelette, plues la particule résultante est grosse. La très petite taille des particules d'argent induit une diminution de leur température de fusion. En considérant la température de calcination, la taille des domaines d'argent à l'intérieur des particules d'oxyde de titane peut être estimée à moins de 2 nm. Le traitement thermique appliqué pour réaliser la calcination provoque la fusion de l'argent mais pas celle de l'oxyde de titane. En conséquence, le volume des domaines d'argent augmente et le métal exsude de la matrice d'oxyde de titane. Lorsque les domaines d'argent fondus atteignent la surface, ils coalescent, ce qui augmente leur taille. La libération d'oxygène par l'argent, due à l'abaissement de la solubilité de l'oxygène, peut également expliquer la forme allongée des particules d'argent. Ces phénomènes produisent une augmentation du volume et entraînent un changement de morphologie des nanoparticules fixées à la surface.

D'autres voies de synthèse ont été testées pour comparer les caractéristiques des matériaux obtenues en fonction de leur mode de préparation. Les mêmes précurseurs ont été utilisés, pour préparer des matériaux Ag@TiO_2 par procédé solvothermal en autoclave. La première expérience de synthèse en autoclave a été réalisée pendant 2 heures. Le matériau ainsi produit est constitué de particules irrégulières en forme de bâtonnets. La même expérience a été réalisée pendant 24 heures. Dans ce cas, deux populations de particules sont formées. L'une d'elles est formée de particules de taille micrométrique à géométrie sphérique. L'autre population de particules a une dimension plus petite mais présente une structure fractale. Cela signifie que la

synthèse par autoclave conduit à des hétérogénéités morphologiques. La synthèse solvothermale ne permet pas de produire des matériaux composites oxyde de titane/argent ayant la même homogénéité en termes de composition chimique et de morphologie que ceux synthétisés par SFS. De plus, cette méthode de synthèse nécessite beaucoup plus de temps et d'énergie pour produire les échantillons.

De l'oxyde de cuivre a été synthétisé en utilisant le système SFS. Trois températures de synthèse différentes ont été utilisées, à savoir 130°C, 145°C et 155°C. Les poudres obtenues (CP 130, CP 145 et CP 155) sont formées de particules fortement agglomérées qui cristallisent en plaques irrégulières et sont composées de matériaux intermédiaires résultant de la décomposition partielle du nitrate de cuivre.

En dessous de 155°C, les espèces intermédiaires sont formées en changeant la sphère de coordination du cuivre (II) sans variation de masse, ce qui explique pourquoi les CP 130 et CP 145 ont la même perte de poids proportionnelle que le précurseur (~65,8%). Au-dessus de 155°C, la sphère de coordination du cuivre (II) change, formant une espèce intermédiaire contenant une proportion de cuivre différente par molécule. Les échantillons d'oxyde de cuivre préparés à 155°C ont été calcinés à 400°C. Ce traitement thermique provoque le frittage des particules en plaquettes en agrégats macroscopiques de type noix. Les particules sont totalement remplies et formées d'une structure polycristalline. La surface spécifique de l'échantillon est très faible. C'est une conséquence du frittage des particules, produit par le traitement thermique.

Plusieurs oxydes mixtes ont été préparés en combinant différentes proportions d'oxyde de titane et d'oxyde de bismuth. Ces matériaux ont été préparés par le procédé SFS en utilisant une proportion stoechiométrique TTIP par rapport à l'eau (1:2 mol/mol).

Un premier matériau a été préparé en utilisant une proportion molaire de titane élevée (Bi/Ti= 1:1.35 mol/mol). Le matériau obtenu par le procédé SFS est constitué de particules élémentaires submicrométriques similaires à celles préparées avec du titane pur, mais qui semblent plus fortement agrégées. Néanmoins, la plupart des particules ont une géométrie quasi-sphérique. L'introduction d'acide acétique pour dissoudre le précurseur du bismuth modifie les propriétés physico-chimiques (pH) de la solution. Cela affecte principalement la viscosité et la tension superficielle, ce qui a pour conséquence d'influencer la formation de gouttelettes au coures de la pulvérisation. L'acide acétique s'évapore à des températures plus élevées que l'isopropanol, ce qui

implique un processus d'évaporation plus lent. Par conséquent, le comportement d'agrégation et la formation de particules sont différents, ce qui conduit à des particules plus agrégées et avec une distribution en taille plus large. La poudre est constituée de particules amorphes, d'une densité homogène, qui forment des groupes de plusieurs dizaines d'unités. Le bismuth et le titane sont parfaitement mélangés dans toutes les directions dans chaque particule. Ce matériau a été calciné à 650°C sous air pendant 4 heures, ce qui a entraîné la cristallisation de la matière. La cristallisation de l'oxyde mixte implique la restructuration de la matière et la répartition des éléments qui la composent. Il en résulte une ségrégation du titanate de bismuth (Bi/Ti= 1:1 mol/mol) d'une part et de l'oxyde de titane pur d'autre part. La calcination s'accompagne d'un frittage des particules qui produit des agrégats microscopiques. Le titane et le bismuth forment un oxyde mixte connu sous le nom de titanate de bismuth ($Bi_2Ti_2O_7$). Selon le diagramme de phase publié dans la littérature, les phases stables observées pour un rapport molaire TiO_2 / Bi_2O_3 égal à 1/1.35, à une température de calcination de 650 °C, sont $Bi_{12}TiO_{20}$ et $Bi_4Ti_3O_7$, $Bi_2Ti_2O_7$ étant une phase métastable en dessous de 1000°C. Néanmoins, l'observation de cette phase à une température inférieure provient du procédé de préparation qui permet d'obtenir un mélange parfait bismuth, titane et de l'oxygène au sein des particules primaires. La partie de l'oxyde de titane qui n'est pas incluse dans la matrice de titanate de bismuth cristallise séparément sous forme de rutile.

Dans le matériaux préparé avec un ratio molaire Bi:Ti égal à 1:1, les particules qui composent la poudre sont presque entièrement sphériques et sont associées en groupes de plusieurs unités. Les particules sont agrégées avec des interconnexions similaires à celles qui se forment lorsque les gouttelettes entrent en collision et subissent ensuite une séparation par étirement, laissant un filament qui finit par agréger les particules. La façon dont deux gouttelettes entrées en collision se séparent dépend des paramètres physiques des liquides, comme la taille ou la viscosité des gouttelettes. La solution contenant le précurseur de bismuth, à base d'acide acétique et acétone, a modifié la viscosité et la tension de surface de la solution. L'augmentation de l'acidité par l'introduction d'acide acétique diminue la tension superficielle des gouttelettes. Le matériau amorphe obtenu est composé de particules dans lesquelles la matière est répartie de manière dense (absence de porosité) et homogène. Les deux métaux, le titane et le bismuth, sont mélangés de maniéré très intime démontre l'intérêt du procédé SFS. Les deux précurseurs étant dissous dans le même solvant, la

précipitation forcée induite par l'évaporation flash contraint les éléments à rester mélangés à l'échelle moléculaire dans le matériau final. Le matériau a été calciné à 650°C sous air pendant 4 heures. Les particules qui constituent la poudre de ce titanate de bismuth sont fortement agrégées entre elles. La calcination élimine les résidus organiques et réorganise la répartition des éléments. La formation de la structure cristalline de la pérovskite est le résultat du regroupement en couches et de l'empilement de l'oxyde de titane et de l'oxyde de bismuth. Cela n'est possible que si les différentes molécules d'oxyde passent du désordre caractérisant l'état amorphe à un ordre périodique. Les particules sont constituées de plusieurs cristallites qui s'organisent en unités polycristallines. La température élevée appliquée durant la calcination du matériaux permet cette réorganisation, mais elle s'accompagne aussi d'un frittage des particules. En conséquence, la taille des particules augmente et les particules perdent leur indépendance. La distribution des éléments est néanmoins conservée après le traitement thermique. Cela provient du fait que les éléments métalliques, titane et bismuth, sont mélangés dans une proportion qui conduira à une phase unique de titanate de bismuth. On peut observer que la composition du matériau cristallisé est pure, car aucun autre pic de diffraction n'est présent. Cela signifie que les deux métaux, le bismuth et le titane, ne forment qu'un seul oxyde. Dans ce cas, le matériau est identifié comme étant le titanate de bismuth $Bi_2Ti_2O_7$. D'après le diagramme de phase publié dans la littérature, la phase stable qui se forme à 650°C avec une proportion équimolaire de bismuth et de titane est le titanate $Bi_{12}TiO_{20}$. La phase obtenue expérimentalement, $Bi_2Ti_2O_7$ n'est stable qu'à 1195°C, ce qui montre que la formation d'une phase ne dépende pas seulement de la composition et de la température, mais aussi du degré d'intimité du mélange des phases initiales.

Un titanate de bismuth avec une teneur plus élevée de bismuth a été préparé en mélangeant dans un rapport molaire Bi/Ti de 2:1 les précurseurs de bismuth et de titane. Cette poudre fine et libre est composée de particules sphériques dont la taille est submicrométrique. La matière dont sont composées les particules est amorphe. Le matériau est traité thermiquement à 650°C sous air pendant 4 heures. Ce traitement thermique induit la cristallisation du matériau. Cela a pour effet secondaire le frittage des particules. Les particules perdent leur morphologie sphérique à cause de la calcination. Le bismuth et l'oxyde de titane s'empilent en une structure de type pérovskite comme dans le cas des autres matériaux à base de bismuth et d'oxyde de titane préparés. Les particules sont formées par l'agrégation de plusieurs cristallites.

D'après le diagramme de phase des oxydes de titane et de bismuth, les phases stables à 650°C, pour un pourcentage molaire Bi/Ti égal à 67/33 sont, le titanate $Bi_{12}TiO_{20}$ et l'oxyde de bismuth (α-Bi_2O_3). Si le matériau obtenu contient bien de l'oxyde de bismuth (excès) la phase de titanate de bismuth formée est $Bi_4Ti_3O_{12}$ ($2Bi_2O_3$ - $3TiO_2$) qui devrait normalement apparaître à 873°C. Cependant, la stabilité de la phase obtenue dépend de la taille. La structure de $Bi_4Ti_3O_{12}$ est différente de celle de la phase $Bi_2Ti_2O_7$. Ce composite est formé d'une couche d'oxyde de bismuth (α-Bi_2O_2) alternée avec une couche de pérovskite comme celle de $Bi_2Ti_3O_{10}$. L'excès d'oxyde de bismuth a conduit à la formation et à la ségrégation de la phase alfa monoclinique. L'oxyde de titane et l'oxyde de bismuth sont tous deux mélangés à l'échelle moléculaire et la qualité de ce mélange est conservée même après calcination. On peut également observer que l'excès de bismuth, sous forme d'oxyde de bismuth, n'a pas formé de zones séparées d'oxyde de bismuth pur. L'oxyde de bismuth recouvre les particules de titanate de bismuth. Ceci pourrait être confirmé par un phénomène de décomposition qui a eu lieu pendant l'imagerie TEM. L'"exsudation" de Bi_2O_3 produit un rétrécissement des particules (10% de la taille). La décomposition de l'oxyde de bismuth en bismuth pur et en oxygène a été vérifiée des analyses EDX. A la périphérie des particules, des excroissances hémisphériques, qui ne contiennent que du bismuth peuvent être identifiées. La facilité de réduction des nanoparticules d'oxyde de bismuth dépend de la taille, ce qui signifie que plus la taille est petite, plus il est facile de former du bismuth métallique. Les échantillons qui sont irradiés par le faisceau d'électrons du émis par le MET s'échauffent d'autant plus facilement qu'ils sont formés des particules isolées et de petite taille. Ces phénomènes ainsi que la présence des électrons, qui facilite les réactions de réduction, pourraient expliquer la décomposition en bismuth des fines particules d'oxyde de bismuth qui sont présentes dans le titanate de bismuth. De plus, le vide favorise la décomposition de l'oxyde de bismuth nanométrique car il facilite la libération d'oxygène. Les particules de BiTi 2:1 proviennent de la fusion de particules plus petites et de la réorganisation de la structure de la matière première. La forme irrégulière des particules de la matière non calcinée est accentuée par la calcination. Le frittage des petites particules en particules plus grosses produit une augmentation de la taille moyenne des particules par rapport à celle de la matière première.

La poudre brute préparée par SFS est composée de particules sphériques submicroniques. Cette poudre est formée de particules fines mais agrégées. Les

particules sont presque totalement remplies de matière, la structure interne n'est pas totalement homogène. Cela est attribué, à la réaction partielle du précurseur de cuivre qui laisse de petits cristaux de rouaite ($Cu_2(NO_3)(OH)_3$) et de nitrate d'ammonium (NH_4NO_3) incorporés dans la matrice d'oxyde de titane amorphe. Ces espèces intermédiaires se forment à la température de travail comme dans le cas de la production d'oxyde de cuivre pur. Elles sont formées par la réaction entre le nitrate de cuivre (précurseur de l'oxyde de cuivre), et l'ammoniac (le réactif partenaire). Toutes les particules contiennent les deux éléments, le titane et le cuivre, distribués à l'échelle moléculaire. Néanmoins, certains domaines présentent une concentration en cuivre plus élevée que d'autres. Cela est attribué à la réaction incomplète du précurseur. Comme le précurseur n'est pas totalement décomposé, il forme des cristallites dans lesquels la concentration de cuivre est plus élevée.

Après avoir été calcinées à 400°C, les particules conservent une morphologie sphérique, mais fusionnent légèrement entre elles. La poudre calcinée a une texture fine et lâche, dont la couleur passe du bleu clair au jaune brunâtre. Les particules calcinées à cette température sont encore amorphes. À cette température, la cristallisation et la réorganisation de la matière n'ont pas eu lieu. C'est pourquoi les particules sont très poreuses. Cette porosité est due à la gazéification des espèces non-métalliques contenues dans le matériau. L'élimination de la fraction gazéifiable et de l'eau se produit avant que le réseau ne se consolide (ce qui nécessite une température plus élevée). Cela explique que ce matériau a une aire spécifique élevée.

La densité de ce mélange, qui a été mesurée par pycnométrie à l'hélium, est inférieure à la valeur théorique calculée. Cela peut s'expliquer par la présence d'une porosité interne qui se forme lors de la calcination par la décomposition de la fraction gazéifiable dans la matrice du matériau. La porosité de ce matériau est de 12.5%. En tenant compte de l'aire spécifique de ce matériau et de la densité mesurée par la pycnométrie, la porosité de surface de ce matériau a été calculée à 6.2%. Ainsi, la porosité interne peut être calculée comme la différence entre la porosité totale du matériau moins la porosité de la surface du matériau. La porosité interne du matériau est de 6.3 %, ce qui représente environ la moitié de la porosité du matériau.

La poudre produite par calcination à 600°C a un aspect fin et meuble avec une couleur rouge-brunâtre. Les particules de cette poudre conservent un aspect sphérique, mais ce sont surtout les plus petites particules qui perdent leur identité et sont fusionnées.

La restructuration de l'oxyde de titane et de l'oxyde de cuivre présents dans le matériau conduit à la cristallisation de ces oxydes sous forme de phases distinctes. La structure poreuse interne et externe est totalement perdue par rapport au matériau calciné à 400°C.

La cristallisation de la matière a conduit à une structure polycristalline d'oxyde de titane comprenant les deux phases principales de cet oxyde, l'anatase et le rutile, ainsi que de l'oxyde de cuivre (II). La présence d'anatase et de rutile dans ce matériau peut être expliquée par la transition anatase - rutile (ART), comme nous l'avons vu précédemment. Dans ce cas, cette transition est également influencée par la présence de l'oxyde de cuivre. On remarquera que l'anatase présente ne forme pas de nouvelle structure cristalline avec l'oxyde de cuivre et n'empêche donc pas la transformation en rutile. La proportion d'anatase qui s'est transformée en rutile est d'environ 30%. Les oxydes sont mélangés de manière homogène dans la majeure partie du volume des particules, principalement dans la partie interne des plus grosses particules. A l'inverse, les plus petites particules et la partie extérieure des grosses particules sont principalement constituées d'oxyde de titane. Comme nous l'avons vu précédemment, le matériau amorphe calciné à 400°C est un mélange parfaitement homogène des deux oxydes, ce qui signifie que la ségrégation et la concentration de l'oxyde de cuivre dans la partie interne des particules se produisent lors de la calcination. Il semble exister deux populations de particules, l'une d'environ 175 nm et l'autre d'environ 275 nm. L'introduction de CuO dans le système TiO_2 conduit à des modifications de limite de grain. Celles-ci affectent fortement les propriétés des joints de grain de l'oxyde de titane. La température de frittage et de densification du matériau est abaissée de plusieurs centaines de degrés. Par conséquent, lorsque la cristallisation a lieu pendant le traitement thermique, les nanocristaux d'oxyde de cuivre forment de très petits domaines d'oxyde de cuivre. La petite taille de ces particules abaisse la température de fusion de l'oxyde de cuivre. Ces deux effets entraînent une diffusion de l'oxyde de cuivre par capillarité à travers la matrice d'oxyde de titane, qui est thermiquement plus stable. L'oxyde de cuivre liquide fusionne alors en domaines plus grands et se solidifie lorsqu'une masse critique est atteinte, ce qui conduit finalement à une séparation des phases. La densité de ce mélange a été mesurée par pycnométrie à l'hélium. La densité mesurée de ce composite est légèrement supérieure à la valeur théorique calculée en tenant compte d'un rapport de 1:1 entre l'oxyde de titane (anatase et rutile) et l'oxyde de cuivre.

Le **quatrième chapitre** traite de l'application pyrotechnique des matériaux qui ont été produits. Le but était de produire un composé énergétique de peu sensible (grâce à l'oxyde de titane) et à haute performance énergétique (grâce à l'oxyde de cuivre). Le composite d'oxyde de cuivre et d'oxyde de titane préparé par SFS a été utilisé pour la production de compositions aluminothermiques. Des nanothermites avec différentes proportions d'oxydant par rapport au combustible (Al nanométrique) ont été préparées et analysées en termes de seuils de sensibilité et de chaleur d'explosion. Enfin, la combustion de ces compositions a été testée dans des tubes.

Le mélange de CuO et TiO_2, préparé par le procédé SFS, a été utilisé comme oxydant pour la production de nanothermites. Pour comprendre les propriétés énergétiques des oxydes mixtes, des nanothermites avec différentes proportions combustible/oxydant (rapports d'équivalence φ), ont été préparées. Les mélanges ont été préparés en ajoutant de la poudre d'aluminium nanométrique soit dans un rapport stoechiométrique (φ=1; CT410 et CT610), soit avec un excès de combustible de 40% (φ=1,4; CT414 et CT614), aux quantités correspondantes d'oxydes mixtes. En outre, pour comprendre l'influence de la surface et de la cristallinité sur les propriétés pyrotechniques, les mélanges d'oxydes calcinés à deux températures différentes: 400°C (CT410 et CT414) et 600°C (CT610 et CT614) ont été utilisés, donnant quatre compositions différentes de nanothermite.

Le comportement thermique des nanothermites préparées a été mesuré par calorimétrie différentielle à balayage (DSC). Tous les échantillons possèdent une bonne stabilité thermique jusqu'à 150°C. Les nanothermites CT410 et CT414 présentent toutes deux un pic exothermique entre 240°C et 250°C. Cette libération d'énergie est produite par la réaction de l'eau avec l'aluminium. L'eau est piégée dans les oxydes mixtes en raison de leur surface spécifique élevée (125 $m^2\ g^{-1}$). Elle se désorbe par chauffage et réagit avec les particules d'aluminium environnantes. La vapeur d'eau réagit, à cette température, avec l'aluminium à proximité de l'interface Al/Al_2O_3. Cela renforce la couche d'oxyde et passive les particules contre une oxydation plus profonde. Cela expliquerait pourquoi seule une partie de l'eau a réagi avec l'aluminium. L'eau désorbée provient principalement de la surface de l'oxyde. Dans le cas des nanocomposites CT610 et CT614, qui ont une surface très faible, des signaux exothermiques faibles sont observés à ~250°C. L'échantillon CT610 est celui qui contient le moins d'aluminium, et donc le moins d'eau adsorbée. C'est la raison pour laquelle le phénomène d'oxydation est moins marqué pour cet échantillon.

L'aluminium contenu dans les échantillons fabriqués à partir de mélanges d'oxydes calcinés à des températures plus élevées, a plus tendance à réagir avec l'oxygène gazeux qu'avec les oxydes solides, ce qui indique que ces derniers sont moins réactifs.

Tous les nanothermites sont moins sensibles aux chocs (>100 J) que les nanothermites constitués d'oxyde de cuivre nanométrique pur et de poudre de nano aluminium (90 J). Ces nanopoudres ont une porosité interparticulaire élevée, ce qui signifie qu'elles ont un volume proportionnellement élevé rempli d'air car les particules sont très peu tassées (TMD < 10%). Les particules étant de nature minérale, elles ne sont pas sensibles à un sollicitation thermique modérée. Cela explique la faible sensibilité de ces nanothermites à l'impact. La nanothermite Al/CuO est plus sensible à l'impact que les mélanges préparés par SFS car la propagation de la réaction, lorsqu'elle est déclenchée par une forte contrainte, est limitée par la présence de l'oxyde de titane. À l'exception de la composition CT610 dont le seuil de sens-au frottement est de 216 N, toutes les nanothermites sont insensibles au frottement car leurs seuils d'activation sont l'effet de supérieures à 360 N. La taille des nanoparticles constituant les nanothermites est beaucoup plus petite que la rugosité des éléments en céramique utilisés dans le dispositif de test de sensibilité à la friction. Par conséquent, l'efft de lubrification atténue la contrainte, qui n'est pas assez forte pour activer la réaction d'aluminothermique. Les seuils de sensibilité à l'ESD sont habituels pur des nanothermites, car dans ce type d'épreuve, une grande quantité d'énergie est transmise aux nanoparticules en un temps très court (forte puissance). En règle générale, les compositions énergétiques contenant des poudres métalliques fines sont sensibles à l'ESD. La sensibilité à l'ESD de l'aluminium pur sous air a été mesurée (1,42 mJ) et s'est avérée plus élevée que celle des nanothermites préparées. Cela signifie qu'il y a une sensibilisation de l'aluminium en présence des oxydes. L'oxydation de l'aluminium par les oxydes avec lesquels ce métal est en contact étroit est plus probable que l'oxydation par l'oxygène de l'air. Les seuils de sensibilité à l'ESD obtenus avec ces composites sont dans la gamme habituelle des seuils de sensibilité `l'ESD des nanothermites.

Les chaleurs d'explosion mesurées dans chaque cas sont supérieures aux valeurs déterminées par le calcul théorique, en considérant les systèmes Al/CuO et Al/TiO_2. L'analyse par diffraction des rayons X a permis d'identifier, les différentes phases cristallines produits par la réaction. La présence de monoxyde de titane indique que TiO_2 n'a pas été totalement réduit. Il y a donc un excès de combustible, car les

proportions des nanothermites ont été calculées en tenant compte de la réduction complète de l'oxyde de titane. Cet excès de combustible disponible permet la réaction entre le cuivre métallique réduit in situ et l'aluminium pour former un alliage. Cet alliage est formé par une réaction intermétallique qui libère de l'énergie supplémentaire.

La combustion des nanothermites a été testée dans des tubes en PMMA transparents. Ces expériences sont fournies des informations sur la combustion des nanothermites préparées. La densité théorique maximale de chaque nanothermites a été calculée à partir de la densité des constituants et de leur teneur dans le mélange. Le pourcentage de densité maximale théorique (TMD) des nanothermites CT410 et CT414 est inférieur à celui des nanothermites CT610 et CT614. Cela signifie que les particules d'oxyde et les particules d'aluminium sont disposées de manière moins compacte dans les deux premiers cas. L'accélération de la combustion observée au du début de l'essai donne une indication sur la sensibilité du matériau à l'inflammation sous l'actions d'une sollicitation thermique. La vitesse de combustion passe par un maximum au début puis commence à diminuer. Les vitesses de propagation de flamme obtenues sont caractéristiques des déflagrations. Le degré d'agrégation des nanothermites a une forte influence sur la valeur d'accélération et donc sur la sensibilité à l'inflammation. Les espèces adsorbées, comme l'eau sur CT410 et CT414, rendent la réaction plus irrégulière car plusieurs réactions ont lieu en même temps. Dans les oxydes calcinés à 600°C, l'absence d'espèces adsorbées rend la réaction plus homogène.

Le **cinquième chapitre** présente l'étude comparative de l'activité photocatalytique de différents matériaux préparés par SFS en vue de la production d'H_2 à partir du photoreformage du méthanol. Les caractéristiques photocatalytiques des matériaux ont été analysées par spectroscopie UV-Vis. Les performances de ces matériaux utilisés comme photocatalyseurs pour le photoreformage du méthanol (CH_3OH) ont été comparées.

Les propriétés photocatalytiques des poudres d'oxyde de titane synthétisées par le procédé SFS selon trois rapports molaires eau/titane différents (1:1, 1:2 et 1:4). Les propriétés optiques des matériaux en termes d'absorbance UV-Vis ont été comparées à celles du dioxyde de titane commercial, TiO_2 P25 (Evonik), composé d'environ 80% d'anatase et 20% de rutile. On peut observer que les échantillons préparés par SFS présentent un domaine d'absorbance décalé vers les longueurs d'onde plus élevées, cet effet étant le plus marqué le TiO_2 synthétisé selon un rapport molaire 1:1. Cet élargissement du domaine d'absorption de la lumière visible pourrait provenir de la présence de résidus à base de carbone incomplètement éliminés lors de l'étape de calcination à température modérée. De plus, les matériaux préparés par SFS sont composés de particules de taille submicrométrique d'anatase pure, ce qui pourrait expliquer la diffusion à des longueurs d'onde plus élevées. La largeur de bande interdite calculée pour les matériaux synthétisés est égale à la bande interdite théorique de l'anatase pure (3.2 eV). Ces matériaux ont été testés dans e dispositif expérimental développé pour étudier le photoreformage du méthanol. Les matériaux préparés par SFS présentent, malgré une surface et un rapport surface/volume plus faibles, un taux de production d'hydrogène plus élevé que le matériau de référence. Cela est d'autant plus remarquable que le temps nécessaire au transfert de charges interfaciales (en particulier pour les électrons) est beaucoup plus long pour les particules plus grosses, ce qui augmente la probabilité de recombinaison des porteurs de charge. Le rendement quantique apparent des matériaux préparés par SFS est jusqu'à quatre fois plus élevé que celui du matériau de référence.

Les propriétés photocatalytiques de la poudre d'oxyde de titane modifiée à l'argent préparée par SFS ont été étudiées. Les propriétés optiques du matériau en termes d'absorbance UV-Vis sont comparées à l'échantillon commercial de TiO_2 P25 (Evonik). Par rapport à la référence, l'oxyde de titane modifié à l'argent présente une absorption plus large dans le spectre visible, ainsi qu'un décalage vers le rouge de l'absorbance du TiO_2. Ces effets pourraient être attribués à la résonance plasmonique de surface

(SPR) des nanoparticules d'argent ou à la formation d'espèces de surface Ag_xO. D'après la spectroscopie d'absorbance, la bande interdite de ce matériau est égale à 2.8 eV. Elle est donc plus petite que celle de l'anatase (3,2 eV) préparée par SFS et que celle du TiO_2 de référence (P25: 3.1 eV). La vitesse de production d'hydrogène est non seulement supérieure à celle qui est observée avec le matériau de référence (P25), mais également à celle du TiO_2 pur préparé par SFS. Ces observations pourraient être attribuées à la résonance plasmonique de surface (SPR) des nanoparticules d'argent ou à la formation d'espèces de surface AgxO. La présence de nanoparticules d'argent, avec de propriétés SPR, pourrait expliquer l'absorption accrue des photons grâce à l'amélioration du champ local ou à l'injection d'électrons chauds dans la bande de conduction du TiO_2. En outre, la présence de domaines Ag_xO de surface en contact étroit avec le TiO_2 peut conduire à la formation d'hétérojonctions bénéfiques pour la performance de la réaction. De plus, les particules d'argent, qui se trouvent principalement à la surface des sphères de titane, peuvent agir comme des pièges à porteurs de charge, réduisant ainsi la probabilité de recombinaison et augmentant la performance photocatalytique globale. L'absorption plus élevée de la lumière due au décalage vers le rouge de l'absorbance permet d'avoir une plus grande quantité de porteurs de charge disponibles pour la réaction catalytique. Ces phénomènes expliquent pourquoi ce matériau a un taux de production plus élevé et une utilisation plus efficace des photons absorbés.

L'activité photocatalytique des trois de titanates de bismuth produits par SFS a été étudiée par spectroscopie UV-Vis et comparée à celle du dioxyde de titane pur P25. Les bandes interdites de titanates de bismuth préparés par SFS sont inférieures à celles du titane pur. La bande interdite inférieure est déterminée par les orbitales 3d du titane qui fournissent la bande de conduction et les orbitales 2p qui fournissent la bande de valence. La modification de la structure du TiO_2 par le bismuth (cationique) introduit des états intermédiaires sous la bande de conduction, ce qui abaisse la bande interdite. Les titanates de bismuth BiTi 1:1 et BiTi 1:1.35 réagissent de manière similaire au matériau de référence (P25). Le matériau à plus forte teneur en bismuth, (BiTi 2:1), a une production d'hydrogène inférieure à celle de tous les autres matériaux. La principale différence entre B1T1 et BiTi 1.35 est la présence d'un excès de titane sous forme de rutile pour le BiTi 1.35 augmente légèrement le taux de production. Le faible taux de production d'hydrogène obtenu avec les titanate de bismuth est attribué au taux élevé de recombinaison des porteurs de charge dans ces matériaux. Le

rendement quantique de ces matériaux est jusqu'à deux fois plus élevé que celui du matériau de référence. C'est une conséquence de l'absorption plus élevée dans la région visible et de la formation de l'hétérojonction entre les différents matériaux semi-conducteurs. Ces phénomènes conduit à une meilleure séparation des charges.

Les propriétés photocatalytiques du mélange d'oxyde de cuivre et d'oxyde de titane sous forme de poudre préparé par SFS ont été étudiées. Les propriétés optiques du matériau soumis à une irradiation UV-Vis ont été comparées à celles d'un échantillon commercial de TiO_2 P25 (Evonik). La bande interdite calculée du matériau composite cuivre/titane est égal à 1.26 eV, soit environ un tiers de la bande interdite de l'anatase pure. Le taux de production d'hydrogène atteint avec ce matériau surpasse celui qui a été obtenu avec tous les autres matériaux produits par SFS. La forte activité photocatalytique de ce matériau est due au contact intime des différentes phases à base de Ti-, Cu- ou Cu-Ti, qui favorise la formation d'hétérojonctions entre les différents matériaux semi-conducteurs, ce qui permet d'accroître les propriétés de séparation de charge mais aussi à la capacité des phases Cu_xO à absorber les photons de la lumière visible. Il convient de souligner que le cuivre peut également agir comme co-catalyseur pour les réactions de photoreformage du méthanol. L'activité globale est accrue parce que les électrons excités sont photogénérés dans les bandes de conduction des deux oxydes, ce qui entraîne une accumulation d'électrons en excès dans la bande de conduction du CuO. L'introduction de l'oxyde de cuivre dans le d'oxyde de titane est bénéfique pour la séparation des charges pendant la réaction photocatalytique et agit comme site de réduction de l'eau. Le rendement quantique du mélange cuivre/oxyde de titane est 8.4 fois plus élevé que celui du TiO_2 de référence. Compte tenu du taux ces phénomènes, la production d'hydrogène est plus élevé et l'utilisation des photons absorbés est plus efficace.

INDEX

INTRODUCTION

Nanotechnology is the field of techniques and knowledge that covers the matter and its interaction with energy at a scale between 1-100 nm. Nanomaterials are the elementary bricks needed to build nanostructured macroscopic objects. By merging this two worlds new characteristics appear. New macroscopic materials and properties arise owing to the structures built from bricks of nanometric dimensions. Nanotechnology is a new branch that found applications in nearly all the known domains, from nanomedicine to nanoelectronics.

The aim of this work is to study and develop a new synthesis method for the production of submicrometric metal oxides and their mixtures. The objective was to produce materials small enough to have the attractive characteristics of the nanometric scale and at the same time big enough to avoid the health problems that involve the use of nanomaterials. Additionally, the production of submicrometric materials made of mixed elements that, from a pyrotechnic and photocatalytic point of view had opposing properties, aimed the idea of producing compounds with intermediate characteristics. Furthermore, this research work had the purpose to study the different kind of phases of the materials produced under these conditions.

Therefore, **the first chapter** analyses the state of the art in nanomaterial synthesis methods. The production ways were compared. This study aimed to understand the various approaches and challenges that arise from the synthesis of this kind of materials and how they were solved up to the present date. Therefore the key parameters (temperature, precursor nature and reaction time) that influence the reaction are highlighted.

Basing on the gathered information, **the second chapter** describes how the initial spray flash evaporation (SFE) system was modified into the spray flash synthesis (SFS) system. The setup was upgraded at several points to reach the necessary stability and reaction conditions to be able to synthetize submicrometric particles. These modifications as well as how they affect the synthesis method are described, from the precision valves up to the upgraded powder recovering system to name a few. After this, the production protocols for the various synthesized materials are detailed. Then, the characterization methods that were applied to analyse the properties and features of the prepared materials are described along with their specific use in this work. Structural, morphological and chemical analysis methods were used to fully

understand the characteristics of the powders. This is followed by the preparation of energetic materials (nanothermites) based on the oxides produced by this method. The description of the specific pyrotechnic characterization methods closes the pyrotechnic subchapter. The materials were likewise applied in the photocatalytic field for the methanol photoreformation. This domain has also its particular characterisation methods, which were equally described in this chapter.

The properties of the different kinds of materials that were produced by the SFS system are detailed in **the third chapter**. The idea was to produce smaller particles than those prepared by similar methods in a continuous process. For this purpose pure titanium oxide was prepared. This material was also modified with silver. Then bismuth titanates were prepared in different bismuth to titanium proportions. To further understand the degree of mixture attained by the process a composite made of titanium oxide and copper oxide was studied. Therefore, pure copper oxide was produced first, followed by an oxide mixture (CuO/TiO_2). These materials were interesting to study the stability of the different phases in which they crystallized.

The fourth chapter treats the pyrotechnical application of the as produced materials. The aim was to produce an energetic compound with a low sensitivity (brought by titanium oxide) and a high energetic performance (brought by copper oxide). The copper oxide and titanium oxide composite prepared by SFS was used for the production of aluminothermic compositions. Nanothermites with different oxidizer to fuel proportions were prepared and analysed in terms of sensitivity thresholds and explosion heat. Finally, the combustion of these compositions was tested in tubes.

The fifth chapter highlights the application of the as prepared material in the photocatalytic domain. The objective was to prepare a more efficient catalyst for the methanol photoreformation. The materials produced were analysed in this perspective. The optical and electronic properties were taken into account along with the morphology and surface area of the particles. The materials were used in a prototype setup built for the methanol photoreformation. The different compounds were compared in terms of reaction yield and quantum yield for this reaction.

The conclusion summarizes the results and the deductions generated within the framework of this research, which pointed out the advantages of the SFS process over the other synthesis methods for the preparation of nanomaterials with unique

properties and charactersitics. The focus is also placed on the main results obtained in the application of nanomaterials prepared by SFS in the photocatalytic and pyrotechnic domain.

STATE OF THE ART

Chapter I

1. Glossary

TTIP: Titanium tetraisopropoxide

SFS: Spray Flash Synthesis

SFE: Spray Flash Evaporation

CVD: Chemical Vapour Deposition

PVD: Physical Vapour Deposition

FSP: Flame Spray Pyrolysis

ESD: Electrostatic Discharge

CSD: Chemical Solution Decomposition

MPA: Microstrip Patch Antenna

UV: Ultraviolet light

PVP: Polyvinylpyrrolidone

PEG: Polyethylene Glycol

TNT: 2,4,6-trinitrotoluene

CL-20: Hexanitrohexaazaisowurtzitane

HMX: Octahydro-1,3,5,7-tetranitro-1,3,5,7-tetrazocine

ADN: Ammonium DiNitramide

RDX: cyclotrimethylenetrinitramine

2. Introduction

The bibliographic chapter is built around the spray flash synthesis (SFS) system and the materials prepared by it. The materials studied are pure titanium dioxide (TiO_2) or silver-charged titanium dioxide; bismuth titanates ($Ti_xBi_yO_z$) and mixtures of copper (CuO) and titanium (TiO_2) oxides. The focus is placed on the classical processes used to synthesize these materials such as sol-gel, hydro and solvothermal synthesis or physical and chemical vapour deposition. Furthermore, this chapter analyses the precursors used to synthesize them, but also their use in different types of applications, especially in photocatalysis and pyrotechnics.

The framework of this study is based on several points. First, the identification of the precursors that can be used as well as the experimental conditions which must be applied in the SFS process to obtain the desired materials. Secondly, to understand how the classical synthesis methods work, to be able to compare them with the SFS process. This will be done essentially through the materials produced by these different techniques. And finally, to introduce the SFE process. This is fundamental, in order to show what are the necessary modifications to pass from physical submicromisation by flash evaporation (SFE) of the solvent to chemical submicromisation by flash spray synthesis (SFS process).

3. Applications of the oxides studied

3.1. Titanium dioxide

Titanium oxide is one of the most investigated nanomaterials. As bulk matter it has been used for different purposes like biomedical devices, cosmetics and pigments or additives for colours. At nanoscale it has a wide application range in the fields of energy, sensors and photocatalysis, which are justified by its optical, dielectric and catalytic properties. This semiconductor shows some advantages compared to others with similar properties, like relative low production costs and chemical and thermal stability. The main factors that influence in the final performance of this material are size, morphology and crystalline phase.

Titanium oxide appears in nature in three allotropic forms. The most stable one and therefore the most common one is rutile, after that brookite and the last is anatase.[1] These three forms of titania have an octahedral configuration.[2] But they differ in the amount of edges they share. Other less common crystallographic phases exist, these are the cases of TiO_2 (II) which has columbite (α-PbO_2) type, TiO_2 (B) with a baddeleyite (ZrO_2) type, TiO_2 (H) with a hollandite type or TiO_2 (R) with a ramsdellite (MnO_2 or VO_2) type. But there exist also metastable phases. This is the case for TiO_2-OI, the fluorite (CaF_2) like cubic phase and for TiO_2-OII, the cotunnite ($PbCl_2$) like phase.[3]

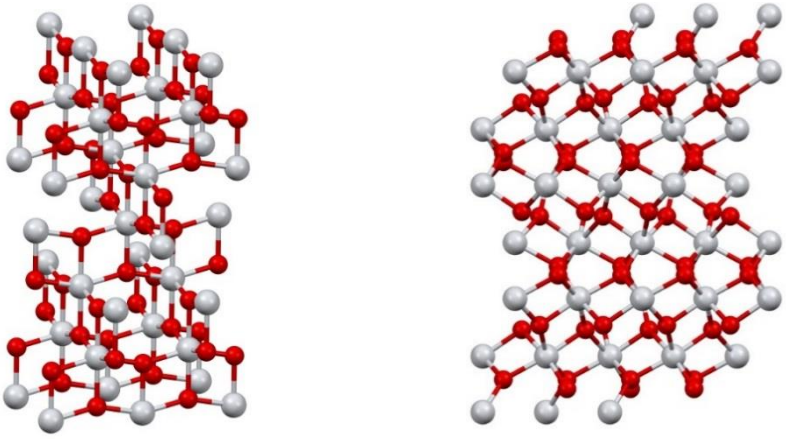

***Figure 1**. From right to left: Titanium oxide in anatase form and titanium oxide in rutile form. (Model by Avogadro)*

The thermodynamic stability of the phase depends on the particle size, due to the fact that energies of rutile, brookite and anatase are close. This means that a phase change can occur by small differences in the surface energy. On the ground this implies that anatase is stable at sizes below 11 nm, brookite is the predominant crystal phase for particles between 11 and 35 nm and finally rutile is the most stable for particles with a size above 35 nm.[4]

As mentioned before there are many different uses for titanium oxide. It is mainly used as white pigment for different kind of products, but also as filling material in the paper and plastics industry.[5] When the average particle size of TiO_2 falls below 100 nm, its optical properties change, its electromagnetic absorbance shifts from the visible region to the ultraviolet, this means, it becomes highly transparent to visible light and becomes absorbent to UV radiation.[6] This nearly transparent appearance of nano-sized titanium oxide particles creates some iridescent visual effects. Consequently, the cosmetic and ceramics industry uses it in coating applications or as additive.

Even if already in 1964, Kato *et al.* published their work using a TiO_2 suspension to photocatalytically oxidise tetralin, the milestone in this domain was the work of Fujishima and Honda in 1972.[7] [8] The "Honda-Fujishima effect" stimulated the research in the photocatalytic domain, creating a completely new research front which has hosted a significant amount of investigation over the last decades. The characteristics of titania makes it an excellent candidate for environmental purification by photocatalysis.[9] The variety in the nature of the wastes produced by humanity is rich, in other words, the amount of chemical compounds of which the waste is build up span over a broad spectrum. Some of them are alkanes, haloalkanes, aliphatic alcohols, carboxylic acids, alkenes, aromatics, haloaromatics, polymers surfactants, herbicides, pesticides and dyes. Picking a few as a representation, some of the photocatalytically oxidised compounds are 4-chlorophenol (C_6H_5ClO), chloroacetic acid ($C_2H_3ClO_2$) or trichloroethylene (C_2HCl_3).[10]

3.1.1. Photocatalytic applications of titanium dioxide in the thesis

The titanium oxide submicrometric powders produced in the thesis were used to study the performance in the photocatalytic reaction, the *production of hydrogen by methanol photoreformation*.

The photocatalytic mechanism depends upon the creation and recombination of electron-hole pairs. For generating these charge carriers, a minimum of energy is needed. This energy corresponds to the energy required to surpass the band gap. The electrons that receive the necessary amount of energy from the photons jump from the occupied valence band to the unoccupied conduction band. The band-gap energies of different semiconductors can be seen in **Figure 2**.[11]

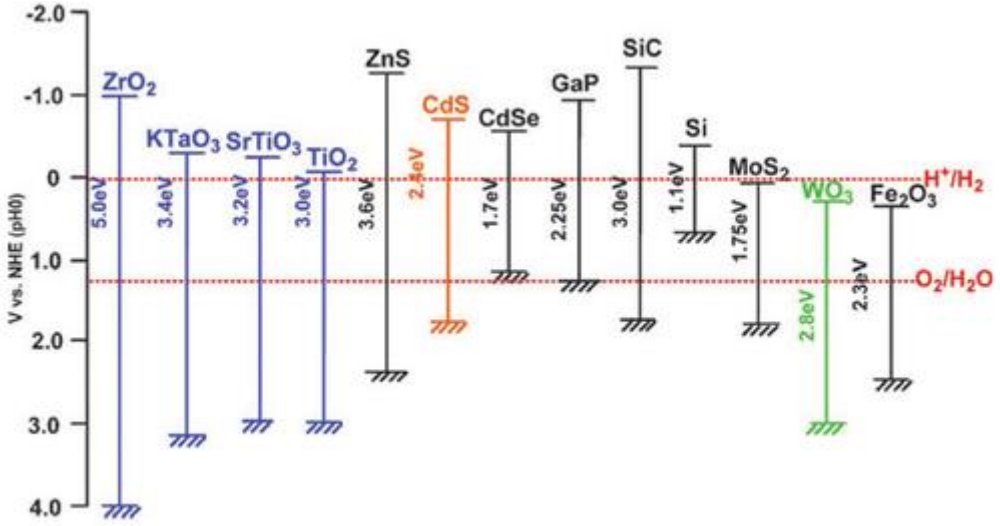

Figure 2. *Band-gap structure of different semiconductors and redox potentials of the water-cleavage reaction.*[11]

These excited electrons leave a positive charge or hole behind. Afterwards this electron-hole pairs are able to initiate chemical reactions. Photogenerated electrons e^- and holes h^+ can diffuse to the surface of the semiconductor particles, and start the following reactions:[12]

Photocatalytic redox pathways:

$$TiO_2 + hv \rightarrow e^- + h^+ \quad (1)$$

$$e^- + Ti(IV)O-H \rightarrow Ti(III)O-H^- \quad (2)$$

$$h^+ + Ti(IV)O-H \rightarrow Ti(IV)O^{\cdot}-H^+ \quad (3)$$

$$h^+ + 1/2\, O^{2-}_{lattice} \rightleftharpoons 1/4\, O_2(g) + Vacancy \quad (4)$$

$$e^- + O_{2,s} \rightarrow O^-_{2,s} \quad (5)$$

$$O^-_{2,s} + H^+ \rightleftharpoons HO_{2,s} \quad (6)$$

Recombination channels:

$$h^+ + Ti(III)O-H^- \rightarrow Ti(IV)O-H \quad (7)$$

$$e^- + Ti(IV)O^{\cdot}-H^- \rightarrow Ti(IV)O-H \quad (8)$$

$$O^-_{2,s} + Ti(IV)O^{\cdot}-H^+ \rightarrow Ti(IV)O-H + O_{2,s} \quad (9)$$

Therefore, to increase the photocatalytic efficiency of the semiconductor it is of uttermost importance to reduce the recombination rate of the excited electrons with their associated holes. Another way to modify the absorption range of titanium oxide is injecting electrons indirectly through other compounds known as dyes. Dyes are organic or inorganic materials with a narrower band gap as titanium oxide this means that they present absorption in a regime with longer wavelengths, this is visible spectrum or infrared.[13] When the attached dye generates a current produced by photoexcitation and consequently transfers it into the conduction band of the titania substrate the sensitization takes place. Dyes are able to catalyse reactions by themselves but the titanium oxide base is necessary to achieve a charge separation and/or a further chemical reaction on its surface. The sensitization leaves the dye in an oxidized state, which needs to be regenerated by an electron donor, usually the electrolyte, to recommence the cycle. The grade of interaction between the elements present in the system, these are the titanium oxide, the sensitizing dye and the electrolyte, will determine the performance of the photoelectrochemical reaction.[14]

Finally, the physical aspects of the titanium oxide nanoparticles like shape, size and crystallinity influence the whole photocatalytic process. The crystal phases present different band gaps (3.0-3.2 eV), as a consequence the light absorption will be

different. Even having the same chemical composition, anatase and rutile present different electronic behaviour. Rutile has a bandgap of 3.04 eV and anatase has a bandgap of 3.20 eV. This can be explained by the difference in the formed bondings in the crystalline matter. The influence on the nonbonding orbitals around the Fermi level are more important in anatase than in rutile.[15] On the other hand the mixture of anatase and rutile has shown synergic effect in photocatalytic performance. The reason is the different electronic affinity of the two polymorphs despite having the same chemical composition. When the transmitted photonic energy impulses the charge carriers inside the crystalline structure, anatase presents a higher electron affinity than rutile. This means that it will migrate from the later one to the former one, increasing the electron-hole separation.[16]

It has been found that, comparing the three phases, anatase is the most active modification, from a photoreactive point of view. Moreover, the energy accessible for subsequent reactions depends directly on the number of photons that are captured by titanium oxide particles. For the absorption of the photons the scattering, when reaching the matter, as well as the penetration into the core of the particles will define the maximum energy that can be taken by excitation. The light scatters when the size of the particles, which it travels through, is the same or smaller than the wavelength. So the radiation scatters more or less depending on the size of the particles, in smaller crystals the scattering is less than in bigger ones, it is proportional to the Rayleigh dispersion. The smaller the particles are, the higher is the surface to volume ratio, and the larger the surface, the higher the chance of interaction between a reactant and the interface. Also, how deep the photons penetrate into the crystals is directly affected by the rate of photons that are reflected on the surface of the particles. At the same time the reflectance of a surface depends on how homogeneous or heterogeneous the morphology of the interface is. The smoother the shallow layer the higher is the probability of reflection for incident photons, so less will arrive at the inside of the crystallites.[17]

The production of hydrogen from water and methanol is an interesting alternative for the future. [18] This hydrogen production route is interesting as alternative to fossil fuel based synthesis because methanol can be obtained from renewable bio sources.[19 20] The use of hydrogen as a clean fuel for energy is a promising and studied proposition

for sustainable energy production.[21] The reaction pathway is similar to the reaction route of the photocatalysis but in the inverse sense as follows:[22]

Excitation of the photocatalyst:

$$TiO_2 + hv \rightarrow e^- + h^+ \quad (10)$$

Oxydation of methanol:

$$CH_3OH + 2h^+ \rightarrow HCHO + 2H^+ \quad (11)$$

$$HCHO + H_2O + 2h^+ \rightarrow HCOOH + 2H^+ \quad (12)$$

$$HCOOH + 2h^+ \rightarrow CO_2 + 2H^+ \quad (13)$$

Reduction of protons:

$$2H^+ + 2e^- \rightarrow H_2 \quad (14)$$

It has been reported that placing noble metals like Pt, Au, Pd, Rh or transition metals like Ni, Cu and Ag, on to the titanium oxide surface helps the charge-carrier separation. The photo-excited electrons tend to transfer from the conduction band to the metals, as their Fermi level is lower than that of titanium oxide, in the meantime the photo-generated holes stay in the valence band. This reduces the chance of recombination.[23]

A different approach to increase the photocatalytic performance of the material is playing on the optical absorption range. Because titanium oxide is a wide band gap semiconductor, its light absorbance lies in the ultra-violet part of the solar spectrum. For this reason, the goal is to increase the energy intake by shifting the absorbed light to the visible region.[24] In this sense, one option is the substitution of the cation Ti^{4+} by a transition metal, *e.g.* Fe, Co, Ni, Cu and Zn, or rare earth metal, *e.g.* La, Ce, Er, Pr, Gd, Nd and Sm. It should be taken into account that carriers need to be transferred to the desired place, the surface, then only here the photocatalytic reaction can take place. So the doping of the metal ions should be done close to the surface to facilitate the transference of the charge. Just as in the case of the noble metals, the creation of metal inclusions deep inside the materials form recombination centres, reducing the charge carrier efficiency. This means that there is an optimum concentration, where the photocatalytic activity is the highest. The other option is to substitute the anion O^{2-} by a non-metal like C, N, F, P and S. Nonetheless, the most suitable candidate seems to be nitrogen, because it pushes the valence band up narrowing the band gap, without

having problem of excessive ionic radius like sulphur or transference problems like carbon and phosphorus.[25]

The idea of introducing different materials into the titanium matrix is to make it more suitable for a broader range of photocatalytic applications. As seen before pure silver and copper placed on the surface are able to reduce the electron-hole recombination rates. The introduction of bismuth oxide intends to reduce the amount of energy necessary to start the photocatalytic reaction. This is because the band gap of bismuth oxide is smaller than the one of titanium oxide. Thus, the energy from the visible spectra can be absorbed from the former and then transmitted to the later.

3.1.2. Pyrotechnic applications of titanium dioxide in the thesis

Titanium oxide has a weak oxidizing power in aluminothermic compositions. Al/TiO_2 compositions burn slowly and the self-propagation of the reaction is difficult. It has a low adiabatic combustion temperature (T_{ad} = 1799 K). Compared to reaction temperatures of other composites (Al/Fe_2O_3: T_{ad} = 3135 K; Al/Co_3O_4: T_{ad} = 4181 K; Al/CuO: T_{ad} = 2843 K), it is one of the lowest.[26] [27] Boggs et al. observed that the addition of TiO_2 (2 wt.% and 8 wt.%) to ammonium perchlorate (AP) has an inhibiting effect on its deflagrating properties. [28] To make titanium oxide react in a pyrotechnic reaction, a strong reducing fuel is necessary, such as aluminium or magnesium. Nevertheless Reid *et al.* found that titanium dioxide either pure or doped by Fe^{3+} improves the combination rate of AP when it is well dispersed in a nanocomposite propellant charge.[29] The reaction of nanometric aluminium with nanometric titanium oxide was studied by Dargar *et al.* by combustion synthesis. In this case, titanium oxide (d_{avg} = 40nm) and aluminium (d_{avg} = 50nm) were mixed, cold pressed and heated up. The mixture reacted at 860°C giving aluminium oxide and titanium aluminates with a grain size of 100-200 nm.[30] One of the aims of this thesis is to evaluate and understand the role of titanium oxide in energetic materials when accompanied by a more reactive oxide, such as bismuth oxide or copper oxide, by creating an intimate physical mixture.

3.2. Bismuth(III) oxide

As material in bulk form, bismuth oxide is used for many different applications. For example, to produce fireproof papers and polymers. It is also used as environmentally respecting substitute for lead tetroxide (Pb_3O_4) for the production of the pyrotechnical firework effect known as Dragon's egg. Other ways to give use to this material is in the preparation of enamelled cast iron ceramics or even in disinfectants. Working as pigment in the glass and porcelain industry, it is able to substitute the lead oxide.[31]

Nevertheless, it finds mainly its use in the electrochemical applications field. The electrical properties of bulk bismuth oxide, like its conductivity, which gives this material applications as electrode, can also be applied as smoke detector devices, capable of working at elevated temperatures.[32] Or even as ion conducting solid oxide fuel cells owing to the high ion conductivity of the δ- Bi_2O_3 phase at elevated temperatures.[33, 34]

3.3. Bismuth titanate

Bismuth titanates, $Bi_xTi_yO_z$, are known since Aurivillius showed for the first time that there is a family of compounds constructed by alternating perovskite-like layers and $(Bi_2O_2)^{2+}$ layers. The perovskite layers can appear as single, double or triple packages.[35] The bismuth titanate family is an interesting group of materials owing to their electrical and optical properties.[36] There are several bismuth titanates like $Bi_2Ti_4O_{11}$, $Bi_2Ti_2O_7$ (ferroelectric pyrochlorite), $Bi_4Ti_3O_{12}$ (dielectric perovskite), $Bi_{12}TiO_{20}$ (refractive sillenite) or $Bi_{20}TiO_{32}$.[37] [38]

One of which received the most attention is $Bi_4Ti_3O_{12}$. This titanate is constructed by alternative stacking of monolayers of $(Bi_2O_2)^{2+}$ and three layers of TiO_6 octahedra. This ferroelectric material has piezoelectric properties and a high Curie temperature (675°C), which makes it useful for high temperature piezoelectric components, memory storage devices or optical screening devices.[39] In a study, $Bi_4Ti_3O_{12}$ nanoparticles were produced that had a spherical morphology with diameters between 10-90 nm. This powder was successfully applied as photocatalyst for the degradation of methyl orange solution under UV irradiation. Nevertheless, comparing to commercial TiO_2 nanoparticles, the photocatalytic activity of these bismuth titanate particles still needs improvement.[40] Bismuth titanate can act as dielectric resonator, having extremely low dielectric losses up to a very high dielectric constant. This makes it suitable for use in microstrip patch antenna (MPA). This class of antenna have a low profile, low cost, low weight and are ease to produce. They are used in both in military and in commercial applications.[38] Another possible application is in the thermal energy storage, where nanometric $Bi_4Ti_3O_{12}$ has been used as highly refractive pigment. Pale yellow in colour, it has a high infrared reflectance, thus has the potential application in coatings for energy saving surfaces.[41] The photocatalytic activity of both the perovskite and the sillenite structure of bismuth oxide have been compared for the degradation of rhodamine B ($C_{28}H_{31}ClN_2O_3$) under ultraviolet radiation. Both $Bi_4Ti_3O_{12}$ and $Bi_{12}TiO_{20}$ were annealed at different temperatures and studied. Photocatalytically speaking most efficient was the $Bi_4Ti_3O_{12}$ annealed at high temperature (900°C).[42]

Another well studied member of the family is the $Bi_{12}TiO_{20}$, its structure corresponds to the sillenite family. These crystals have singular electronic, optical and photoconductive properties. These original set of characteristics confers the material

the photorefractive effect. The refractive index of this material can change reversibly by light. This feature opens potential applications like reversible recording media for real-time holography or image processing applications. For this purpose, micrometric translucent $Bi_{12}TiO_{20}$ crystals were synthetized and analysed, yielding matter with optical transmission.[43] In an analogous study for the photodegradation of methyl orange, the efficiency of $Bi_{12}TiO_{20}$, instead of $Bi_4Ti_3O_{12}$, was analysed. In this case, it is made of Bi-O polyhedral forming a network connected to TiO_4 tetrahedra. The synthesis method applied was the same, by chemical solution decomposition (CSD). However, this material was not suitable for the photodegradation of methyl orange as the absorption in the visible spectra was weak and mainly overlapped by the absorption of methyl orange.[44] The photodegradation of phenol (C_6H_6O) in water by the sillenite structure of bismuth oxide either under UV or visible light irradiation has also been studied.[45] In another study, the photocatalytic degradation of acid orange 7 ($C_{16}H_{11}N_2NaO_4S$) by $Bi_4Ti_3O_{12}$ under visible light was investigated.[46]

3.4. Copper oxide

In bulk form, copper oxide is used as antifouling paint for materials exposed to sea water. This material is also used to produce ruby-red glass and for the preparation of copper salts. It is also seen as reducing agent in brazing pastes or fungicides.[31] One of the focus of interest of copper oxide is the use for the production of high temperature superconductors. The best known is $YBa_2Cu_3O_7$, which is an oxygen deficient perovskite.[47]

In nanometric form, copper oxide has attractive properties as a p-type semiconductor. In this case, it is used for many applications like gas sensing, catalysis and photovoltaic applications.[48] [49] In catalysis, copper oxide has been used either as direct catalyst or as support for the degradation of nitrous oxide with ammonia and the oxidation of carbon monoxide, hydrocarbon and phenol in supercritical water.[50] Nanometric copper shows antimicrobial properties for a wide range of different bacteria.[51]

Copper oxide excels as oxidizer in the pyrotechnical field. It is one of the most reactive oxides, which is consequence of the oxygen release by the thermal decomposition of cupric oxide (CuO) into cuprous oxide (Cu_2O).[52] It is used also as nanoenergetic gas generator. Al/CuO mixtures release a large amount of gases (34 wt.% of the mass is transformed into gas with a ϕ=1 composition).[53] Nanometric copper oxide hollow spheres were prepared for this purpose leading to a high pressurization rate of 0.745 MPa μs^{-1} and a transient peak pressure of 0.896 MPa.[54]

3.5. Copper oxide/Titanium oxide mixture

There exist different kind of combinations of copper oxide and titanium oxide nanomaterials. Cu_2O/TiO_2 composites preparation methods were reported by several authors. This material is used as photocatalyst for hydrogen production. It is an interesting material owing to the junction of a p-type semiconductor (Cu_2O) and a n-type semiconductor (TiO_2) which can absorb a wider part of the radiation of the solar spectrum and a better charge carrier separation.[55]

However, most of the literature describes titanium oxide modified by copper oxide nanomaterials. This kind of modified or doped materials have been used as photocatalysts. In one study, copper oxide nanparticles were loaded onto the surface of commercial titanium oxide by photodeposition. This material was used as catalyst for the photodegradation of cyanide ions (CN^-).[56] A core-shell material made of a titanium oxide core and a copper oxide shell was prepared in another study. In this case, the material was used as photocatalyst for the hydrogen production though water-splitting.[57] A more intimate mixture of these elements was prepared where the nanoparticles were built of divalent copper oxide ordered with lepidocrocite-type titanium oxide in a layer-by-layer configuration. This material was used for the photodegradation of methyl orange under visible light.[58]

4. Classical synthesis routes for pure and mixed oxides

4.1. Titanium dioxide (TiO_2)

The production of titania has been studied in several ways along the recent history of material science. There are organic as well as inorganic precursors available. The most common routes to obtain titanium oxide have been based on the hydrolysis or precipitation of Ti(IV) salts, like $TiOSO_4$, $Ti(SO_4)_2$ and $TiCl_4$. However, the counter-anion of the salt usually will be present in the product. This could have an influence on the performance of the TiO_2 prepared from these precursors. This will be described in detail for each precursor. The resulting product strongly depends upon the reaction conditions, this means that specific parameters must be found for each synthesis procedure.[59]

Among the Ti(IV) salts, suitable candidates for the production of titania are the **titanium sulphates** ($Ti(SO_4)_2$) and **titanium oxysulfates** ($TiOSO_4$).[60] These precursors have a very well-studied reaction mechanism, however they produce sulphuric acid as by-product which is very corrosive and this would attack the metallic structure of the setup.[61]

Another often used Ti(IV) salt is **titanium tetrachloride** ($TiCl_4$). This precursor reacts easily with water and oxygen giving titanium hydroxide, hydrochloric acid (HCl) and chlorine. Titanium tetrachloride can also be used as a reagent in non-hydrolytic reaction. The main routes involve either a metal alkoxide or an organic ether acting as oxygen donors, as follows:[62]

Alkoxide route:

$$MCl_n + M(OR)_n \rightarrow 2MO_{n/2} + nRCl \quad (26)$$

Ether route:

$$MCl_n + (n/2)ROR \rightarrow MO_{n/2} + nRCl \quad (157)$$

The reaction speed of the non-hydrolytic routes and the structure and texture of the resulting titanium oxide base on certain reaction parameters. The reactant used, alcohol or ether, will influence the characteristics of the nanoparticles of titania and the temperature at which the reactions take place will control the, otherwise relatively slow, reaction rate.[62] However, the presence of hydrochloric acid and chlorine is both harming for the system and the operator owing to its corrosiveness and its toxicity. The production of organochlorine compounds is to be avoided, first because they are very heavy compounds which would be difficult to evaporate but also because they are extremely toxic.

Several organic compounds used as precursors of titanium oxide have been studied systematically in order to modify its characteristics or to introduce new ones.[63] Amongst the compounds soluble in organic species the family of the **titanatranes** [Monotitanate: $(C_6H_5)_3SiOTi(OC_2H_4)_3N$] can be found.[64] The triethanol-amine coordinates around the metal forming a metal complex which makes it soluble. They are resistant to hydrolysis which in this case is a disadvantage as the unreacted components form an insoluble, highly viscous liquid which makes the separation of the so obtained particles difficult.[65]

Another family of organic precursor are the **alkoxides**, which are broadly used owing to their easiness and safety to handle and to the fact that they do not contaminate the product with undesired side products. Alkoxides are a metal-organic compounds with a general formula $Ti(OR)_n$, where R is an alkyl group. The most used alkoxides for preparing

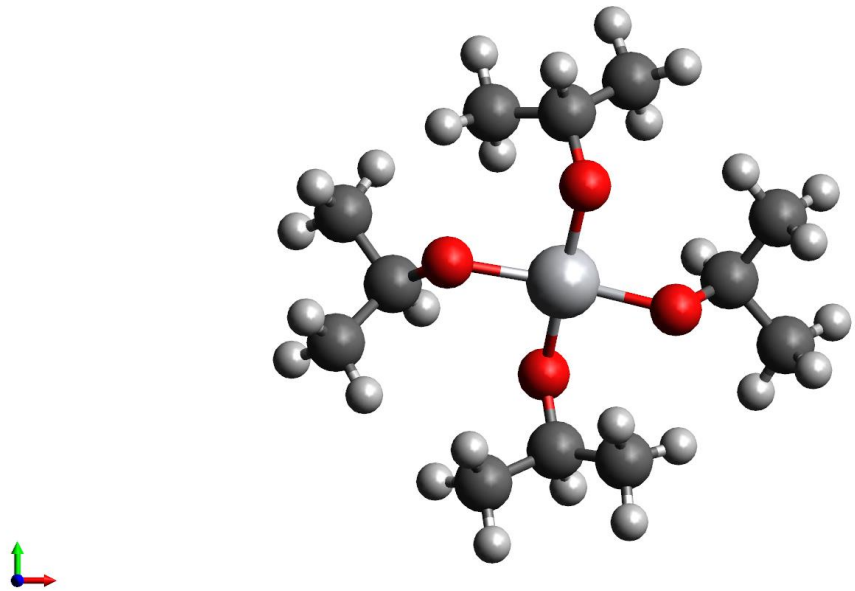

Figure 3. *Titanium tetraisopropoxide (TTIP) molecule. (Model by Avogadro)*

titanium dioxide are titanium tetraisopropoxide or TTIP, with the radical R= $CH(CH_3)_2$, titanium butoxide, where R= $(CH_2)_3CH_3$, and titanium tert-butoxide, here R= $C(CH_3)_3$.

The main products in the case of **titanium isopropoxide** are propene, propanol and water. These inert products are interesting from a technical point of view for the spray flash synthesis system because they do not corrode the materials of the different devices of the process and they are easy to evaporate. In the absence of catalyst, the reaction mechanism consists in hydrolysis and condensation. Both reactions are the chemical processes that orchestrate the formation of the matrix made of metallic oxides. These two reactions take place by nucleophilic substitution mechanisms. It starts with the hydrolysis, which begins with the nucleophilic addition of water to the positively charged metal atom (Ti). The metal now is in a metastable state with a coordination number which exceeds in one compared to the base state. After this, a proton transfer occurs. The proton, originally from the aqueous molecule, migrates to the negatively charged oxygen of an alkoxy group. Then follows the condensation, where three competing mechanisms have to be considered. In all of them hydroxo groups are generated. [66] The titanium oxide synthesis reaction through TTIP takes place as follows:[67]

$$Ti(OCH(CH_3)_2)_4 \rightarrow TiO_2 + 4C_3H_6 + 2H_2O \quad (28)$$

$$Ti(OCH(CH_3)_2)_4 + 2H_2O \rightarrow TiO_2 + 4(CH_3)_2CHOH \quad (29)$$

$$Ti(OCH(CH_3)_2)_4 \rightarrow TiO_2 + 2C_3H_6 + 2(CH_3)_2CHOH \quad (30)$$

These reactions have a very complex pathway, which strongly depends on the reaction conditions like pH, temperature, reaction atmosphere and even the nature precursor. Changing these conditions has a direct impact on the properties of the product, for example obtaining different crystallographic phases, leading to rutile or anatase polymorph. The addition of surface agents has proven an influence in different elements like the predominant appearance of certain crystallographic facets of the oxide, thus changing the surface and the performance for photo-catalytic applications. For instance, tetramethylammonium hydroxide (Me_4NOH) is used for this purpose. It allows to generate pure anatase phase TiO_2 nanocrystals with different sizes and shapes.[67]

Titanium tetraisopropoxide has been used in very different conditions to achieve, understand and master the synthesis of titanium oxide nanoparticles. The basic approach is the generation of uniform particles by hydrolysis of the alkoxide in alcohol solutions.[68] The as-prepared particles of titanium oxide are amorphous and hydrated, this is why it has been widely studied to change the characteristics of the final product, for example by the use of surfactants or additives. The agents used to tune the surface or morphology of the particles are different in nature, among others: amines, including triethanolamine ($C_6H_{15}NO_3$) to tune the reaction in a sol-gel synthesis. Organic long chain molecules like oleic acid ($C_{18}H_{34}O_2$) were used to do a solvothermal synthesis in a solution of TTIP in toluene (C_7H_8) and the combination of oleic acid and oleylamine ($C_{18}H_{35}NH_2$) to aminolyse the titanium oxide precursor to finally form nanorods of titania.[69] [70] [71] Basing on the same precursor, TTIP in a solution of isopropanol, hydrofluoric acid (HF) is also used as shape tuning agent assisting the hydrolysis of TTIP creating facet oriented crystals of titanium oxide. Even an hydrochloric acid solution can be used to force the crystallization of amorphous $Ti(OH)_4$ precipitates into anatase or rutile. [72] [73]

4.1.1. Preparation of the pure oxide

In order to produce nanostructured TiO_2, and tailor the properties of this material, multiple production methods have been developed along the past decades. The ever-expanding method range includes for example: sol-gel synthesis, hydrothermal and solvothermal approaches or chemical and physical vapour deposition.

The **sol-gel method** is commonly used to prepare diverse ceramics materials such as metal oxides.[74] The chemistry of the sol-gel synthesis of titanium oxide is based on hydrolysis continued by condensation. These reactions follow the schemes:

Hydrolysis:

$$Ti(OiPr)_4 + H_2O \rightarrow Ti(OH)_4 + iPrOH \quad (31)$$

Condensation:

$$Ti(OH)_4 + (OH)_4Ti \rightarrow -Ti-O-Ti- + H_2O \quad (32)$$

$$Ti(OiPr)_4 + (OH)_4Ti \rightarrow -Ti-O-Ti- + iPrOH \quad (33)$$

The completion of the condensation and the exit of the solvent yields' solid titanium oxide. Several treatments can be used to achieve this polymerization. If the aim is to create a thin layer on the surface of titanium oxide, a substrate can be coated by spinning or dipping. On the other hand, if the gel is withdrawn under supercritical conditions, the gel transforms into an aerogel. This material possesses a much lower density and a higher porosity than the solid. From a chemical point of view, producing titanium oxide particles by the sol-gel method is a relatively facile synthesis route. As main advantage, the sol or the gel can be used to create a cast with the desired form of the particles, like shades, rods or monodisperse particles.[75] Water to precursor ratio, temperature, concentration and solvents used are some of the parameters on which will depend deeply the properties of the future particles. However, it is difficult to avoid agglomeration of the so-created powder. This will impact directly on the surface and nanostructure of the material, usually leading to a lower performance and limiting its production at a larger scale. The formation of particles within of this mother-solution is strongly dependent of the kinetics of the chemical reaction itself. Thus the ageing time

is one of the conditions that control the properties of the materials. Nevertheless it is unavoidable to leave the solution mature for hours or even days.[76] The spray flash synthesis (SFS) capitalizes from these transition from liquid to solid. The properties of the material can be controlled through the same parameters, this means, temperature, solvent, type of precursor, etc. Owing to the flash conditions generated by the SFS technique, the solvent is evaporated at a very high rate. Thanks to this unique setup, the SFS is able to produce titania nanoparticles basing on the sol-gel method avoiding the maturing process (*i.e.* the gel step). Additionally, as the compounds are under pressure, the system is able to work at temperatures higher than the corresponding boiling temperatures. This means that SFS includes both the chemical reaction itself as well as the removal of the exceeding solvent.

In the **hydrothermal method** the reaction takes place in an aqueous solution, where parameters as temperature and pressure are controlled.[77] The simplicity of the setup and the low equipment costs make it a widely used industrial synthesis technique for nanometric particles.[78] A standard procedure is to place the aqueous solution, containing the reactants, inside a high pressure autoclave where the reaction will be carried out. The pressure will be mainly a result of the temperature and the amount of solution used. The temperature and time are the main physical parameters that are controlled to create the different nanostructured materials. The temperature usually ranges between 100°C and 1000°C.[79] The limitation of this method is based on its dependency on water. This means that only water-soluble precursors and additives can be used for this process.

The **solvothermal method**, which is analogous to the hydrothermal but basing on non-aqueous solvents is also a common synthesis process for titanium oxide.[80] Compared to the hydrothermal approach, a wider range of solvents, and their combinations can be used. This leads to new solutions and new attainable morphologies and sizes.[81] This implies that, because there are more possible solvents at hand there is also a larger variety of precursors available. And on the other hand, the reaction of the experiment can take place at higher temperatures since, depending on the precursor, solvents with higher boiling points can be employed. The solvothermal synthesis is carried out under harsher conditions and thus there is no need of post-annealing. This helps to avoid the loss of surface area of the particles. All these parameters can be modified and allow a control over shape, size and crystallinity of the titanium oxide

particles. It is even possible to reach the decomposition temperature of the precursor without the presence of an auxiliary reactant present.[82] Additionally a more diverse number and range of surfactants and additives can be used to achieve specific shapes and dimensions.[83]

Nevertheless, both techniques, hydrothermal and solvothermal, are batch production methods which makes them highly time dependent and non-continuous. The reaction time for these techniques usually ranges from 2 to 24 hours. Additionally, the materials need further steps to be ready to use. In most of the cases they need at least to be washed out and further dried, this reduces the performance and increases the total synthesis time. The SFS benefits from both. It is based on the mixture of two independent solutions, this means that both inorganic and organic soluble compounds can be used. These solutions are mixed and heated up at high pressure, similar to an autoclave operating with a short reaction duration and in a continuous way.

The fundament of **chemical vapour deposition** lies in the solidification of a vapour which is originated by a chemical reaction (CVD).[84] If there is no chemical reaction involved in the generation of the matter, then it is called **physical vapour deposition** (PVD). It generally consists of three parts: (i) the feeding system, which provides the vapour to the chamber; (ii) the reactor, where the reaction and the condensation of the material take place; (iii) the outlet module, which has the task to maintain the system, especially the reacting chamber, under vacuum. The transformation into a solid-phase material usually takes place on a heated surface, to form a thin coating film, powder or single crystals.[85] These processes are usually used for changing the surface properties of different substrates, such as high-temperature materials, like ceramics, solar cells, high-temperature fibre composites and particles with narrow size distribution.[86]

The method is regulated by the limiting mass control in the vapour of the chamber and by the kinetics of the deposition on the surface of the substrate. These regimes are competitive. When the surface kinetics govern the system the fast diffusion of the gaseous phase is slowed down by the surface reaction. Whereas when the mass transport is the limiting one it will restrict the surface kinetics.[87] This means that usually one of them is prevalent, nevertheless there are also cases where the process can be controlled by both of them. Therefore, owing to the nature of the system it makes it difficult to control. Usually the vaporization is followed by a high energy induced crystallization step, requiring the use of advanced heating technologies such as high

temperature furnace, flame pyrolysis, plasma pyrolysis, laser pyrolysis or ultrasonic pyrolysis. [88 89 90 91 92 93]

Special mention must be done to one of the most successfully used techniques, the **flame pyrolysis**. This method is widely used for the production of aerosol materials like nanometric fumed silica. Flame spray pyrolysis can use both liquid and gaseous feeding to perform the reaction. Nonetheless, it is mainly known as the technique used to produce the titanium oxide nanomaterial used as reference par excellence. This reference is the P25 from Degussa (Evonik), this nanometric titanium oxide is produced by the Aeroxide ® procedure.[94] In this process, titanium chloride as liquid is vaporised along with air and hydrogen. This mixture of gases reacts in a form of combustion at temperatures between 1000 and 2400°C, yielding titanium oxide and hydrochloric acid. This process is able to produce nanoparticles of pure titanium oxide with a high surface area. Nevertheless, not only does this technique consume a lot of energy, also due to the high temperatures reached during the synthesis, the use of any functional organic groups, for example as surface or structure modifier, is unthinkable. Additionally, there is no or poor control over the formation of aggregates or agglomerates. The main barrier is the lack of understanding of the phenomena that take place between the interface of the liquid and the particle formation to be able to produce homogeneous composites of known characteristics.[90]

Titanium oxide nanoparticles were successfully produced in a continuous way by **hydrothermal synthesis** using **water** under **supercritical** conditions. This synthesis methods used $Ti(SO_4)_2$ and $TiCl_4$ as precursors for the reaction. An aqueous solution was made with the precursors and fed as a stream into the reactor. In another stream, distilled water is put under supercritical conditions and also fed into the reactor. When the two streams meet, the rapid heating leads to the reaction. Then the metal oxides are recovered in the effluent. This produces spherical titanium oxide nanoparticles with a size of around 20 nm. The same methodology is also used for other kind of metallic oxides (CeO_2, Fe_2O_3, NiO, etc.).[95 96]

By using **ammonia of carbon dioxide** under **supercritical** conditions in a continuous process, titanium oxide nanoparticles were produced. Ammonia under supercritical conditions shows a high reducing powder. This is used to react with the precursor, in this case $Ti(OPr^i)_2(acac)_2$ (titanium diisopropoxide bis(acetylacetonate)), which is dissolved into methanol. Two pumps are in charge of feeding the reactor with both

reactants. The decomposition reaction takes places inside the reactor and the particles are recovered in a collector by a metal filter. The experimental pressure was of 16 MPa and the temperatures varied from 180 to 290°C. The titanium oxide produced was in the rutile phase with a particle size between 4-50 nm forming shapeless aggregates.[97]

In comparison to the presented production methods, the SFS is able to produce homogeneous submicrometric particles. Particles with this size are interesting for all kinds of applications where the beneficial characteristics are needed without having negative effects for health. Submicron particles are small enough to preserve the surface/volume depending properties but do not present the negative effects of nanoparticles for human health. Generally speaking, they have a higher probability of reaching deep into the lung and owing to their higher surface area, their surface reactivity is increased which can lead to cell death, mitochondrial damage, DNA damage and oxidative stress lesions. However, each material is a particular case.[98] Additionally, different precursor can be used at the same time in this system to produce nanoparticles which are built with perfectly mixed compounds.

4.1.2. Preparation of TiO_2 doped with metallic particles

The properties of semiconductors can be changed by intentionally introducing impurities into the crystalline lattice, this is known as doping.[99] The modification in the chemical composition and the arrangement of the atoms leads to changes in the electronic, optical and magnetic properties of the semiconductor.[100] Therefore new materials are available for applications like laser, bioimaging and solar cells.[101 102 103]

The introduction of metals into the titanium oxide matrix from a photocatalytic point of view is very interesting. Titanium oxide acts as a photocatalyst for degradation of pollutants, for the reduction of CO_2 or the production of H_2 by water-splitting.[10 104] However, titanium oxide has a very low quantum yield and a wide band gap which limits its use in applications driven by solar light. The introduction of a metal diminishes the electron-hole recombination rate and promotes the electron transfer.[105] More specifically, the introduction of noble metals on the surface of titanium oxide like gold, platinum or silver have been intensively studied owing to their easy production and reduction properties.[106] Silver is a very promising candidate in photocatalysis as it can trap excited electrons, reducing the recombination rate, and it shifts the light absorption of the material into the visible range, increasing the energy available in addition to the plasmon resonance effect of metallic silver nanoparticles that facilitates the excitation of the electrons.[107] Silver as dopant has successfully been used for the reduction of nitro compounds, alkylations of arenes and for sensor applications.[108]

There are several theoretical models proposed to explain the doping phenomena in semiconductor nanocrystals. The “turnbull” model bases on the idea that nanocrystallites are less charged with impurities because less matter is present in each particle.[109] The “self-purification” model explains the exit of the doping material to the surface of the nanoparticles of the host-material in terms of dopants solubility, which is lower in the nanocrystals than in the bulk matter.[110] Another hypothesis is the “trapped dopant model”, which is constructed on the growth kinetics of the particles. Here the impurity adsorbs on the surface and is included while the particle continues growing.[111]

To prepare titanium oxide nanomaterials doped with metal trace impurities there are many different methods.[60] For example iron was used as dopant by **hydrothermal method**.[112] Both precursors were mixed together with a solvent and heated up in the presence of water. Afterwards the resulting solution was dried, then washed and

calcined. In another study, the doping of titania with lithium, sodium and potassium was analysed by comparing sol-gel and impregnation techniques.[113] In another case, transition metals (Ag, Fe, Pd, Pt, Zn and Zr) were used as dopants in titanium oxide by **sol-gel**.[114]

More complex methods were also applied to induce this modification into the titanium oxide particles though. The properties of titanium oxide were modified by introducing into the matter metal ions with high acceleration energy. This method is known as **high-voltage metal ion-implantation**, the materials produced in this way need to be calcined afterwards. In this way several metals (V, Cr, Ni, Mn and Fe) could be introduced into the matrix of titania.[115] [116]

The **CVD** method was also used for doping but some additional modifications were needed. In one case, titanium was doped with Sn by **plasma-enhanced CVD**.[117] In another case, titanium was doped by **ion beam induced CVD** with different metals (Cr, V, Fe, Co).[118] Supercritical conditions were also applied to this process known as **supercritical fluid chemical deposition** (SFCD) for modifying carbon nanotubes with palladium nanoparticles.[119]

Generally, silver doped TiO_2 is produced by **wet impregnation** method, where the silver precursor adsorbs at the surface of the titania particles and is reduced by calcination, photo or chemical reaction.[120] However, efforts have been made recently to simplify the process into a single step production method. These approaches aim to introduce the silver ions during the hydrolysis of the titanium precursor. For example, through a sol-gel process which used TTIP as titanium precursor, silver nitrate as silver precursor and sodium citrate tribasic hydrate ($HOC(COONa)(CH_2COONa)_2 \cdot H_2O$) as reducing agent.[121] Other additives like acetic acid or ammonia were also used for studies based on **sol-gel** methods.[107] [122] More advanced techniques were used like sol-gel spin coating, an urea template and glucose reductant sol-gel method or **electrochemical deposition of silver** on TiO_2.[123] [124] [125] In any case, all these synthesis methods introduce a relative small amount of silver into the titanium matrix (1-10%). This is not the case for the SFS system, which provides the possibility of producing titanium oxide particles modified with silver with higher content of silver.

The nanometric combination of silver and titanium has led to symbiotic effects for example as bioactive material or increased performance in the photocatalytic area.[126]

Studies show that at nanoscale this matter has high antimicrobial as well as antifungal effect and low cytotoxicity.[126] These characteristics can lead to materials used for medical devices to avoid the microorganism colonization and device-associated infection.[127] [128] On the other hand, when the surface of titanium oxide nanoparticles are covered by nanoparticles of silver the well-studied plasmon resonance effect comes on stage. This photo-induced increase of the electric field amplitude produces an enhancement of the photocatalytical efficiency of the material compared to pure titania.[129]

4.2. Bismuth(III) oxide (Bi_2O_3)

Bismuth oxide, also known as bismuth sesquioxide, is a semiconductor with a yellowish appearance. Bismuth dioxide is a semiconductor with interesting optical and electrical properties, arising from its singular structure.[34] Bismuth oxide has high refractive index ($n_{\delta\text{-}Bi2O3}$ = 2.9), high oxygen-ion conductivity (1.0 S cm^{-1}), dielectric permittivity (ε_r = 190) and thermal stability.[130] Furthermore it resists water with a neutral pH and its band gap lies in the visible spectrum (2.8 eV).[131] It appears in five different polymorphic phases, these are α-Bi_2O_3 (monoclinic), β-Bi_2O_3 (tetragonal), γ-Bi_2O_3 (body-centred cubic), δ-Bi_2O_3 (face-centred cubic), ε-Bi_2O_3 (orthorhombic).[132] [133] [134] [135] Only two of the crystallographic phases are stable.[136] The monoclinic α-Bi_2O_3 is the only one stable at room temperature. It transforms into the cubic modification δ-Bi_2O_3 in an endothermic transition at 729°C. The cubic δ-Bi_2O_3 phase is stable between 710°C and its melting point at 825°C, the transition is reversible, which means that δ-Bi_2O_3 is not stable at room temperature.[137] The other two phases, β-Bi_2O_3 and γ-Bi_2O_3, are metastable and exist below 650°C.

Among the inorganic precursors of bismuth oxide, one occurs naturally, it is known as bismutite. The chemical formula of this mineral is $(BiO)_2CO_3$ (bismuth subcarbonate), but the crystal structure is formed by alternating layers of Bi-O and CO_3.[138] With an appearance like white powder, it is sensitive to light and decomposes by heating. Another inorganic precursor is bismuth trichloride ($BiCl_3$). By heating it up in air or by hydrolysis, this compound leads to an intermediate reactant known as bismuth oxychloride (BiOCl). The oxychloride converts into bismuth trioxide in hot concentrated alkali solutions. Also commonly used is the bismuth trinitrate pentahydrate ($Bi(NO_3)_3 \cdot 5\ H_2O$). It hydrolyses in water to basic salts. On the other side are the bismuthines, organic bismuth compounds which decompose in the presence of water or alkaline solutions.

Preparation of bulk Bi_2O_3

Traditionally, bulk bismuth oxide has been prepared by different methods:

» The direct oxidation of the metallic bismuth using oxygen at temperatures between 750 and 800°C,
» The thermal decomposition of different inorganic compounds, like bismuth subcarbonate or bismuth nitrate ($Bi(NO_3)_3$) at temperatures between 700 and 800°C,
» The precipitation of the hydrated bismuth trioxide by the addition of an alkali metal hydroxide to a solution of a bismuth salt and then followed by the removal of the water.[139]

Preparation of nanometric Bi_2O_3

For the synthesis of bismuth oxide nanoparticles other techniques were applied. The simplest one is the well-known **sol-gel synthesis**.[131] In one study the precursor bismuth nitrate pentahydrate and citric acid ($C_6H_8O_7$) were used. The study showed that by this procedure homogeneous α-Bi_2O_3 nanoparticles of less than 20 nm could be produced at milder conditions than conventional solid state methods.[140] Thin films of bismuth oxide were also created by an aqueous sol-gel route using bismuth nitrate as precursor and polyethyleneglycol (PEG 200) as chelating agent. The subsequent film was annealed at 450°C for 1 h. The formed films were of around 150 nm thick per layer deposited.[141]

A different approach was by **calcination of intermediate compounds**. For example, bismuth oxalate ($Bi_2(C_2O_4)_3$) was synthetized, basing on the same precursor, and then calcined at 350°C. By addition of L-lysine as crystal growth modifier the intermediate compound formed nanoflakes. Additionally, by controlling the crystal phase of the precursor and the calcination temperature α-Bi_2O_3 or β-Bi_2O_3 could be produced.[142] Different precursors (bismuth nitrate, bismuth subcarbonate and bismuth oxychloride) and different production methods were applied for the synthesis of nanomaterials for photocatalytic applications. The resulting α-Bi_2O_3 was produced either by thermal decomposition, by the washing of bismuth subcarbonate followed by calcination or by the precipitation of bismuth hydroxide and subsequent calcination.[143]

A different approach was to use bismuth nitrate to produce a nitrate-glycine solution as precursor for a **combustion synthesis** in a furnace preheated at 250°C. By changing the oxidiser to fuel ratio, the reaction temperature could be varied. This change influenced crystallinity as well as average particle size (20-100 nm).[144]

More complex nanostructures made of bismuth oxide were also produced. One setup of horizontal tube furnaces, called **oxidative metal vapour transport deposition**, was used to synthetize bismuth oxide nanowires of down to 7 nm in diameter and several micrometres in length. The synthesis was performed along approximately 8 hours at 300°C.[130]

δ-Bismuth oxide nanorods were produced by a method called halide **chemical vapour deposition** under atmospheric pressure (AP-HCVD). The synthesis was performed under atmospheric pressure using bismuth iodide (BiI_3) as precursor and oxygen gas. The morphology of the 2-30 µm long and 0.2-0.5 µm in diameter rods could be controlled by the deposition temperature, the partial pressure of BiI_3 and O_2. In this case the growth temperature was of 750°C for 30 min. Nevertheless, the nanorods did not grow in a homogeneously manner on the thin substrate. The synthesis was performed with poor control over size and shape.[145]

Another method produced α-Bi_2O_3 nanoparticles at room temperature by femtosecond **laser ablation** without synthesis. The pre-sintered target was bathed into pure ethanol and subsequently nanosized fragments were removed by means of the laser. Two size distribution populations were found of around 10 nm and 60 nm. This highly energetic procedure gives particles with poor homogeneity; additionally, there is no control over the shape or size fragments. Owing to the nature of the procedure, the surface area of these particles is very low compared to similar nanoparticles made by other meanings.[146]

In another setup, *i.e.,* **flame spray pyrolysis** (FSP), different kinds of bismuth oxide nanoparticles were produced. By dissolving bismuth nitrate in a solution of ethanol and either nitric acid or acetic acid, mixtures of hollow (1 µm in diameter), shell-like and solid nanograined particles could be produced (50-100 nm). The homogeneity could be increased by playing on the amount of acetic acid added to the solution. The use of acetic acid to dissolve the precursor may have produced bismuth acetate, facilitating the evaporation and thus the gas formation. Even if this technique results to be very

efficient for the production of this kind of particles, it lacks of the versatility and particle control of other systems. The combustion reaction impedes the introduction of any organic modifying agent and the control of the final particle morphology is limited.[147] This synthesis method has certain similarities to the SFS system as it also uses a spraying based production of a solution to produce nanoparticles.

Bismuth precursors are known for their poor solubility, in all these production methods the starting compounds needed to be dissolved in acids like acetic acid or nitric acid. These highly aggressive media make bismuth precursors difficult to handle in synthesis devices comprising elements which are not compatible with acids, such as metallic or organic components.

4.3. Mixed oxides from titanium dioxide and bismuth(III) oxide

There are different mixed oxides defined by the molar ratio of bismuth oxide to titanium oxide. The most common bismuth titanate phases are $Bi_{12}TiO_{20}$, $Bi_4Ti_3O_{12}$, and $Bi_2Ti_2O_7$. The preparation of bismuth titanate compounds has been reported by several ways.

Preparation of $Bi_{12}TiO_{20}$

By the **hydrothermal process** $Bi_{12}TiO_{20}$ nano-sized powders can be obtained. As bismuth source, ammonium bismuth citrate ($C_6H_{13}BiN_2O_7 \cdot H_2O$) was used, while as titanium source, titanium (III) chloride ($TiCl_3$), titanium (IV) chloride ($TiCl_4$), titanium (IV) sulfate ($Ti(SO_4)_2$) and TTIP were used. The bismuth precursor was dissolved into nitric acid and the titanium precursors were separately dissolved into distilled water. Both solutions were mixed and kept in an autoclave at 180°C for different reaction times. The only titanium precursor which led to pure cubic $Bi_{12}TiO_{20}$ particles after 2 hours was $TiCl_3$ because it does not precipitate and has a high solubility compared to the other precursor. The particles obtained were spherical in shape and the average particle size was below 10 nm.[46]

$Bi_{12}TiO_{20}$ was also produced by **co-precipitation**. For this purpose, bismuth nitrate was dissolved into nitric acid (HNO_3), on the other hand tetrabutyl titanate ($Ti(C_4H_9O)_4$) was dissolved in a mixture of nitric acid and anhydrous ethanol (CH_3CH_2OH). The resulting precipitate was washed several times with ammonia followed by calcination at 550-650°C.[45]

Preparation of $Bi_4Ti_3O_{12}$

The classical preparation method for $Bi_4Ti_3O_{12}$ is based on **solid-state reactions** of Bi_2O_3 with TiO_2 at elevated temperatures (1000-1200°C).[35] [39] More recently, the techniques that are developed enable a better control over the reaction.

Sol-gel has also successfully been used for the production of $Bi_4Ti_3O_{12}$. For this synthesis bismuth acetate ($Bi(CH_3COO)_3$) and TTIP were mixed into methoxy ethanol ($C_3H_8O_2$) along with acetic acid (CH_3COOH). Bismuth acetate was added to methoxy ethanol and acetic acid and distilled to obtain a clear solution. In another flask TTIP was added to methoxy ethanol and refluxed at 124°C under argon for 6 h. Both were

mixed in a flask and put under reflux at 124°C in argon atmosphere for 6h, followed by hydrolysis through addition of water. The resulting powder was dried in an oven at 100°C and calcined at 300°C for several hours. The apparent grain size of the obtained powder is less than 1 µm. The study proposes the following dehydration reactions:[148]

(50-340°C) $$Bi(OH)_3 \rightarrow BiO(OH) + H_2O \quad (34)$$

(400-550°C) $$2\,BiO(OH) \rightarrow Bi_2O_3 + H_2O \quad (35)$$

(50-400°C) $$Ti(OH)_2 \rightarrow TiO_2 + H_2O \quad (36)$$

Another technique is the **co-precipitation**. In this case the precursors used were bismuth titanate and potassium titanium oxide oxalate dihydrate ($K_2[TiO(C_2O_4)_2] \cdot 2H_2O$) which were mixed along with water diluted ammonia (NH_3) to control the pH value. However it was necessary to calcine the precipitate ($BiOHC_2O_4$+$TiO(OH)_2H_2O$) at 750°C to obtain pure $Bi_4Ti_3O_{12}$.[149]

A procedure known as **metalorganic decompositions** was used to obtain nanoscaled $Bi_4Ti_3O_{12}$ powders. In this study, bismuth nitrate was dissolved into glacial acetic acid along with titanium butoxide. This mixture was precalcined in a muffle at 350°C and later on annealed at different temperatures between 350 and 650°C. The morphologies of the particles changed from rod-like grains with 200 nm width and 1 µm length at 350°C, agglomerates with an average grain size between 50 and 200 nm and coarsened particles of around 300 nm. Basing on the XRD results the synthesis of $Bi_4Ti_3O_{12}$ takes place through the intermediate $Bi_2Ti_2O_7$.[150]

Basing on the **hydrothermal process** the synthesis of $Bi_4Ti_3O_{12}$ powder was performed at low temperature. The bismuth containing precursor, bismuth nitrate, was dissolved into nitric acid. In parallel, TTIP, the titanium containing precursor, was mixed with nitric acid and hydrogen peroxide (H_2O_2) to obtain titanyl nitrate ($TiO(NO_3)_2$). Both solutions were mixed together, the pH level was adjusted using sodium hydroxide (NaOH), and annealed at 150°C for 5, 10 and 15 hours. The resulting particles were completely crystallized only after 10 hours. The obtained particles are irregular in shape and agglomerated with an average grain size of 0.5 µm for the short annealing.

At longer annealing times the particle became spherical with grain sizes between 0.5 and 1.2 μm.[151]

The **solution combustion technique** was applied to produce $Bi_4Ti_3O_{12}$. The precursor, bismuth nitrate pentahydrate, was dissolved into 2-methoxyethanol ($C_3H_8O_2$) while TTIP was mixed with acetyl acetone ($CH_3COCH_2COCH_3$). For the exothermic reaction to take place, glycine (NH_2-CH_2-COOH) was used as fuel. The resulting mixture was heated up to 200°C for 1 hour, and the resulting material was calcined at 800°C for 3 hours. Finally, the particles were sintered at 1050°C for 5 hours. The powders do not have a regular shape, are agglomerated and the particles have a wide size distribution between the nanometre and sub-micrometre scale.[152] In a different study, the production of $Bi_4Ti_3O_{12}$ by combustion synthesis was analysed with different fuels. In this case, bismuth nitrate and titanyl nitrate ($TiO(NO_3)_2$) were mixed with glycine, carbamide ($CO(NH_2)_2$) and glycerol ($C_3H_8O_3$). The mixture was heated to 500°C.[153]

$Bi_4Ti_3O_{12}$ has also been prepared by **complex polymerization method**. TTIP was mixed into citric acid and deionized water to form a titanium citrate ($C_{12}H_{10}O_{14}Ti_3$) solution. To this solution bismuth nitrate pentahydrate, along with ethylenediamine ($C_2H_4(NH_2)_2$) to adjust the pH, was added. Finally, ethylene glycol ($C_2H_6O_2$) was introduced to promote the polymerization. The formed resin was treated in a furnace at 300°C for 12 hours followed by further heat treatments from 300 to 700°C for 2 hours under oxygen flow.[154]

Preparation of $Bi_2Ti_2O_7$

The bismuth titanate $Bi_2Ti_2O_7$ was produced by **solvothermal** synthesis. Therefore, bismuth nitrate and tetrabutyl titanate were used as reactants in ethanol and glycerine. The mixture was kept in an autoclave at 383K for 12 hours. Then when the precipitate was filtered, it was dried at 353K and calcined at 773K for 3 hours.[155]

The same phase was also prepared by **chemical solution deposition**. Here the precursors were bismuth nitrate and titanium butoxide. In this case, the solvent used was glacial acetic acid, the viscosity and surface tension was adjusted with 2-methoxyethanol (CH_3OCH_2OH) and acetylacetone ($C_5H_8O_2$) was used to stabilize the solution. The solution was left for 1 hour, followed by drying at 100°C along 24

hours and then calcined at 800°C during 30 minutes. The particles have a raspberry like morphology in the micronsized range.[156]

Thin films of this titanate were produced by **aerosol assisted chemical vapour deposition**. Therefore, a solution of bismuth nitrate in acetylacetone was prepared which was diluted with methanol. To this solution titanium isopropoxide was added and more methanol. This solution was sprayed upon a heated substrate at 600°C. This process was performed during 1 hour to create a 1 µm thick film. This film was washed two times with water, acetone, isopropanol and ethanol.[157]

This material was also produced by the **co-precipitation** route. For this, a basic titanium solution was mixed with an acidic bismuth solution. Metallic titanium was added to a hydrogen peroxide and ammonia solution. This solution was poured into a bismuth nitrate solution in nitric acid under stirring. The precipitate was washed with diluted ammonia and dried at 50°C. Then it was pressed into discs and calcined at 400°C and 500°C during different periods of time (16 and 96 hours).[158]

4.4. Copper oxide (CuO)

Copper oxide nanoparticles can be prepared by the **sol-gel** technique. For this purpose, copper acetate ($Cu(CH_3COO)_2$) was put in an autoclave, maintained under autogeneous pressure and at different temperatures (90-180°C) for 20 hours. The average particle size (3 - 9 nm) varied depending on the synthesis temperature.[159]

A different approach for the CuO nanoparticle synthesis is the direct **thermal decomposition**. The precursor used is copper sulphate ($CuSO_4$) which reacts with sodium carbonate (Na_2CO_3) giving the precipitate basic copper sulfate ($Cu_4(SO_4)(OH)_6$). The precipitate is calcined at 750°C for 2 hours which produced nearly spherical submicrometric particles of around 170 nm.[160]

Also commonly used for the preparation of these particles is the **chemical precipitation** synthesis. In this case, copper nitrate trihydrate ($Cu(NO_3)_2 \cdot 3H_2O$) is used in a water-ethanol mixture using as reactant partner sodium hydroxide (NaOH) at 77-82°C and 1 atm. This created nanorods of copper oxide with a width between 5 and 15 nm. [161]

Nanoparticles of copper oxide with varying morphologies can be obtained by the **sonochemical** method. Here, copper acetate was used as precursor to react with urea or sodium hydroxide as reducing agents with the aid of polyvinylpyrrolidone (PVP) as stabilizing agent. The reaction takes place under ultrasound for 2 hours at 100°C to create the material. When using urea, quasei-spherical particles can be obtained, while when using NaOH, long-straw like structures are produced.[162]

The method known as **solution plasma** synthesis can also be used for the production of this material. For this, a copper wire as cathode is used with potassium carbonate (K_2CO_3) or a citrate buffer solution with various voltages (105-130 V). The copper melts locally owing to the concentration of current leading to CuO nanoflowers (d_{avg} = < 100 nm) when using K_2CO_3 or spherical particles when using the citrate buffer (d_{avg} = 500 nm – 2 µm).[163]

Copper oxide nanorods were prepared by the **pulsed wire explosion** method. In this process, a copper coil is fed between two electrodes that are connected to a high voltage source (10^4-10^5 V, 10^{10} A m^{-2}) in deionized water. The temperature of the water influenced in the diameter and morphology of the particles. At lower temperatures

(<30°C) spherical particles with an average diameter 10-20 nm formed, while at higher temperatures (60°C) spindle like particles with a width of 40-80 nm and 650 nm of length were produced.[164]

In a totally different method, copper oxide nanoparticles were prepared by **biosynthesis**. Brown alga (Bifurcaria bifurcate) extract acted as phytoreducing agent transforming $CuSO_4$ into CuO after 24 hours at 100-120°C. The particles produced had an average diameter of ~21 nm with a spherical shape in its majority with some of them being slightly elongated.[165]

4.5. Mixed oxides from titanium dioxide and copper(II) oxide

The mixed oxide of copper and titanium was produced by **wet impregnation** process. TTIP was used for the synthesis of titanium oxide nanoparticles which were impregnated by $Cu(NO_3)_2$ using diatomite (kieselguhr) as support. This solution was maintained under stirring for 3 hours. Once completely dry, the powder was calcined at 400°C. The Cu/Ti ratios varied between 90/10 and 50/50.[166] In a similar approach, the method was applied to copper acetate as precursor on commercial titanium oxide nanoparticles. The suspension was stirred for 30 min and dried in a rotatory evaporator. The particles were calcined at 400°C for 1 hour under air. This synthesis produced a mixture of CuO and Cu_2O on the titanium oxide particles.[167]

In one study, different types of production methods for CuO_x-TiO_2 composites were compared. Wet impregnation was compared to microwave reduction method and photodeposition method. The **microwave reduction** process used copper acetate to load copper oxide nanoparticles onto the surface of commercial titanium oxide particles. This was done by dispersing the particles into benzyl alcohol ($C_6H_5CH_2OH$) and adjusting the pH with NaOH. Then, the suspension was irradiated with microwaves at 700 W with a 2.45 GHz frequency for 4 min. The **photodeposition** was performed using $Cu(NO_3)_2$ as precursor in methanol. The commercial titanium oxide particles were loaded by irradiation the sample with a UV lamp with 400 W for 30 min.[168]

CuO_x/TiO_2 thin films were preparey by **RF reactive magnetron sputtering**. The material was grown on a quartz glass substrate fixed at 450°C. The targets were plates made of metallic titanium and Cu-C composite that were put under 130 W and 120 W respectively. This produced thin films with a thickness of ~1250 nm made of nanorods with diameters ranging from 50 to 100 nm with different copper contents.[169]

The synthesis of Cu_2O/TiO_2 received much more attention because in photocatalytic applications CuO is usually not stable and reduces into Cu_2O. Nevertheless, literature focuses on the surface modification of titanium oxide instead of the creation of intimate mixture of both oxides, which probably means that these phases form separately.

4.6. Main advantages and drawbacks of the production methods

	Production method	Advantages	Disadvantages
" 3D" technique / powder objects	Sol-Gel	- Versatility - Tuneable chemistry - Simple setup	- Batch synthesis - Indirect control of the process - Ageing needed for long periods of time - Poor crystallinity - Phase difficult to control - Slow process - Complex mechanism
	Hydrothermal	- Simple procedure - Good crystallinity	- No control over product characteristics - Usually surfactants needed - Physical and chemical limitations of water - Energy-consuming
	Solvothermal	- Large variety of solvents - Large variety of surfactants	- Complex reaction chemistry - Possible side-reactions with solvent - Low solubility of polar compounds - Energy-consuming
" 2D" techniques / deposits	CVD	- Good throwing power, for coatings and films with low porosity - Localized deposition - No annealing needed - Good reaction control - Wide variety of materials	- Complex process - High energy demands - Expensive - Generally low deposition rates - Sensitive to contamination
	PVD	- Good throwing power, for coatings and films with low porosity - Localized deposition - No annealing needed - Wide variety of materials	- High energy demands - Expensive - Generally low deposition rates - Sensitive to contamination

Table 1. *Comparison of the principal nanometric ceramic synthesis methods*

5. The spray flash-evaporation (SFE) process

The spray flash-evaporation (SFE) is a process able to produce submicrometric or nanometric organic particles in a facile way. This method was developed and patented by the NS3E laboratory (Nanomatériaux pour les Systèmes Sous Sollicitations Extrêmes, UMR 3208 ISL-CNRS-UNISTRA) to face the demand of an industrial scale production method for nanoscale particles.

Up to now, this technique was used to produce a wide variety of organic nanoparticles in a single step. For example the production of nano-β-HMX as a promising approach to the desensitization of nano-energetic materials has been achieved.[170] The production of nanoscale 2,4,6-trinitrotoluene (TNT) has also been performed by using the SFE process.[171] Furthermore the SFE process allows the addition of polymeric additives as polyvinylpyrrolidone (PVP) and polyethylene glycol (PEG) to arrive at a more accurate particle growth control.[172] New interesting paths appear when introducing two different materials into the system. Following this idea, the NS3E laboratory was able to nanocrystallize a nanodiamond – cyclotrimethylenetrinitramine (ND-RDX) mixture into a core-shell structure.[173] Even more, the production of RDX-TNT core-shell nanoparticles was made by SFE for the production of nanodiamonds by detonation synthesis.[174] Also the production of pure HMX (Octahydro-1,3,5,7-tetranitro-1,3,5,7-tetrazocine) or HMX based nanocomposites was achieved.[175] The downsizing of inorganic oxidizing agents like ammonium dinitramide (ADN) by the SFE technique has shown that properties like the critical detonation diameter or the impact sensitivity can be changed.[176] Another interesting pathway was opened by the crystallization of nanometric cocrystals. Caffeine/oxalic acid 2:1, caffeine/glutaric acid 1:1, TNT/CL-20 1:1 and HMX/CL-20 1:2 nano- and submicronsized cocrystals were produced by the SFE setup in the NS3E laboratory.[177]

These examples are only intended to highlight the versatility of the technique to produce not only pure nanoparticles but also new and interesting nanocomposites and tailor their properties. This technique is able to produce nanomaterials in a single step setup basing on a simple and at the same time efficient way. The controlled conditions, added to the abrupt change through the flash step, render unique morphologies and sizes. The sudden evaporation of the solvent will produce pure matter. But all these studies base on the dissolution and further recrystallization of the molecules, which

means, the matter is not chemically altered during the process. Therefore, the question, if the SFE can be modified to produce nanometric particles through synthesis, arrives. The answer to this question will be exposed in this work.

6. Conclusion

This chapter aims to place the research performed in this thesis into its scientific context.

Different types of nanomaterials and their properties were studied. Their characteristics interesting for the photocatalytic and pyrotechnic domain were identified. The materials on which the focus was placed are titanium oxide (TiO_2), silver modified titanium oxide ($Ag@TiO_2$), bismuth oxide (Bi_2O_3), bismuth titanate family ($Bi_xTi_yO_z$), copper oxide (CuO) and the mixture of copper oxide and titanium oxide (CuO/TiO_2).

Synthesis process for this kind of nanomaterials starting from different precursors were described. Titanium oxide can be produced by methods like sol-gel, hydro and solvothermal, chemical and physical vapour deposition or flame pyrolysis. The common used precursors are Ti(IV) salts and titanium alkoxides. Silver is introduced by doping or wet impregnation onto the titanium oxide particles normally using silver nitrate as precursor. Bismuth oxide nanoparticles can be made by sol-gel, thermal decomposition of oxalates, laser ablation or combustion synthesis. The precursor which is mostly used is bismuth nitrate. The bismuth titanates can be produced by sol-gel, co-precipitation, hydrothermal synthesis, polymerization or combustion synthesis. Depending on the synthesis method different precursor are used but TTIP and bismuth nitrate are among the most used. Copper oxide is produced by sol-gel, thermal decomposition, chemical precipitation, sonochemical synthesis, solution plasma synthesis, biosynthesis or pulsed wire explosion. Copper nitrate, copper sulphate and copper acetate are the common precursors. Copper oxide modified titanium oxide composites are made by microwave reduction, photodeposition, mostly wet impregnation or RF magnetron sputtering. The titanium oxide particles used as support for the copper oxide are commercially available, while the copper precursor is copper acetate or copper nitrate.

Most of these production methods are non-continous (batch) synthesis processes that do not provide the possibility to control the synthesis itself owing to its complexity (scale effect). Another common major inconvenient is the multi-step process, these techniques require several independent operations to obtain the desired product.

This leads to the development of a new process the spray flash evaporation (SFE), also patented by NS3E laboratory, to produce this kind of materials. This chapter helped to choose certain precursors adapted to the synthesis methods basing on the information found in literature.

PREPARATION PROTOCOLS AND CHARACTERIZATION TECHNIQUES

Chapter II

1. Glossary

SFE: Spray Flash Evaporation

SFS: Spray Flash Synthesis

FFKM: Perfluoroelastomer compounds with high amount of Fluoride

TTIP: Titanium tetraisopropoxide

HPLC: High-performance liquid chromatography

TGA: Thermogravimetric analysis

DSC: Differential scanning calorimetry

FTIR: Fourier transform infra-red spectroscopy

XRD: Powder X-Ray diffraction

SEM: Scanning electron microscopy

TEM: Transmission electron microscopy

BET: Brunauer-Emmett-Teller theory

RDX: Cyclotrimethylenetrinitramine

ESD: Electrostatic discharge

UV-Vis: Ultraviolet-visible region

2. Introduction

This chapter is dedicated to describe the techniques and methods used to prepare and analyse the materials studied in the thesis. The modifications of the original spray flash evaporation (SFE) system to obtain a process capable of synthesizing nanomaterials (SFS) will be discussed here. The synthesis protocols followed to produce the different materials along with the process parameters will also be detailed.

The different characterisation techniques used to ascertain the properties and features of the as prepared materials will be addressed from a general point of view followed by a discussion about their specific use for the purposes of this work. From a structural and morphological point of view, the samples were analysed by thermogravimetric analysis, differencial scanning calorimetry, Fourier-transformed infrared spectroscopy, and Raman spectroscopy, powder X-ray diffraction, scanning electron microscopy, and transmission electron microscopy, specific surface area and porosity measurements by nitrogen and mercury absorption, respectively.

Pyrotechnic compositions were formulated from some of the materials synthesized by SFS process. The preparation process of these energetic materials, as well as the techniques used to determine their sensitivity, their explosion heat and to characterize their combustion are also described in this chapter. This chapter also highlights the experimental devices used to investigate the photocatalytic activity of several materials synthesized by SFS and the techniques used to characterize these properties.

3. The Spray Flash-Synthesis (SFS) process

3.1. From Spray Flash-Evaporation (SFE) to Spray Flash-Synthesis (SFS)

The spray flash evaporation (SFE) process is able to produce nanoparticles, it was developed and patented by the NS3E laboratory.[178] The aim of this technique is to produce nanoparticles at industrial scale in a single and facile way. The SFE process (**Figure**) is based on the crystallization of organic molecules dissolved in an organic solvent. This crystallization is the result of letting the solution undergo a sudden energy shift. This shift is achieved by spraying the pressurized and overheated solution into vacuum. The solvent evaporates abruptly owing to its vapour pressure, and the temperature of the remaining matter drops. Therefore the droplets inside of the chamber are formed of supersaturated of solution, where the crystallization takes place.[179] Thanks to the SFE process pure nanoparticles can be produced which are ready to use.[171] Even the production of nanoparticles made out of different materials

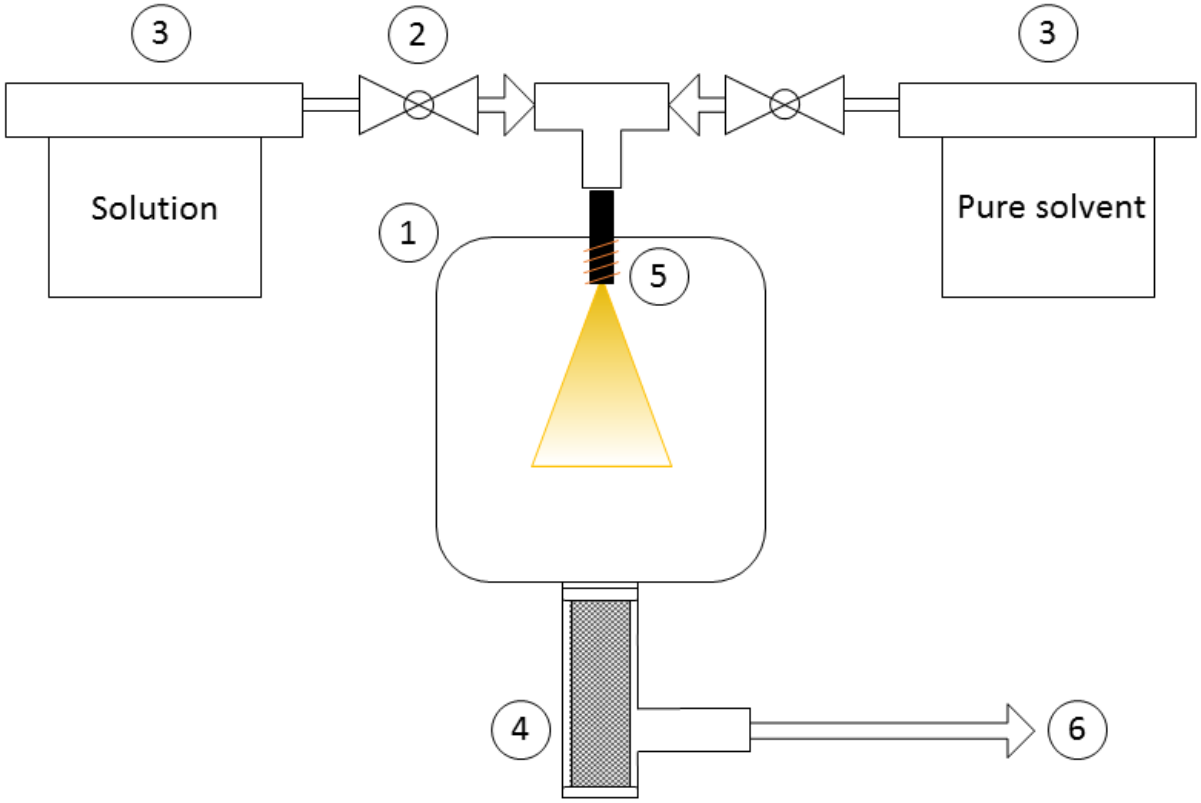

Figure 4. *Schematic of the SFE system. 1. Vacuum chamber; 2. Ball valve; 3. Solution tanks; 4. Powder recovery system (filter; cyclones); 5. Nozzle and heating system; 6. Vacuum pump*

intimately mixed can be performed by this method. For example producing core-shell structures of two different materials.[173] Another example is the elaboration of perfectly mixed nanosized mater, that builds a new crystalline structure (cocrystal).[177] It provides a controlled production way for nanocomposites as it the case with surface agents, *e.g.* polymeric additives.[172] Like this, different nanocomposites could be studied by adding different compounds to the base material.[175]

However, the SFE process bases on purely physical phenomena. This condition makes it inadequate for the synthesis of new matter. Rather than just solidifying the same material in an extremely fine configuration, for the synthesis of new compounds an unprecedented process is needed, the Spray Flash Synthesis (SFS).

The SFS is a new process which is capable of synthesis nano and submicron sized materials basing on chemical reactions. In this work the SFS was used for producing simple ceramic powders like titanium oxide or copper oxide to name a few and more complex oxides like bismuth titanates. It was also used to add a metal to oxide nanoparticles. Inhere will be explained which were the requirements found along, which modifications were performed and how the problems that appeared were solved.

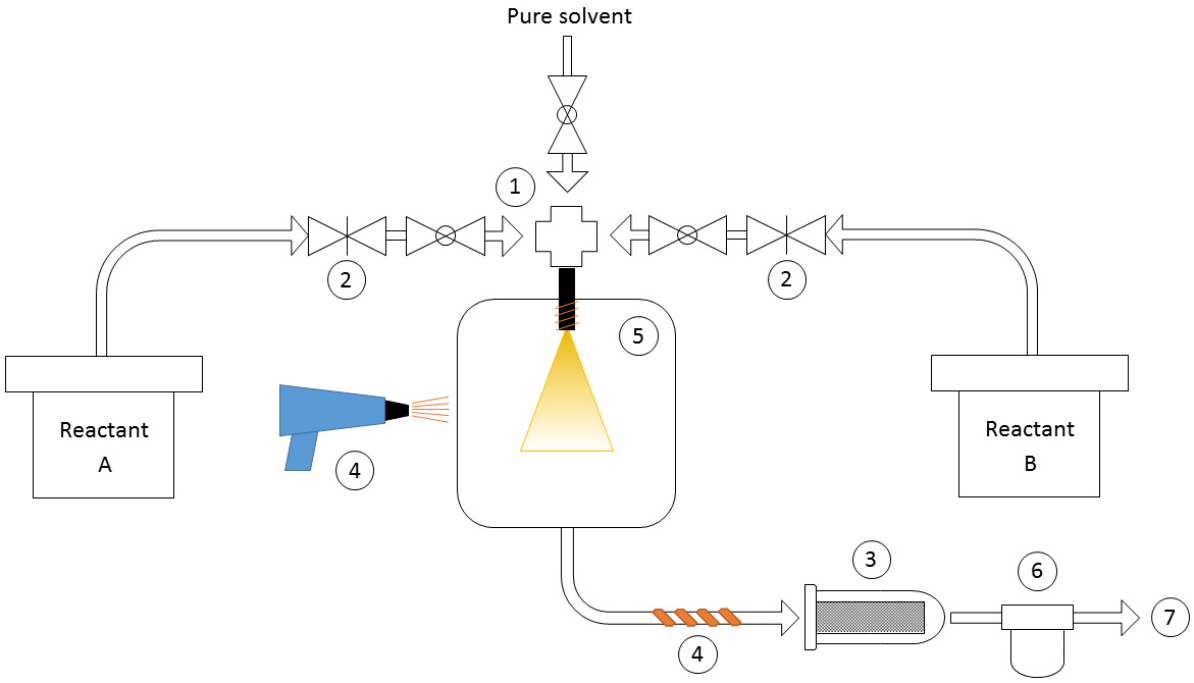

Figure 5. *Schematic of the SFS system. 1. Mixing of liquids; 2. Flow rate control; 3. Powder recovery system; 4. Auxiliary heating system; 5. Joints and sealing; 6. Acid recovery device; 7. Vacuum pump*

In this sense, several modifications were conducted on the original setup to allow the required synthesis conditions to be fulfilled. This modifications serve to create stable reaction conditions so that the reaction can take place, as well as a precise control of parameters to avoid undesired fluctuations along the synthesis process.

3.1.1. Mixing of liquids

To avoid the undesired start of the reaction in the tanks, the liquids containing the reactants are separated in two different tanks. These will flow in parallel towards the tank. To ensure that the reaction takes place in the chamber, the fluids are mixed just beforehand. Additionally, another feeding way was installed to supply the system with reactant free solvent. Consequently, a four-way union cross configuration was chosen (**Figure** , 1). By adding three ball valves at every entry of the cross, an independent control over each path could be obtained. This cross-plus valve setup provides the possibility to regulate which flows are feeding into the chamber at a given moment. In a standard experiment the valve controlling the pure solution tank is open for warm up and cleaning phases. Whereas the valves that connect the tanks containing the reacting solutions are only open when the synthesis phase is taking place. In this configuration the two solutions meet at the union cross and start mixing before reaching the chamber. This part is not heated, therefore the liquids travel during around 20 seconds through the tube at room temperature. Then, they enter the heated part just before the nozzle for around 2 seconds. In this way what is happening in the system can be easily managed. The union cross part was a SS-6M0-4 model from Swagelok made of stainless steel with 6 mm tube fitting.

3.1.2. Flow rate control

For ensuring the reproducibility and homogeneity of the obtained materials it was necessary to maintain the flow of both reactants, which were fed into the chamber, at a constant and calibrated rate during the whole synthesis process (**Figure** , 2). This was crucial to ensure steady conditions, so the chemical reaction could take place at the desired requirements. Additionally, the flow was adjusted to lower values so that the vacuum pump was able to preserve the reaction conditions inside the chamber. This varied depending on the quantity of water used for every system. The water present condensates much easier than the other compounds. However, as the

chamber is under vacuum, the water is forced to re-evaporate. This on the other hand produces a temporal increase of the pressure inside of the chamber, and as consequence the flash conditions are altered.

The flow control was achieved by restricting it with a precision valve with a needle type for every feed way. This device allows to modify the flow with high accuracy at low flow rates. Needle valves use tapered pins to let pass through a confined space a certain amount of fluid. It takes advantage of the Vernier's effect of the ratio between the needles length and its diameter, and consequently the difference between diameter of the needle and the diameter of the hole. The space that is left for the liquid can be adjusted thanks to the position of the needle in relation to the pinhole. As explained above, the flow rates needed to be low, thus making this device perfectly fitting for the control of the system.

With this device, the flow rates of feeding were adjusted for every system. As the viscosity of the fluid depends on the chemical composition, by varying the composition, the quantity of matter that passes through a given diameter, at a given pressure and temperature, changes. This was ensured by calibrating the valves before each experiment. The amount of matter passing through the nozzle at a given valve position was measured in relation with time. The flow of solution passing through the tubes depends on temperature, pressure, density and viscosity. Taking into account that under normal circumstances both solutions were at same pressure and temperature and that both were mixed using the same solvent, the flow was majorly affected by the viscosity, influenced by the concentration of the compounds that are present. Additionally, to verify that the flow was stable at the desired value along the duration of the experiment, the amounts of remaining solution in the tanks were compared.

The precision valves used were the model SS-SS6MM-VH supplied by Swagelok. The body of the valve is made of stainless steel 316. The valves were connected to the feeding tubes with 6 mm Swagelok tube fitting on both sides. The flow could be adjusted thanks to a micrometric Vernier handle on top of the body.

To ensure that the variations of pressure affect both solutions in the same manner, all the tanks are connected to the pressure in parallel. This connection in parallel stays open during the whole process, to ensure that all the system is under the same pressure.

3.1.3. Powder recovering system

As one of the aims of this work is to use the different materials for diverse applications, the quantity per run was influential factor to take into account. Earlier versions of the SFE process based on a cyclonic design. It profits from the forces that result from the inertia of the particles that are dragged into this part. This inertia, which is translated into centrifugal force, presses the particles against the walls of the glass recipient, slowing them down. As a result, the powder can be recovered at the bottom of the vessel. Nonetheless, does the efficiency of device depend on several independent variables like particle size or electrostatic charge. To avoid this, a different approach was used to enable the withdrawing of the particles from the flow of gas. This was carried out by using a cylindrical filter made out of stainless steel with an average mesh size of 5 µm (**Figure** , 3).

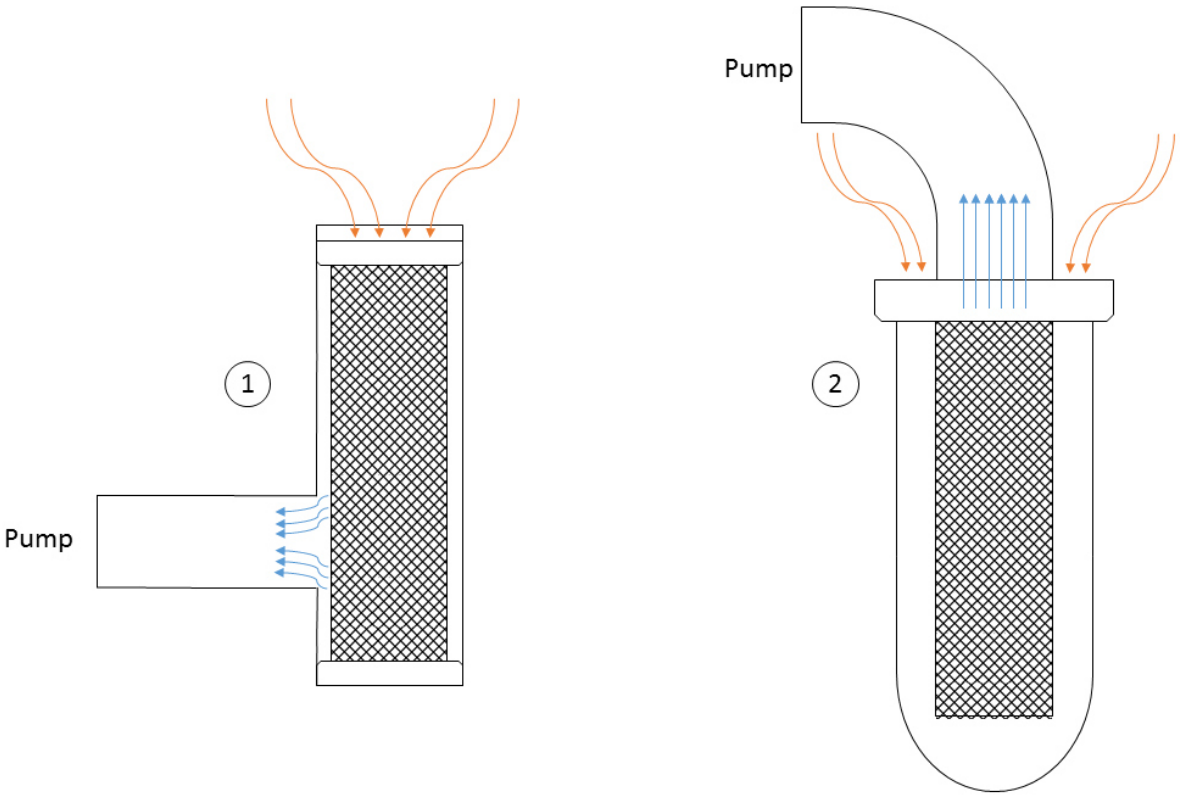

Figure 6. *SFE and SFS filter: 1. Classical in-out filter and 2. Adapted out-in filter*

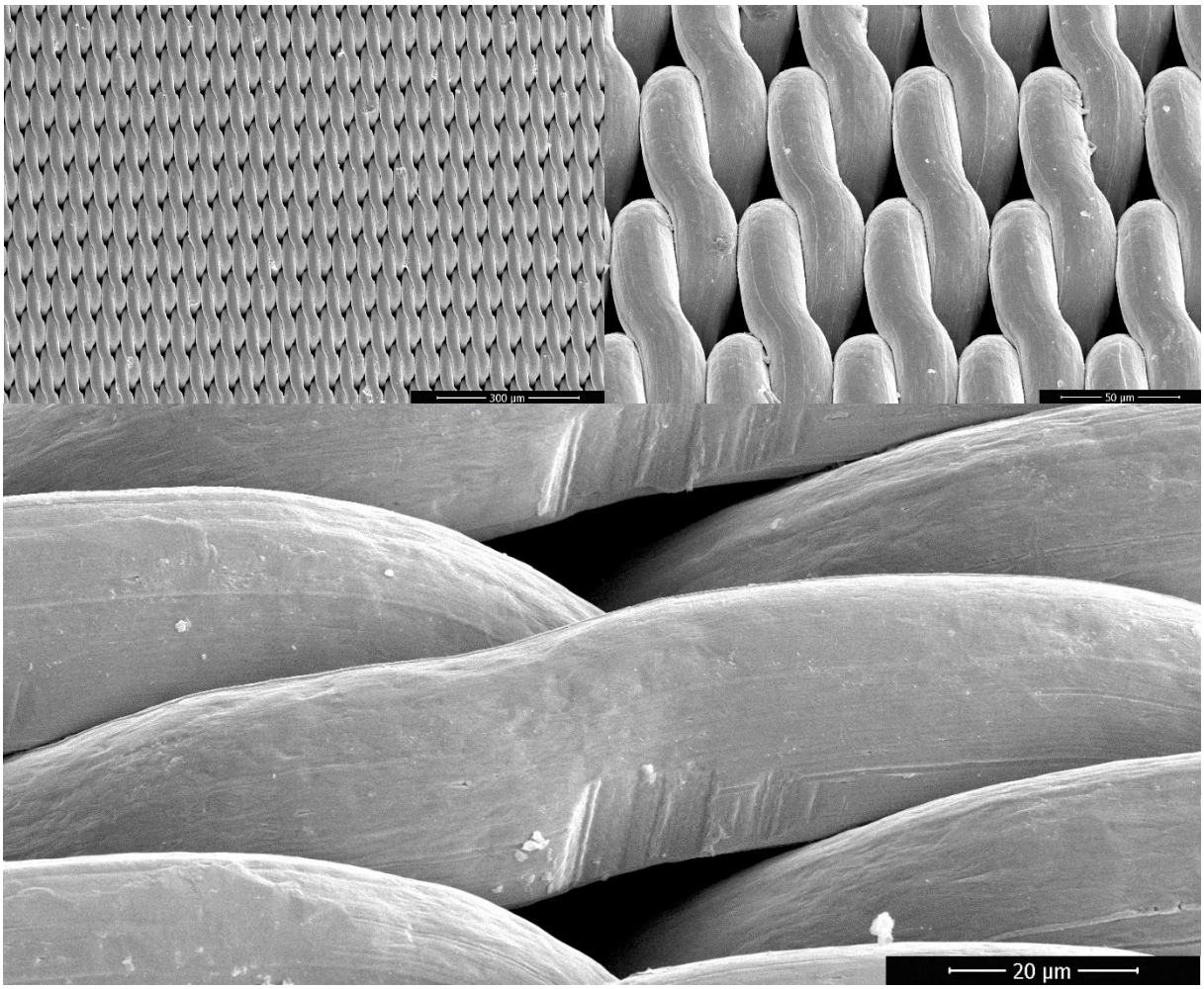

Figure 1. *SEM images at different magnifications of filter used*

This filter was situated at the bottom of the crystallization chamber, inside of solid cylinder with bigger diameter (**Figure** , 4). Like this the vapours are forced to pass through it for exiting the system. As the gas flows through the filter, the particles are retained at the inner part of the cylinder. Even so, a high proportion of the surface of the filter could be optimised. This was achieved by inverting the sense of the flow with regards to the filter (**Figure** , 2). The filter was situated inside of a recipient with a curved bottom made out of glass. The cylindrical filter was fixed around the extraction tube, like this the gas would penetrate from the outside. This led to a less turbulent flow regime around the filter, which favours the deposition.

During the synthesis a layer of particles grows on the outside of the filter. As this layer gets thicker, the charge loss produced by the filter augments. This increase of charge loss results in a lower overall performance of the vacuum pump, and as a consequence an increment of the pressure in the chamber. To restrain the accelerated increase of

the pressure in the camber, and therefore extend the time during which the synthesis can be carried out, a filter with a higher surface was installed. The outcome of a higher area is that the superficial density (g/m^2) of the product on the filter decreases. Thus, the same quantity of material, which deposits on the filter for a given amount of time, settles forming thinner layers. Hence for the same reaction time, the charge loss augments more slowly.

3.1.4. Auxiliary heating system

Owing to the higher vapour pressure of water it condensates easier than the other solvents present in the chamber during the process. This condensation takes place on the walls of the chamber, which are the parts of the system at the lowest temperature. As the system is maintained under vacuum the water takes the energy needed to evaporate from the walls. Consequently, the body, which is made of stainless steel, cools down as an effect of the high specific heat capacity of the water. This results in an additional charge loss, which lowers the efficiency of the pump. Thus, a negative feedback loop is initiate. Where, due to the loss of vacuum quality, the condensation is even more pronounced and the pressure increases. This situation impedes a stable vacuum inside of the chamber and therefore a continuous flash of the spray.

This can be prevented by heating the metallic mass of the body of the chamber. By doing so, the loop is interrupted at the beginning, when the water condensates. As the metallic body of the SFS system is heated up, the necessary energy for the water to stay in gas phase is supplied. The external heating was applied in two different forms.

The heating of the main body of the system was performed by using a heat gun. This was pointing at the metallic body at a close distance (**Figure** , 4 heat gun). This device is able to blow a stream of hot air up to 600 °C, which thanks to thermal conductivity of the metal, was sufficient to heat up the whole chamber, leading to an inner-wall temperature of around 150 °C. The heat gun used was a Steinel HL 1910 E with an energy output of 1500 W and a temperature range from 49 °C up to 593 °C.

Additionally, a silicone belt heater was wrapped around the steel tube that leads the flow from the chamber into the filter (**Figure** , 4 belt heater). This was installed because the flow makes a 90° turn, impacting directly on the tube, thus leading to easier condensation.

3.1.5. Joints and sealing

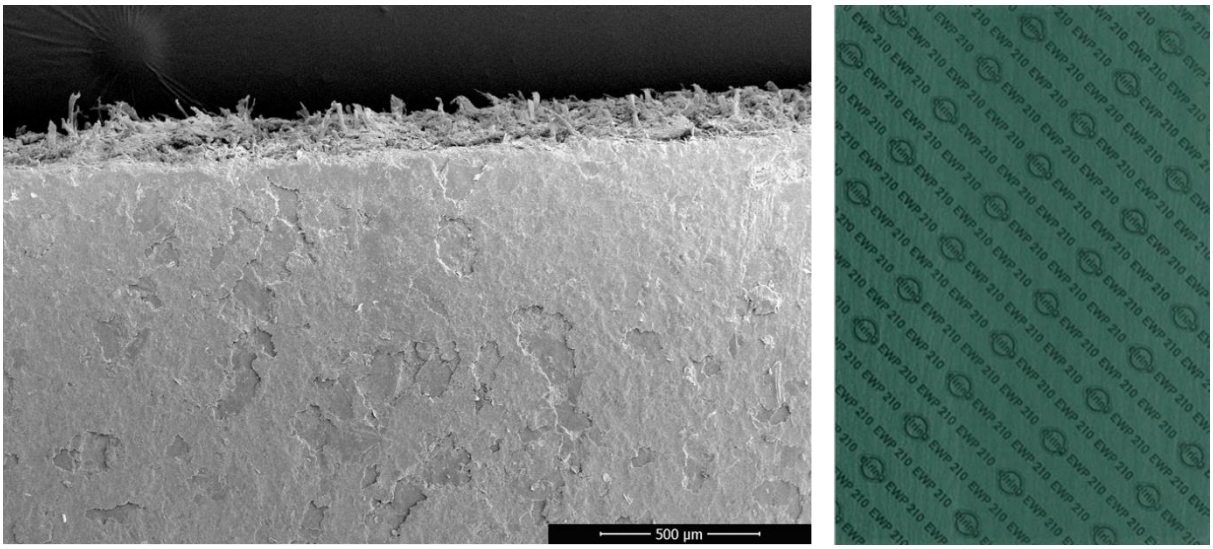

Figure 7. *SEM image and photo of sealing material used to produce the tailor-made joints.*

The material selected for the joints to seal the different parts of the main body, this is the chamber of the SFS, had to bear dynamic thermal solicitations and resist in face of aggressive chemical compounds. For this purpose, the sealing material was cut to an O-ring to fit the space between the lid and the chamber. Several sealings were also cut in an O-ring shape of smaller size (**Figure** , 5). This was done for the joint of the chamber to the elevator ring, the nozzle-to-nozzle holder, the nozzle holder to the heating tube, the heating tube to the lid and the lid to the feeding tube. The material chosen was a nitrile butadiene rubber linked to aramid fibres (**Figure**). This material is used to avoid leaking against hot and cold oils, fats, fuels, etc. It is stable under working conditions up to temperatures of 400 °C and pressures of 100 bar. The cardboard like material was supplied by Elring and the selected model was the EWP 210. It has a thickness of 0.75 mm with a density of 1.7 ± 0.15 g/cm^3.

3.1.6. Acid recovering device

In some of the synthesis reactions the precursors are only soluble in concentrated acidic solutions, as for example in the case of the bismuth precursors. The vapours that result from the evaporation of these solutions do attack easily the metallic parts of the system. Especially the vacuum pump is affected as the vapours tend to condensate in the refrigeration oil. The acidic media and the heat produce to corrosion of metallic

elements and the degradation of organic gaskets (seals). The oil as well as the finely adjusted pieces are concerned. For this reason, an acid trap is placed just before the pump.

This trap consists of two concentrically placed cylinders in between a strong solid base captures the acid vapours yielding innocuous salts. The exchangeable cartridge is filled with calcium hydroxide. Additionally, a pH indicator is included so that, once the basic salt is depleted, the change in pH can be determined visually. The chosen device is the 1420H-20 model from Welch Vacuum. It has a capacity of up to 12 CFM (340 L/min). This acid neutralization trap is filled with calcium hydroxide and includes ISO NW flange connections.

3.1.7. Vacuum pump

The pump at the end of the setup (**Figure ,** 7) is in charge of maintaining the system under vacuum. The vacuum is one of the conditions that produces the flash which forces the solvents to evaporate and triggers the crystallization. On the other hand, the pump extracts constantly the gases present inside of the chamber to enable the flow of matter.

The pump used is a two-stage rotatory vane vacuum model ZEBRA RH 0060B from Busch. Taking into account the solvent that is pumped into the system, the volume of gases produced that needs to be extracted is between 5.5 – 16.5 m^3/h. The pump is able to produce the vacuum with a nominal pumping speed of 60 m^3/h and arriving at an ultimate total pressure of 6.7 * 10^{-3} bar. The motor is a three-phase type with a nominal motor rating of 2.2 kW.

3.2. Experimental synthesis protocols

In general, all the synthesis processes follow similar steps which are described below. The first case will be described in detail followed by synthesis protocols where just the important differences are highlighted.

These two solutions are poured into separate tanks. All the tanks are put under pressure, the tanks holding the solutions of precursors as well as the tank containing pure isopropanol. The liquid of this tank is mainly used for the warm up phase, cleaning of the system and pre-synthesis tests. This pressure is obtained by introducing gaseous nitrogen into the system at 40 bars.

The heating gun and the filter heating belt are turned on before the synthesis to preheat the system, to avoid fluctuations for example owing to the condensation of the spray. The heating gun is set at level 7, this corresponds to flow of air at around 400 °C, which heats the walls of the chamber up to approximately 150°C. Additionally the heating belt is set to 80 °C.

The system is designed to support the use of hollow cone nozzles. The nozzle size will define the flow rate of the liquid that enters the chamber as well as the cone size of the spray. In this case, taking into account the size of the chamber and the power of the vacuum pump, the nozzle used was a “00” nozzle. This corresponds to a nozzle with an orifice of 80 µm in diameter. The standard nozzle is equipped with a polymeric plug to avoid dropping of the nozzle and seals made of the same polymer. The plug was removed to avoid the decomposition and clogging of the nozzle, and the seal was replaced by a Kalrez® 6375 FFKM seal, a perfluor-elastomer O-ring by Du Pont Dow elastomers. These seals are resistant to acids, bases, amines, steam, ethylene oxide and many other aggressive chemicals. The maximum service temperature is 275 °C whereas the minimal service temperature is -20 °C.

Using pure isopropanol, several system parameters and conditions abnormalities are checked. This includes obstruction in the nozzle, leaks in the nozzle, irregular temperature measurements, irregular spray cone geometry and irregular behaviour of the pump and leaks in the hermetic connection between parts. Once the system has been checked, the warm up phase begins.

The warm up phase is intended to put the system under working conditions before starting the synthesis. This is done by using the same solvent as the one used for preparing the solutions without any solute. By doing so, the synthesis will start in stable reaction conditions and without disruptive fluctuations because of the entry of liquid into the system can be avoided. It is recommended to warm up slowly to avoid the decomposition of the seals by thermal gap. The warm up phase ends once several requirements are met. On one hand, the temperature of the nozzle reaches and maintains stable at the working temperature (generally 160 °C). On the other hand, the reaction conditions and the pressure inside the chamber (usually between 1.9 and 2 mbar) show little to no oscillations. Then the synthesis starts.

During the main part of the process the nozzle needs to be maintained at the same temperature. The flow of the nozzle is influenced by the thermal expansion of the metal of which it is made of. Thus, the nozzle is affected by a feedback loop. This means that when the body of the nozzle increases in temperature, the metal dilates and as consequent inner diameter diminishes and the flow is constrained. This in turn lowers the flow rate, which diminishes the heat of the nozzle that is absorbed by the fluid. As the cooling of the nozzle is less important, the temperature raises faster. The opposite effect can be observed when the nozzle cools down too much. The dilation of the metal reverts and the flow rate increases, increasing in turn the cooling of the nozzle. This effect is more important at certain temperatures, which also depends on the solvent used. In the case of isopropanol, one of the “steps” can be found at around 150 °C. Furthermore, to maintain all the components in gaseous phase in the chamber during the process is of uttermost importance. At a pressure of 30 mbar, small water droplets are formed inside of the chamber. Taking into account the phase diagram of water, the temperature of the droplets can be estimated to be at ~25°C. As the layer of particles grows on the filter, the charge loss increases and therefore the vacuum in the chamber is lost gradually. When the layer is so thick that the pressure inside the chamber arrives at 30 mbar, the synthesis reaction is stopped. The valves that control the feeding are closed and the heating is stopped. The system is left under vacuum a few minutes to remove any remaining solvent vapours.

When the pressure inside of the chamber and the temperature of the nozzle reach the desired value the synthesis phase starts. This is done by changing the feeding from the pure HPLC isopropanol to the reacting solutions. In this synthesis process water is

present in the system, so the reaction is stopped when the pressure of the chamber reaches 30 mbar. The valves controlling the feeding ways are closed and the heating devices of the system are turned off. The system is maintained under vacuum for approximately 2-3 minutes to evacuate the remaining gases and vapours.

3.2.1. Preparation of pure titanium dioxide

Titanium oxide nanoparticles are produced in the SFS system following several steps. The first one is the preparation of the two solutions containing the reactants involved in this synthesis: TTIP and water. The solution containing titanium tetra-isopropoxide (TTIP) is prepared by mixing the titanium precursor in 500 mL of HPLC grade isopropanol to form a 1 wt. % solution. To avoid undesired spontaneous reaction of TTIP with the ambient moisture, a certain amount of solvent is first put in the flask, then the precursor is introduced and finally the flask is completed with isopropanol. On the other hand, the water containing solution is prepared by using the same solvent. To the 500 mL of isopropanol different quantities of water are added. For the 1:1 H_2O to TTIP ratio the quantity added corresponds to 0.25 mL, for the 1:2 ratio 0.50 mL and for the 1:4 ratio 1.00 mL.

The precision valves are adjusted to the position needed to ensure equal flow for both feeding ways. This means that for every synthesis that bases on different solutions, mixed with different compounds or at different concentrations, a new position for the valves has be found as the viscosity, and hence the flow rate changes. At the end of each experiment, the masses of the resting solution are measured and compared to the estimated mass flow rate. This is done to ensure the stability of the flow during the experiment and to ensure a controlled synthesis.

Prec. ratio	**VP_{Ti}**	**G_{Ti} (g/min)**	**VP_{H20}**	**G_{H2O} (g/min)**
1:1	0.19	9.9	1.00	9.8
1:2	0.13	8.6	0.19	8.7
1:4	0.13	8.8	0.20	8.9

Table 2. *Precision valve positions and corresponding average flow rates for different TTIP to H_2O ratios; VP_{Ti}: titanium solution valve position, G_{Ti}: mass flow rate of titanium solution, VP_{H2O}: water solution valve position and G_{H2O}: mass flow rate of water solution.*

Once the filter is extracted from the support, the solid powder is recovered under an ionized airflow to avoid material loss due to electrostatic charge. To remove organic impurities and to crystallize the ceramic material, the powder is annealed in a furnace. The powder was annealed up to 400 °C with a heating rate of 5 °C/min. The matter was held under these conditions for 4 hours under air. Finally, it was left cooling down to room temperature.

3.2.2. Preparation of titanium dioxide doped with silver

The synthesis process of silver charged titanium oxide is similar to the one to produce pure titanium oxide. The solution of TTIP in HPLC grade isopropanol is prepared following the same procedure, to obtain 500 mL of 1 wt. % solution. The silver precursor used for this material is silver nitrate ($AgNO_3$). Silver nitrate is dissolved into water. Then this water is used to create the partner solution (0.002 wt. %). The proportion of the reactants chosen for this reaction is the 1:2 TTIP to H_2O ratio, therefore 1 g of $AgNO_3$ is mixed with 0.5 mL of water.

VP_{Ti}	G_{Ti} (g/min)	VP_{Ag}	G_{Ag} (g/min)
1.01	13.6	1.14	13.3

Table 3. *Precision valve positions and corresponding average flow rates for the titanium and $AgNO_3$ system; VP_{Ti}: titanium solution valve position, G_{Ti}: mass flow rate of titanium solution, VP_{Ag}: silver solution valve position and G_{Ag}: mass flow rate of silver solution.*

The powder removal from the filter is also performed under the ionized air to avoid the material loss. To remove the organic subproducts and to crystallize the ceramic material, the powder is annealed in a furnace. The powder was annealed up to 400 °C with a heating rate of 5 °C/min. The matter was held under these conditions for 4 hours under air. Finally, it was left cooling down to room temperature.

3.2.3. Alternative preparation of titanium dioxide doped with silver

The synthesis process of silver charged titanium oxide in an autoclave was performed using the same solutions. For this, the solution of TTIP in HPLC grade isopropanol is prepared following the same procedure, to obtain 500 mL of 1 wt. % solution. The silver precursor used for this material is silver nitrate ($AgNO_3$). Silver nitrate is dissolved into

water. Then this water is used to create the partner solution (0.002 wt. %). The proportion of the reactants chosen for this reaction is the 1:2 TTIP to H_2O ratio, therefore 1 g of $AgNO_3$ is mixed with 0.5 mL of water. Both solutions are mixed, and 45 mL are placed in the autoclave, which is heated up in an oven at 160°C. This operation is performed for 2 hours and 24 hours.

3.2.4. Preparation of copper(II) oxide

The synthesis process copper oxide starts by mixing the solutions that will react in the SFS. One solution is mixed by putting 3.9 g of copper nitrate pentahemihydrate ($Cu(NO_3)_2 \cdot 2.5\ H_2O$) in 500 mL of HPLC grade isopropanol. This gives a 1 wt. % solution. The partner solution is created by adding 500 µL of 30 % ammonia (NH_3) in water solution. The ammonia added reacts with the copper nitrate to form copper hydroxide.

To initiate the synthesis, the system is warmed up by letting liquid isopropanol into the system. At the same time the nozzle heater warms up until the temperature set previously at 155 °C.

VP_{Cu}	**G_{Cu} (g/min)**	**VP_{NH3}**	**G_{NH3} (g/min)**
0.20	9.2	0.10	10.5

Table 4. *Precision valve positions and corresponding average flow rates for the $Cu(NO_3)_2 \cdot 2.5\ H_2O$ and NH_3 system; VP_{Cu}: copper solution valve position, G_{Cu}: mass flow rate of copper solution, VP_{NH3}: ammonia solution valve position and G_{NH3}: mass flow rate of ammonia solution.*

The powder removal from the filter is also performed under the ionized air to avoid the material loss. The powder is annealed in a furnace to remove the organic byproducts and to crystallize the amorphous material. The powder was annealed up to 400 °C with a heating rate of 5 °C/min. The matter was held under these conditions for 4 hours under air. Finally, it was left cooling down to room temperature.

3.2.5. Preparation of titanium dioxide and copper oxide composite

The synthesis process of the copper oxide and titanium oxide mixture is similar to the one to produce pure titanium oxide. The solution of TTIP in HPLC grade isopropanol is prepared following the same procedure, to obtain 500 mL of 1 wt. % solution. The

copper precursor used for this material is copper nitrate hemi(pentahydrate) ($Cu(NO_3)_2 \cdot 2.5\ H_2O$). This compound is added in a 1:1 molar copper/titanium ratio. Therefore 3.19 g of $Cu(NO_3)_2 \cdot 2.5\ H_2O$ are added to the TTIP solution. The partner solution is created by mixing 0.5 mL of water and 0.5 mL of ammonia (30 % in water) into 500 mL of HPLC grade isopropanol. The ammonia added reacts with the copper nitrate to form copper hydroxide. The proportion of the reactants chosen for this reaction is the 1:2 TTIP to H_2O ratio.

$VP_{Ti/Cu}$	$G_{Ti/Cu}$ (g/min)	$VP_{H2O/NH3}$	$G_{H2O/NH3}$ (g/min)
1.00	11.5	0.10	10.2

Table 5. *Precision valve positions and corresponding average flow rates for the TTIP and $Cu(NO_3)_2 \cdot 2.5\ H_2O$ system $VP_{Ti/Cu}$: titanium/copper solution valve position, $G_{Ti/Cu}$: mass flow rate of titanium/copper solution, $VP_{H2O/NH3}$: water/ammonia solution valve position and $G_{H2O/NH3}$: mass flow rate of water/ammonia solution.*

The powder removal from the filter is also performed under the ionized air to avoid the material loss. To take out the organic byprodcuts and to crystallize the material, the powder is annealed in a furnace. The powder was annealed up to 400 °C with a heating rate of 5 °C/min. The matter was held under these conditions for 4 hours under air. Finally, it was left cooling down to room temperature.

This compound was re-annealed at 600 °C for 2 hours under air and using the same heating rate of 5 °C/min. This process was repeated a second time using the same conditions but heating up to 800 °C.

3.2.6. Preparation of bismuth titanate ($Bi_4Ti_3O_{12}$ or $2Bi_2O_3 \cdot 3TiO_2$)

The synthesis process of bismuth titanate ($Bi_4Ti_3O_{12}$) requires additional steps as the solutions are more complex than for the titanium oxide synthesis. For mixing the solution that contains the bismuth precursor, 2.049 g of bismuth nitrate pentahydrate ($Bi(NO_3)_3 \cdot 5\ H_2O$) are dissolved into a water, acetone ($(CH_3)_2CO$) and acetic acid (CH_3COOH) mixture. The acetic acid was necessary to dissolve the bismuth precursor. The composition of this mixture is 0.12 mL of water, 160 mL of acetic acid and 340 mL of acetone at room temperature. The proportion of TTIP to H_2O ratio is 1:2. The relation of bismuth and titanium present in the crystalline network of the powder depends on

the relative amounts used for the synthesis. For the case of $Bi_4Ti_3O_{12}$, 0.94 mL of TTIP are added to 500 mL of isopropanol HPLC grade.

VP_{Ti}	G_{Ti} (g/min)	VP_{Bi}	G_{Bi} (g/min)
0.20	12.6	0.11	9.3

Table 6. *Precision valve positions and corresponding average flow rates for the titanium and bismuth system; VP_{Ti}: titanium solution valve position, G_{Ti}: mass flow rate of titanium solution, VP_{Bi}: bismuth solution valve position and G_{Bi}: mass flow rate of bismuth solution.*

The powder removal from the filter is also performed under the ionized air to avoid the material loss. To remove the organic subproducts and to crystallize the as-prepared material, the powder is annealed in a furnace. The powder was annealed up to 650 °C with a heating rate of 5 °C/min. The matter was held under these conditions for 4 hours under air. Finally, it was left cooling down to room temperature.

3.2.7. Preparation of bismuth titanate ($Bi_2Ti_2O_7$ or $Bi_2O_3{\cdot}2TiO_2$)

The synthesis process of bismuth titanate ($Bi_2Ti_2O_7$) requires additional steps as the solutions are more complex than for the titanium oxide synthesis. For mixing the solution that contains the bismuth precursor, 2.049 g of bismuth nitrate pentahydrate ($Bi(NO_3)_3 \cdot 5\ H_2O$) are dissolved into a water, acetone ($(CH_3)_2CO$) and acetic acid (CH_3COOH) mixture. The acetic acid was necessary to dissolve the bismuth precursor. The composition of this mixture is 0.154 mL of water, 160 mL of acetic acid and 340 mL of acetone at room temperature. The proportion of TTIP to H_2O ratio is 1:2. The relation of bismuth and titanium present in the crystalline network of the powder depends on the relative amounts used for the synthesis. For $Bi_2Ti_2O_7$, 1.2 mL of TTIP are added to 500 mL of isopropanol HPLC grade.

VP_{Ti}	G_{Ti} (g/min)	VP_{Bi}	G_{Bi} (g/min)
0.20	12.1	0.11	9.9

Table 7. *Precision valve positions and corresponding average flow rates for the titanium and bismuth system; VP_{Ti}: titanium solution valve position, G_{Ti}: mass flow rate of titanium solution, VP_{Bi}: bismuth solution valve position and G_{Bi}: mass flow rate of bismuth solution.*

The powder removal from the filter is also performed under the ionized air to avoid the material loss. The crystallization of this material and the removal of the organic byproducts is performed by annealing in a furnace. The powder was annealed up to 650 °C with a heating rate of 5 °C/min. The matter was held under these conditions for 4 hours under air. Finally, it was left cooling down to room temperature.

4. Chemical, morphological and structural characterization of the materials

4.1. Thermogravimetric analysis (TGA)

This method puts the material under a controlled increase in temperature under a certain atmosphere and records the variations in mass. This mass changes can be related to chemical and physical phenomena. There are thermal phenomena in the material that have a positive or a negative mass variation. Among the most common phenomena that include a weight gain is the oxidation, when performed in an oxygen containing rich atmosphere. Similar mass gains also occur for nitrogen or methane when performed in the corresponding atmospheres (nitriding, carburation). Weight loss phenomena include the removal of chemical water, adsorbed species or the thermal decomposition of compounds like carbonates, oxalates or the oxidation of organic molecules in gaseous species. The TGA was used during the thesis mainly to study the removal of both chemical water and organic residues. At which temperature and in which degree the mass changes are specific for every compound, and like this data can be withdrawn.[180]

The instrument used for this purpose is the Seiko EXSTAR 6200. This apparatus allows to perform thermogravimetric analysis as well as differential thermal analysis (DTA). The measurements can be performed under air, inert gas or vacuum (10^{-2} Torr). The balance method of the analyser works as a horizontal differential type using alumina as crucible reference material.

A standard procedure consists in introducing the sample, usually from 5 – 10 mg of it, in am alumina crucible. The sample will be heated up from 25 to 1000 °C with a heating rate of 5 °C/min. The measurement is normally performed under air with a flow rate of 100 mL/min, but also using inert gases like nitrogen or argon. Once reached the desired temperature the system cools down to room temperature.

The information obtained from this analysis method is crucial to understand the material. This analysis permits to elucidate the composition of the material, like this all the powders synthetized by the SFS system were examined by TGA. Basing on the calcined rest, and the difference in weight that occurs during the heating, it is possible to identify the mother-compound and the intermediate states. The thermal decomposition that the compound undergoes can be studied thanks to this analysis method basing on the mass change. Additionally, the calcination conditions can be

optimized by studying the compound under these circumstances. Therefore, necessary information, like the temperature that needs to be reached in the calcination process to crystallize the amorphous powder, can be withdrawn from this method.

4.2. Differential scanning calorimetry (DSC)

The DSC is an analysis method based on measuring the difference in heat necessary to increase the temperature of a given material compared to a reference. In comparison to the DTA, where the heat flow to the reference and the sample is the same, in DSC the temperature for both bodies is the same. This means that, when both samples are heated up using the same energy, the thermally induced processes that take place in the measured sample will produce a temperature variation compared to the reference. These thermally induced processes can be of two different kinds depending on the quantity of heat needed to get both samples at the same temperature. When the sample absorbs heat during this phase the process observed is endothermic. Likewise, if the sample undergoes an exothermic stage it will generate its own heat, which means that the input of heat necessary to reach a certain temperature is less. Crystallization, phase transition or chemical reactions are some of the most common examples.[181]

The DSC device used is a Q1000 model from TA instruments. This equipment is equipped with an auxiliary cooling system which permits the temperature to range between -80 and 500 °C. Special pressure resistant crucibles (SWISSI M20) for differential scanning heat flux calorimeters are used for the measurements. These crucibles are recovered by 10 µm thick gold coating for corrosion resistance. The crucibles have a mass ~ 0.98 g, with an internal volume of 20 µL. The maximum operating pressure is 217 bar and the maximum operating temperature is 400 °C.

A typical test using this device is carried out as follows. The powder sample (3 – 4 mg), is put into one of these special crucibles. It is sealed afterwards applying pressure on the lid and creating a hermetic vessel. This vessel is heated up from 25 to 450 °C with a heating rate of 5 °C/min under gaseous nitrogen flow of 50 mL/min.

The thermal decomposition that the compound undergoes can be studied thanks to this analysis method basing on the energy difference. Endothermic or exothermic characteristic reactions that take place during this processes can be easily identified and measured. The most common endothermic process are melting, evaporation of

the material or some chemical reaction. On the other hand, common exothermic phenomena are crystallization or certain phase changes, along with exothermic chemical reactions.

4.3. Fourier transform infra-red spectroscopy (FT-IR)

The FT-IR permits to obtain of information regarding the chemical bonds of the molecules that form the analysed material. In other words, infrared spectra are obtained as a result of the part of infrared light that is absorbed or emitted by the sample by passing through it. The characteristic of the FT-IR is that the spectra is made of a back-calculation of the data obtained by applying the Fourier's transform algorithm. These data come from irradiating the sample with discrete frequencies over a broad range, producing one for each frequency. Thus, the molecules do absorb certain radiation frequencies when they match with the vibrational frequency of the bonds. In accordance to the amount of energy in form of infrared radiation and the wavelength of the radiation that is absorbed, information of the chemical structure of the molecule can be deduced.

The measurement of the infrared spectra was performed by a Tensor 27 from Bruker equipped with a MIRacle single reflection ZnSe ATR from Pike technologies. This FT-IR spectrometer is able to render measurements in a spectral range from 7500 to 370 cm^{-1} using a standard KBr beamsplitter. The resolution is better than 1 cm^{-1} and the wavenumber accuracy is better than 0.01 cm^{-1}. The interferometer is a RockSolid™ permanent aligned.

The powder was put on the FT-IR spectrometer after measuring the background. Under air and by pressing the powder on the sensor the measurements were taken by transmittance. The FT-IR spectroscopy was principally used to identify the presence or absence of the different organic compounds present before and after the calcination. Like this it could be evaluated if the powder was totally free of any organic byproducts. The reaction conditions inside of the SFS system were optimised by comparing the peaks that resulted from the organic precursor to the peaks that were measured as result of the reacted species.

4.4. Raman spectroscopy

This technique bases on the interaction between light and the molecules to gather information about their chemical structure. It is similar to infrared spectroscopy, and can give additional, complementary information. It is able to determine the vibrational modes of the molecules by measuring the photons which are not absorbed as a result of inelastic scattering.[182] The light source, in most of the cases a monochromatic laser, interacts with the matter, producing a shift in the energy as it passes through. Afterwards the light is collected into a filter by lenses to remove the undesired light, this is the elastic scattered radiation. After passing through a detector, which extracts the information. The shift of energy of the laser can be associated with the vibrational modes of the sample and thus the chemical structure of the compound.

The microscope used for characterization is the confocal raman microscope inVia™ by Renishaw. It is equipped with a Stellar-RMN green laser working on 514 nm with an output power of 50 mW.

The samples were put on a glass substrate and dispersed for the analysis. The single particles were searched using 10x, 20x and 50x magnification lenses. Once an interesting particle or agglomerate is found, the laser is focused on it. The measurements were performed at room temperature and ambient pressure. The laser beam was adjusted to 1 or 5 % of the total energy output and measurements ranged from 3200 cm^{-1} to 100 cm^{-1}. Like this several particles were studied for each compound until a clear and reproducible idea of the composition and distribution could be drawn.

The Raman microscopy was used as an analysis method complementary to FTIR to identify the species present in the materials. Supported by other techniques, the homogeneity of a sample can be verified by analysing different particles of the same sample. The crystal phase or the degree of crystallization can be determined by this method by comparing the position and the intensity of the peaks to those found in literature. This means that, by analysing the presence and the importance of the peaks associated to organic species the degree of the reaction and its efficiency can be tracked. Moreover, the amorphous nature of the particles could be verified through the position of broad hill-like peaks in comparison to the well-defined peaks associated to crystalline structures.

4.5. Powder X-Ray diffraction (XRD)

The compounds produce by the SFS technique were analysed by XRD before and after calcination. XRD bases on the interaction of the X-rays, but the use of neutrons or electrons is also common, with the matter. The wave that is emitted by the diffractometer has a known frequency. In the case of X-rays, the wavelength is around 1 Å, which is the appropriate length for the interaction between the rays and the compound at atomic scale. Depending on the arrangement of the matter, the waves can interfere constructively or destructively. If the matter is arranged in a symmetrical structure along the space, this is a crystal structure, some of the waves will produce a diffraction peak of a certain intensity, following Bragg's law, in the diffraction pattern. There will be certain points where the waves interact in a destructive manner with the matter and with each other, in these cases no peaks will be formed in the diffraction pattern. The space between these points is equal to the atomic spacing in the matter.

The device used for this purpose is a D8 Advance from Bruker which uses a copper anode (λ_{Cu}=1.54056 Å) to emit the X-rays. The diffractometer is equipped with a Lynxeye detector also from Bruker.

During this work, XRD was used to identify the phases of the produced samples. The presence or not of the peaks shows if the atoms are arranged in a crystalline or amorphous manner. Furthermore, the position and the relative intensity of the peaks, that appear when analysing crystalline products, can be correlated to JCPDS database from literature to identify the phase in which the powder has crystallized. In this way, different synthesis conditions could be compared. To understand the influence of the morphology and particle dimensions in the phase predilection of the oxides. Additionally, basing on the shape and dimensions of the peaks, the crystallinity of the powder can be identified as amorphous materials produce a broad background signal. Therefore, by comparing the resulting area of the sharp peaks, it can be determined which one is better crystallized. The size of elementary crystallites can be calculated by Scherrer's method. The formula is as follows:[183]

$$\tau = \frac{K\lambda}{\beta \cos\theta} \qquad (37)$$

Where τ is the mean size of the crystallites, K is a shape factor, λ is the wavelength of the X-ray, β is the broadening of the light at the half maximum intensity (FWHM) and θ is Bragg's angle.

4.6. Scanning electron microscopy (SEM)

SEM provides high resolution images of samples by using an electron beam. The electrons interact with the atoms at various depths of the surface of the particles giving back different kind of signals. The resulting signals are captured by a raster scan pattern. These signals, like secondary electrons or back-scattered electrons, will not only depend on how the electrons interact with the matter of the sample but also the topology of it. Some of these signals tend to be highly localized or will depend on the electronic structure of the atoms from which, with the adequate sensors, different kind of informations can be extracted. By this technique, characteristics like morphology, distribution of different species or identification and quantification of elements present in the sample can be analysed.

The SEM system used for producing the images for this work is a Nova NanoSEM 450 from FEI. For the emission of the necessary electron beam the SEM system is equipped with a thermoelectric field emission gun (FEG). Additionally, an X-ray sensor is installed, this permits to perform energy dispersive X-ray spectroscopy (EDX) on the samples for element mapping. The sensor is a Nano Quantax device from Bruker.

A small amount of the sample, a few milligrams, is placed on a conductive adhesive support that withstands the vacuum in the device. In some cases, to enhance the conductivity of the samples, necessary to avoid artefacts in the images, and to increase the stability of the compounds in vacuum, the powders are covered by an ultrathin gold layer (≈ 10 nm) by cathode sputtering deposition.

SEM is a crucial characterization technique for material analysis as it makes it possible to visualize the particles with high magnification. In this sense, SEM images were mainly used to ascertain the topology of the particles as well as the size and size distribution of them. Moreover, how the particles are arranged among themselves was particularly interesting. The degree of aggregation and/or agglomeration gives a hint to understand the differences and the influences of the reaction process itself and the thermal treatment.

4.7. Transmission electron microscopy (TEM)

TEM also uses an electron beam, like SEM, but instead of aiming at detecting the signals that arise from the surface, it extracts the information from the electrons that pass through the matter. Depending on the setting of the device, like lenses, apertures or detectors, TEM is able to produce a different kind of informations. As the electron need to penetrate the material, the samples need to be prepared so they do not exceed 100 nm in thickness. By using imaging, diffraction, spectroscopy and combination of these, a huge amount of information on the matter at atomic and nanometric scale can be obtained. In this sense, the degree of crystallization of specific regions, details of the inner structure (dense or hollow) and outer structure (plain or a porous surface) of the particles can be distinguished. Furthermore, to identify which elements are present in the specimen as well as how they are distributed along the particles can be studied. It is also possible to examine locally the crystal structure of the different matter along the sample.

The equipment is an ARM-200F from JEOL equipped with a cold field emission gun (CFEG) installed in the “Institut de Science des Matériaux de Mulhouse” (IS2M) laboratory at the “Université Haute-Alsace” (UHA). Additionally, the system includes a double correction of spherical aberrations of the objective and the condenser lenses.

The samples are dispersed in a liquid to create a suspension. The solid particles are deposited on the support by evaporation of the solvent. The support consists of a polymer layer framed by a copper grid. This would guarantee that the particles are dispersed and isolated. Therefore, the samples are thin enough to be penetrated by the electron beam, thus enabling the analysis.

In a normal procedure, the particles were analysed in different ways. Firstly, the high-resolution images of the particles were taken so that the morphology, structure and overall dimensions could be recognised. Afterwards, X-ray diffraction was performed on the particles to examine their crystallinity. The planar space was compared to values from the literature to identify the crystallographic phases. This was followed by the study of the chemical compositions and the relative proportion of the elements present in the samples by EDX. Finally, coupling EDX to the imaging procedure, the distribution of the different elements inside of the particles was determined by chemical mapping.

These steps were performed several times on different portions of the sample to ensure that the measurements were representative for all the powder.

4.8. Specific surface area measurement by nitrogen adsorption (BET)

The most common method to measure the specific surface area of nanomaterials is based on the Brunauer-Emmett-Teller (BET) theory.[184] This theory describes the distribution and absorption of a given gas on a solid surface. It bases on the idea that gases form layers, first monolayers and afterwards multilayers, on the surface of a solid. Usually nitrogen (N_2) at the boiling point (77 K) is used as inert gas for the measurements. Therefore, depending on the morphology of the structure and the surface to volume ratio of the particles the quantity of gas physically adsorbed on the samples will change.

The measurements were performed on an ASAP 2020 from Micromeritics. This system is able to measure surface area, to perform porosimetry and to provide isothermal chemisorption. Furthermore, basing on a dense spherical model of the particles, the average size of them can be estimated. The formula for spherical particles is:

$$S_{BET} = \frac{6}{\rho \, \emptyset_{avg}} \qquad (38)$$

Where S_{BET} is the specific surface area basing on the BET theory, ρ is the density of the material and $\emptyset_{avg}$ is the average diameter of the spherical particles.

Specific surface area measurements were only performed on calcined powders after degasification. The degasification was performed under vacuum at 350 °C for 3 hours. Once the powder was free of adsorbed species, the measurement of specific surface area was performed as well as adsorption/desorption isotherms to characterize the porosity. The shape of the hysteresis of the isotherms could be classified basing on models found in the literature.

4.9. Mercury porosimetry

The technique is used to analyse the characteristics of the porous structure of the material. The nature of the pores, like pore diameter, pore volume and specific surface area, can be measured. This procedure bases on the forced intrusion of liquid mercury into the pores by applying a building pressure. The pressure will increase filling up step by step smaller pores, therefore the pore size can be calculated basing on the pressure applied and the surface tension of the mercury. This method bases on the assumption that the pores have a cylindrical geometry.

The used device for this measurement method is a model AutoPore IV 9500 series from Micromeritics. This porosimeter is able to the measure pore size distributions of pores ranging from 0.003 to 1100 µm.

Mercury porosimetry was applied to the ceramic materials to obtain complementary information about the pores of the matter. Due to its nature, this analysis method is able to measure bigger pore sizes than those measured by nitrogen absorption porosimetry. Thus, it is better adapted for materials with macro-porosity and is able to obtain more accurate results.

5. Pyrotechnic applications of materials prepared by SFS
   5.1. Preparation of energetic materials
      5.1.1. Nanothermites

A traditional thermite is a pyrotechnic composition made of an oxidizer (metal oxide) and a fuel (metal) which, undergoes a strong exothermic redox reaction.[53] In this sense, a nanothermite is a composite where not only the size of the constituents can be found at nanometric scale but also the mixing occurs at nanometric degree.[52] This enhances dramatically the reactivity of composite owing to the high surface area and the intimate mixing of the reactants. The high flame propagation velocities in nanothermite powders arises from their high porosity, which favours the convection of hot gases.[185]

The metallic fuel used in this work to prepare aluminothermic compositions is aluminium from Intrinsiq Materials Ltd. The average particle size of the aluminium particles is around 100 nm. The outer layers of aluminium are oxidized under controlled conditions to create a passivation layer. This formed shell of alumina (Al_2O_3) has thickness of 2 to 5 nm, and becomes the more important the smaller the particles are. Therefore, to know the amount of pure aluminium present in the material, the sample was analysed by TGA and resulted in 70.9 wt. % of pure aluminium, the rest being alumina. The specific surface area (23.7 $m^2 g^{-1}$) of the particles was also measured by BET. The metallic oxides used to prepare nanothermites were all prepared by the SFS.

The nanothermites were prepared by physical mixture of the components. For this a suspension of aluminium and metal oxides is formed using 50 mL of acetonitrile (CH_3CN) as liquid. The suspension is homogenised using a magnetic stirrer at 600 rpm for 10 min, followed by ultrasonic agitation during another 10 min. This will tear apart the agglomerates and also mix the different compounds. Once the suspension was uniform, the fluid was removed in a rotatory evaporator operating at 80 rpm, with a bath temperature set at 80°C. The acetonitrile is first evaporated by decreasing the pressure to 200-300 mbar. The condensed acetonitrile is then removed. The nanothermite sample is finally dried by decreasing the pressure to 20 mbar during 20 min.

5.2. Characterization of pyrotechnic properties

5.2.1. Determining the sensitivity thresholds to impact, friction and ESD

The sensitivity of explosives is defined as the amount of energy needed to initiate the reaction by impact, heat, friction or electrostatic discharge. The sensitivity of all the energetic materials prepared and studied by and for this work were determined following BAM standards. The sensibility thresholds to the three different solicitations, is defined as the highest energy input level at which the specimen does not react after being tested six consecutive times.

The shock sensibility of the sample was measured in a BAM Fall-Hammer model BFH Pex from OZM. This equipment measures the impact energy by gravitational potential energy. A hammer of known mass (0.25 kg to 10 kg) drops on the energetic sample from a known height, from 15 to 100 cm. Therefore, the amount of energy transferred to the sample, powder (40 mm^3) put in a steel cell, can be calculated as follows:

$$U_g = m * g * h \tag{39}$$

Where U_g is the gravitational potential energy (J), m is the mass of the reference body (kg), g is the gravitational acceleration (9.81 m s^{-2}) and h is the height of the reference body (m).

The equipment is able to perform the energy measurements between 1 and 100 J. The minimal ignition energy value considered as safe for the transport of energetic materials on public roads is 2 J.[186]

The sensibility to friction of the energetic compounds was measured in a BAM Friction apparatus FSKM 10 from OZM. The energetic sample (10 mm^3) is placed on ridged porcelain plate. A porcelain pen moves back and forth over the plate and over the powder. The pen applies a force over the surface proportional to the mass that is placed on the penholder. The energy measurement margin able to attain by this device is between 5 and 360 N. The minimal friction energy value considered as safe for the transport of energetic materials on public roads is 80 N.[186]

The electrostatic discharge (ESD) sensitivity of the energetic material was measured by an ESD 2008A device from OZM Research. The sample, powder fills around 7 mm^3

in volume, will be exposed to an electric discharge. This discharge will take place in form of an electric arc which can be controlled by the capacity of the system, between 0.045 and 200 nF, and the voltage of the system, between 4 and 10 kV. The energy that this electric discharge transmits to the powder can be calculated as follows:

$$E = \frac{0{,}5 * U^2 * C^2}{C + C_k} \quad (10)$$

Where E is the electric energy transmitted through the electric arc (J), C is the capacity of the capacitor (F), C_k is the Intrinsic capacity of the electric circuit of the device (F) and U is the voltage applied (V).

This device is able to produce an electric arc that delivers energy between 0.14 mJ and 10^4 mJ. The human body is able to produce electric arcs generated by static electric energy from 5 to 20 mJ.[187] [188]

5.2.2. Flame propagation measurement

Flame propagation velocity in the nanothermites prepared from the oxides synthesized by SFS was measured in tubes.

A standard test consists in filling the energetic compound in loose powder in transparent poly(methyl methacrylate) (PMMA) tubes to enable the follow-up of the reaction by means of a high-speed video camera. To ensure that the reaction reaches the steady state, the tube needs a minimal length. In this research, tubes of 15 cm of length were used for the experiments. Additionally, should the inner diameter of the tubes not be too small to restrain the speed of the propagation front. Studies show that the propagation velocity increases linearly with the inner diameter for similar tubular setups.[189] The outer diameter of the tubes used for the experiments performed during the thesis was 25 mm. The diameter of the central channel is 3 mm, which is, on one hand, large enough to study the propagation of the combustion front in most of aluminothermic nanocompositions and, on the hand, does not involve using large amounts of energetic material. To ensure that the density of the prepared samples is the same along the tube and between tubes, the tubes were filled stepwise, by noting down the height for every step. Once the tube is nearly completely filled, a space of

5 mm is left empty. This space is filled with an Al/CuO nanothermite with an equivalent fuel ratio of 1.4, which is necessary to ignite the nanocomposite.

These tubes are placed in a detonation chamber that withstand the detonation of 3 g of Trinitrotoluene (TNT). This chamber is equipped with an armoured glass window through which the camera records the phenomena. The camera used for this purpose was a v1610 from Phantom Ametek, which is capable of recording 16600 fps at a resolution of 1280 x 800 and up to 10^6 fps at a resolution of 128 x 16. The tests were performed at 50000 fps with a resolution of 1152 x 450.

To start the combustion reaction of the energetic materials, airbag igniters were used. The empty support, from Autoliv NCS, were filled with two layers of nanothermites. The first layer, is made of Bi_2O_3/B (90/10 wt. %/wt %) which is a composition sensitive to ignition. This reaction yields molten droplets of bismuth which start reaction of the second layer. The second layer is formed of a WO_3/Al nanothermite, the combustion of which forms molten tungsten droplets. The two layers were loaded successively and pressed with a force equivalent to 8 bar.

The flame propagation velocity can be calculated by dividing the distance travelled by the front for a given time. The real distance travelled can be calculated by proportional relation using the apparent distance of the front measured in the movie and knowing the value of the real length of the tube. The time can be calculated from the recording rate of the camera, whose inverse is the amount of time between frames. The distance travelled by the flame front is plotted in function of time. The slope of this curve corresponds to the propagation velocity of the reaction, which can be an accelerated, stable or decelerated phenomenon.

5.2.3. Explosion heat measurement

The energy liberated by the explosion of nanothermites can be measured in a bomb calorimeter. This apparatus, a type C 2000 from IKA, is designed to withstand the sudden pressure and temperature increase that is released by the reaction. The sample is put in a stainless-steel crucible which is placed in a hermetic steel cylinder (bomb C62) that is capable of resisting such conditions. This cylinder is submerged inside of a known amount of water. The temperature of the water jacket is constantly measured by a thermometer. The reaction is started by an electrically heated wire,

which gives enough energy to ignite a grain of GBTU 125, a double base powder made of nitrocellulose (~58 %) and nitro glycerine (~42 %).

In a standard measurement, the sample (~1 g), is place at the bottom of the bomb. The igniter (grain of GBTU 125 and fuse) is attached to the lid. The whole ensemble is placed inside of an agitated water reservoir (1.5 L). The reaction is started by an electrical current passing through the wire, which ignites the propellant. The temperature increase of the surrounding water is measured by the thermometer. Knowing the amount of reacted matter and the temperature increase, the heat of combustion can be calculated following these equations:

$$Q = q_r + q_i = \Delta T * (C_{v(bomb)} + C_{v(water)}) \quad (41)$$

Where Q is the total energy of the process, q_r is the energy output of the reaction, q_i is the energy input of the fuse, ΔT is the temperature increase, $C_{v(bomb)}$ is the heat capacity of the bomb and $C_{v(water)}$ is the heat capacity of the water reservoir.

The heat capacity of the calorimeter itself needs to be determined beforehand, to be able to perform any measurement. This is done by igniting a substance with a well-known heat of combustion. In this case cyclotrimethylenetrinitramine (RDX) is used, which has heat of combustion of 5749 J g^{-1}. The values for the fuse system are: 55 J g^{-1} for the electric fuse and 5021 J g^{-1} for the GBTU 125 grain. The heat capacity of the water is 4.18 J g^{-1} K^{-1}. Therefore:

$$C_{v(bomb)} = \frac{q_r + q_i}{\Delta T} - C_{v(water)} \quad (42)$$

Once the heat capacity of the calorimeter is determined, the heat of combustion of a specific reaction can be obtained as follows:

$$q_r = \Delta T * \left(C_{v(bomb)} + C_{v(water)}\right) - q_i \quad (43)$$

6. Photocatalytic applications of materials prepared by SFS
   6.1. Methanol photoreformation

The production of hydrogen by photocatalysis of methanol has been studied in a setup as the one represented in **Figure** . The materials synthesized by SFS, which act as catalysts to promote the redox reactions, were suspended in the liquid bath.

In a standard experiment, the suspension is prepared so that the concentration is 0.1 g L^{-1}. Therefore 630 mL of Methanol (MeOH) are mixed with 270 mL of deionized water. In this solution, 90 mg of the material are placed to obtain a suspension with the desired concentration. To disperse the solid particles, and thus obtain a homogeneous suspension, the liquid and the powder are stirred with a magnetic stirrer at 300 rpm and at the same time sonicated thanks to an ultrasonic tip for 2 minutes. Then the vessel is closed hermetically with a lid. The lid supports an UV-lamp which is surrounded by a water jacket. The UV lamp is a 150 W Ceramic-Metal-Halide Hg Lamp that artificially simulates solar light (31.9 mW cm^{-2}). This light contains 7.8% UV of the total irradiation wavelength emitted (280-400 nm). The water jacket is part of a thermal bath system, which maintains the temperature of the lamp at 20 °C. The suspension is

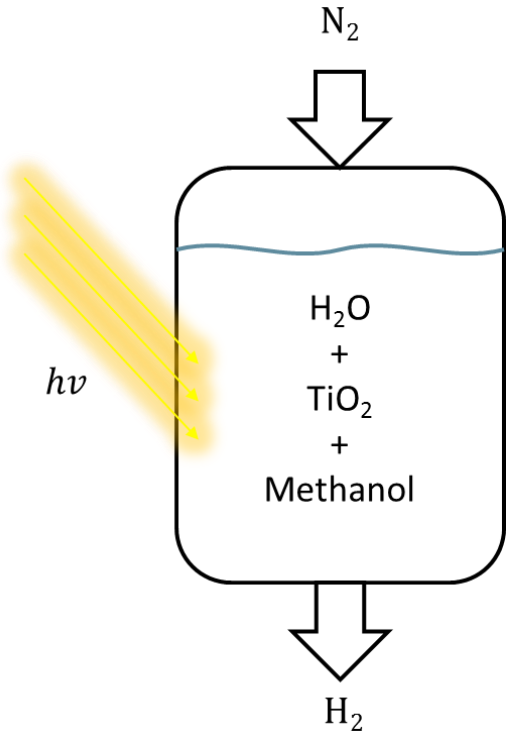

***Figure 8**. Schematic representation of the prototype used for the photoreformation of methanol*

kept homogeneous using a magnetic stirrer at 700 rpm during all the experiment. A gas inlet penetrates into the system through the lid, which feeds the system continuously with 100 mL min^{-1} of nitrogen. Additionally, an exit is provided for the system to extract the resulting gaseous products. These are fed into a gas chromatograph, which analyses the compositions and their relative proportion. To use the chromatograph the position of the signals need to be identified by using references beforehand. To remove the air present inside of suspension and to check the hermeticity of the setup, the system is left under the nitrogen flux for 1 hour without light. Once this is verified, the lamp is turned on and process is performed during 3 hours, extracting samples every minute, to guarantee that the reaction reached a steady state.

6.2. Characterization of photocatalytic properties

6.2.1. UV-Visible spectroscopy

One of the main characteristics of a semiconductor from a photocatalytic point of view is the band gap. This is the difference between the HOMO (Highest Occupied Molecular Orbital) and the LUMO (Lowest Unoccupied Molecular Orbital). This energy, measured in electronvolt (eV), is the minimum necessary for one electron to pass from the ground state to the excited state by radiation. This value can be obtained basing on the reflectance spectra measured under ultraviolet and visible light.

The spectrophotometer used was a Lambda 950 model from PerkinElmer. A special sample holder known as integrating sphere, in this case 100 mm, is used to be able to analyse solid powders. The measurements were usually performed in a wavelength range between 200 and 800 nm. Additionally, the obtained results were processed using the Kubelka-Munk function[190] :

$$\alpha = \frac{(1-R)^2}{2R} \tag{44}$$

Where α is the absorption coefficient and R is the reflectance value.

Afterwards, to obtain the band gap value of the semiconductor, the Tauc's equation was applied. Basing on the following equation:

$$\alpha h\nu = A\,(h\nu - E_g)^n \tag{45}$$

Where α is the absorption coefficient, h is the Planck constant, ν is the wavenumber, A is the band tailing constant, E_g is the energy of the band gap (eV) and n is a value depending on the electronic nature of the transition.[191]

Therefore, the energy of band gap can be obtained by plotting $(\alpha h\nu)^{1/n}$ versus the incident energy, i.e. $h\nu$.[192] The plot presents different parts, depending on the slope. The intersection with the abscissa of the extrapolation, obtained from the part where the slope is constant, is equal to the value of band gap.

7. Conclusions

The SFS system was successfully adapted to the production of nanomaterials by chemical reaction. These modifications were of different nature to control the reaction conditions but also to enhance the synthesis stability and to increase the production yield. In a typical synthesis experiment, the SFS system was able to produce between 500 mg and 1 g per hour.

In this chapter the different experimental protocols, which were used for this research, were described. These protocols served to produce titanium oxide, pristine or loaded with silver, bismuth titanates with different proportions, copper oxide in pristine form or as a mixture of oxides with titanium oxide.

The experimental techniques used (TGA, DSC, FTIR, Raman, XRD, SEM, TEM, BET, Hg porosimetry, sensitivity, flame propagation measurement, explosion heat measurement and UV-Vis) for the characterisation of the produced materials by SFS were described.

Finally, the specific experimental techniques used to study the photocatalytic and pyrotechnic applications of the as-produced materials were detailed.

PROPERTIES OF THE OXIDE MATERIALS

1. Glossary

SFE: Spray Flash Evaporation

SFS: Spray Flash Synthesis

FFKM: Perfluoroelastomer compounds with high amount of Fluoride

TTIP: Titanium tetraisopropoxide

HPLC: High-performance liquid chromatography purity degree

TGA: Thermogravimetric analysis

DSC: Differential scanning calorimetry

FTIR: Fourier transform infra-red spectroscopy

XRD: Powder X-Ray diffraction

SEM: Scanning electron microscopy

TEM: Transmission electron microscopy

EDX: Energy-dispersive X-ray spectroscopy

BET: Brunauer-Emmett-Teller theory

SSA: Specific Surface Area

CP: Copper precursor

ACN: Ammonium Copper Nitrate

2. Introduction

This chapter details the properties and the characteristics of the materials prepared by the SFS system. The produced materials are TiO_2, $Ag@TiO_2$, CuO, $Bi_xTi_yO_z$ and CuO/TiO_2. The materials that are described here were analysed from different points of view. The focus of this analysis is placed on the morphology, the size distribution, the crystal structure and the elemental distribution.

The first material studied is titanium oxide. The analysis of the particles made of the intermediate compounds that are produced by the SFS process is followed by a detailed discussion about the particle formation mechanism. Furthermore, the properties of the ceramic material after calcination are highlighted. This is followed by the characteristics of silver loaded titanium oxide particles, which were studied before and after calcination. The properties of this composite are compared to those of the same composite obtained hydrothermal synthesis.

The next oxide that is described is copper oxide. Therefore, the intermediate compounds, which were produced at different temperatures by the SFS system, were studied. Then, the properties of pure copper oxide, which is formed after calcination, are detailed.

Bismuth titanate produced by SFS at different titanium to bismuth ratios (1:1.35, 1:1 and 2:1) are depicted next. The different characteristics for each of these proportions are put under focus before and after calcination.

Finally, a mixture of copper oxide and titanium oxide was synthesized by SFS. This material, as well as the oxides prepared by its calcination at 400°C and 600°C, were characterized.

3. Materials based on Titanium oxide

3.1. Synthesis of pure TiO_2

Titanium oxide was synthesized according to three TTIP/H_2O molar ratios: 1/1, 1/2 and 1/4. The in-depth characterization of these materials made it possible to understand the influence of the TTIP/H_2O ratio on the final properties of the TiO_2 obtained.

3.1.1. Properties of pure TiO_2

All the titanium oxide powders produced by SFS are constituted of spherical submicron sized particles that are agglomerated in groups of several units.

For a TTIP/H_2O 1:1 molar ratio the particles have an average size of 153 ± 68.6 nm. The particles are dense, homogeneous and totally amorphous as can be seen in **Figure** . The quasi-spherical particles are slightly fused together forming agglomerates of a few dozens of units. These particles are less independent than for the other molar ratios. This is a direct consequence of the amount of water present during the reaction. As there are less water molecules present in the reaction per TTIP

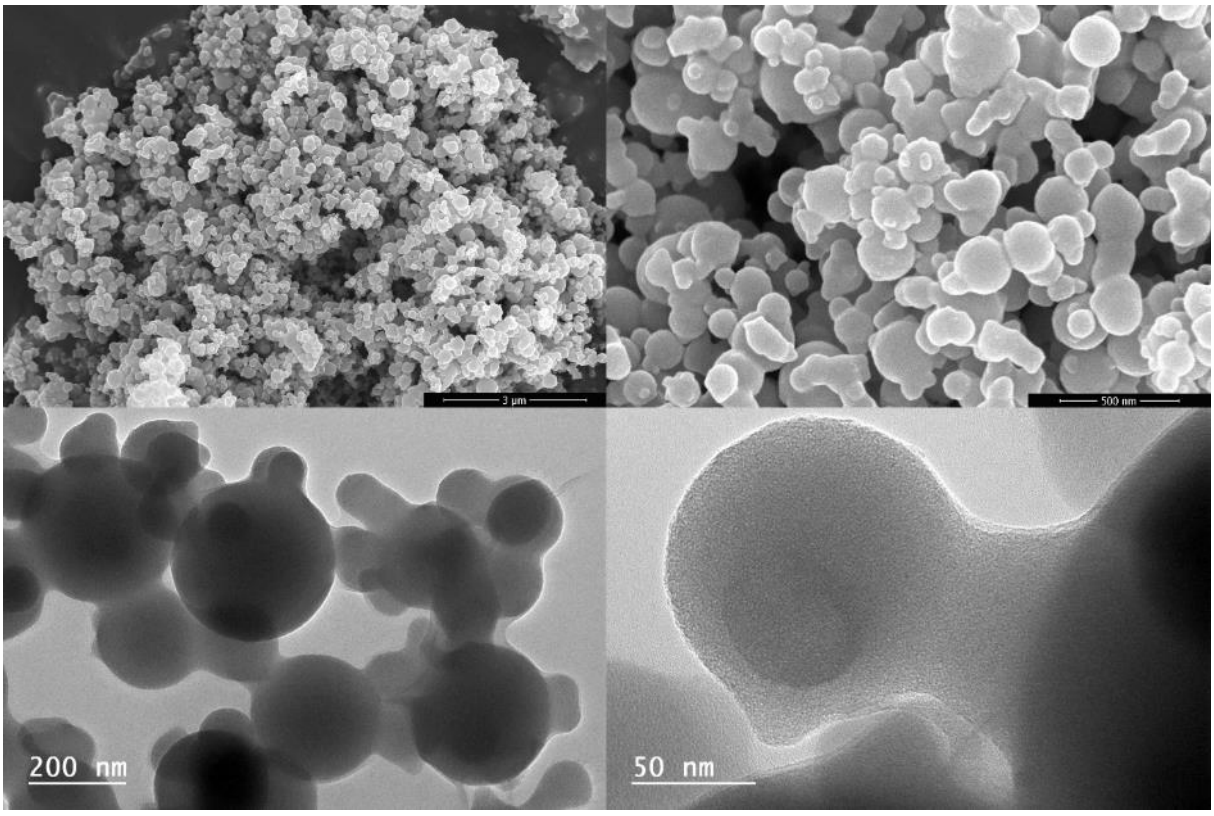

Figure 9. *SEM and TEM images of 1:1 TiO_2 precursor.*

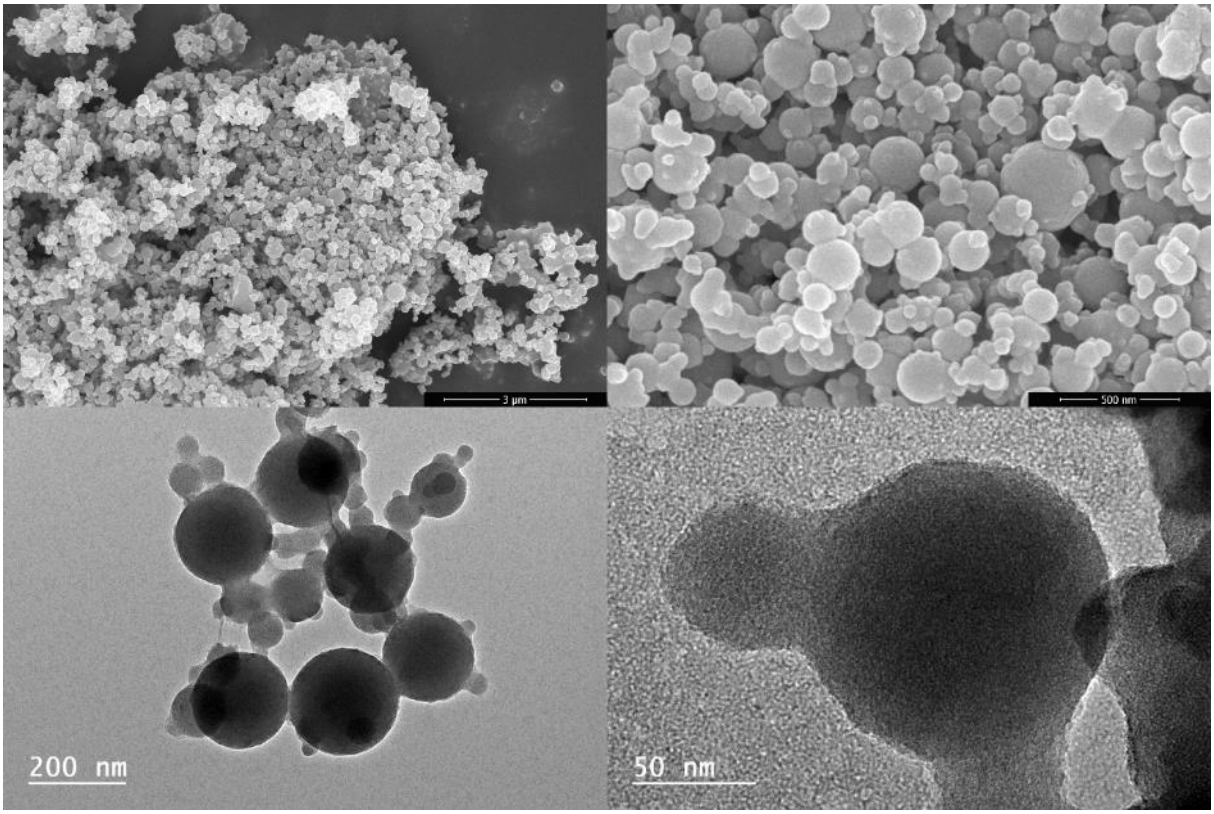

Figure 10. *SEM and TEM images of 1:2 TiO_2 precursor.*

molecule, the isopropyl-groups that are removed from the titanium “core” of the molecule will be less. This means that the reaction will be less complete, leaving TTIP molecules with several isopropyl unreacted groups. Taking into account that the water molecules preferentially react with TTIP molecules rather than with partially hydrolysed ones, the oxide network formed is more irregular because the titanium “cores” will less probably form bonds between each other. Owing to the limited amount of water present, the more advanced the hydrolysis of a TTIP molecule is the less probable it will be. This implies that less free hydroxyl groups will be available during the particle formation. Therefore, as there is not sufficient water present to hydrolyse TTIP, the titanium tends to form chain like networks instead of three-dimensional networks when the water molar ratio is higher.

For the 1:2 molar ratio, which is the stoichiometric value of the chemical reaction, the particles have an average size of 108 ± 50 nm. These particles are equally dense, homogeneous and totally amorphous as for the 1:1 ratio. Nevertheless, do these particles present a more defined spherical shape and are more independent. This can

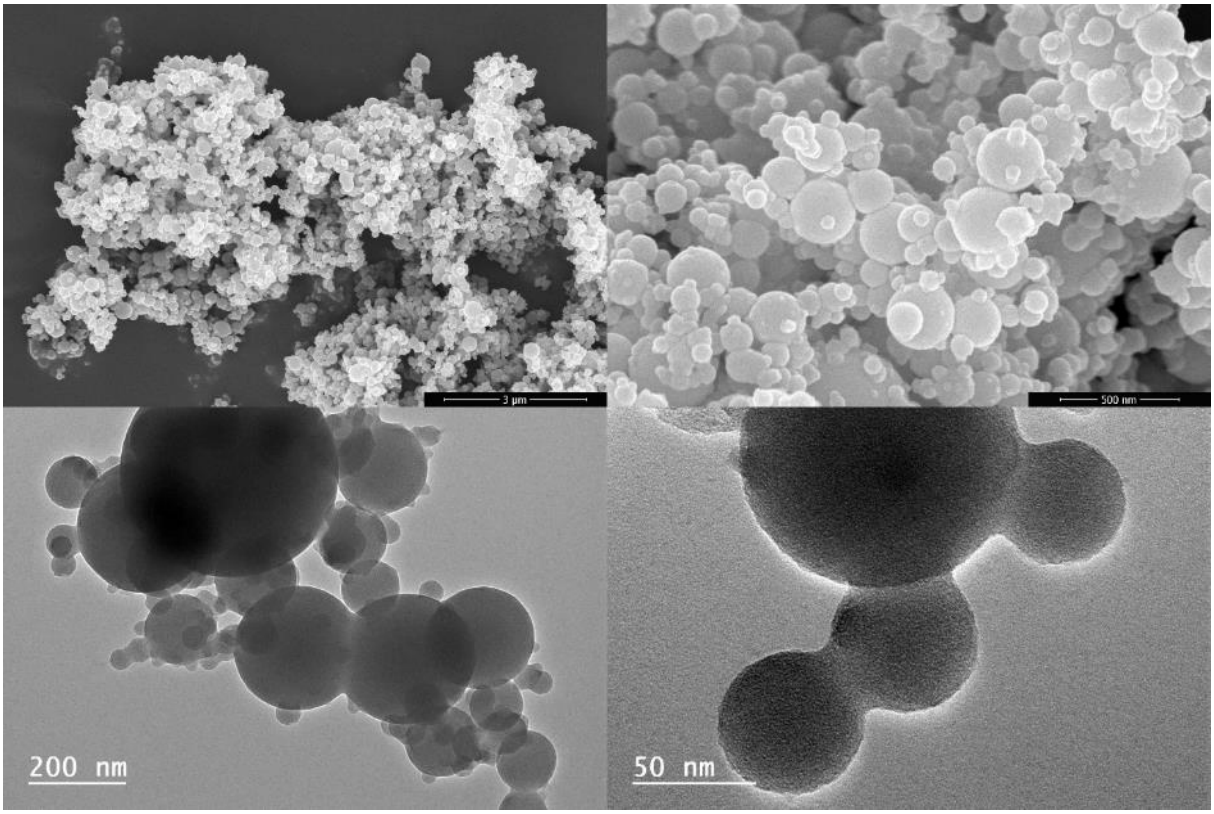

Figure 11. *SEM and TEM images of 1:4 TiO_2 precursor.*

be observed in the **Figure** . In this case the relative amount of water is enough to remove isopropyl groups from the TTIP molecules to form a more regular titania network. This means that during the particle formation, the chain reactions that are taking place in parallel between the different titania “cores” are fast enough to form the network during the spraying.

In the case of the 1:4 molar ratio, the particles formed are similar to those produced for in the case of the 1:2 molar ratio. This means that, once the minimal amount of water is satisfied for the reaction, the excess of water does not influence. The particles formed by this system have an average size of 116 ± 92 nm. These particles are also fully dense, homogeneous and totally amorphous with a spherical morphology. This is highlighted in the images in **Figure** .

The chemical composition of the titanium oxide nanoparticles produced is around 40 % of organic compounds and 60 % of titanium oxide. This is the same for all the cases studied. The TGA curves are shown in **Figure** . The mass variation has a pronounced negative slope up to ~220 °C. This corresponds to the removal of the organic species present in the sample.

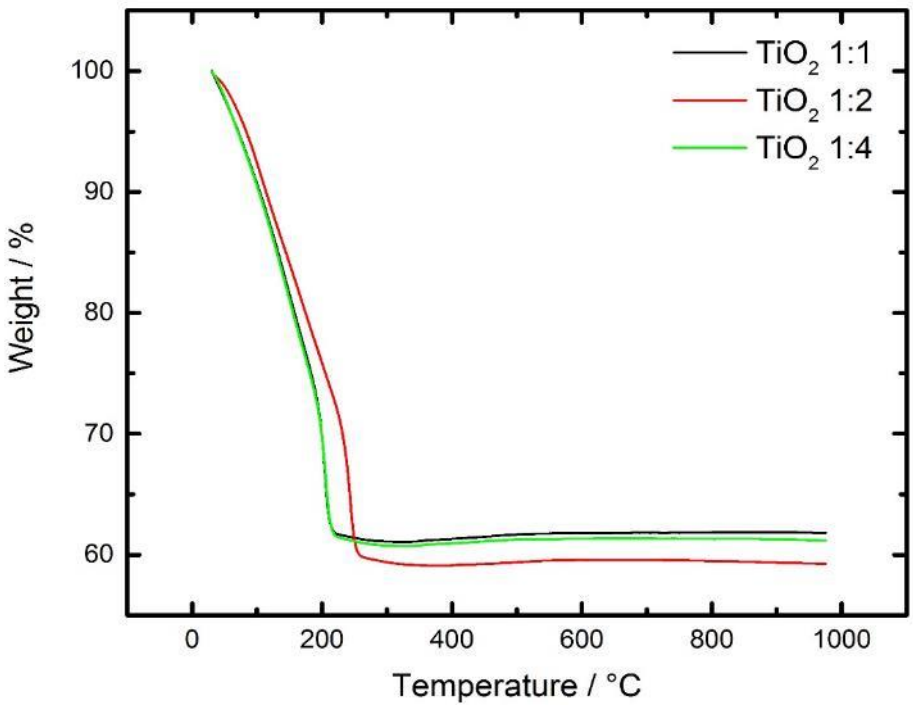

Figure 12. *TGA curve for different TiO_2 samples.*

According to literature, when the water to titanium ratio is between 1 and 4 which applies to all the cases studied, the first steps of hydrolysis will occur depending on the partial charges (δ) of the (OR) and the (Ti) parts as shown in **Table** .[66]

Precursor	h	δ(OPr^i)	δ(OH)	δ(OPr^i OH)	δ(H_2O)	δ(Ti)
$Ti(OPr^i)_4$	0	-0.15	-	-	-	-
$Ti(OPr^i)_4$ (OH_2)	1	-0.08	-0.38	+0.01	-0.28	+0.62
$Ti(OPr^i)_3$ OH	1	-0.08	-0.38	+0.02	-0.28	+0.62
$Ti(OPr^i)_3$ OH (OH_2)	2	0.00	-0.36	+0.10	-0.26	+0.64
$Ti(OPr^i)_2$ $(OH)_2$	2	+0.04	-0.36	+0.15	-0.25	+0.64
$Ti(OPr^i)_2$ $(OH)_2$ (OH_2)	3	+0.13	-0.34	+0.25	-0.22	+0.65
$Ti(OPr^i)$ $(OH)_3$	3	+0.28	-0.32	+0.41	-0.18	+0.67
$Ti(OPr^i)$ $(OH)_3$ (OH_2)	4	+0.38	-0.30	+0.52	-0.16	+0.68
$Ti(OH)_4$	4	-	-0.19	-	+0.01	+0.76

Table 8. *Partial charges for functional groups in TTIP molecules.*

This means that, energetically speaking, the most favourable state is the one where two (OR) groups are removed and replaced by hydroxyl groups because the δ(OR)<0 and δ(Ti)>0. They form polymeric chains like in the **Figure** :

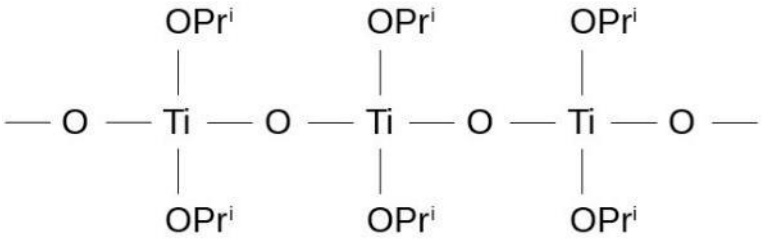

Figure 13. *Polymeric chain scheme of partially reacted TTIP molecules*

The hydrolysis does not completely remove the ^{i}OPr groups as the partial charge of the OR group becomes more and more positive. Therefore an increase in the hydrolysis ratio does not increase the hydrolysis degree. This is in accordance with the TGA analysis. Taking into account the mass of the TTIP with two hydrolysed isopropyl groups and the final mass of $TiOH_4$, the mass ratio of one to the other is 57,91 % which corresponds approximately to the 60 % mass loss of the TGA curve. This means that the hydrolysis rate is constant for all the systems studied.

From that point on, the mass does not show significant variation as the powder became pristine titanium oxide which is stable when temperature increases. Basing on the data obtained on the DTA analysis, see **Figure** , the exothermic peak at ~360 °C

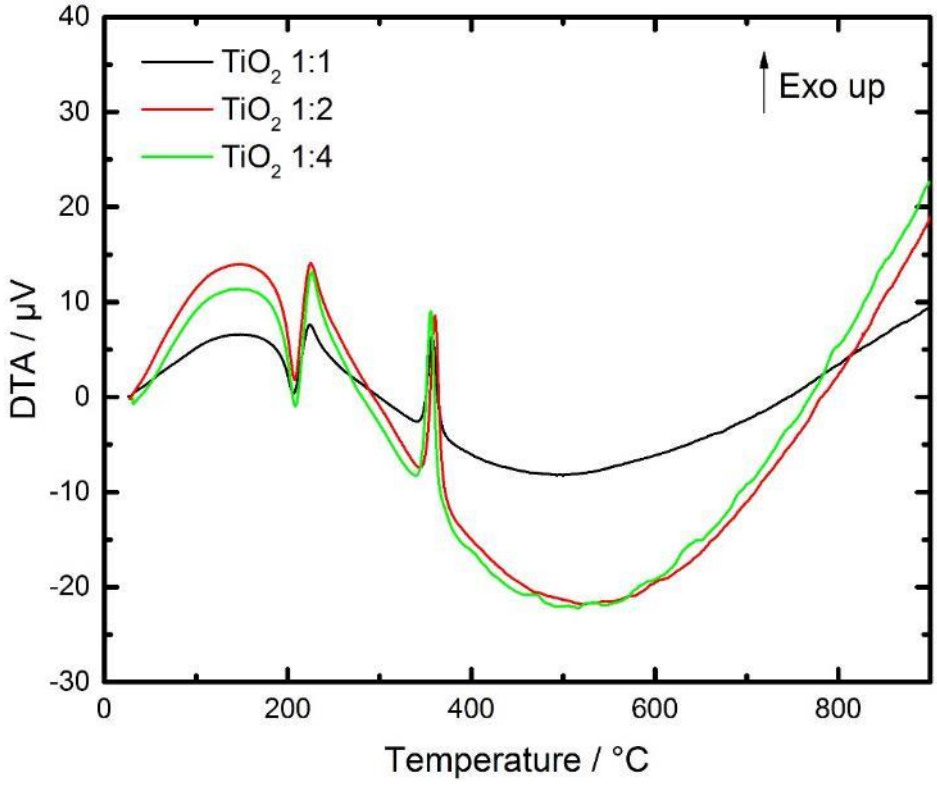

Figure 14. *DTA curve for different TiO_2 samples.*

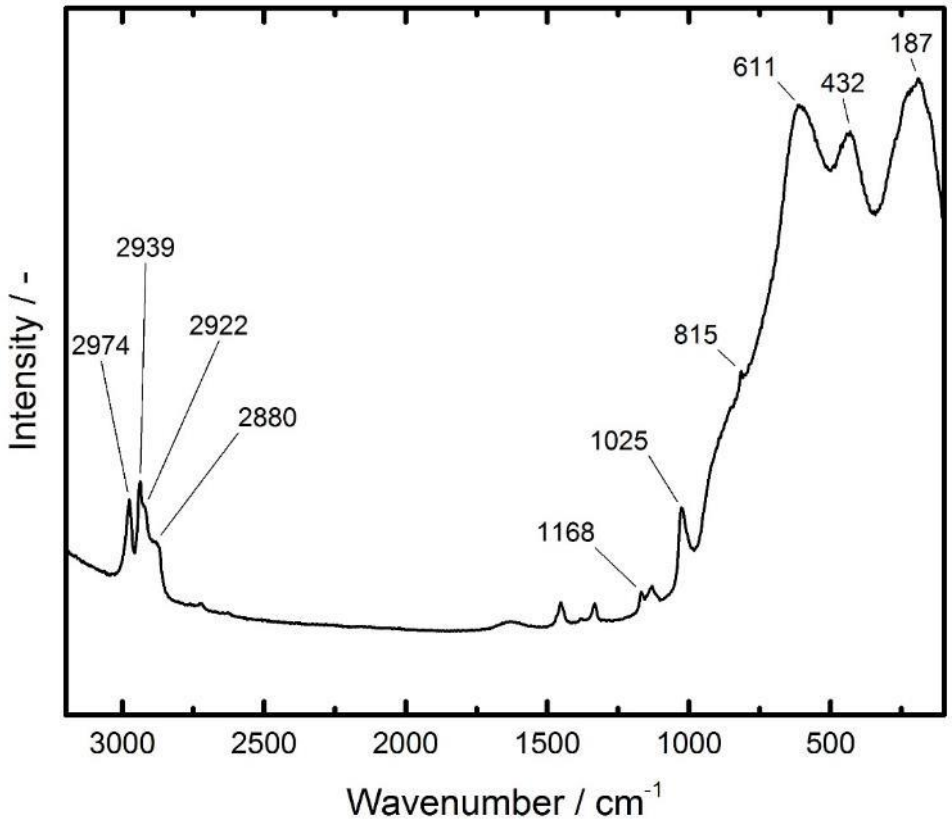

Figure 15. *RAMAN spectra of uncalcined TiO_2 1:2 sample.*

corresponds to the crystallization of the amorphous titania into the anatase phase.

The chemical nature of the organic molecules present in the amorphous particles has been identified by RAMAN spectroscopy. The three signals in form of peaks at 187 m^{-1}, 432 cm^{-1} and at 611 cm^{-1} correspond to amorphous titania.[193] The characteristics peaks that are highlighted in **Figure** are the ones that make the difference between the TTIP molecules and the isopropanol molecules.[194] Basing on the literature, the peaks at 825 cm^{-1} can be assigned to the stretching vibrations of the CCC bond and at 1168 cm^{-1} to the rocking vibrations of the CH_3 groups in the isopropanol molecules. Meanwhile, the peak situated at 1025 cm^{-1} corresponds to the stretching vibrations of Ti-O and of C-O bonds in the TTIP molecules. The peaks at higher wavenumbers, *i.e.* 2880 cm^{-1} for the stretching vibrations of the CH_3 and the C-H bonds, and the peaks at 2922 cm^{-1}, 2939 cm^{-1} and 2974 cm^{-1} for the stretching vibrations of the CH_3 groups, can be associated to isopropanol molecules as their values are closer to those of this molecule than to the values for the TTIP molecules.

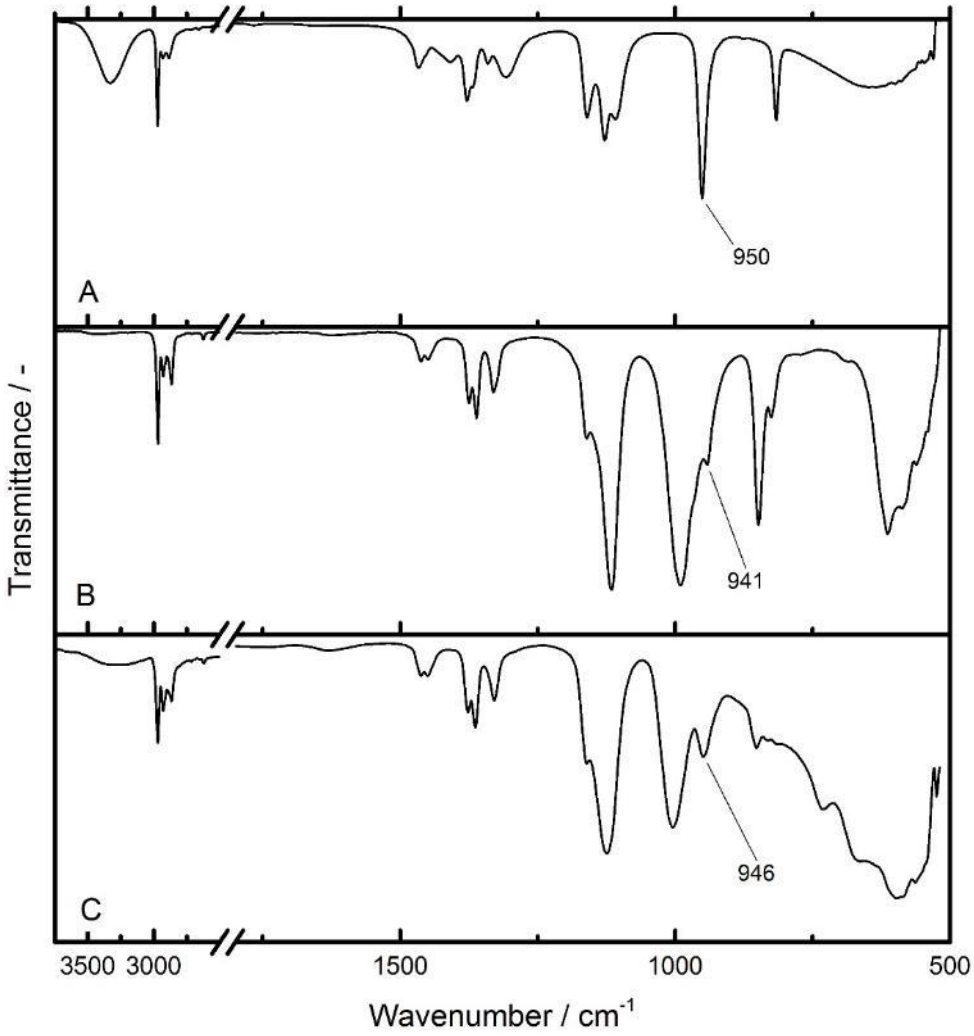

Figure 16. *FTIR spectra: A) 2-Propanol, B) TTIP and C) TiO_2 1:2 precursor.*

Additionally, Fourier-transformed infrared spectroscopy (FTIR) was performed to further clarify which kind of organic species are present in the particles. **Figure** shows the spectra of the solvent, the precursor and the amorphous particles. The position and the intensity of the peak at 946 cm^{-1} for the sample spectra is found between the peak at 950 cm^{-1} for the 2-propanol spectra and the peak at 941 cm^{-1} for the TTIP spectra. The peak at 941 cm^{-1} in TTIP corresponds to the stretching vibrations of the C-O and Ti-O bonds.[194] This implies that both isopropanol and isopropyl are present in the amorphous particles. This suggests that the organic compounds that can be found in the particles are sub-products of the chemical reaction and solvent that was trapped into the particles during their formation. A peak at ~3300 cm^{-1} in the 2-propanol curve, associated to –OH groups, can be found in the amorphous TiO_2 precursor curve. This indicates that the isopropoxide groups are substituted by –OH groups.

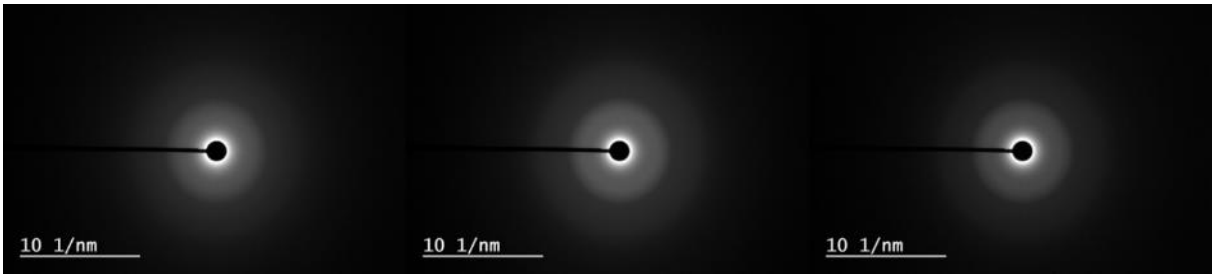

Figure 17. *TEM diffraction pattern of the three titanium oxide precursor samples, from left to right: 1:1, 1:2 and 1:4.*

The titanium oxide precursor present in the cases before calcination is always amorphous as can be seen in the diffraction pattern of TEM image in **Figure** . The XRD pattern (not shown) presents no peak, characteristic for amorphous matter.

3.1.2. Mechanism of formation

The chemical reaction starts as soon as the two reactants come in contact. One isopropyl group is replaced by an hydroxyl group and one 2-propanol molecule leaves. Afterwards, this hydroxyl group reacts with another hydroxyl group from another TTIP molecule forming the titania network and leaving a water molecule as sub-product. This water molecule restarts the loop, triggering the chain reaction which will ultimately form the titania particles.

There is very little data found in literature about the hydrolysis rate for metal oxides. A minimum value of the hydrolysis rate for $Ti(OR)_4$ is estimated as $k_h = 10^{-3}\ M^{-1}s^{-1}$. Taking into account this value and that the hydrolysis rate and condensation rates are of the same order for TTIP in isopropanol, it can be said that main part of the reaction takes place in the droplets.[66] There, the concentration increases very fast owing to the evaporation of the solvent. This accelerates both hydrolysis and condensation, which leads to the particle formation.

According to literature, in the case of the classical spray drying method, the particles are formed via atomization followed by solvent removal.[195] In the classical production method each particle is formed as a single object by a single droplet. A similar process occurs during the SFS process. The spraying conditions that arise during the SFS process, force the solvent to evaporate and as consequence accelerate the chemical reaction and therefore the crystal growth. In other words, during the droplet size reduction in the chamber, the clusters of titania that are formed (nucleation) are forced to form the particle without creating an ordered network (forced condensation). As consequence, the particles formed are amorphous, as the clusters were not able to form an ordered periodic network but only a single particle.

This is in accordance to the replication phenomenon, this means that the particle will reproduce the morphology of the mother-droplet at a smaller size. The most stable geometry for a free-flowing liquid is the sphere, as the surface tension in this geometry is the lowest.[196] Therefore the spherical shape of the particles is a consequence of the spherical shape of the droplets. This is because out of one droplet, on particle is formed. During the spraying, when the nucleation and condensation take place, the clusters grow together forming the amorphous particle in the same shape of the droplet as the solvent evaporates.[197] Taking into account the particle size, the density of

anatase, the molar mass of titanium oxide and the concentration of the solution, the droplet size can be estimated as ~900 nm.

The particle diameter results from the size of the droplet and the ratio of product/solvent, *i.e.* the concentration of the product.[198] The size of the droplet mainly depends on the characteristics of the atomization step. The main parameters in this setup that play a role during the atomization step are the temperature, the pressure, residence time of the droplets and the type and dimensions of the nozzle. As the temperature, the pressure and the nozzle stay the same for all the experiments, the droplet size and therefore the final size of the particles are similar for the three samples.

3.1.3. Properties of calcined TiO_2 powders

The influence of the calcination on the morphology and particle size of the nanomaterials was similar in all cases. The spherical shape of the nanoparticles is kept even after the annealing. For the 1:1 molar ratio the particles keep their interdependency during the calcination process (**Figure 18**). Furthermore, for the 1:2 and 1:4 molar ratios, the particles are spherical and independent as before the crystallization (**Figure 19** and **Figure**).

The perfect mixing of the precursors before the nozzle creates a homogeneous mother liquid from which the spray droplets are formed. This is highlighted in the image of **Figure** , by linking the EDX spectra with image generation.

The calcination of the powders produced by the SFS process expels the organic species of the particles and provides enough energy to induce the reorganization of the titania network. The thermal treatment also produced an internal porosity in the particles which can be identified in the TEM images as consequence of the crystal formation. All the calcined powders transform from the amorphous phase into the anatase phase. This can be observed in the diffraction patterns of the TEM

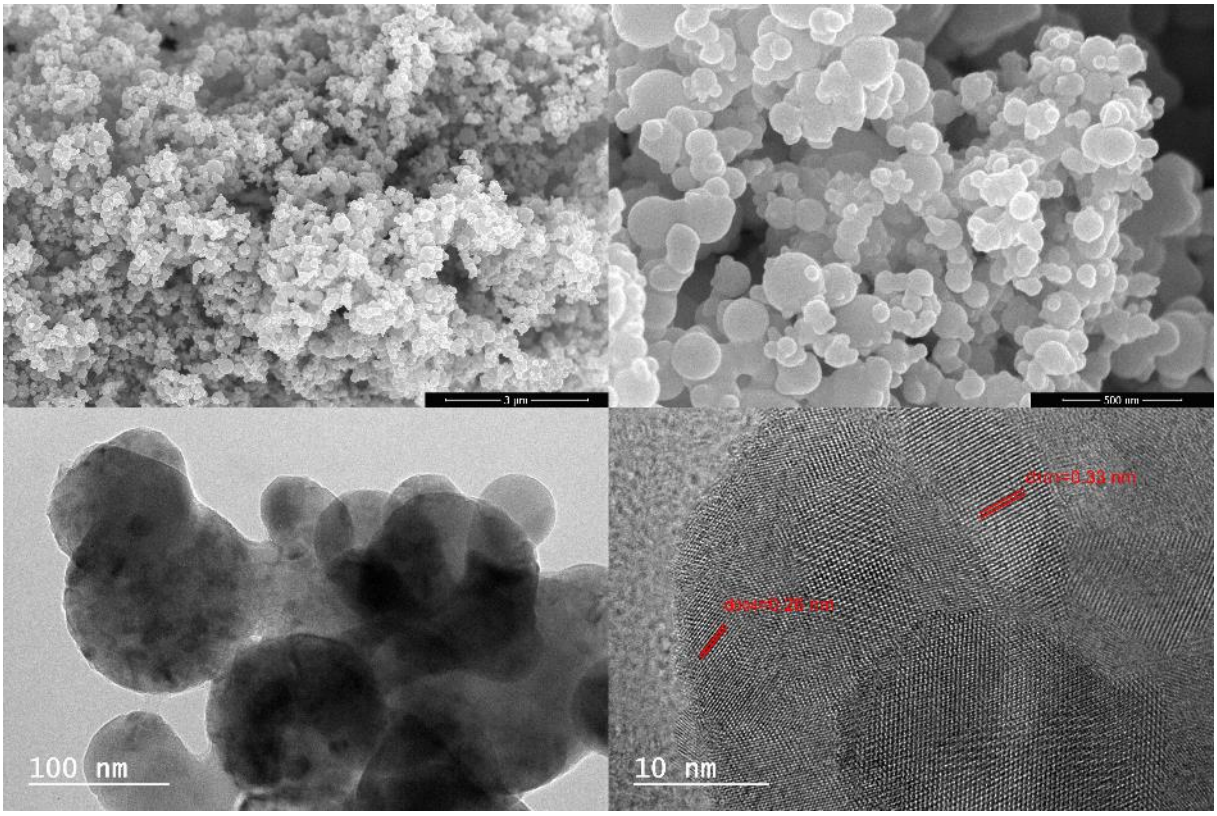

Figure 1. *SEM and TEM images of TiO_2 1:1.*

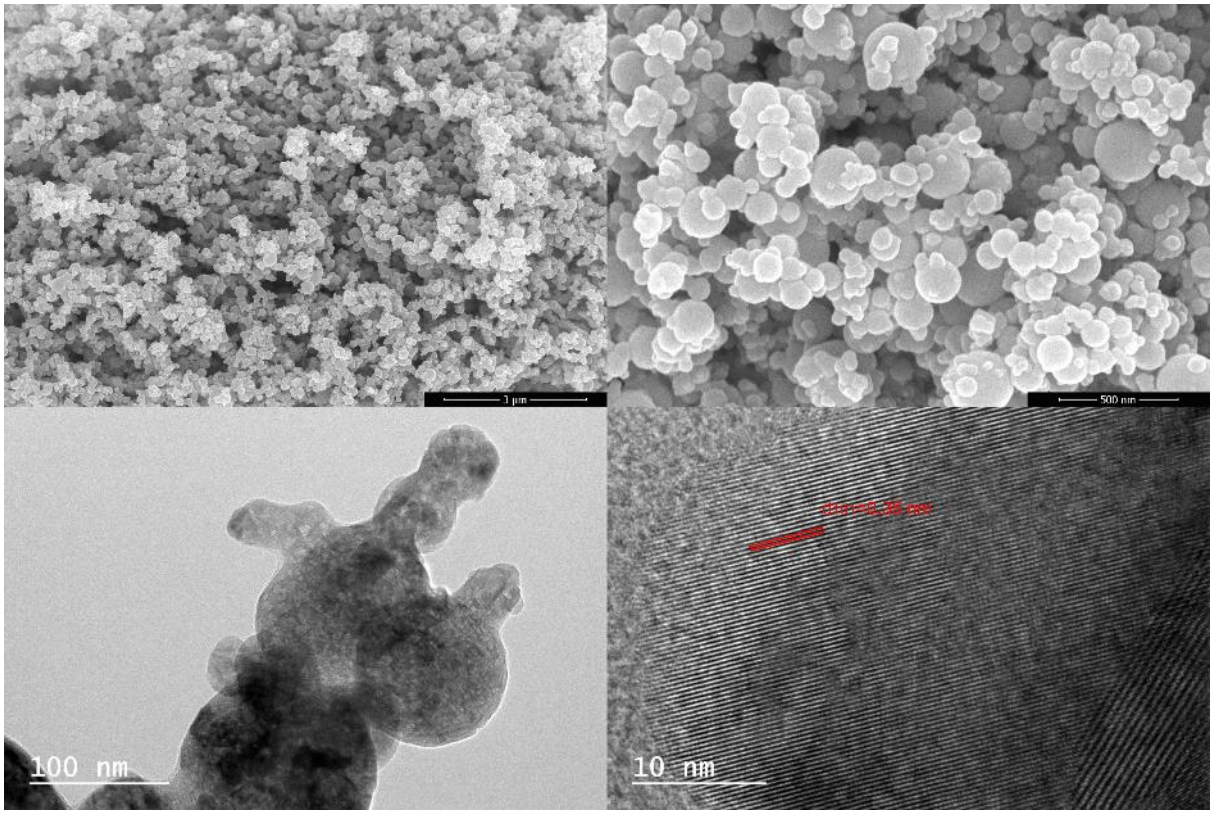

Figure 2. *SEM and TEM images of TiO_2 1:2.*

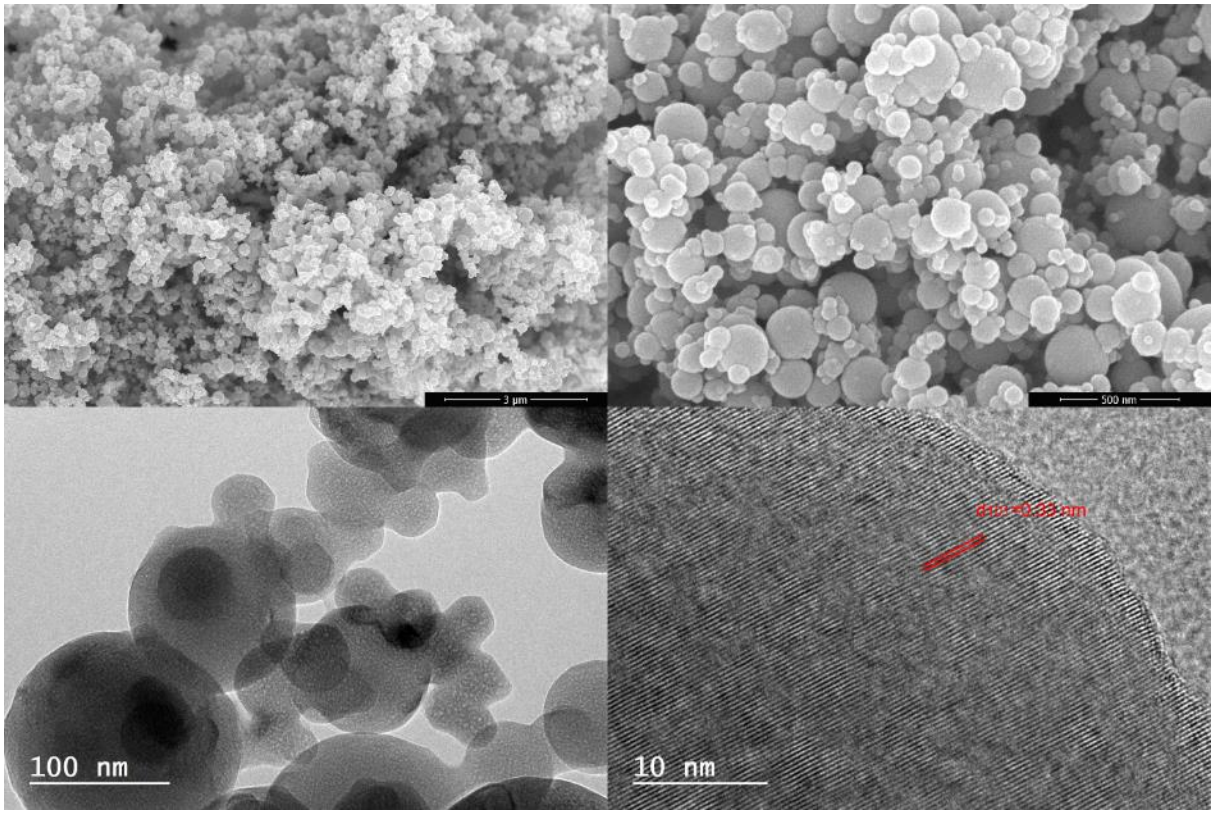

Figure 20. *SEM and TEM images of TiO_2 1:4.*

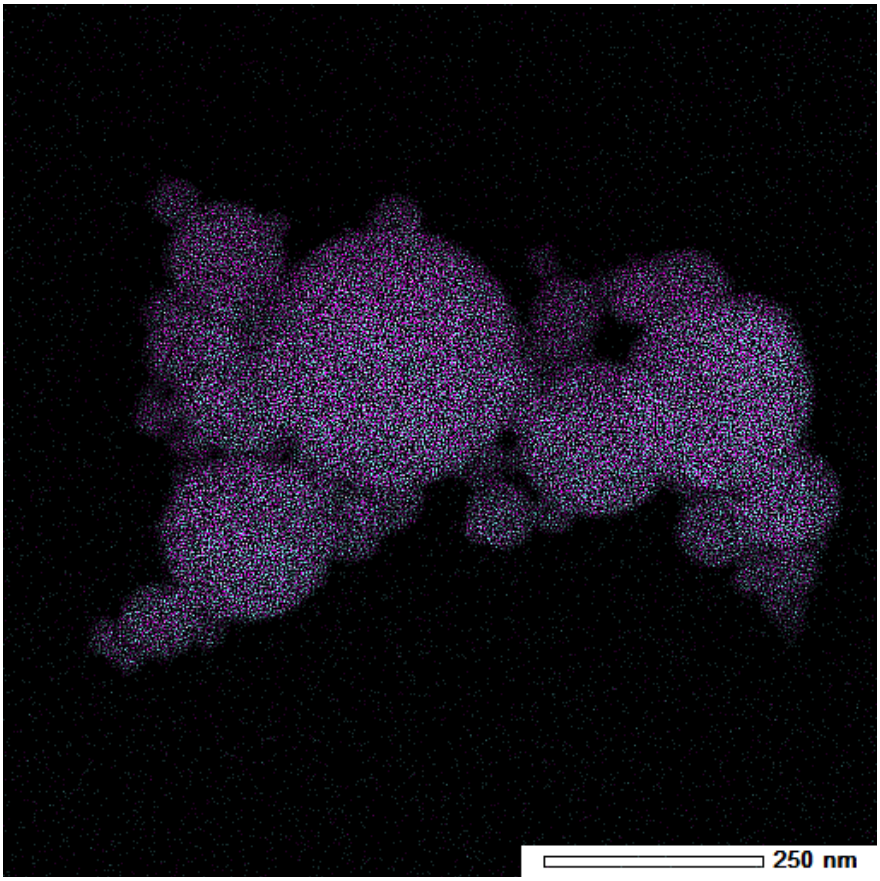

Figure 21. *EDX of TiO_2 sample (Titanium = purple; oxygen = blue).*

measurements in **Figure** and the XRD patterns in **Figure** . As shown in the TEM images, the spherical particles are a construct made out of several crystallites disposed in differing orientations.

The presence of pure anatase phase could be verified by Raman spectroscopy. The spectra in **Figure** show peaks at 142 cm^{-1}, 194 cm^{-1}, 396 cm^{-1}, 514 cm^{-1} and 639 cm^{-1} which are characteristic for the anatase phase.[199] Additionally, no other peaks are present in

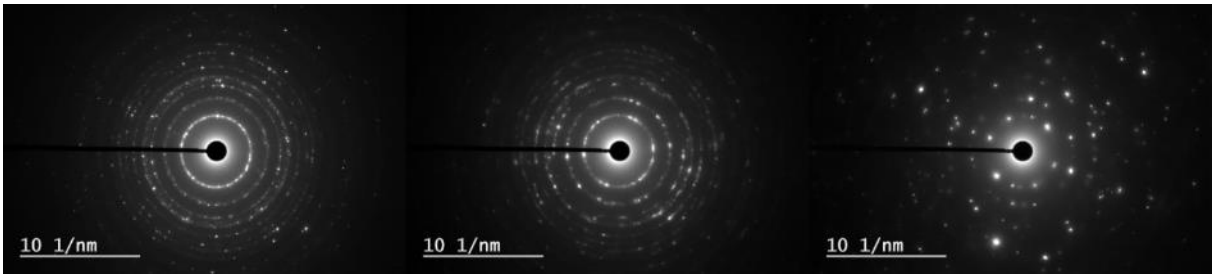

Figure 22. *TEM diffraction patterns on TiO_2 samples, from left to right: 1:1, 1:2 and 1:4.*

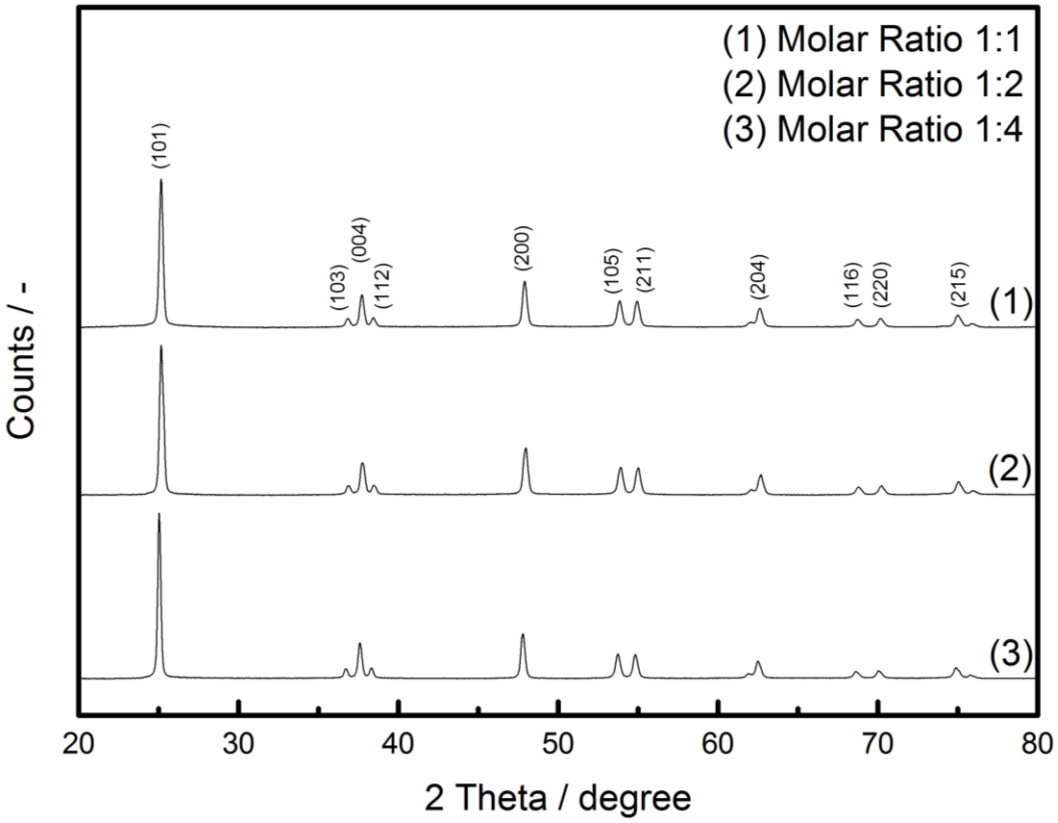

Figure 23. *XRD patterns for TiO_2 samples.*

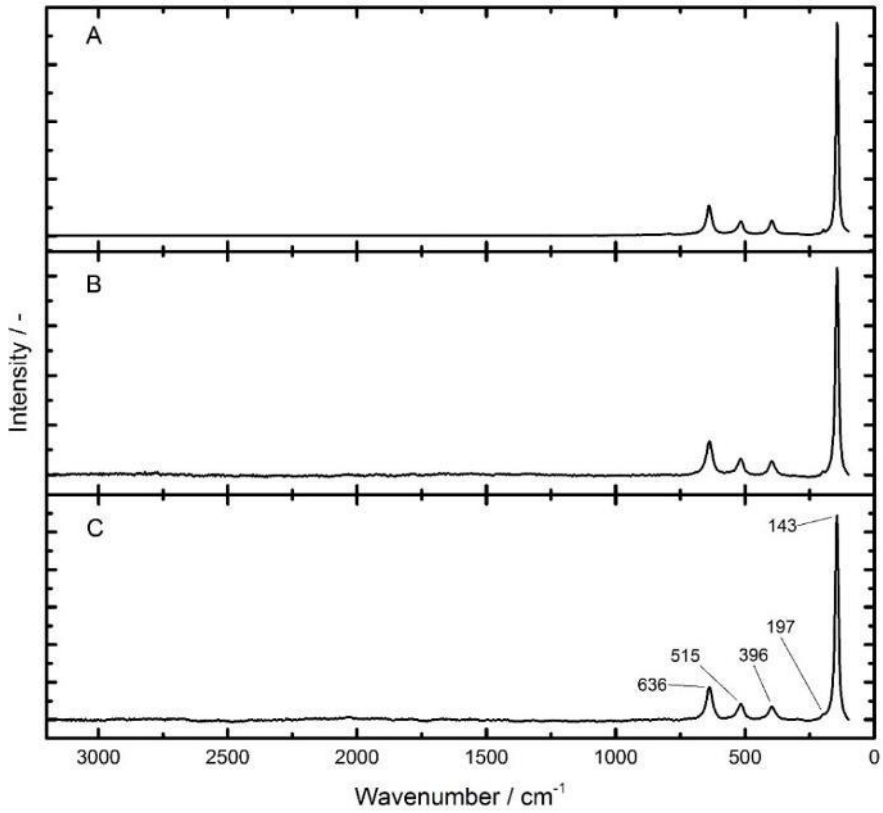

Figure 24. *RAMAN spectra of TiO_2 samples: A) TiO_2 1:1; B) TiO_2 1:2; C) TiO_2 1:4.*

Molar ratio	Average crystallite size (nm)
1:1	31.5
1:2	26.4
1:4	27.9

Table 9. *Elementary crystallite sizes for the three titanium oxide systems.*

the spectra which implies that, once annealed, the particles are made of pure ordered titanium oxide.

The sintering during the thermal treatment added to the relatively big dimensions of the particles, explains the low specific surface area (**Table**). The size of the particles decreases slightly in every case after calcination. This constriction can be explained by the exit of the organic species that accompanies the structuration of the titania network. The average particle sizes have been calculated using different methods (Fehler! Verweisquelle konnte nicht gefunden werden.). The BET average particle size calculated confirms that the particles should be smaller to obtain the SSA measured. This evidences the existence of an internal porosity.

The particle size distributions of the different materials were obtained through TEM images (**Figure**). It can be observed that the average particle sizes can be found between 100 and 200 nm, which classifies these particles as sub-micron sized material. The values measured by means of images have the drawback that the smaller particles could be less easily discerned and therefore taken into account.

Molar ratio	Φ TEM (nm)	Φ BET (nm)
1:1	135 ± 66	131.68
1:2	122 ± 54	107.19
1:4	112 ± 57	114.97

Table 10. *Average particle size diameter of the titanium oxide samples*

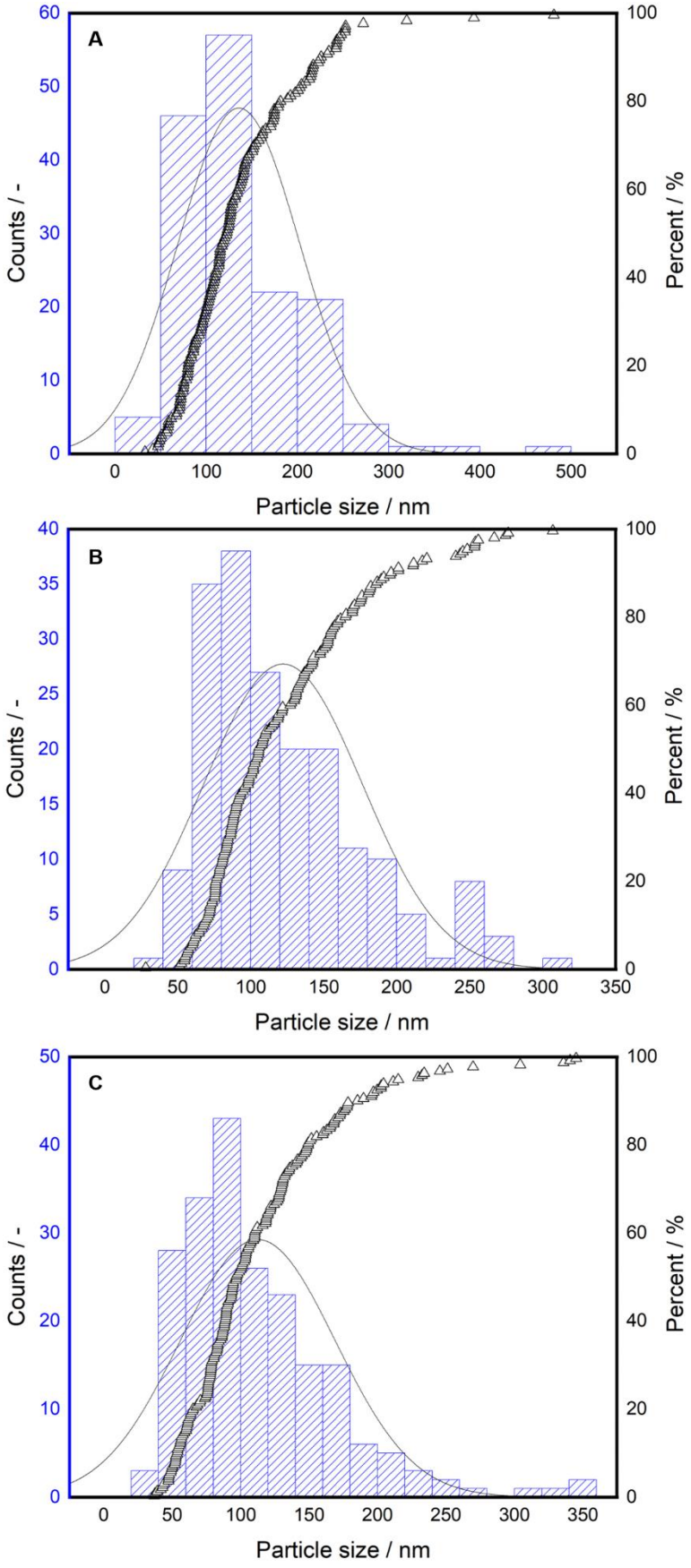

Figure 25. *Histogram and cumulative particle size distribution for A) TiO_2 1:1; B) TiO_2 1:2 and C) TiO_2 1:4.*

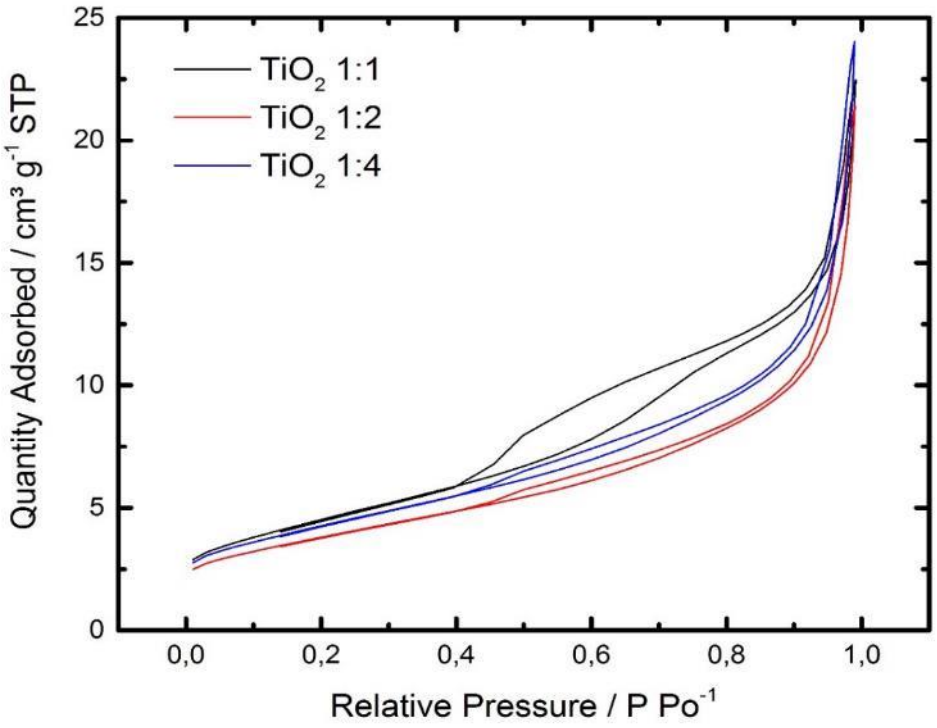

Figure 26. *TiO_2 samples isotherms by BET measurements.*

The average size of the single units of these polycrystalline structures have been calculated basing on XRD measurements. To this end, the Scherrer's equation was used on the (101) peaks from the XRD patterns for each molar ratio (**Table**). It can be observed that the crystallite size for all the systems is roughly the same.

The surface of the particles is affected as consequence of the sintering of the matter, producing a loss on specific surface area. As a result, the particles present little to no porosity on the surface. This can be observed in the adsorption/desorption isotherms performed on the three materials in **Figure** . The isotherms show a type IV shape, characteristic for having a hysteresis loop. These phenomena are associated with capillary condensation which occurs in the pores.

The part where the hysteresis loop coincides, this is at low relative pressures, is associated to monolayer-multilayer adsorption. The hysteresis loop is a type H3, which is associated with aggregates.[200] Taking into account the shape and the difference between the absorption and the desorption, these particles are aggregates that have no microporous surface. However, the analysis of the particles density showed that they were porous by comparing the theoretical surface area to the measured one. This can be explained by a internal, closed porosity in the particles which is not measured by BET.

The specific surface area measured by BET (**Table**) was compared to the specific surface area (SSA) calculated from the size of TiO_2 particles measured on TEM pictures and the density of anatase (ρ=3.79 g cm^{-3}). The SSA values for each TiO_2 material was determined by applying the following formula, assuming a spherical model:

$$SSA = \frac{3\sum(r)^2}{\rho\sum(r)^3} \quad (47)$$

Molar ratio	BET ($m^2\ g^{-1}$)	Calculated ($m^2\ g^{-1}$)	True density ($g\ cm^{-3}$)	Porosity (%)
1:1	14.18	5.56	1.81	52.3
1:2	14.18	8.62	2.28	39.8
1:4	14.55	8.19	2.32	38.7

Table 11. *Comparison of measured by BET and calculated SSA of the samples.*

Where r is the radius of the spheres and ρ is the density of anatase. The SSA is markedly smaller than the surface measured by BET, which means that the true density of the TiO_2 samples is smaller than the one of bulk anatase. The true density of TiO_2 particles can be determined from the measured BET values:

$$\frac{S_{BET}}{SSA} = \frac{\rho_{anatase}}{\rho_{true}} \quad (48)$$

Therefore, there exists probably a closed, internal porosity in the synthesized TiO_2.

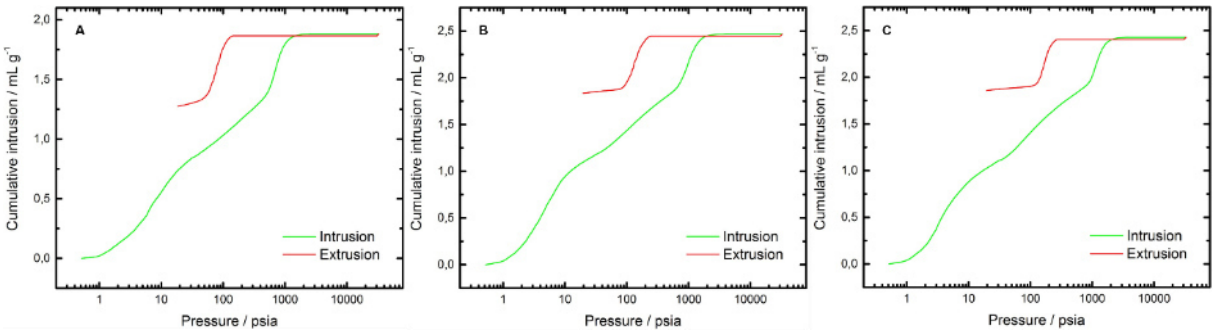

Figure 27. *Mercury porosimetry intrusion curves of the titanium oxide samples for A) TiO_2 1-1; B) TiO_2 1-2 and C) TiO_2 1-4.*

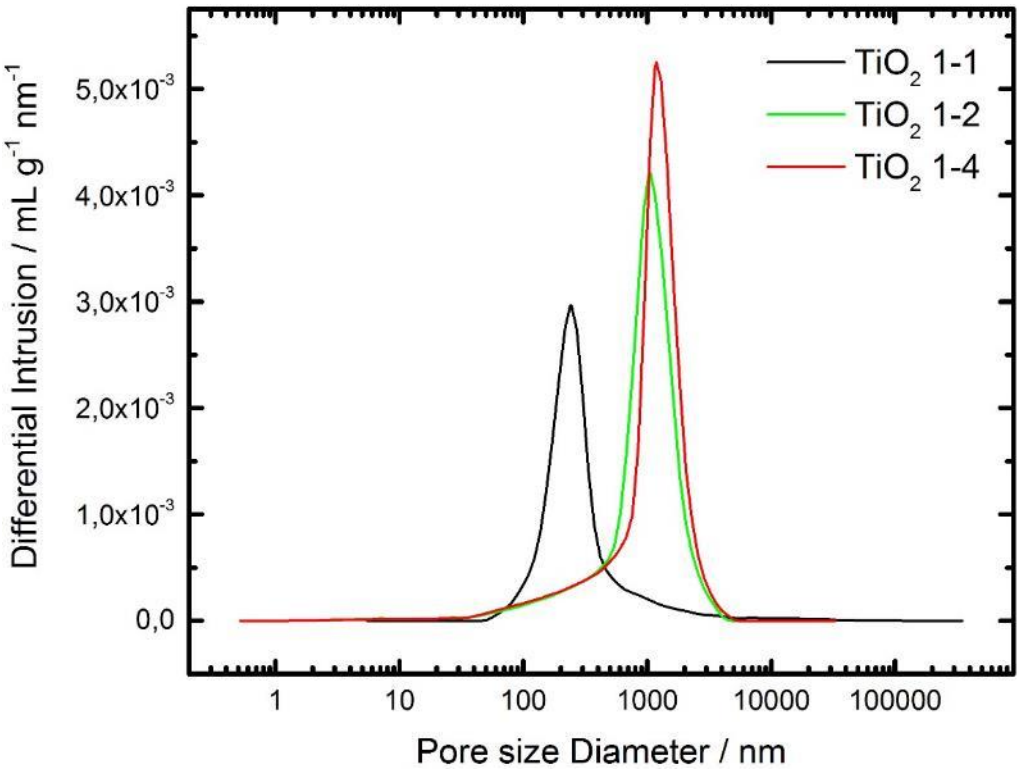

Figure 28. *Pore volume distribution of the titanium oxide samples measured by mercury porosimetry.*

Additionally, mercury porosimetry was performed on the samples (**Figure** and **Figure**). **Figure** shows the volume that enters the samples as the pressure increases. It can be seen that during the measurement, when the pressure increases the volume intruded scales linearly with it. This is a consequence of the breakdown of the agglomerates. The resulting pieces and particles move and are compressed inside of the measurement bulb. Between 700 and 800 psia the slope of the curves changes which comes from an actual intrusion of the mercury in the porosity. However this intrusion is associated to intra-particle voids that are formed during the breakup of the agglomerates. Afterwards at high pressure values a plateau is seen where no more mercury can penetrate the sample. This behaviour is common for agglomerated particles with low specific surface area.

This is in accordance to the pore volume distribution showed in **Figure** . In can be seen that for all the samples, the porosity values exceed the dimension of the particles. There is a difference between the values obtained for TiO_2 1-1 (248.02 ± 1.39 nm), TiO_2 1-2 (1156.20 ± 8.53 nm) and TiO_2 1-4 (1305.19 ± 9.47 nm). This disparity arises from the particle morphology. These values correspond to “cylindrical” pores that are bigger than the particles themselves. Thus, this is an indication of the free space

between particles that is originated by the high pressures of the measurement method. The difference between these values arises from the difference in aggregation between the particles. The particles of TiO_2 1-1 are less strongly aggregated than the other two materials. As consequence, the particles are more easily crushed together (less pressure needed) which gives a value for smaller “pore” sizes. The TiO_2 1-2 and TiO_2 1-4 materials present a similar aggregation degree, which explains why the “pore” size values (similar pressure needed) are closer.

3.2. TiO_2 modified with silver

The introduction of silver into the titania particles has been studied for TiO_2 prepared from the 1:2 molar ratio. It corresponds to the stoichiometric ratio of the chemical reaction. The molar ratio of Ti:Ag is 1:0.42 mol/mol.

3.2.1. Properties of TiO_2 with silver

The titanium oxide powders loaded with silver produced by SFS are constituted of spherical submicron sized particles that are agglomerated in groups of several units.

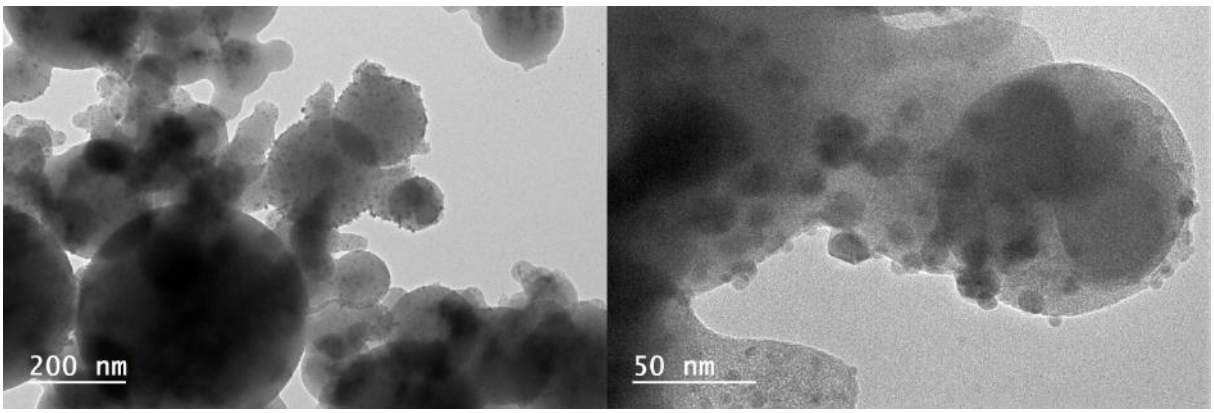

Figure 3. *TEM images of silver loaded titanium oxide nanoparticles.*

These particles are equally dense, homogeneous and totally amorphous as for the systems made out of pristine titania. The particles have an average size of 156 ± 7.6 nm. However, these particles have nanoparticles of silver on their surface. These silver nanoparticles are irregular spheres attached to the titanium oxide surface. They have an average size of 6.9 ± 2.3 nm (**Figure 29**). **Figure** shows the distribution of the particles of the silver loaded titanium oxide particles. Most of the particles, around 80% of the total number of particles measured, can be found between 50 and 200 nm as can be seen on the histogram and the cumulative curve.

The presence of the silver particles on the surface of the titanium spheres can be explained by difference in radius of the ions constituting the particles. The radius of Ti^{4+} ion is nearly the half of the radius of the Ag^{+} ion (68 pm vs. 126 pm). This difference exceeds the critical threshold necessary for a crystal to be stable.[201] The silver ions migrate out of the titanium ions matrix while the particle builds itself up. This is in

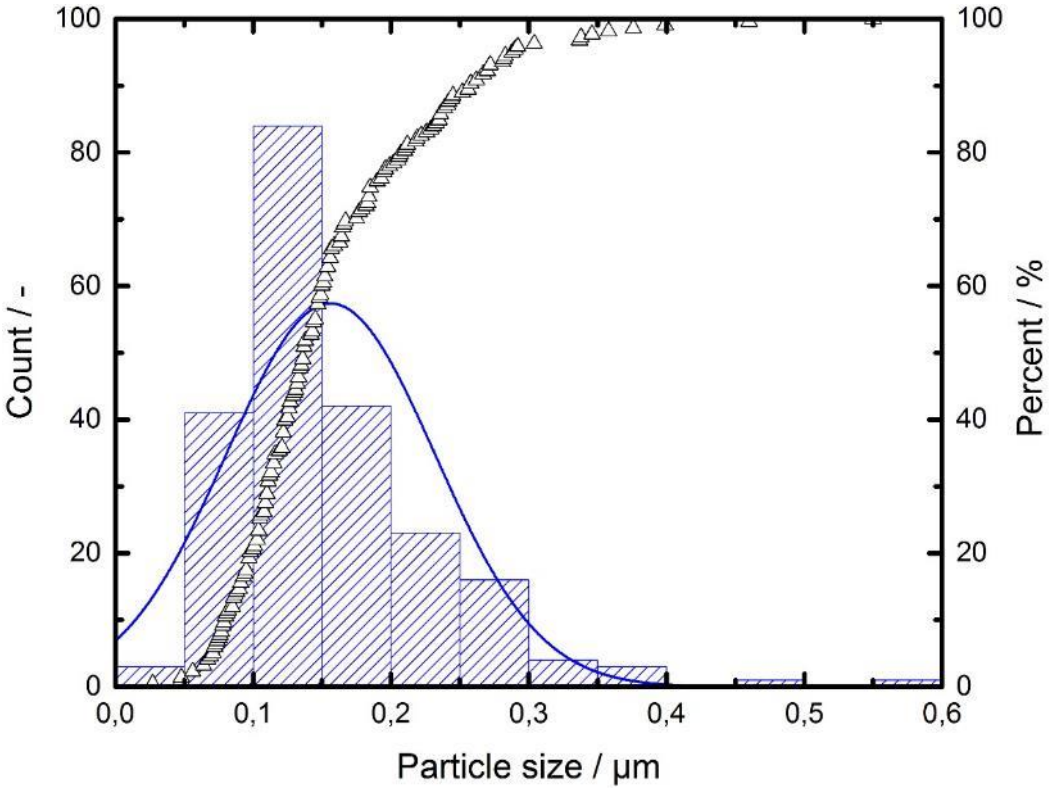

Figure 30. *Histogram and cumulative particle size distribution for raw Ag@TiO_2.*

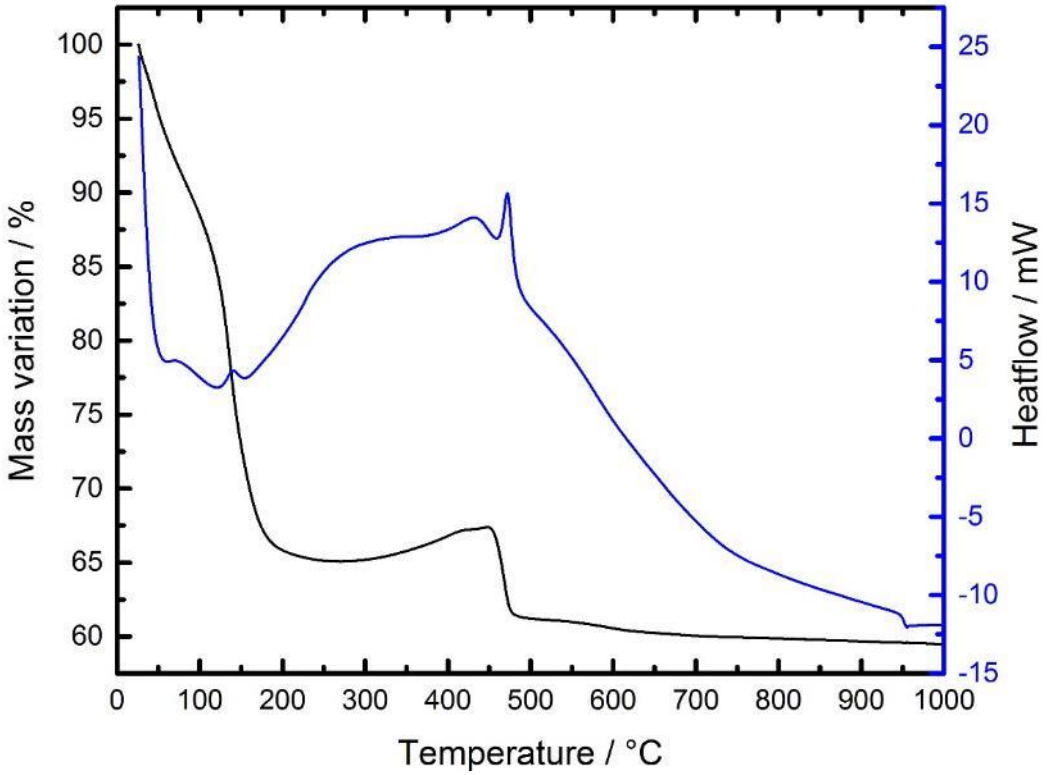

Figure 31. *TG analysis of amorphous, silver loaded titanium oxide particles at a heating rate of 5°C/min with and 100 mL/min of Ar/O_2 80%/20%.*

agreement with the “self-purification” phenomenon which explains it as a “solubility” difference which leads to the migration of the particles to the surface.[110 99]

On the thermogravimetric curve shown in **Figure** , the weight loss which takes place until ~220 °C is associated with the removal of the organic species present in the sample. Afterwards, the silver nanoparticles on the surface of the titania particles oxidize forming silver(I) oxide, calculated as a 2.2% of weight increase which corresponds to the increase measured in the TGA. At ~450°C the remaining silver oxide and silver nitrate present in the particles thermally decompose into silver particles.[202 203] From that point on the mass does not show significant variation as the powder became pure silver doped titanium oxide and therefore stable to thermal influences. The silver covered titanium oxide powder before calcination is amorphous as can be seen in the diffraction pattern of TEM image in **Figure** .

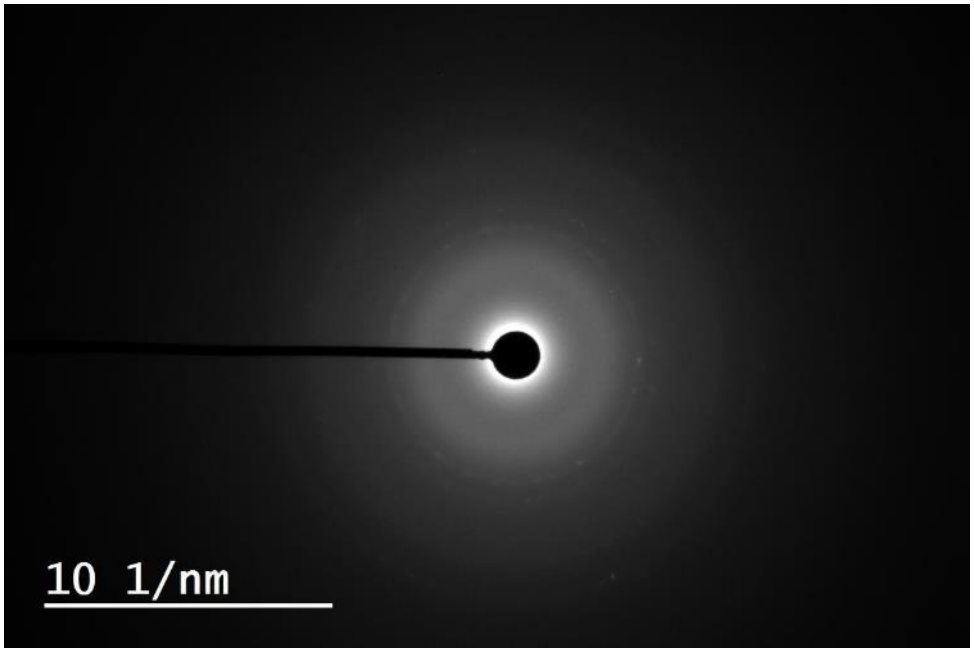

Figure 32. *TEM diffraction pattern of uncalcined silver loaded titanium oxide.*

3.2.2. Effect of the calcination

The titanium spheres which support the silver oxide nanoparticles are identically affected by the thermal treatment as in the case for the pristine material. The material obtained after calcination is a fine, loose powder with greyish colour. The morphology and the particle size of the material were studied by TEM microscopy. They were also compared to those of pure titanium oxide (**Figure**). The prepared powders are made of spherical titanium oxide particles. The particles of the pristine sample have a mean size of 139 ± 5.4 nm in diameter, while the loaded sample presents a mean size of 157 ± 7.3 nm in diameter. The loaded particles are covered by rod like particles made out of silver which are 12 ± 2.8 nm in diameter. The presence of silver seems to increase the size of TiO_2 particles. This is consistent with the replicant theory, if there is more matter in a droplet the resulting particle will be bigger.

The distribution of the elements in the particles was obtained by EDX spectroscopy as can be seen in **Figure** . It can be seen that silver concentrates mainly in the particles on the surface. These changed in shape from irregular spheres in the raw material to

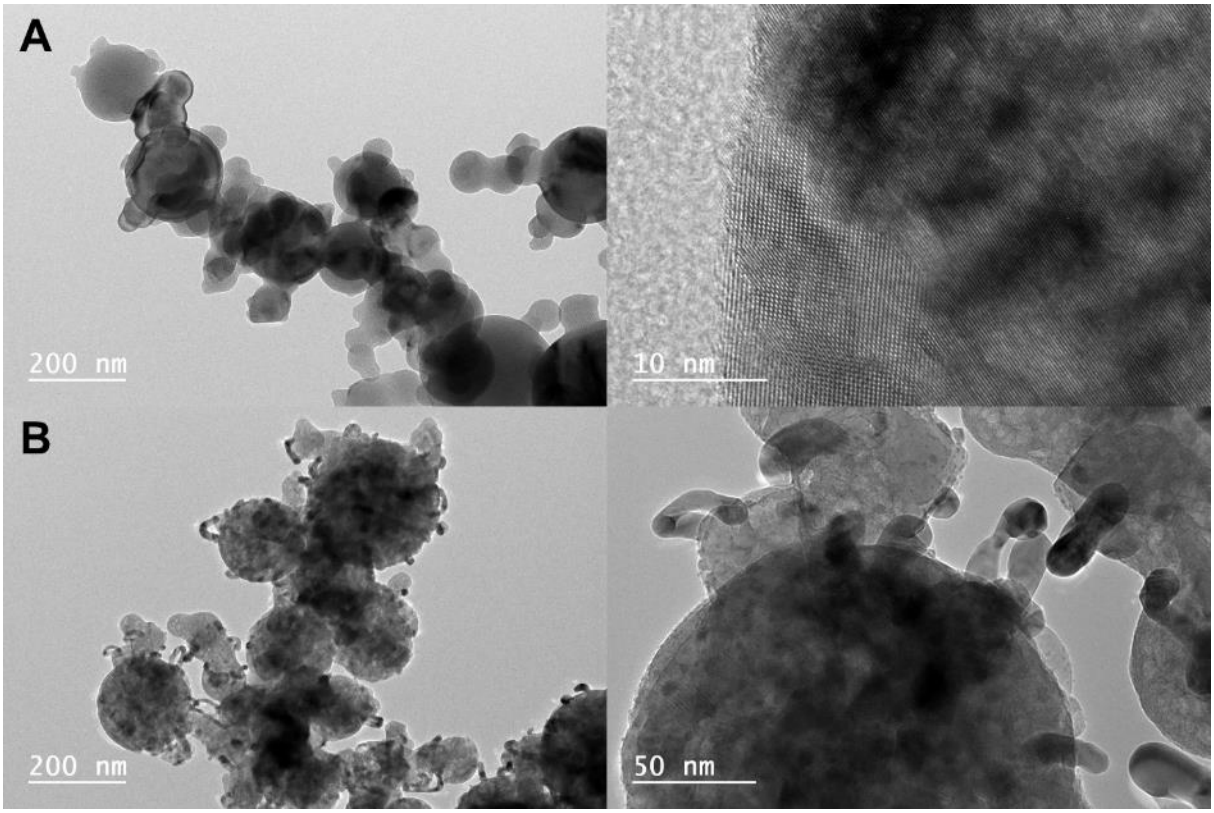

Figure 33. *TEM images of pristine (A) and silver oxide (B) loaded titanium oxide particles.*

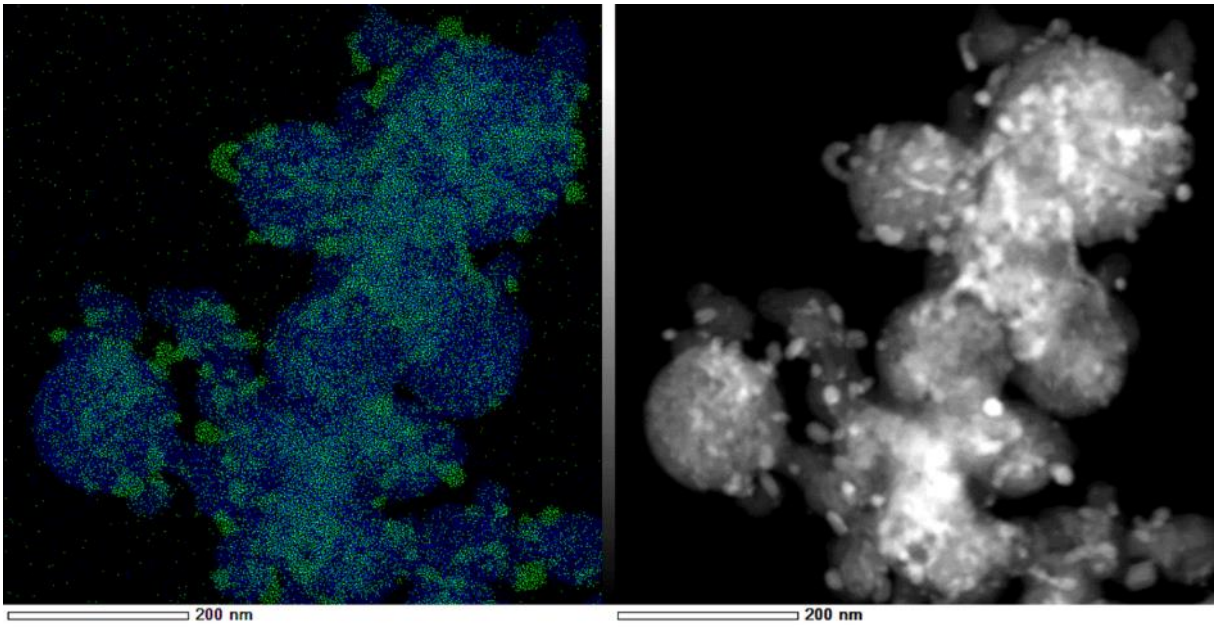

Figure 34. *EDX of silver oxide covered titanium oxide (Blue: titanium; Green: silver).*

elongated geometries for the crystallized species. The size decrease of silver particles induces a decrease in their melting temperature. Taking into account the calcination temperature the silver domains inside of the titanium oxide particles must be very small (< 2 nm).[204] Thus silver melts by the thermal treatment but not titanium oxide. The density of solid Ag (10.49 g cm^{-3}) is higher than the density of molten Ag (9.34 g

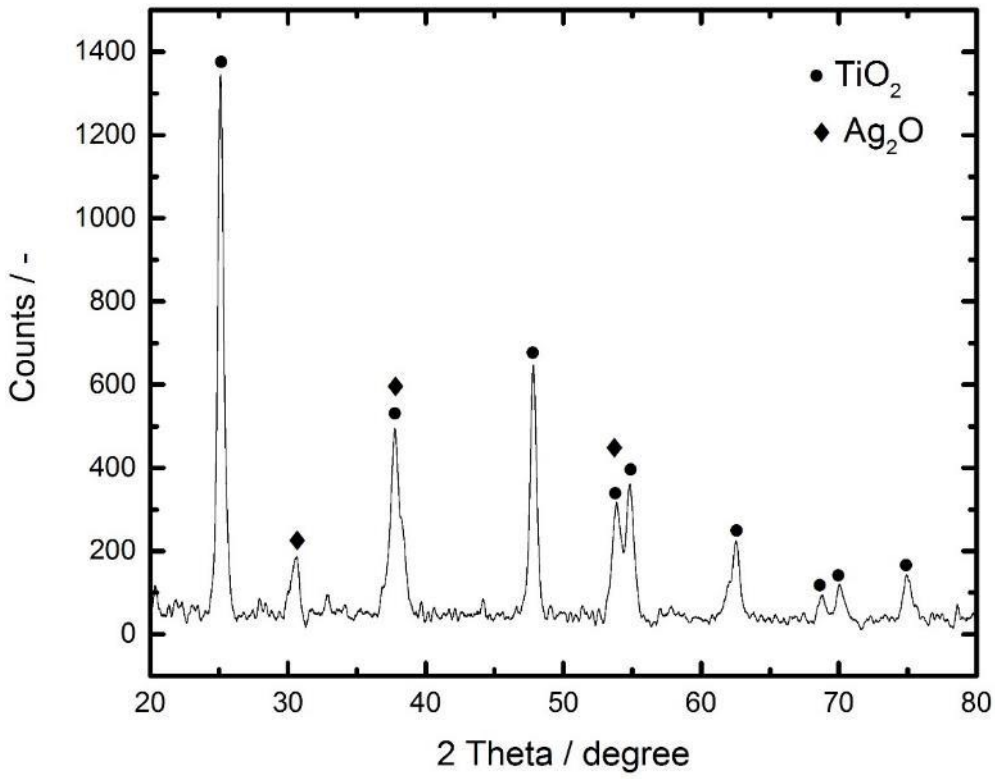

Figure 35. *XRD pattern of Ag@TiO_2 sample calcined at 400°C.*

cm^{-3}).[205] As consequence, the volume of the silver domains increases and they exit the titanium oxide matrix. Once they reach the surface they coalesce with other silver droplets, increasing their size. The release of oxygen by silver, owing to the lowering of the oxygen solubility, can also account for the elongated shape of the silver particles.[206] These phenomena produce an increase of the volume and result in change in morphology of the nanoparticles attached to the surface.

The particles are made of anatase and silver oxide (**Figure**).[207] The crystalline size of anatase is 14.6 ± 2.7 nm and the crystallite size of silver(I) oxide is 9.3 ± 0.8 nm.

Figure shows the Raman spectra for the samples of titanium oxide doped with silver before and after calcination and for the pristine anatase phase. For the uncalcined sample, the three signals in form of valleys at 187 cm^{-1}, 432 cm^{-1} and at 611 cm^{-1} correspond to amorphous titania. The peaks at higher wavenumber, *i.e.* 2880 cm^{-1} for the stretching vibrations of the CH_3 and the C-H bonds, and the peaks at 2922 cm^{-1},

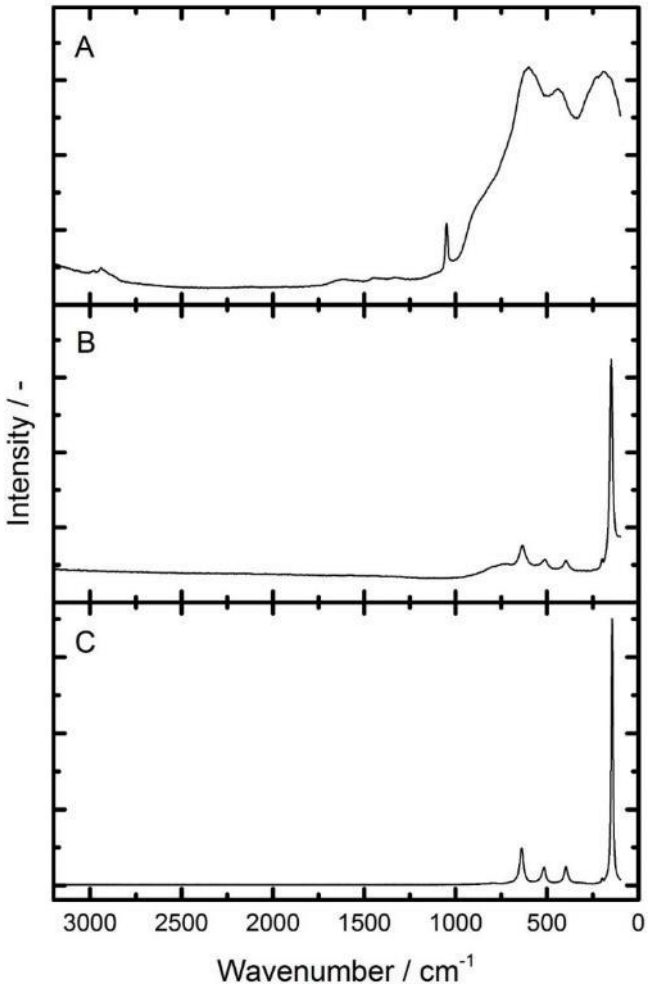

Figure 36. *RAMAN spectra of uncalcined (A) and calcined (B) doped titanium dioxide and calcined (C) pristine titanium dioxide.*

2939 cm^{-1} and 2974 cm^{-1} for the stretching vibrations of the CH_3 bonds, are associated to isopropanol.[3] The peaks present in the calcined samples at 142 cm^{-1}, 194 cm^{-1}, 396 cm^{-1}, 514 cm^{-1} and 639 cm^{-1} which are characteristic for the anatase phase.[199]

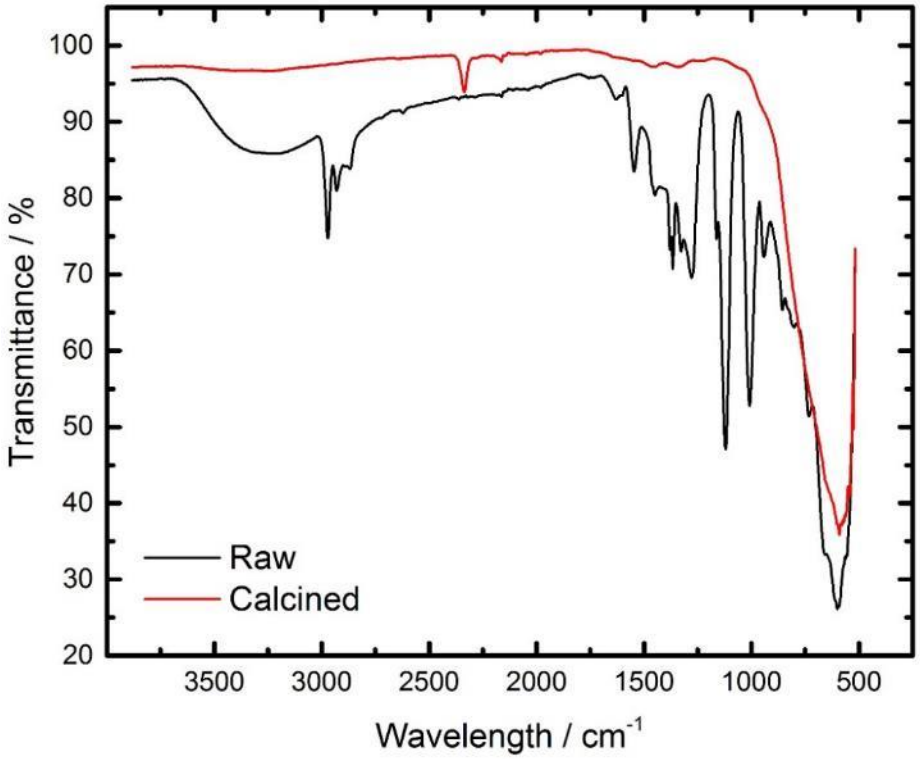

Figure 37. *FTIR of uncalcined and calcined silver loaded titanium oxide nanoparticles.*

The FTIR spectra before and after calcination can be seen in **Figure** . The characteristic peaks before calcination cannot be found after calcination, additionally no peaks can be found but at 2336 cm^{-1} which corresponds to carbon dioxide adsorbed at the surface of the particles.[208] This enhanced fixation of carbon dioxide is consequence of the Lewis acidic nature of silver.[209] This property could be crucial for future potential applications. This indicates that the particles after calcination are free of organic species.

3.2.3. Comparison of silver loaded titanium oxide prepared by solvothermal synthesis

Alternative synthesis routes were tried out to compare the synthesis depending characteristics of the materials. The same precursors were used in alternative synthesis apparatus, to prepare the materials by autoclave (synthesis details **Chapter II – 3.2.3.**). The synthesis has been performed during different time frames.

The first autoclave synthesis experiment was performed during 2 hours. The resulting material is made of irregular rod-like particles as can be seen the SEM images in **Figure 38** (**A**, **B**). Here the particles have elongated irregular shapes and they are highly agglomerated. In this case sphericity is absent as well as the homogeneity of the sample. Even the distribution of the particles is much broader compared to the particles prepared by SFS.

The same experiment was performed during 24 hours. The as-prepared materials can be observed in the SEM images in **Figure 38** (**C**, **D**). In this case two populations of particles are formed. One of them is formed of micrometric sized particles with

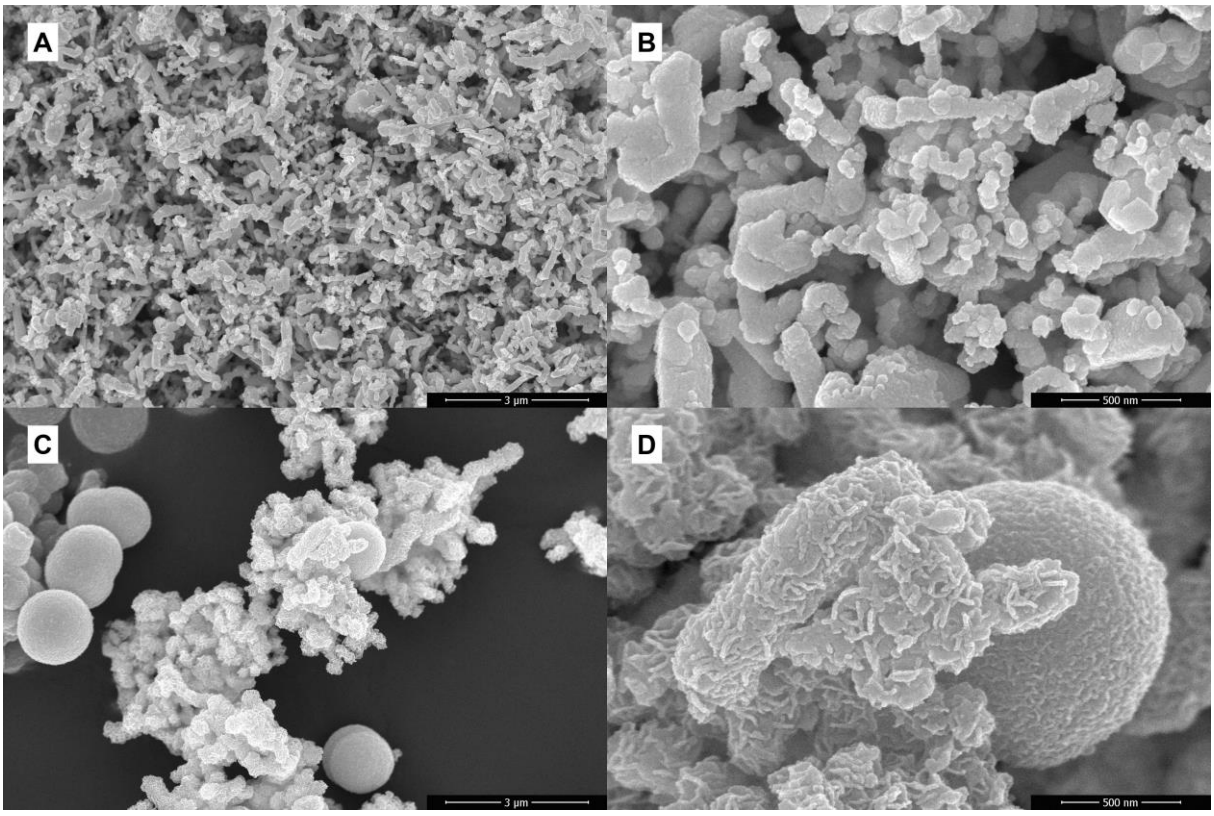

Figure 4. *SEM images of titanium oxide with silver particles prepared by autoclave for 2 hours.*

spherical geometries. The other population of particles have smaller dimension but presents fractal like bodies. This means that the synthesis by autoclave leads to morphological heterogeneities. All the particles are made out of web of rod-like parts.

The solvothermal synthesis does not allow to produce titanium oxide/silver composite materials having the same homogeneity in terms of chemical composition and morphology than those synthesized by SFS. Additionally, this synthesis method takes much more time and energy to produce the samples.

3.3. Conclusions

In summary, the SFS system was used to produce sub-micron particles of pure titania as well as introducing silver in this oxide in a controlled way. The synthesis of pristine titanium oxide was studied in three different water to TTIP ratios. The formed particles were made up of partially hydrolysed TTIP, spherically shaped and amorphous at the exit of the system in all cases. The size of the particles is between 150 and 200 nm in average. In all the cases, the reaction degree tended to the hydrolysis of two isopropyl groups from the four, which is in agreement with other studies. The water ratio had an influence in the particle morphology for the 1:1 ratio. The organic species present were identified as isopropyl groups and isopropanol. Taking into account the hydrolysis and the condensation kinetic rates, the reaction mainly takes place in the chamber, which has as consequence that the particles have similar diameters in the submicrometric range. After calcination the powders crystallized into anatase phase, with a crystallite size of around 31, 26 and 27 nm respectively in the cases studied. In the calcined materials, there exists a closed, intern porosity in the TiO_2 particles, in addition to an interparticle porosity between the aggregates. It seems that the 1:1 ratio TiO_2 is less strongly aggregated basing on the measurements. The thermal treatment also reduced slightly the average particle size and reduced the specific surface area of the surface. However, it produced an internal porosity which could be identified by calculi and more invasive mercury porosimetry.

The introduction of silver oxide nanoparticles was performed by the same method. In this case only the stoichiometric ratio was used. The particles obtained had a spherical morphology with a similar submicrometric average size as the pristine oxide. The material prepared by SFS presented a chemical homogeneity in the distribution of the elements in the particles as well as a morphological homogeneity. Additionally, the thermal treatment also induced the formation of anatase phase, as in the cases of the titania alone. The silver oxide nanoparticles are distributed around the titania particles, located on the surface. They elongate as an effect of the thermal treatment and obtain a rod-like shape.

4. Materials based on Copper oxide

Copper oxide was synthesized by using the SFS system. Three different synthesis temperatures were used, which are 130°C, 145°C, 155°C known as CP (copper precursor) 130, CP 145 and CP 155 respectively. The in-depth characterization of these materials made it possible to understand the influence of the synthesis temperature on the final properties of the CuO nanomaterial obtained.

4.1. Properties of pure CuO

The synthesis of pristine copper oxide was performed with the SFS process. The obtained powders (CP 130, CP 145 and CP 155) are made of strongly agglomerated particles that crystallized in irregular plate like geometries (**Figure 39**) of an intermediate material resulting from the partial decomposition of copper nitrate.

The powders obtained at each temperature differ in the reaction degree of the precursor, this is the copper nitrate pentahemihydrate. In the case of the 130°C reaction, the copper oxide precursor is still present in the final powder along with copper nitrate hydroxide also known as Rouaite ($Cu_2(NO_3)(OH)_3$) and ammonium copper nitrate ($(NH_4)_3(Cu(NO_3)_4(NO_3)$). For the synthesis performed at 145°C, powders produced do not present copper nitrate any more. They contain Rouaite and ammonium copper nitrate. And for the 155°C synthesis, the powder is made of Rouaite and ammonium nitrate (NH_4NO_3). These species were identified by XRD pattern as can be seen in **Figure** . The crystallite size for Rouaite in CP 155 is of 18.3 ± 1.8 nm.

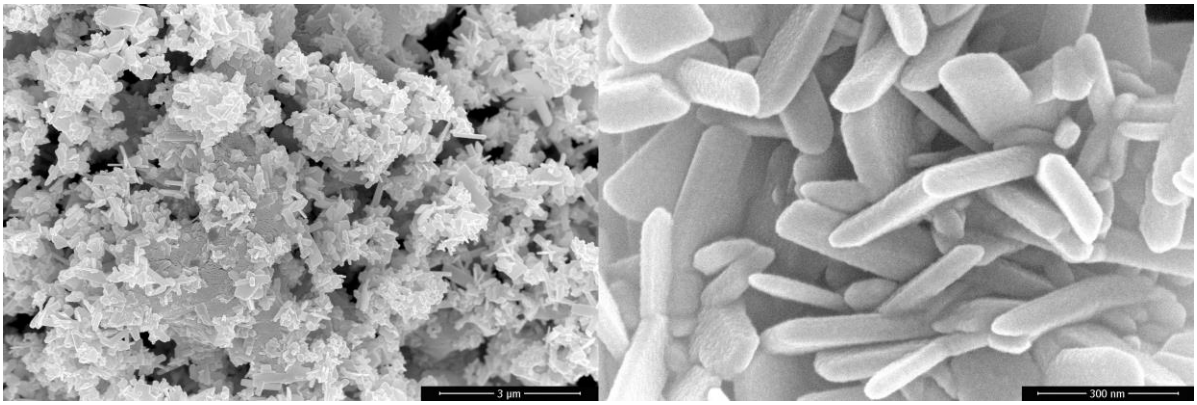

Figure 5. *SEM images of untreated intermediate species of copper nanoparticles synthetized at 155°C.*

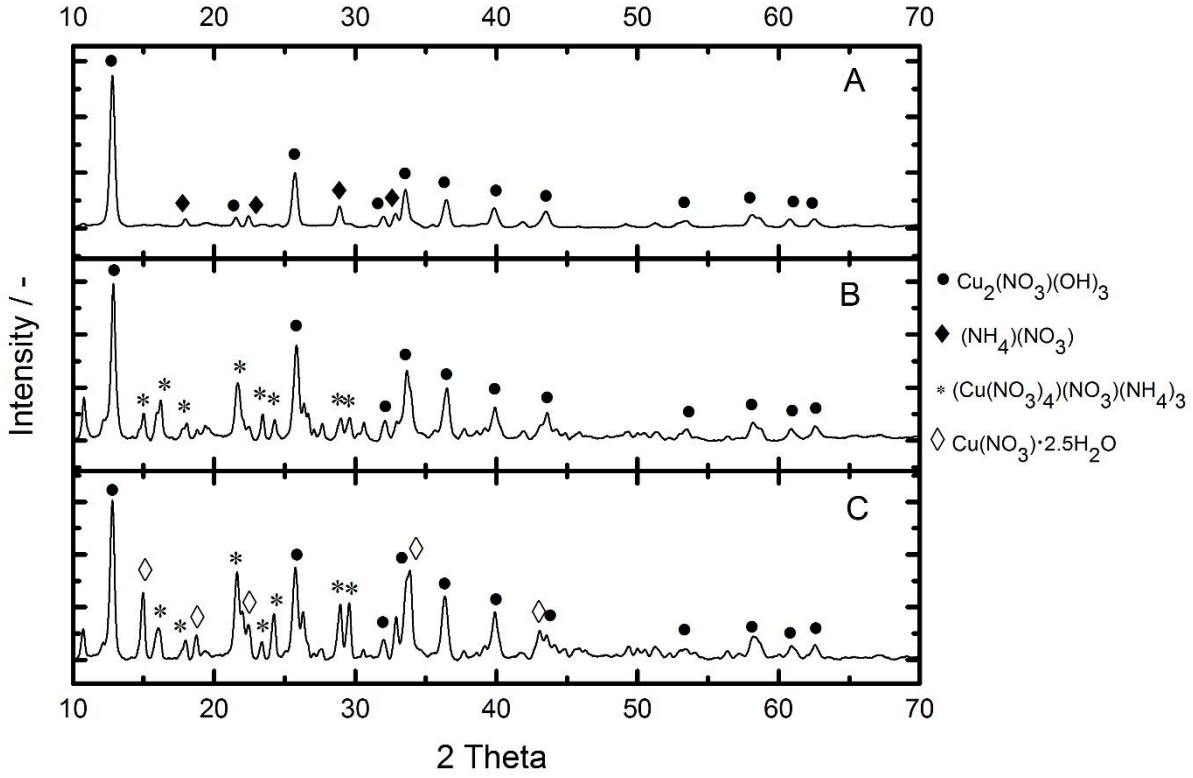

Figure 40. *XRD pattern of copper oxide precursor prepared by SFS at A) 155°C; B) 145°C and C) 130°C.*

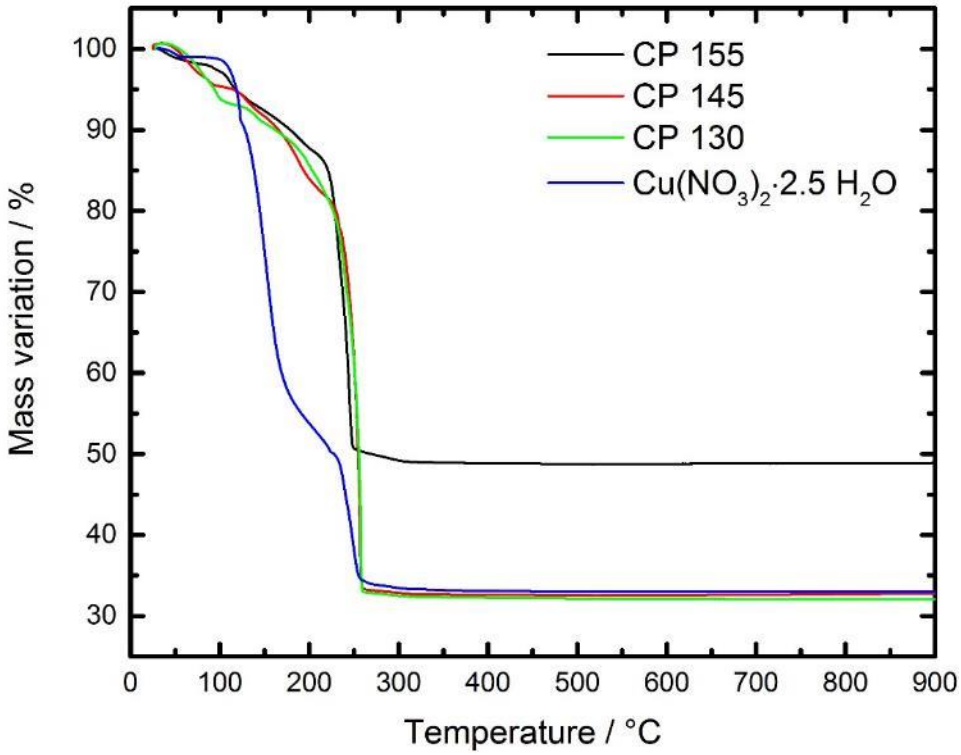

Figure 41. *TGA curves of copper oxide precursors prepared by SFS and of their precursor (copper nitrate pentahemihydrate) at 5°C/min under air.*

Figure shows the mass change of the different copper samples prepared and also of the precursor. The decomposition of copper nitrate hemihydrate starts at ~95°C where the formation of the basic nitrate begins.[210] This reaction takes place between the water present in the compound and the copper nitrate, where the nitrate ligands are stepwise substituted by hydroxyl groups, which means that nitric acid is removed. As consequence, the intermediate species between copper nitrate ($Cu(NO_3)_2$ → $(NH_4)_3(Cu(NO_3)_4(NO_3)$ → $Cu_2NO_3(OH)_3$) and Rouaite are formed depending on the temperature. This explains why, the higher the synthesis temperature, the closer the intermediate species are to copper hydroxide ($Cu(OH)_2$). However, at this temperatures copper hydroxide would not be stable, instead copper oxide is directly formed. Rouaite differentiates itself to the other intermediate species because it presents more copper atoms per molecule. Which means that, below 155°C, the intermediate species are formed by changing the coordination sphere of Cu^{II} without mass variation, which explains why both CP 130 and CP 145 have the same proportional weight loss as the precursor (~65.8%). While above 155, the coordination sphere of Cu^{II} changes, forming an intermediate species with a different quantity of copper per molecule. This explains why the mass variation is the same for CP 130 and CP 145 and copper nitrate, compared to CP 155 which has a lower mass loss. In CP 130, both the precursor (copper nitrate) and ammonium copper nitrate (ACN) are in the material. In CP 145, copper nitrate cannot be found anymore, instead, the copper is distributed between ammonium copper nitrate and Rouaite. However, in CP 155 all the copper is found in the Rouaite species, which has two copper atoms per molecule. Therefore, the coordination sphere of copper(II) changed at 130°C and then at 155°C the copper content of the material is increased. The presence and the concentration of the different compounds can be identified optically by the difference in colour (Copper nitrate: blue to Rouaite: turquoise) of the powders at macroscopic scale as shown in

Figure 42. *Macroscopic comparison of copper oxide precursor samples prepared at A) 130°C; B) 145°C and C) 155°C.*

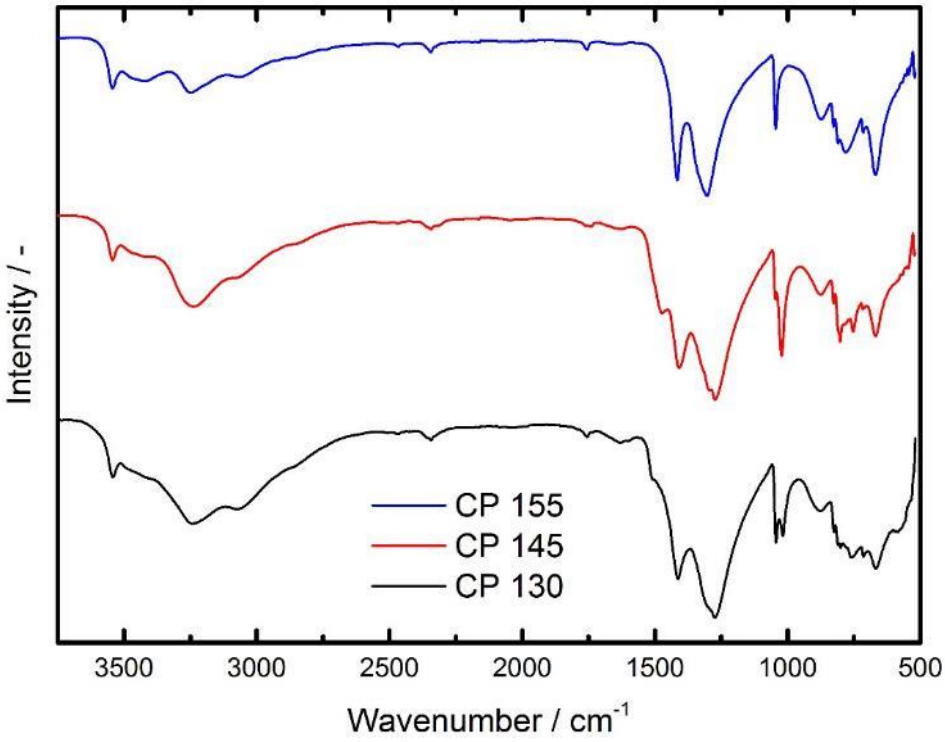

Figure 43. *FTIR spectra of copper oxide precursor samples prepared by SFS at different temperatures.*

Figure .

Regarding the species present in the powders, the powders CP 130 and CP 145 have very similar FTIR spectra along the whole wavelengths domain. This goes well along the species found in the XRD pattern, both powders presented the same species but the unreacted precursor (copper nitrate pentahemihydrate) found in the 130°C powder. On one hand, the peak at 1415 cm^{-1} peak is present in all materials. This one is associated to Rouaite. However, the peak at 1270 cm^{-1} is only present in CP 130 and CP 145, which is associated to ammonium copper nitrate. The signal at 3245 cm^{-1} associated to chemical water clearly diminishes in intensity as the temperature rises, which is in accordance with loss of nitric acid explained before. This can be observed in the FTIR spectra (**Figure**).

4.2. Properties of calcined CuO powders

The samples of copper oxide prepared at 155°C were further calcined at 400°C. This thermal treatment fused the plates together into macroscopic walnut like aggregates (**Figure**).

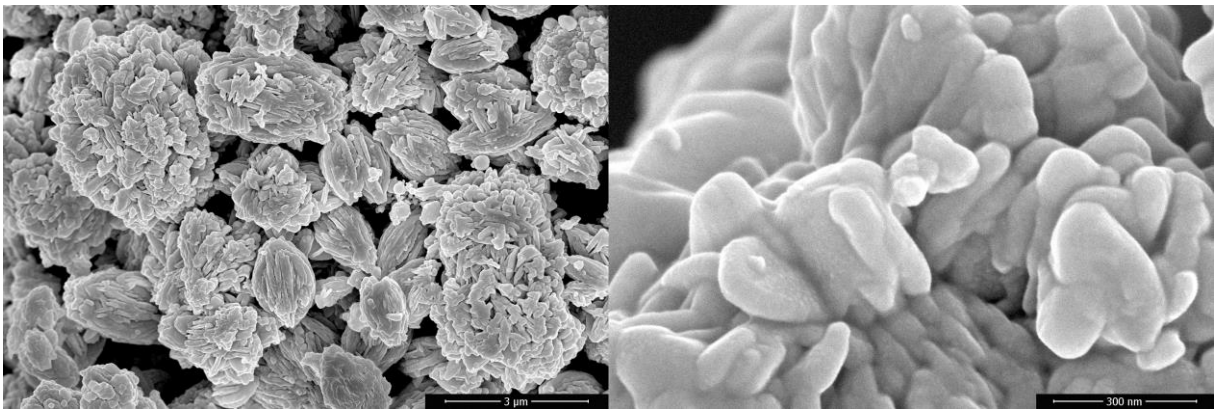

Figure 44. *SEM images of CuO samples calcined at 400°C at increasing magnifications.*

The particles are totally filled and densely packed. They are formed of a polycrystalline structure. The inner structure of the particles can be seen in **Figure** .

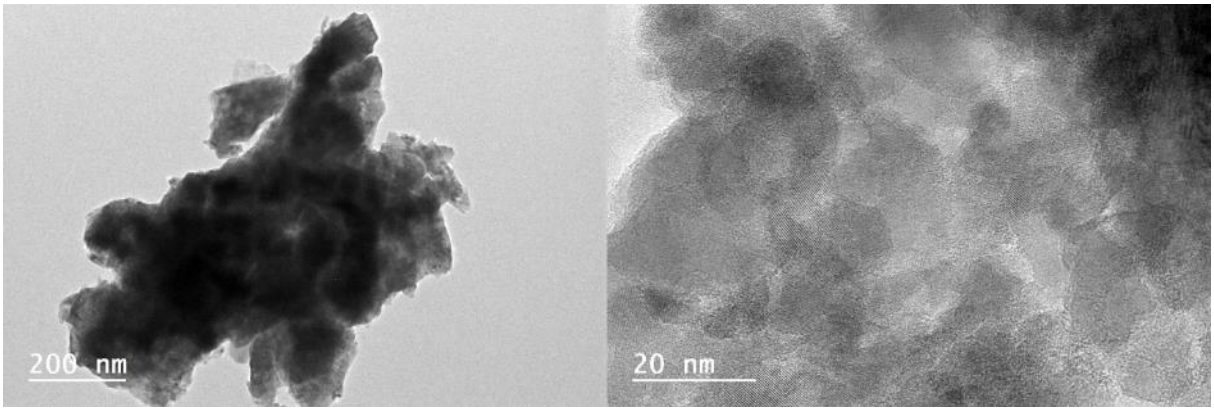

Figure 45. *TEM images and diffraction pattern of CuO samples calcined at 400°C.*

Figure shows the particles observed by EDX. It can be seen that both the oxygen and copper atoms are homogeneously distributed along the particle. This implies that the copper present in the particle is fully oxidized all along the particle.

The thermal treatment at 400°C under air totally oxidized the material produced by SFS. This process forced the organization of the resulting copper oxide molecules into orderer structures. This phenomenon also led to the sintering of the previously amorphous flakes. The material obtained by this procedure is made out of particles of pure CuO with an average crystallite size of 14.9 ± 2.2 nm. This was ascertained by

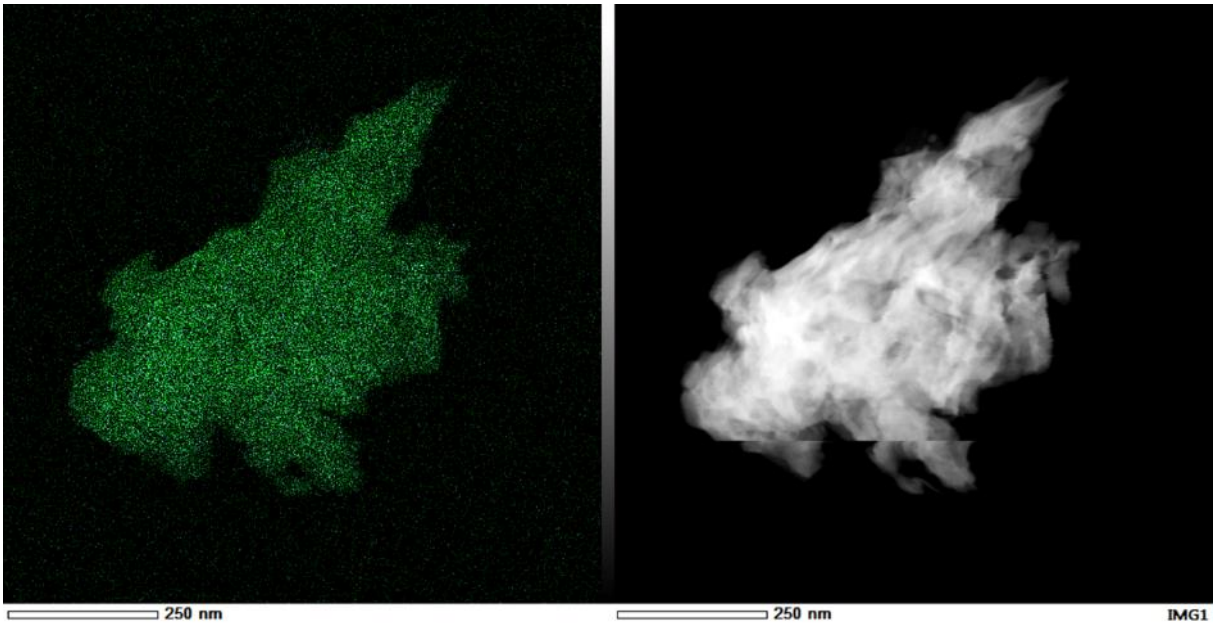

Figure 46. *EDX image of calcined copper oxide sample (Cu in green and O in light blue).*

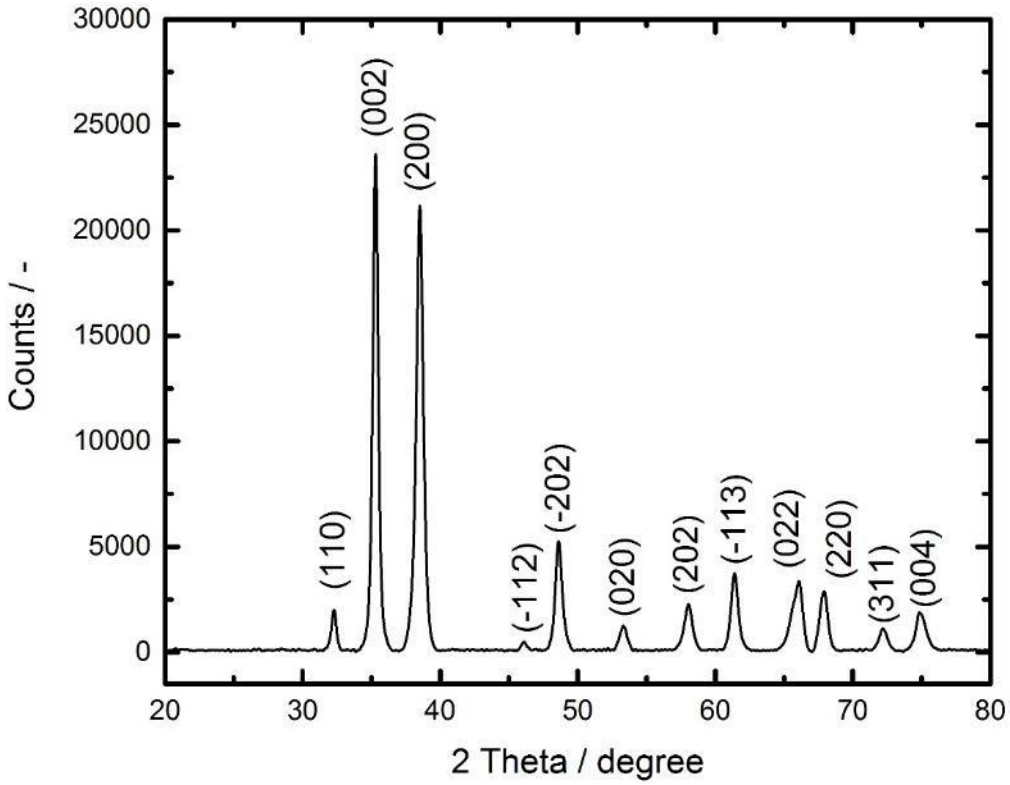

Figure 47. *XRD pattern of CuO sample calcined at 400°C.*

XRD analysis (**Figure**). This implies that the particles, which are strongly aggregated are made or small elementary crystals. The small crystal size is a consequence of the smal crystal size of the precursor (~18 nm). The thermal treatment

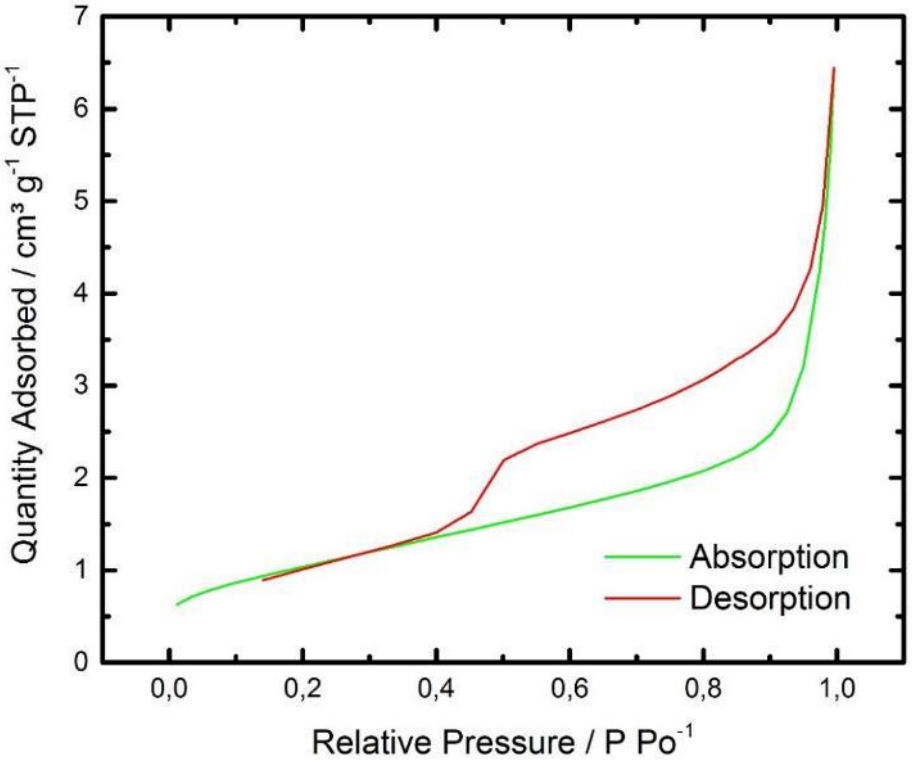

Figure 48. *BET isotherm of copper oxide sample calcined at 400°C.*

induced a coalescence of the irregular particles leading to big aggregates, but did not affect deeply the crystal size.

The specific surface area of the calcined particles were measured by BET nitrogen adsorption. The resulting isotherm can be seen in **Figure** . The specific surface area of the sample is of 3.78 m^2 g^{-1}. This very low specific surface area is a consequence of the sintering of the particles, produced by the thermal treatment. The analysis of the BET values shows that the material is made up of submicrometric particles of CuO which are strongly aggregated, forming the prolate ellipsoids seen before (SEM). This is in accordance with the type 2 isotherm which presents a H III hysteresis. This corresponds to a material with no porosity or only macroposity. The hysteresis is common for macroscopic aggregates of particles. This fits with the morphology and dimensions identified by the other measurement techniques.[200]

4.3. Conclusions

The submicronization of a copper oxide precusor was perfomed by SFS system. This modification takes place at 155°C, leading to a precursor ($Cu_2(NO_3)(OH)_3$) mixed with a byproduct (NH_4NO_3) which is obtained by the thermal decomposition of copper nitrate pentahemihydrate.

Copper oxide is obtained by calcination at 400°C of the products made by SFS. In this material, the elementary crystallites are very small, but they are sintered into submicrometric, angular particles which themselves are aggregated in larger micrometric particles with a prolate ellipsoidal shape.

5. Materials based on the mixture of titanium and bismuth

Various oxide mixtures were prepared by combining different proportions of titanium oxide and bismuth oxide. Three materials were prepared by the SFS process using a stoichiometric TTIP to water proportion (1:2 mol/mol).

5.1. Bismuth Titanium with higher titanium proportion

5.1.1. Properties of raw BiTi 1:1.35

The molar proportion of the material prepared with a higher relative amount of titanium is Bi/Ti 1:1.35 (mol/mol).

The material obtained by the SFS process is made of elementary submicrometric particles similar to those prepared with pure titanium, but which seem to be stronger aggregated. Nevertheless, most of the particles have a quasi-spherical geometry (**Figure**). The introduction of acetic acid for dissolving the bismuth precursor changes the physicochemical properties (pH) of the solution.[211] This affects mainly the viscosity and surface tension, which as consequence influences the droplet formation

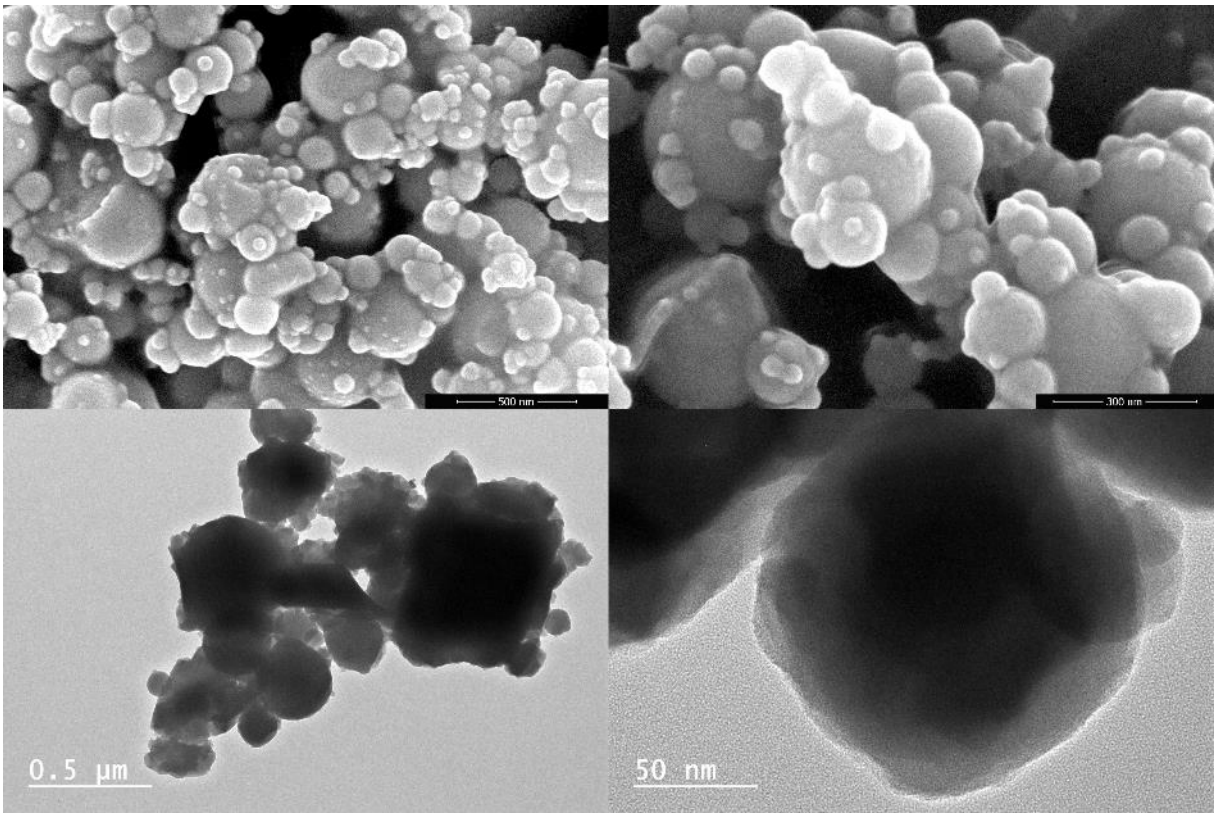

Figure 49. *SEM (above) and TEM (below) images of raw BiTi 1:1.35 powder.*

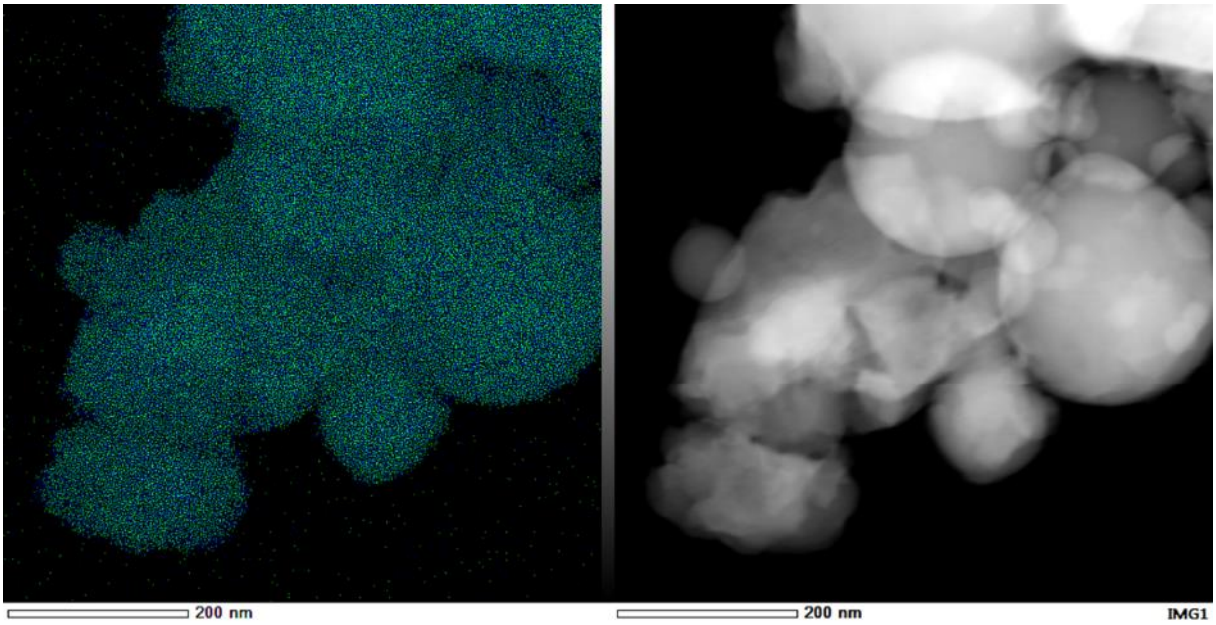

Figure 50. *EDX image of particles of BiTi 1:1.35 powder (Bismuth in green and titanium in blue).*

in the spray.[198] [40] Acetic acid evaporates at higher temperatures then isopropanol, which implies a slower evaporation process. Therefore, the aggregation behavior and the particle formation is different, leading to more aggregated particles with polydisperse

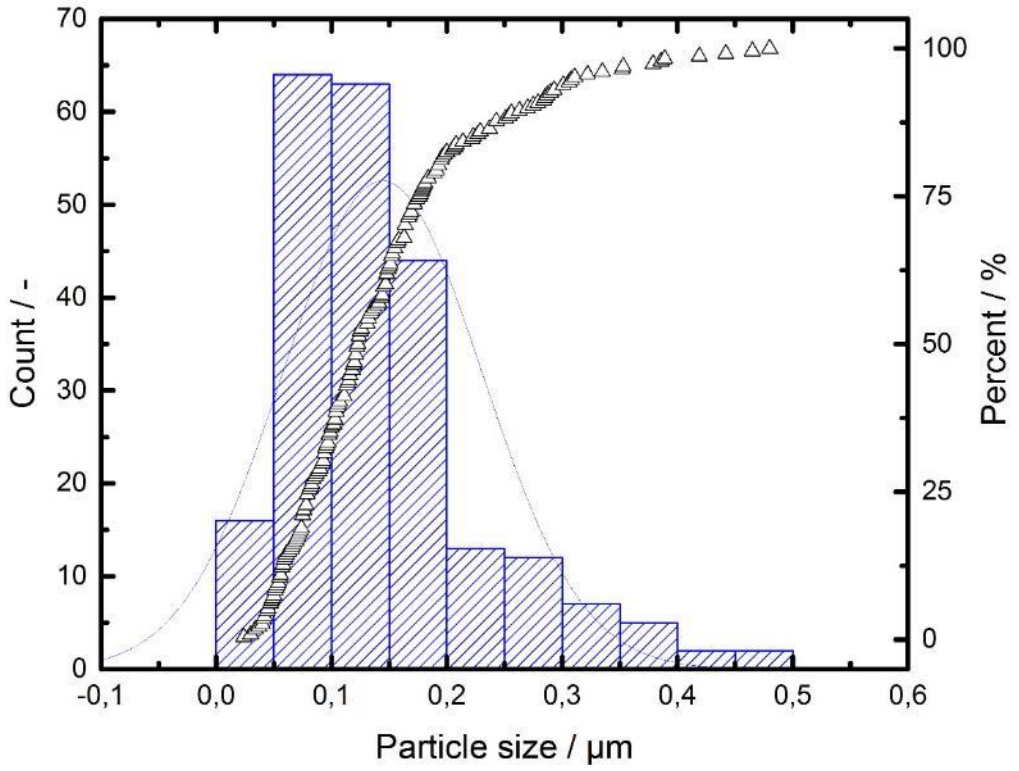

Figure 51. *Histogram and cumulative particle size distribution for BiTi 1:1.35.*

particle size distribution ranging from ~50 nm for the smaller particles up to ~ 200 nm for the bigger ones.

The powder is made of homogenously dense, amorphous particles which form groups of several dozens of units (**Figure**). Both bismuth and titanium are perfectly mixed along all the directions in every particle, which shows the high degree of homogeneity of the mixture (**Figure**).

The size distribution of the particles (**Figure**) was calculated basing on the TEM images. The particles have an average size of 144.2 ± 86.5 nm. The polydispersity of the particles can be identified by looking at the high value of the standard deviation (86.5 nm versus 6.6 nm of TiO_2). Furthermore, the biggest size populations of the spheres can be found between 50 nm and 200 nm. Around 75 wt.% of the totality of the particles can be found below 175 nm as can be seen on the cumulative particles size graph.

The response of the material to thermal stress is by TGA (**Figure**). The raw powder obtained is made of amorphous oxides along with organic species. The reaction process is described in literature.[212] First, the evaporation of free solvent can be identified as a weight loss of around 12 %. Then, an important loss of mass can be

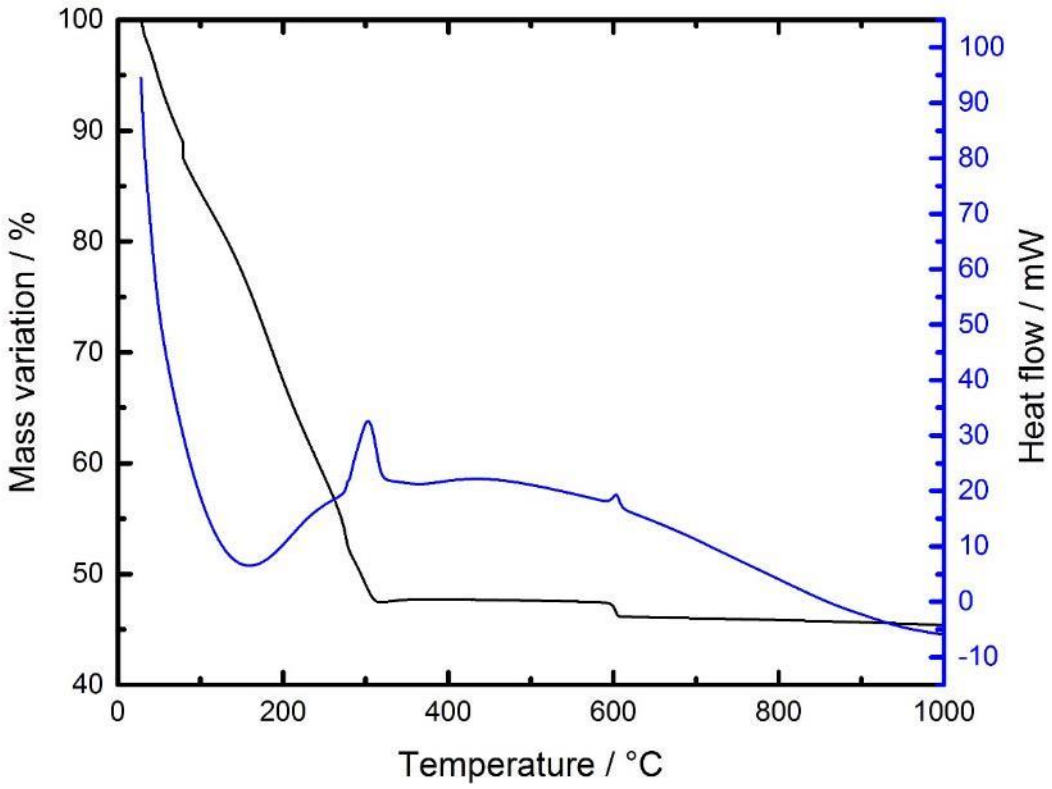

Figure 52. *TG analysis of BiTi 1:1.35 powder.*

identified which corresponds to the removal of species like organic molecules and water, which are part of the amorphous matrix of titanium and bismuth.[213] [147] This is associated to the weight loss of 47.5% as well as the broad endothermic peak in the DTA curve at around 160°C. A small change in the slope at around 280°C can be identified which corresponds to removal of water molecules when the acetobismuth complex transform into bismuthyl hydroxide (BiO(OH)). From this point on BiO(OH) is thermally stable, which as described in literature, does not crystallize in this kind of systems.[212] Therefore it is amorphous as could be verified by XRD analysis on a 400°C sample. At 300°C the formation reaction of the mixed oxide takes place which is characterized by the well-marked exothermic peak at 600°C. The crystallization of the mixed oxide involves an exit of the resting water molecules which is estimated to be 2.2 % which is close to the 1.7% registered in the TGA curve. This can be recognized through a second step at 600°C. This step is accompanied by a small exothermic peak in the DTA curve.

5.1.2. Properties of calcined BiTi 1:1.35

The previous material was calcined at 650°C under air during 4 hours, which led to the crystallization of the matter.

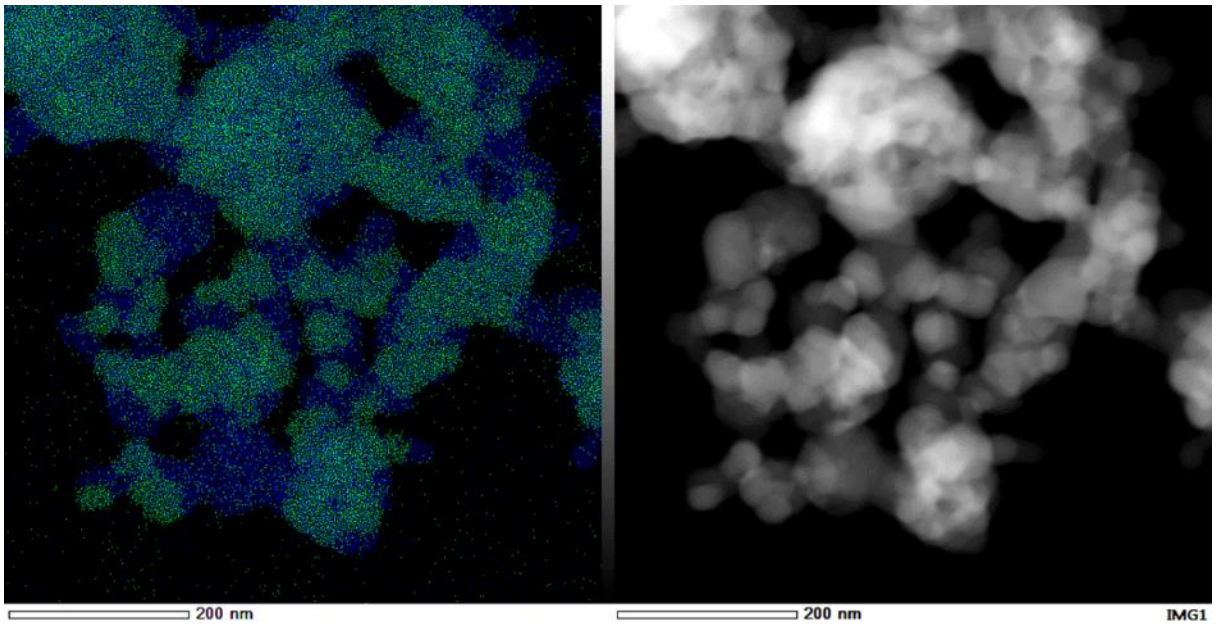

Figure 53. *EDX image of particles of bismuth titanate BiTi 1:1.35 powder (Bismuth in green and titanium in blue).*

The crystallization of the mixed oxide involves the restructuration of the matter and the distribution of the elements in it. This results in a segregation of the bismuth titanate on one hand and pure titanium oxide on the other hand (**Figure**). This reorganization and segregation lead to a sintering effect which aggregates the particles together. They fuse together forming microscopic aggregates. However, the former single particles can still be identified. **Figure** shows the morphology of the particles after calcination.

The powder was analyzed by XRD to identify the crystal phase in the materials formed (**Figure**). The segregated titanium and bismuth form a mixed oxide known as bismuth titanate ($Bi_2Ti_2O_7$). Taking into account the phase diagram found in literature, at this TiO_2 to Bi_2O_3 molar ratio (1/1.35) and at a temperature of calcination like this (650 °C) the stable phases should be $Bi_{12}TiO_{20}$ and $Bi_4Ti_3O_7$.[214] It is specified that the $Bi_2Ti_2O_7$ is a metastable phase under 1000°C. Nonetheless, the presence of this phase at lower temperature is caused by a stabilization effect of the phase owing to the small size of the primary particles.[214] The part of titanium oxide which is not included in the bismuth titanate matrix crystallizes separately in the form of rutile. Taking into account

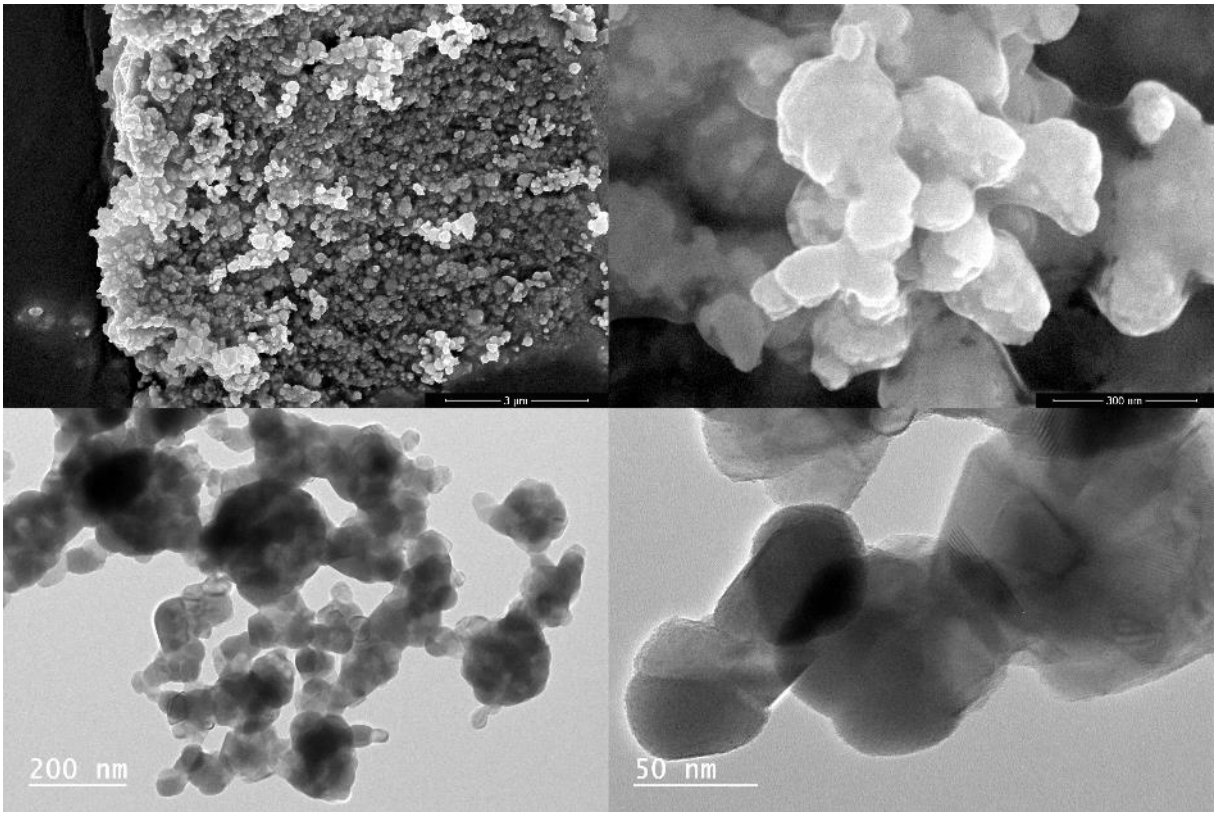

Figure 54. *SEM (above) and TEM (below) images of bismuth titanium BiTi 1:1.35 powder calcined at 650°C.*

that the crystallization takes place at 650°C the stable phase is rutile and not anatase. From a thermodynamic point of view anatase is more stable at smaller sizes than rutile, owing to the fact that the lower surface free energy of this phase.[199] However, in this case a transition from anatase to rutile took place. The anatase to rutile transition (ART) is reconstructive because the change in the crystalline structure breaks up and forms new bonds. At which temperature and at which time rate this transformation takes place depends on factors like particle morphology, calcination atmosphere and heating rate, impurities, etc. The transition temperature of pure bulk anatase is widely considered to be around 600°C. In this case, “impurities” like bismuth titanate are present during the anatase to rutile transition. Additionally the calcination temperature is higher (650°C for the formation of bismuth titanate compared to 400°C for the crystallization of pure anatase nanoparticles). Both phenomena lead to a transformation rate fast enough to convert all the remaining anatase into rutile. Titanium oxide prepared by SFS was calcined at up to 1000°C under air. The obtained phase was anatase. Compared to this material, the presence of bismuth titanate promotes the anatase to rutile transition.

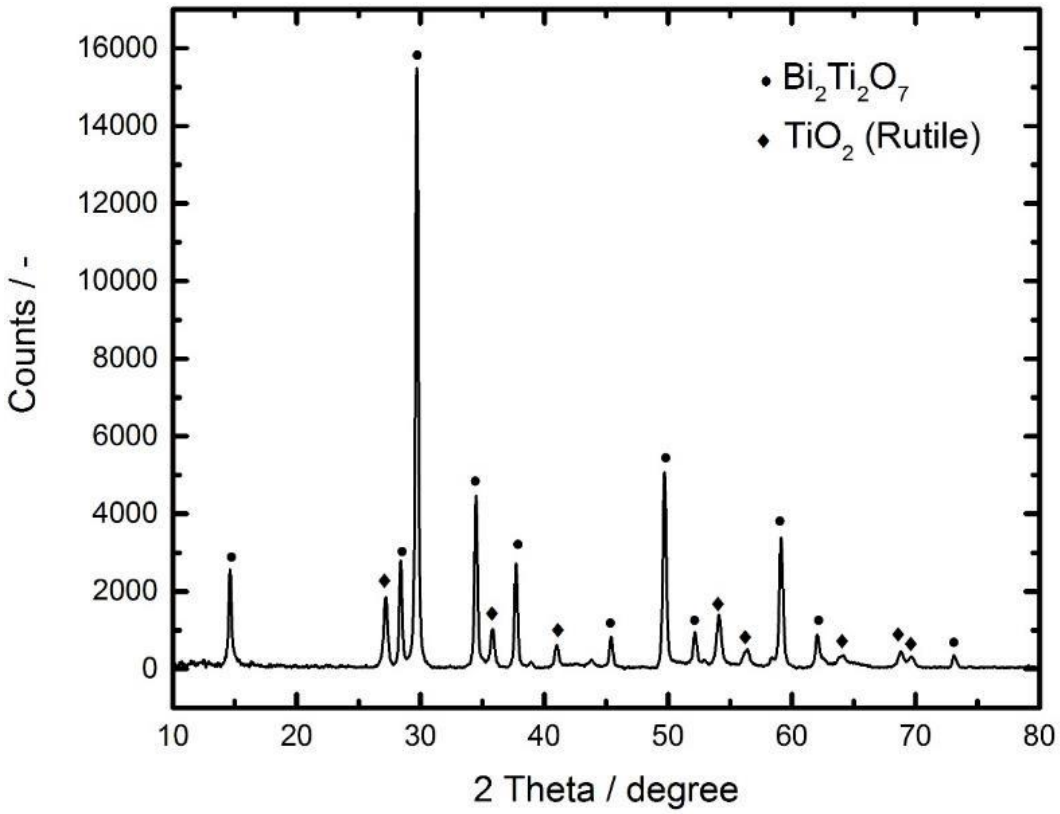

Figure 55. *XRD pattern of BiTi 1:1.35 sample calcined at 650°C under air.*

The size distribution of the particles after calcination was measured and calculated basing on the TEM images. The average particle size of this powder is 134 ± 69 nm. The particles are distributed along a broader size range (**Figure**). This broader size distribution comes from an already wide distribution of the amorphous particles. Furthermore, the slope of the cumulative distribution of the particles seems to form three steps, equal to three size populations at ~75 nm, ~125 nm and ~210 nm. This is a consequence of the thermal treatment that induced the sintering of the particles. It could be explained because the element distribution in the particles is heterogeneous. The smaller particle population is made of the titanium oxide which crystallized independently. The intermediate population is made of the bismuth titanata particles that formed during the thermal treatment. The biggest population is made of particles that sintered together during the process, where titanium oxide and bismuth oxide are intimately mixed.

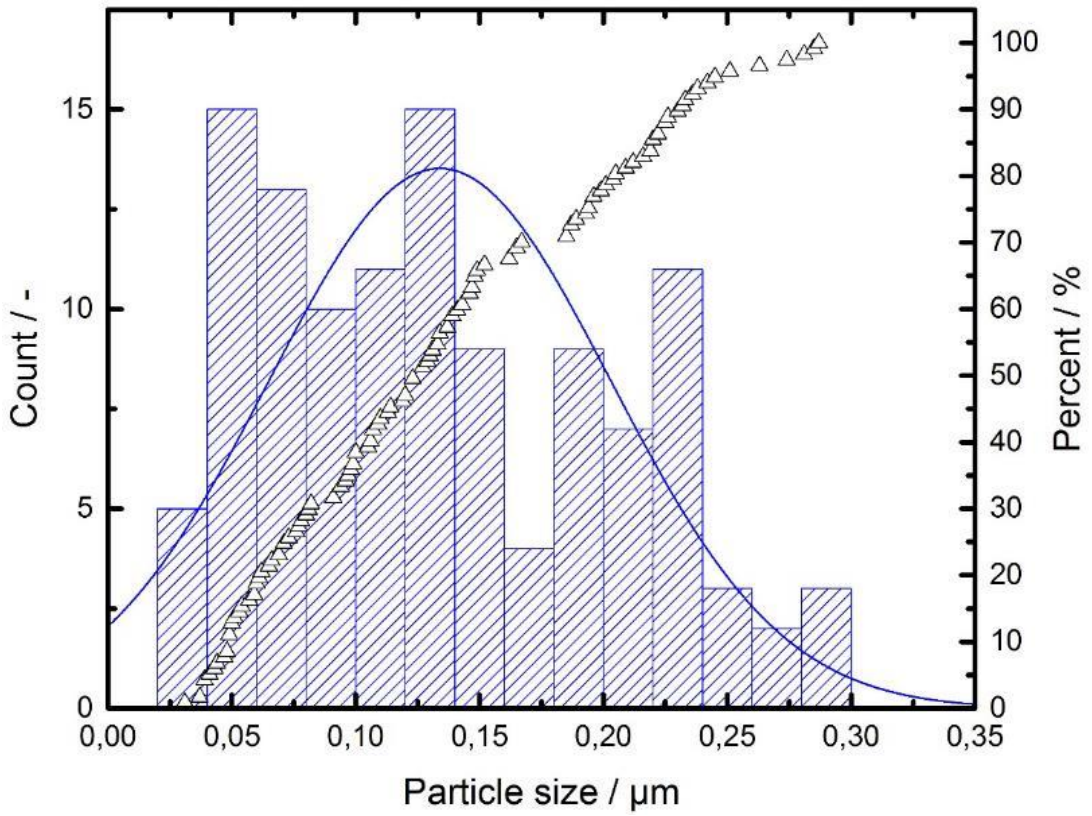

Figure 56. *Histogram and cumulative particle size distribution for calcined BiTi 1:1.35.*

The crystallite size of $Bi_2Ti_2O_7$ is 29.9 ± 1.7 nm while for TiO_2 it is 22.1 ± 1.2 nm. These values are similar to the crystallite size of the particles of other materials which were prepared by the same methodology. This is a consequence of the crystallization process and its conditions. For all the materials, the time, the energy transmission method, *i.e.,* furnace, and the calcination atmosphere were the same. These crystals built the particles in form of a polycrystalline structure. The titanium oxide phase obtained is in accordance to the stability of rutile over anatase (> 14nm).[4]

The FTIR spectra of bismuth titanate before and after calcination can be seen in **Figure** . The spectra show a wide peak at ~3200 cm^{-1}, which is associated to O-H stretching vibrations from different functional groups. This signal corresponds to the intermolecular hydrogen bonded O-H group (3550-3230 cm^{-1}) that forms the amorphous titanium network and other functional groups like chemical water (3600-3100 cm^{-1}) which are still part of the material.[208] Additionally, the CH_3 stretching vibrations of bismuth titanate are found in this area. The peak at 1525 cm^{-1} is associated to the CO group from bismuth acetate. The peak at 1045 cm^{-1} can be associated to the CH_3 rocking vibrations and the C-O streching, the 611 cm^{-1} peak

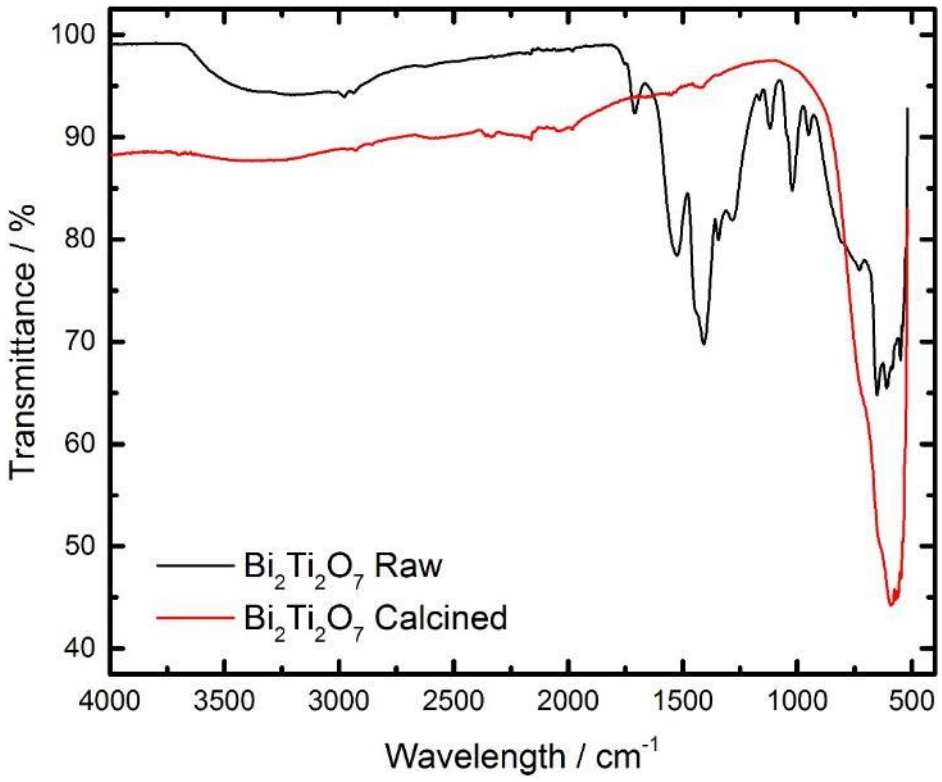

Figure 57. *FTIR spectra of raw and calcined bismuth titanate BiTi 1:1.35.*

resembles to the C=O in plane pending and the 524 cm^{-1} peak could be associated to the C=O out of plane bending of bismuth acetate.[215] The spectra of the calcined sample does not present any peak which could be attributed to organic species or water. The differences between the spectra illustrates that the organic species, present in the synthesized material, are totally removed after the thermal treatment. The differences between the spectra illustrate that the organic and adsorbed species are totally removed after the thermal treatment.

5.2. Bismuth Titanium with stoichiometric proportion

5.2.1. Properties of raw BiTi 1:1

The molar ratio of bismuth to titanium of this composite was Bi:Ti 1:1. The particles that make the powder are close to fully spherical and are attached to each other forming groups of various units (**Figure 58**).

Taking into account the morphology of the powder observed, the particles are aggregated with interconnections similar to those formed when droplets collide and afterwards undergo a stretching separation, leaving a filament that ultimately aggregates the particles.[216] The way two colliding droplets separate depends on the physical parameters of the liquids like droplet size or viscosity. The solution based on acetic acid and the bismuth precursor, altered the viscosity and surface tension of the solution. The increase of the acidity by the introduction of acetic acid lowers the surface tension of the droplets.[211] The inner structure of the particles is homogeneous and dense along all the body of the particle and is identical for all the particles. The elements did not form an organized structure and are in amorphous phase. The particles are homogeneously filled and dense.

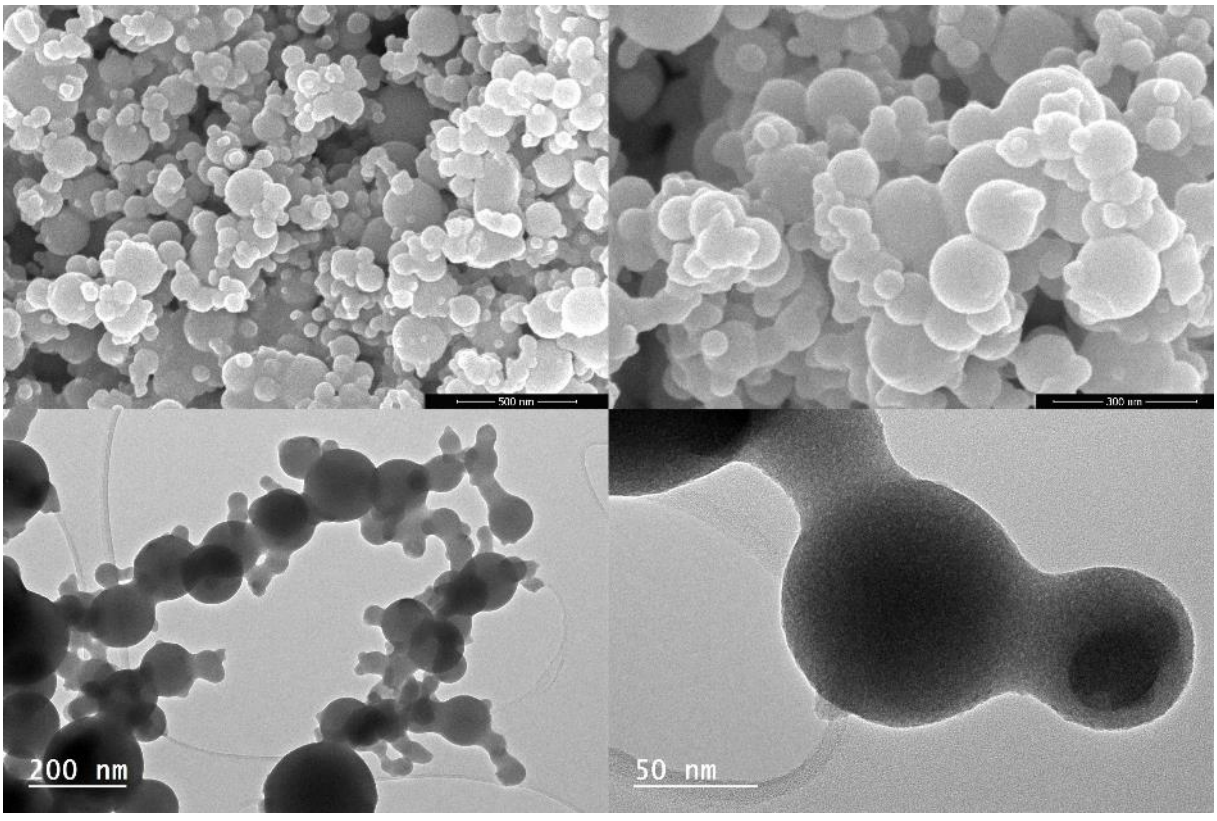

Figure 6. *SEM (above) and TEM (below) images of raw BiTi 1:1 powder.*

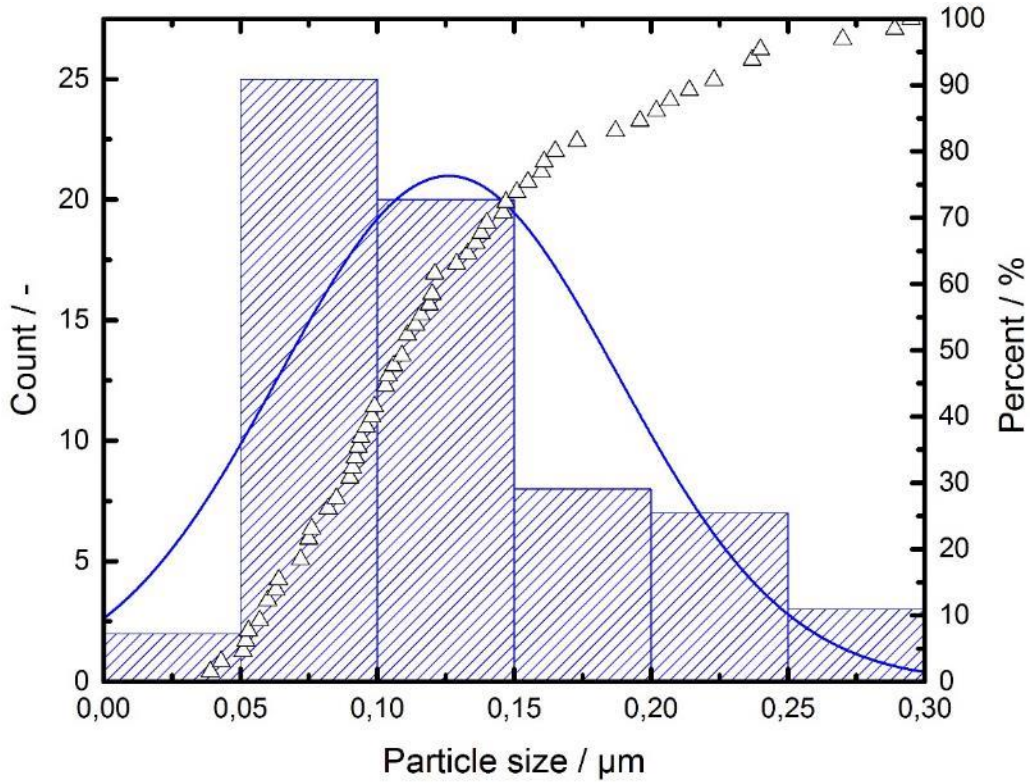

Figure 7. *Histogram and cumulative particle size distribution for BiTi 1:1.*

The particles of this material are submicrometric and have an average size of 126.1 ± 61.8 nm (**Figure 59**). The size distribution of the particles shows that most of them can be found around 125 nm, though an important part is located between 50 and 100 nm. The change of slope at 150 nm shows that ~80% of the particles measured are below this value.

Both elements, titanium and bismuth, are mixed up to a perfect degree as can be seen in **Figure** . This very intimate mixture is a consequence of the production process. As both precursors are solved in the same solvent, when sprayed and forced to precipitate in flash conditions, the elements stay in this mixed state.

The TGA curve (**Figure**) of the stoichiometric BiTi 1:1 composite material shows that the first step of the decomposition, which occurs from room temperature to ~ 300°C, corresponds to the loss of water and organic molecules present in the material. This is associated with the endothermic peak of the DTA curve until ~280°C. This mass loss (~37 wt.%) is less important than for the mass variation of BiTi 1:1.35 (~55 wt.%). The proportion of organic residues that are removed by the thermal treatment is more important in the amorphous titanium matrix ($Ti(OH)_x(OCH(CH_3)_2)_{4-x}$) than in the bismuth matrix ($Bi(C_2H_3O_2)_3$). This would explain why the mass loss is less

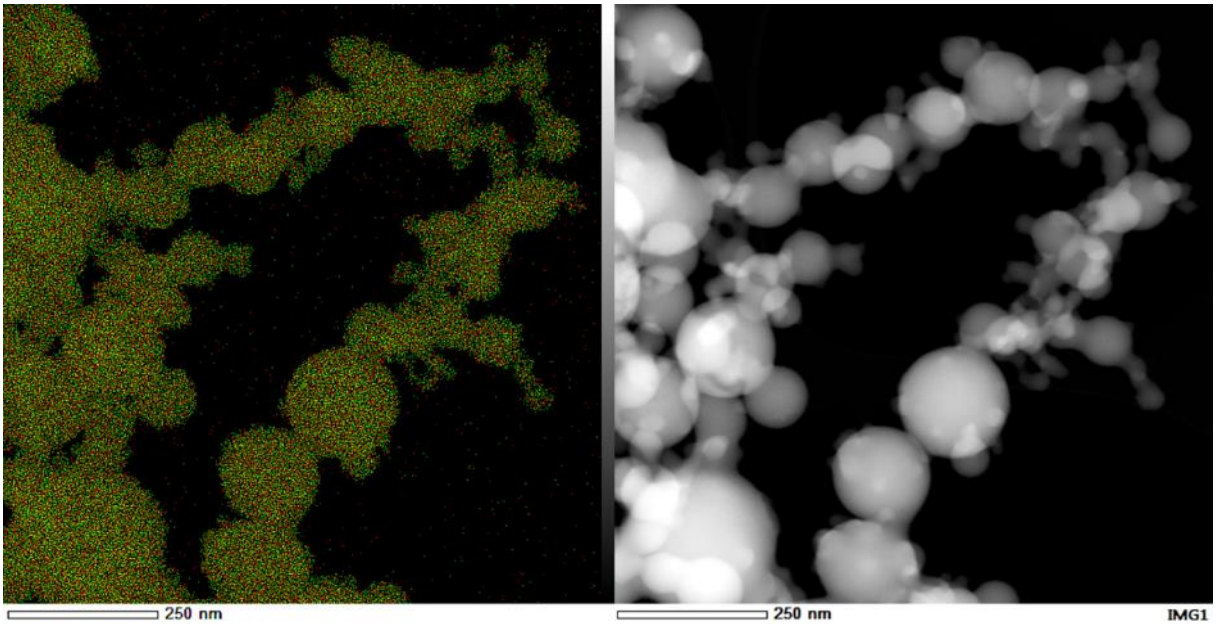

Figure 60. *EDX image of particles of BiTi 1:1 powder (Bismuth in green and titanium in red).*

marked for this composite than for the one richer in titanium. Taking into account the proportions of titanium and bismuth, and the corresponding weight loss for the pure materials, the proportionality would be of 25%. In this case peak around 280°C, which corresponds to the transformation of the chelated bismuth complex into bismuthyl

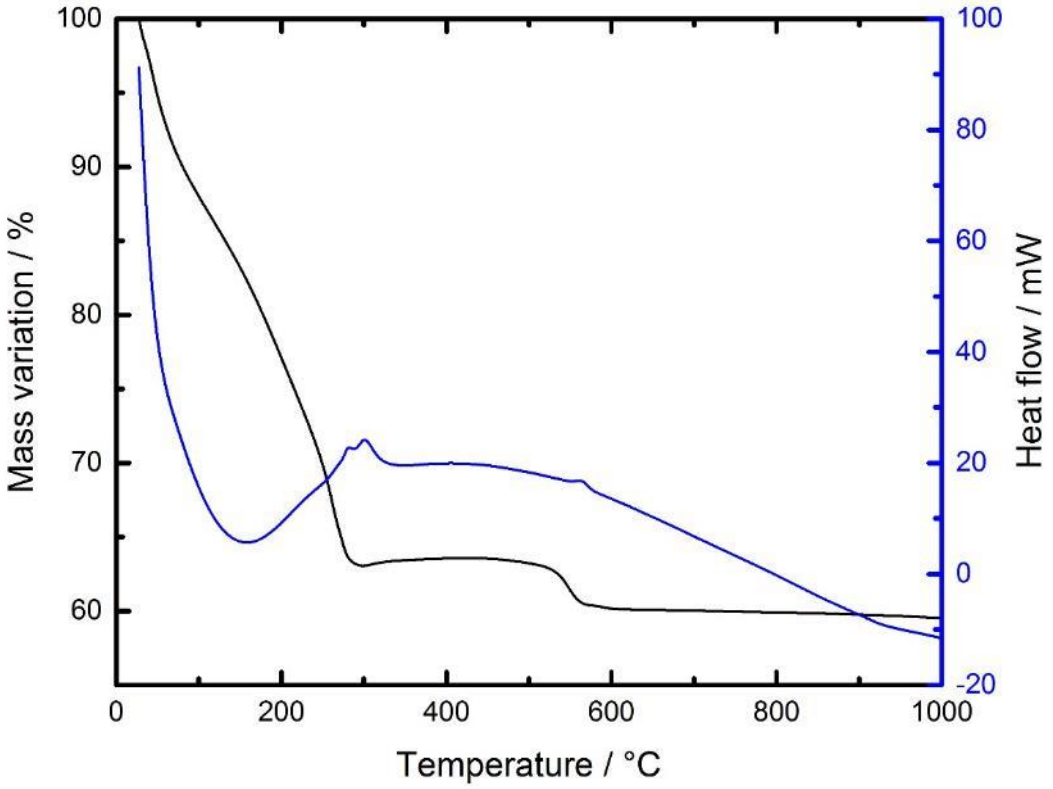

Figure 61. *TG analysis of raw BiTi 1:1 molar ratio.*

hydroxide, can be easily identified.[213] [147] At 300°C the formation reaction of the mixed oxide takes place which is characterized by the second exothermic peak. Finally, the crystallization of the mixed oxide involves an exit of the resting water molecules. This can be recognized by a second step at 565°C. This step is accompanied by a small exothermic peak in the DTA curve.[212] The temperature at which this phenomenon takes place is lower than for the BiTi 1:1.35 composite. In the case of the mixed oxides build by titanium oxide and bismuth oxide the thermal evolution has a unique behavior depending on the relative proportion. This means that the dehydration and removal of organic species as well as the formation and crystallization of the mixed phase of oxides are dependent of the Bi:Ti proportion. In this case, the amorphous oxides, which compose the material, cannot longer be differentiated. At which temperature the dehydration and the crystallization takes place is therefore different because the crystal structure formed will be different. However, basing on the experiments performed it can be seen that the higher the Bi:Ti ratio the lower the crystallization temperature of the amorphous materials. The crystallization temperature of Bi:Ti 1:1.35 is higher because the whole material segregates during the thermal treatment owing to the titanium oxide in excess. In the case of the Bi:Ti 1:1 composite, the material is made of pure bismuth titanate. Therefore, the energy for the segregation is not needed, which would explain why the crystallization takes place at lower temperatures.

5.2.2. Properties of calcined BiTi 1:1

This material was calcined at 650°C under air for 4 hours. The particles (**Figure**) that form the powder of this bismuth titanate are strongly fused together. The calcination removes the organic residues and reorganizes the distribution of the elements. The formation of the perovskite crystal structure is the result of titanium oxide and bismuth oxide grouping in layers and stacking.[35] This is only possible if the different oxide molecules move from the amorphous disorder into a periodic order. The particles are made of several crystallites which organize in polycrystalline units. The particles are covered by bubble like elements on the surface. This is metallic bismuth which forms as a product from the decomposition of bismuth titanate by interaction with the electron beam of the TEM device.[217] This phenomenon will be explained in detail for the next material BiTi 2:1.

The high temperatures allow the reorganization which also leads to the loss of the morphology. As consequence the size changed and independence of the particles is lost. The size of these particles is 158.5 ± 84.4 nm. The size distribution of the

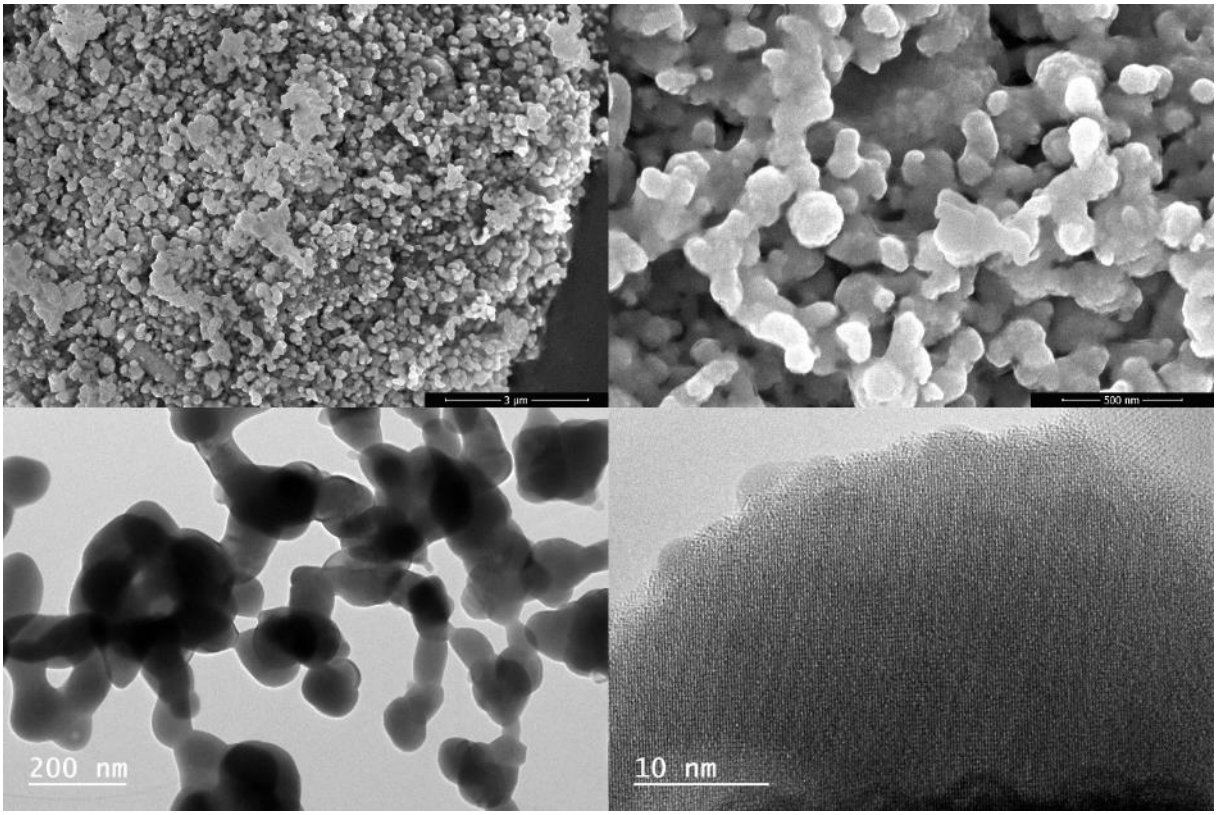

Figure 62. *SEM (above) and TEM (below) images of calcined BiTi 1:1 powder.*

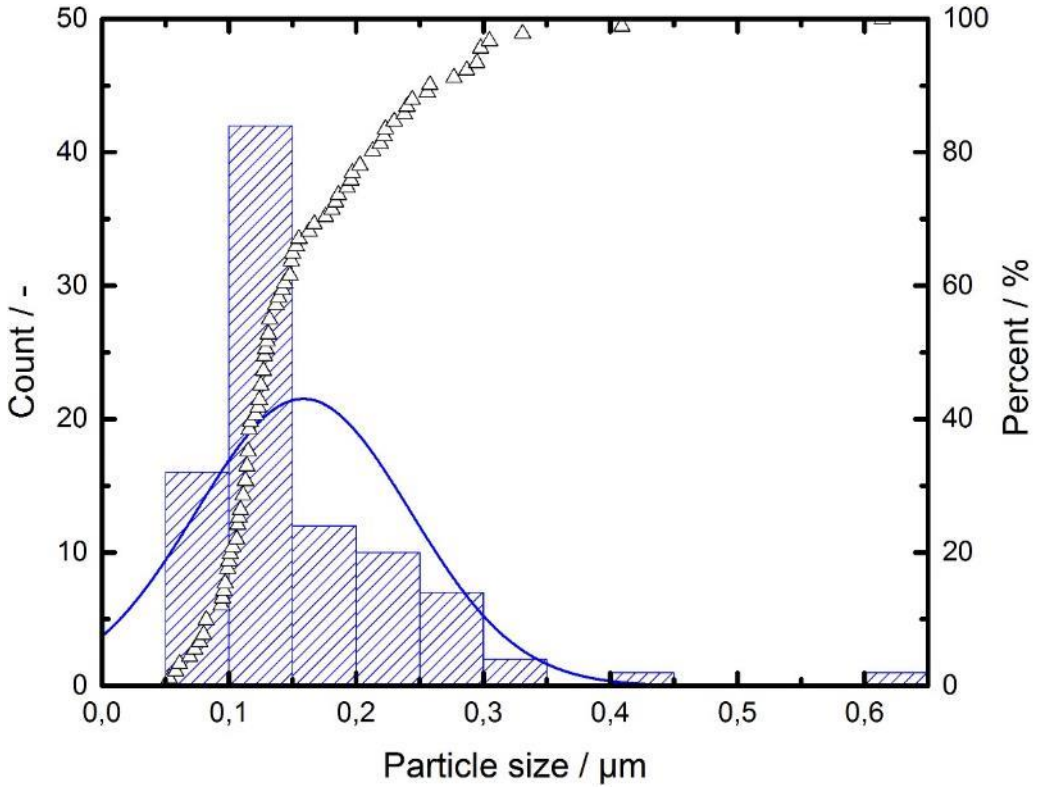

Figure 63. *Histogram and cumulative particle size distribution for calcined BiTi 1:1.*

particles can be seen in **Figure** . The dimensions of the particles are mainly concentrated in the range between 100 and 150 nm. Compared to the bismuth titanate produced with an excess of titanium, the particles are less broadly distributed. This is because the raw amorphous particles had a much more defined morphology and

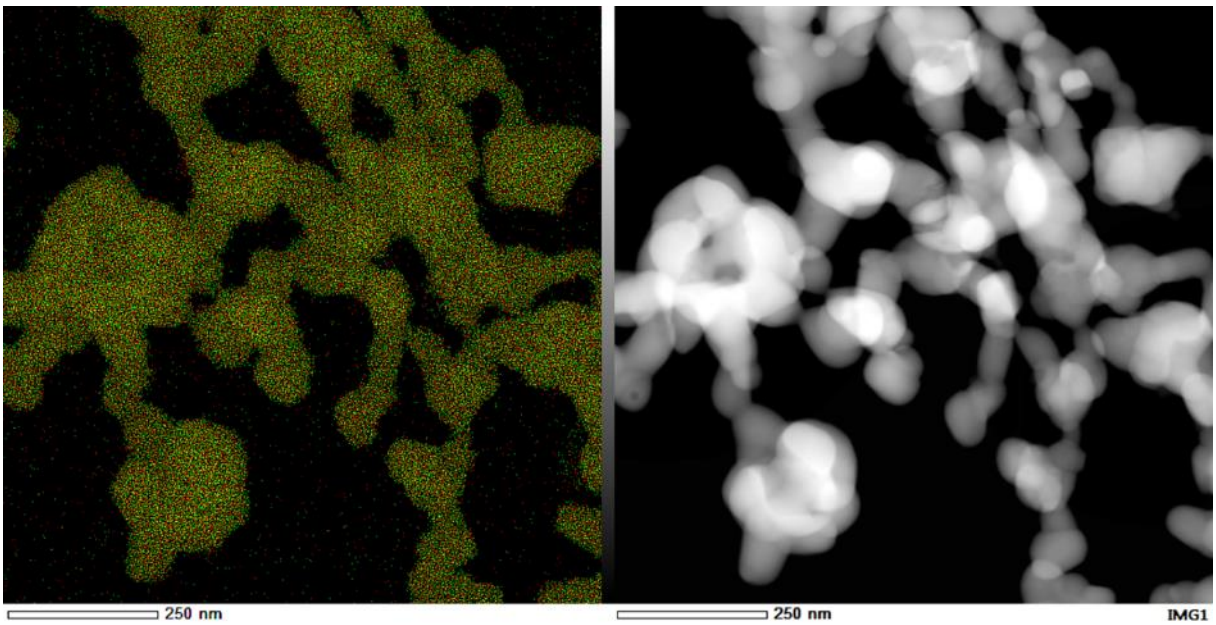

Figure 64. *EDX image of particles of calcined BiTi 1:1 (Bismuth in green and titanium in red).*

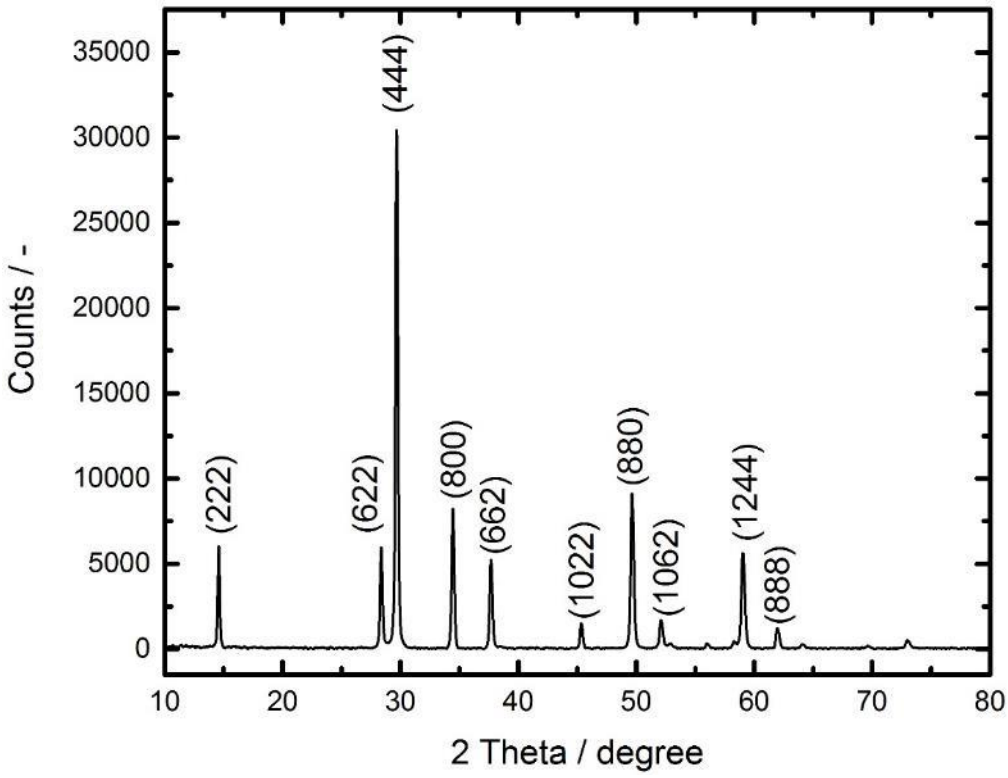

Figure 65. *XRD pattern of BiTi 1:1 sample calcined at 650°C under air.*

already thinner size distribution. In addition, the fact that only one component is present implies that the calcination is more uniform. Thus, when the thermal treatment fuses the particles together the sintering effect is less important.

As can be seen in **Figure** the element distribution is nevertheless maintained after the thermal treatment. This comes from the relative proportion of the metallic elements, titanium and bismuth, as they are mixed in a proportion that will lead to a unique bismuth titanate phase.

Figure shows the XRD pattern of the calcined sample. It can be observed that the crystallized material is pure in composition as no other peaks are present. This means that the two metals, bismuth and titanium, formed one single oxide. In this case the material is identified as the bismuth titanate $Bi_2Ti_2O_7$. Taking into account the phase diagram found in literature, the crystallization temperature (650°C) and the Bi:Ti molar percentage (50 mol%), the $Bi_2Ti_2O_7$ phase is only stable at 1195°C.[136] The phase formed should be the $Bi_{12}TiO_{20}$ bismuth titanate. Nevertheless, in this case as in the BiTi 1:1.35 case, the phase stability is strongly influenced by the fine particle size. The calculated crystallite size basing on Scherrer's equation is 32.42 ± 2.97 nm.

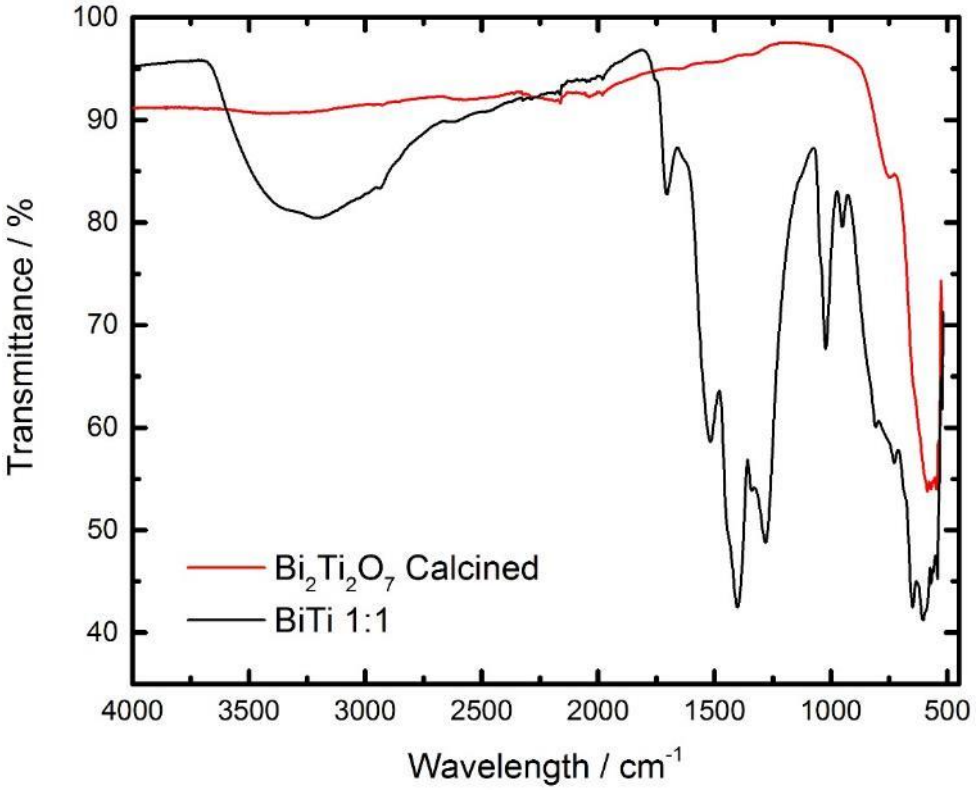

Figure 66. *FTIR spectra of raw and calcined BiTi 1:1 prepared by SFS.*

Figure shows the FTIR spectra of the 1:1 molar ratio mixed bismuth titanate for both the raw and the thermally treated samples. The raw BiTi 1:1 spectra shows a wide peak at ~3200 cm^{-1}, which is associated to O-H stretching vibrations from different functional groups. This signal corresponds to the intermolecular hydrogen bonded O-H group (3550-3230 cm^{-1}) that forms the amorphous titanium network and other functional groups like OH (3600-3100 cm^{-1}) which are still part of the material.[208] Additionally, the CH_3 stretching vibrations of bismuth titanate are found in this area. The peak at 1520 cm^{-1} is associated to the CO group of bismuth acetate. The peak at 649 cm^{-1} can be associated to the O-C-O in plane bending, the 603 cm^{-1} peak resembles to the C=O in plane pending and the 522 cm^{-1} peak could be associated to the C=O out of plane bending of bismuth acetate.[215] The spectra of the calcined sample does not present any peak which could be attributed to organic species or water. The differences between the spectra illustrates that the organic species present in the material synthesized are totally removed after the thermal treatment.

5.3. Bismuth titanate with higher bismuth proportion

5.3.1. Properties of raw BiTi 2:1

This material was prepared by mixing in a 2:1 molar ratio the bismuth and the titanium precursor. This fine and loose powder is made of spherical particles which have a size that is in the submicrometric range as seen in **Figure** . This indicates that the particle formation is affected in the same way by the material synthesis characteristics of the production method. The particles are made of an amorphous network. The particles have an average size of 135.4 ± 56.9 nm. Comparing the standard deviation of these particles to the other BiTi composites (± 86.5 nm for BiTi 1:1.35; ± 61.8 nm for BiTi 1:1), it can be seen that the higher the bismuth proportion the narrower the standard deviation is. This is a consequence of the decrease pH of the solution. The higher the acidity, the lower the surface tension of the solution.[211] This has a strong influence in the droplet collision behavior during their evaporation. As the surface tension lowers, when the collision of two or more droplets happens, they will less likely tend to regain the spherical morphology. This leads to more strongly attached droplets, which when dried, form strongly attached irregular particles.

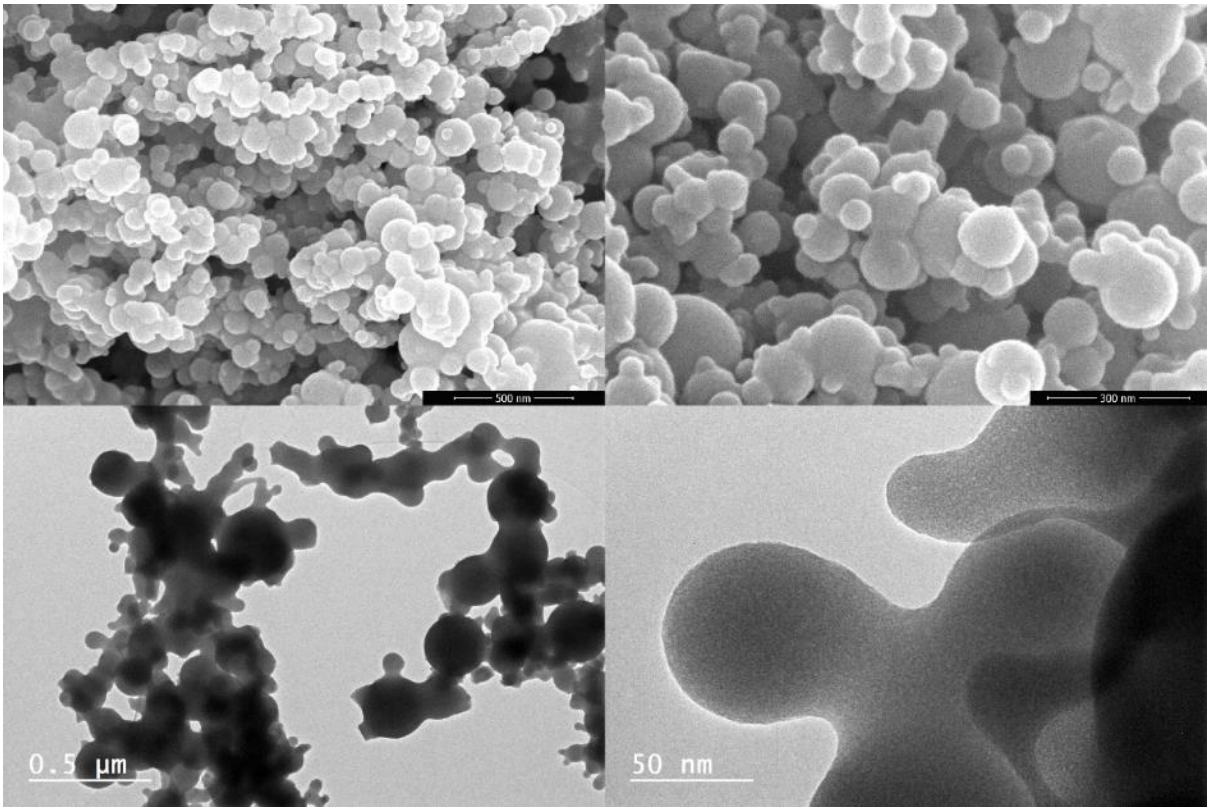

Figure 67. *SEM (above) and TEM (below) images of raw BiTi 2:1 powder.*

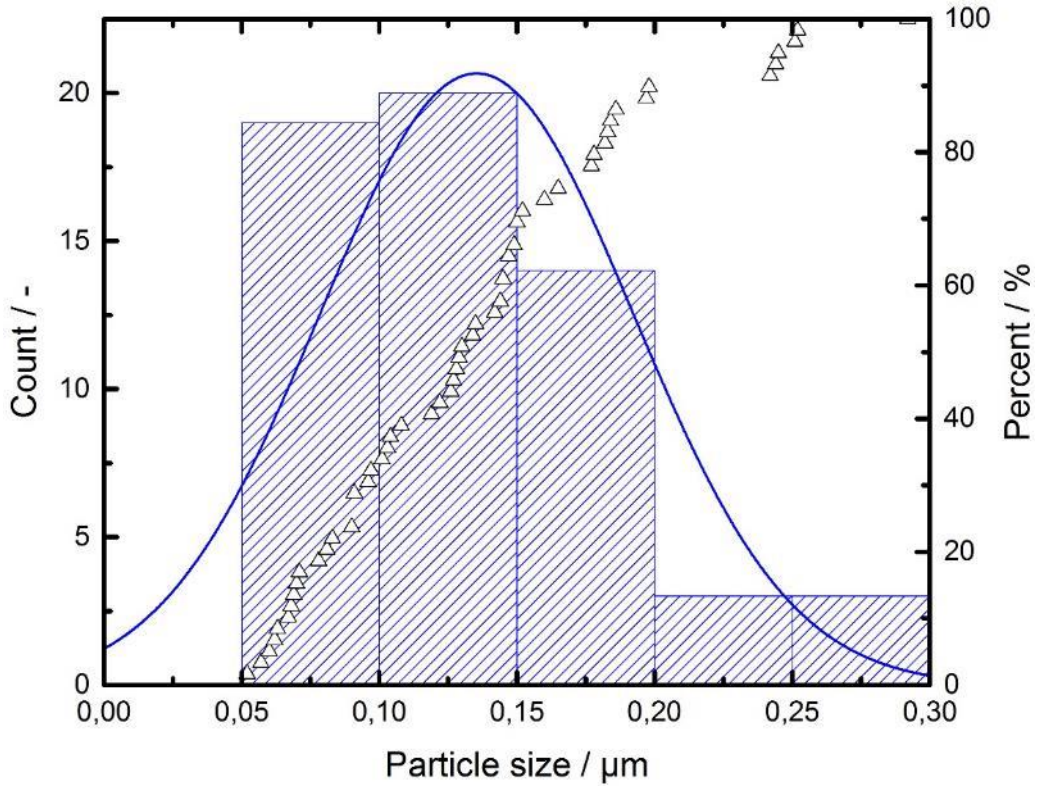

Figure 68. *Histogram and cumulative particle size distribution for raw BiTi 2:1.*

The particles can mainly be found in the range between 50 nm and 200 nm. In this case 80% of the particles are smaller than 180 nm (**Figure**).

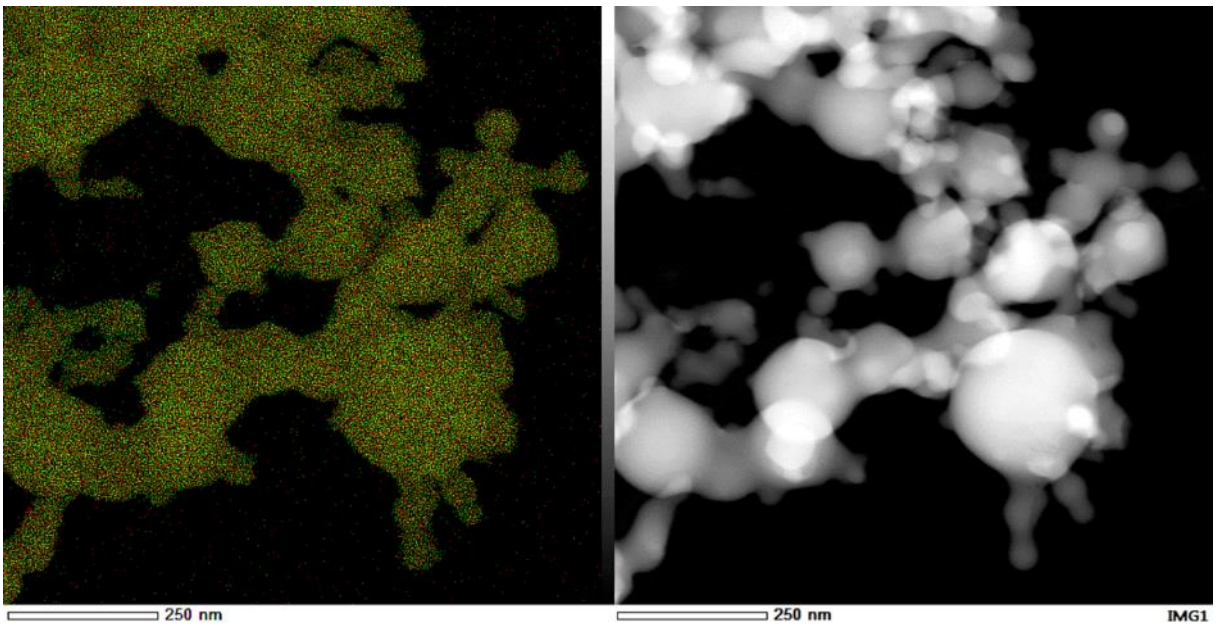

Figure 69. *EDX image of particles of BiTi 2:1 (bismuth in green and titanium in red).*

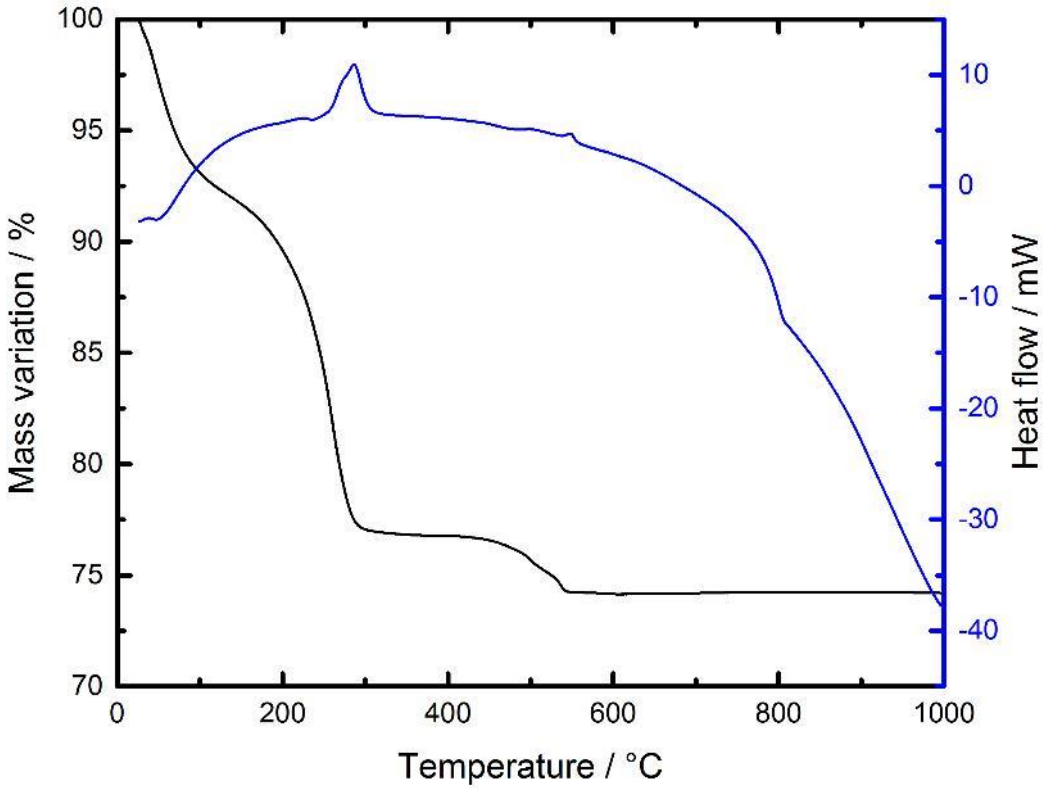

Figure 70. *TG analysis of raw BiTi 2:1 molar ratio.*

The distribution of the metallic elements in the oxides, this are bismuth and titanium, was identified by EDX (**Figure**). Both bismuth and titanium are evenly distributed filling the whole body of each particle of the powder. The metals are embedded in an amorphous oxide network, which is a result of the synthesis method.

The higher proportion of bismuth in this material will influence the thermal behavior of the material making it more similar to the thermal response of pure bismuth oxide. The curve of the thermal response of the material is shown in **Figure** . At low temperatures (< 100°C) the material loses species like water (6.8 wt.%). Afterwards, organic molecules which still remain in the matrix after the reaction are removed, resulting in total weight loss of 23 wt.%. This step, at lower temperatures, is marked by an endothermic peak at around 50°C in the DTA curve which accompanies the weight loss. The weight loss that corresponds to the removal of organic residues is even lower in comparison to BiTi 1:1.35 (~55 wt.%) or BiTi 1:1 (~37 wt.%). This is in accordance with the explanation that the lower the titanium content in the particles, the less important is the organic residue amount in the material and therefore less weight loss is experimented by the material by the thermal treatment. Basing on literature, after the organic subproducts leave the materials, the transformation of bismuth acetate into

bismuthyl hydroxide takes place. This reaction takes place at 285°C, which is highlighted by an exothermic peak in the DTA curve. Finally the formation and crystallization of the mixed phase happens at 550°C accompanied by a weight loss of 2.6 wt.% where the bismuthyl hydroxide transforms into bismuth oxide. This value is in line with the theoretical mass loss of 3.0 wt.%.[212]

5.3.2. Properties of calcined BiTi 2:1

The raw material is thermally treated at 650°C under air for 4 hours. This thermal treatment produces the crystallization of the material. This has as side-effect the sintering of the particles. In **Figure** different images of the powder can be observed. The particles lose their spherical like morphology owing to the calcination. Both bismuth and titanium oxide stack into a perovskite like structure as in the other bismuth and titanium oxide materials prepared.[35] The crystalline structure can be observed. They form particles by the aggregation of several crystallites.

Taking into account the phase diagram of bismuth titanate, the stable phase at this crystallization temperature (650°C) and the Bi/Ti molar percentage (33 mol.%) the stable phase should be $Bi_{12}TiO_{20}$ plus α-Bi_2O_3.[214] Even though it is correct for the bismuth oxide in excess, the bismuth titanate phase formed is $Bi_4Ti_3O_{12}$ ($2Bi_2O_3 \cdot 3TiO_2$) which should appear at 873°C. However the phase stability is size dependent. The structure of this is phase different from the structure of the $Bi_2Ti_2O_7$ phase. This composite is formed of a bismuth oxide (α-Bi_2O_2) layer alternated with a perovskite like $Bi_2Ti_3O_{10}$ layer.[218] The bismuth oxide in excess led to the formation and segregation of

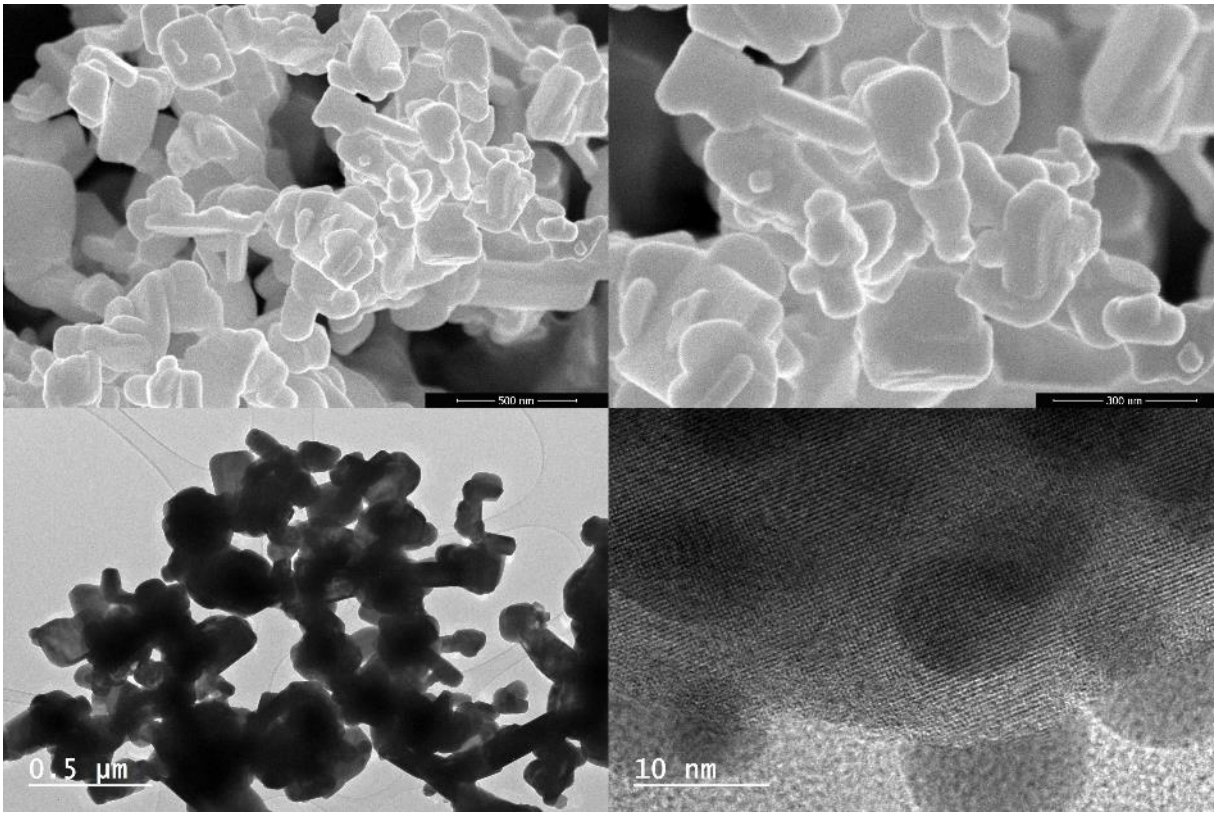

Figure 71. *SEM (above) and TEM (below) images of calcined BiTi 2:1 powder.*

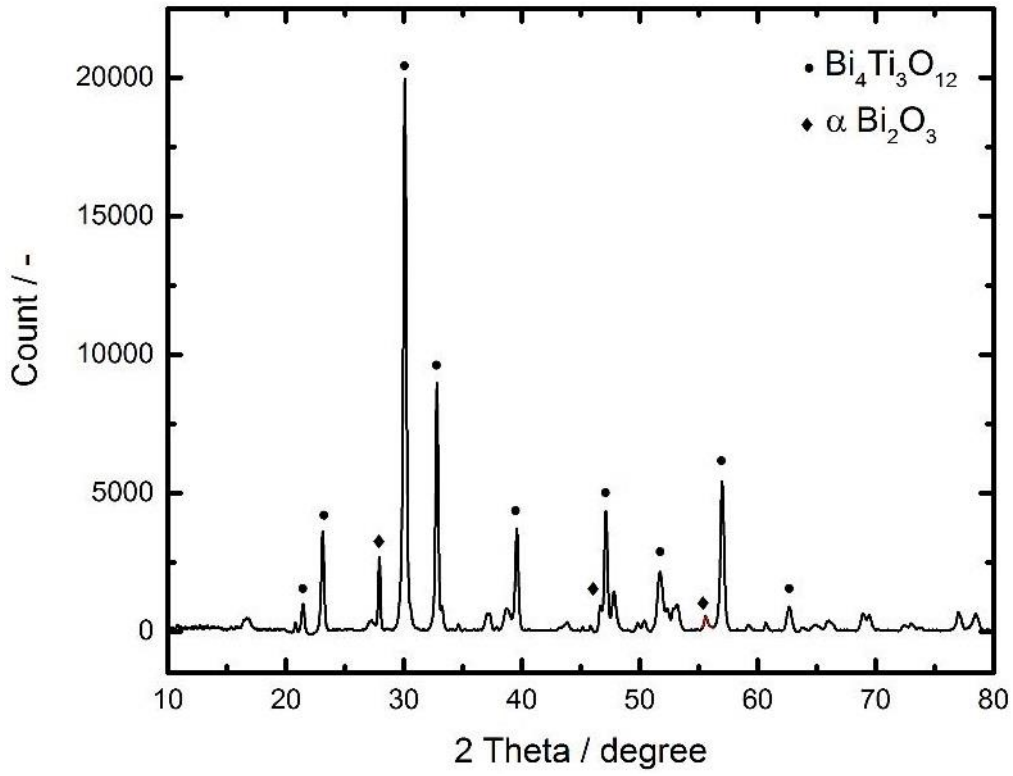

Figure 72. *XRD pattern of BiTi 2:1 sample calcined at 650°C under air.*

monoclinic alfa phase as can be seen in the XRD pattern in **Figure** . The crystallite size of the bismuth titanate is 28.9 ± 3.3 nm. The crystallite size of the bismuth oxide

in excess is 34.1 ± 9.3 nm. Both values are in accordance to those for other polycrystalline structure obtained by the SFS process.

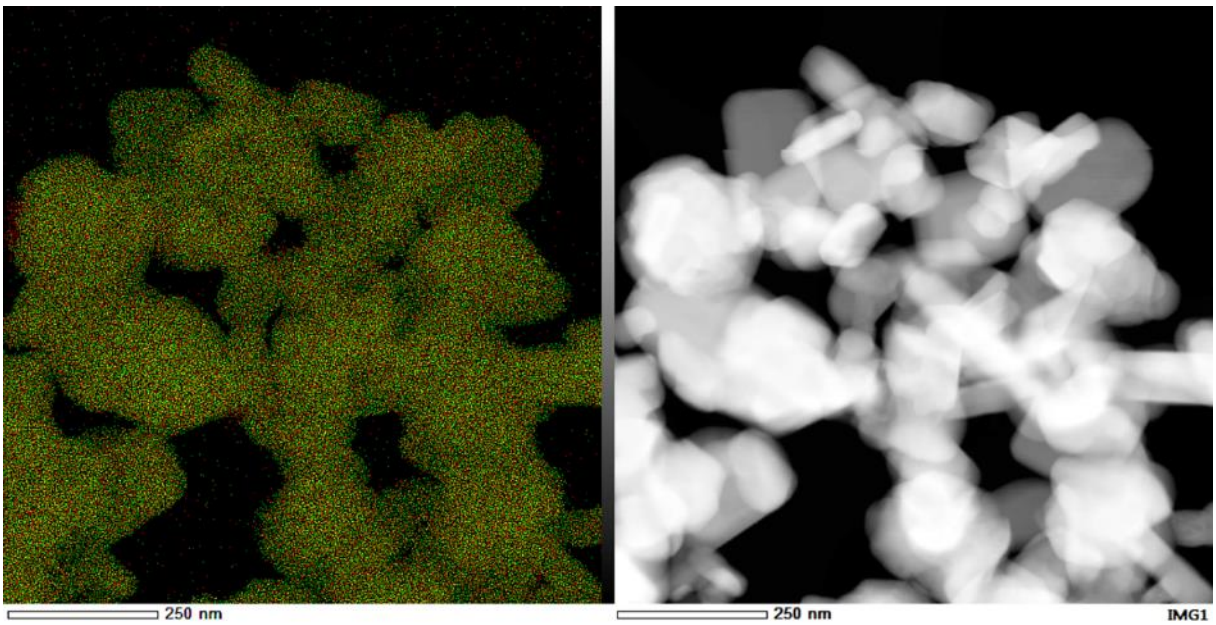

Figure 73. *EDX image of particles of BiTi 2:1 (bismuth in green and titanium in red).*

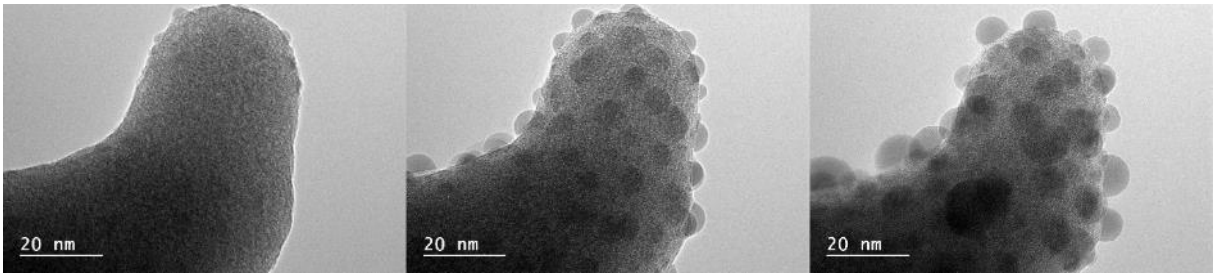

Figure 74. *TEM images of uncalcined BiTi 2:1 highlighting the decomposition of bismuth oxide under the electron beam after a few seconds.*

Figure shows the elemental distribution of bismuth and titanium in the particles after calcination. Both titanium oxide and bismuth oxide are mixed at molecular scale and keep this mixture grade even after calcination. It can also be observed that the excess of bismuth, in the form of bismuth oxide, did not form separated areas of pure bismuth oxide. This means in this case, no segregation took place during the formation of the crystal structure. The particles of bismuth oxide are distributed evenly along the particles made of bismuth titanate.

This could be confirmed by a phenomenon of decomposition that took place during the TEM imaging in **Figure** . The “exudation” of Bi_2O_3 produces a shrinkage of the particles (10% of the size). The decomposition of bismuth oxide into pure bismuth and oxygen

was verified by the EDX images in **Figure** . In the outer radius of the particles spherical bodies can be identified but only in the case of bismuth. In those bodies neither titanium nor oxygen is present. The easiness of the reduction of bismuth oxide nanoparticles is size dependent, this means the smaller the size, the easier it is to form metallic bismuth.[219 220] The samples that are irradiated by the electron beam of the TEM device do heat up. However, this heating, which is a consequence of energy

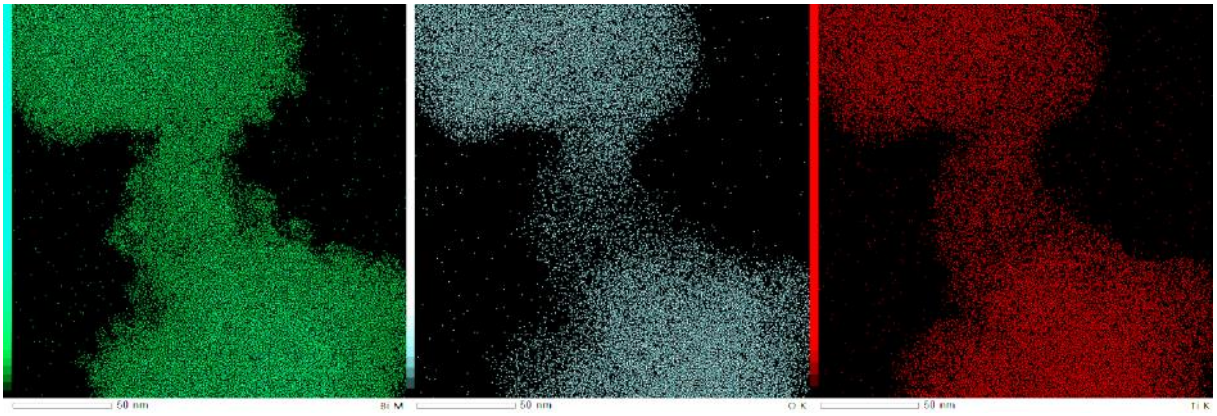

Figure 75. *EDX of BiTi 2:1 particles after irradiation (bismuth in green, Oxygen in blue and titanium in red).*

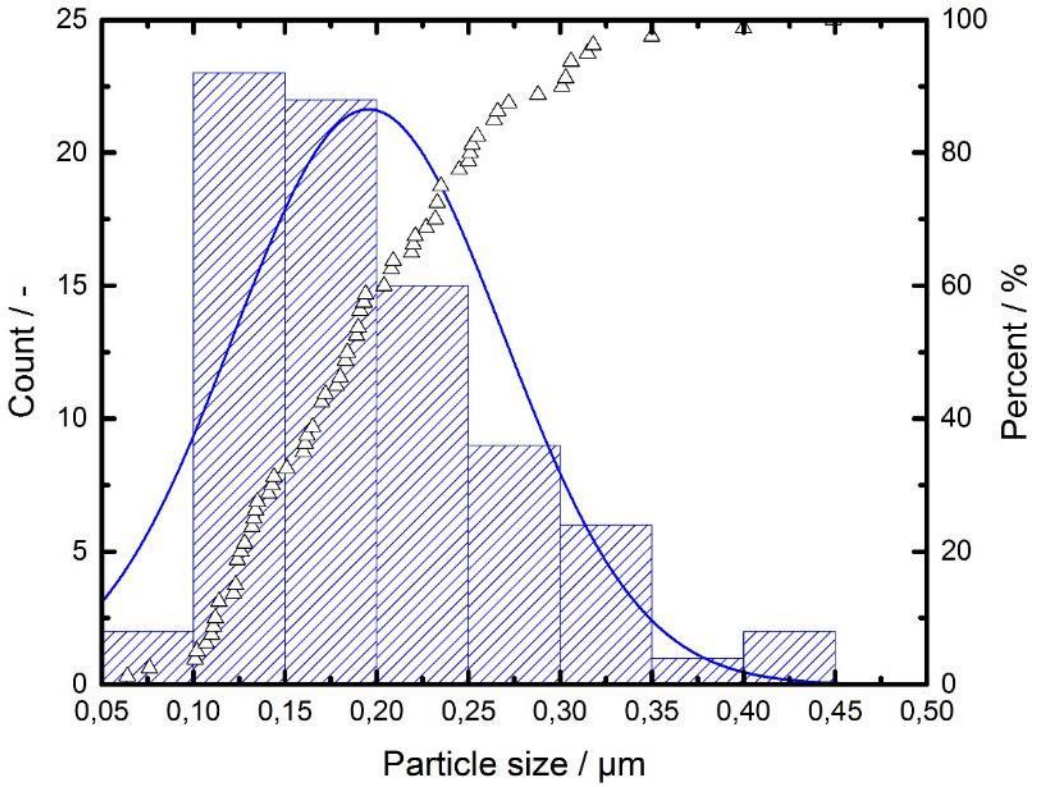

Figure 76. *Histogram and cumulative particle size distribution for calcined BiTi 2:1.*

transferred from the electrons to the material as the pass through, is usually dissipated leading to a maximum increase of 6K in the center of the irradiated zone. Small

particles have less contact between each other and to the substrate, this leads to a lower thermal conductivity and allows the superheating of the particles. These phenomena along with the presence of the electrons, which facilitates reduction reactions could explain the decomposition in bismuth of the fine bismuth oxide particles that are present in the bismuth titanate. Additionally, the vacuum helps the decomposition of the nanometric bismuth oxide as it favors the oxygen release.

The particles of BiTi 2:1 are result of the fusion of smaller particles and the reorganization of the structure of the raw material. The irregular shape of the particles of the uncalcined material is accentuated by the calcination. The sintering of the smaller particles into the bigger particles produces an increase of the average particle size compared to the one of the raw material. The particle size distribution of the calcined material can be seen in **Figure** . The average particle size is 195.6 ± 73.8 nm. The cumulative percentage of the particles has a steep slope which indicates that most of the particles have a size between 100 and 250 nm. This wider distribution and bigger particles size comes from the loss of a regular morphology.

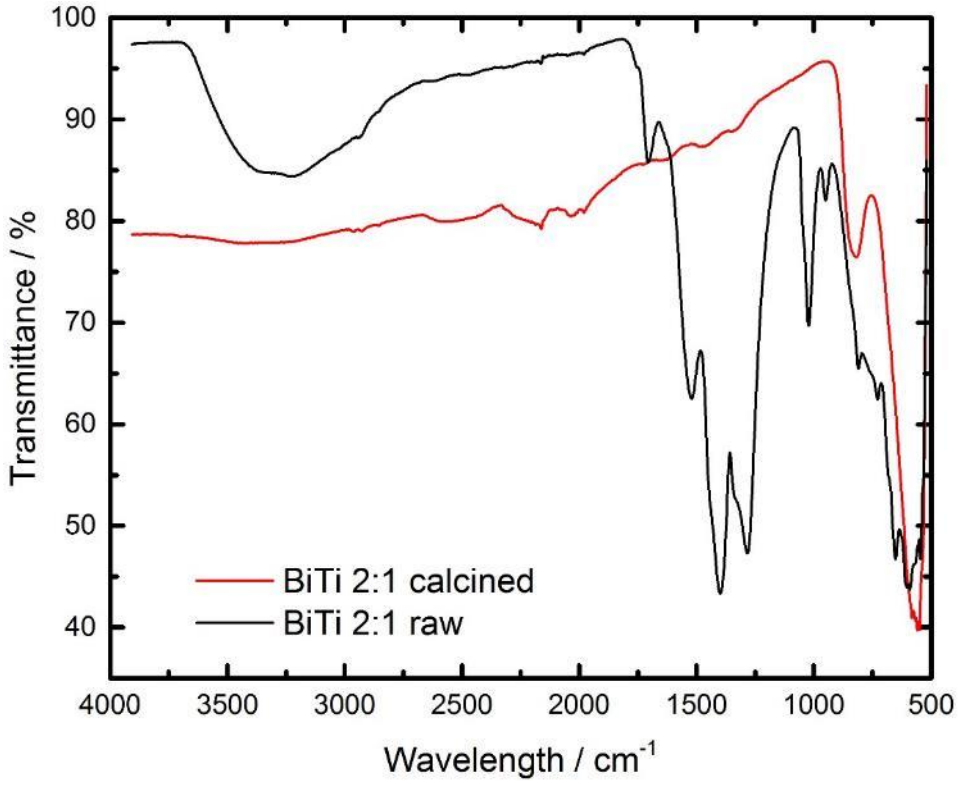

Figure 77. *FTIR spectra of raw and calcined bismuth titanate prepared by SFS.*

Figure shows the FTIR spectra of the 2:1 molar ratio mixed bismuth titanate for both the raw and the thermally treated samples. The raw BiTi 2:1 spectrum shows a wide

peak at ~3200 cm^{-1}, which is associated to O-H stretching vibrations from different functional groups. This signal corresponds to the intermolecular hydrogen bonded O-H group (3550-3230 cm^{-1}) that forms the amorphous titanium network and other functional groups like OH (3600-3100 cm^{-1}) which are still part of the material.[208] Additionally, the CH_3 stretching vibrations of bismuth titanate are found in this area. The peak at 1520 cm^{-1} is associated to the CO group of bismuth acetate. The peak at 1045 cm^{-1} can be associated to the CH_3 rocking vibrations and the C-O stretching, the 649 cm^{-1} peak can be associated to the O-C-O in plane bending and the peak at 534 cm^{-1} could be associated to the C=O out of plane bending of bismuth acetate.[215] The spectra of the calcined sample does not present any peak which could be attributed to organic species or water. The differences between the spectra illustrates that the organic species present in the material synthesized are totally removed after the thermal treatment.

6. Materials based on the mixture of titanium and copper

6.1. Properties of raw copper/titanium precursor mixture

The raw copper-titanium mixed oxide powder prepared by SFS is made of submicron spherical particles as can be seen in **Figure 78**. This powder has a fine and loose structure where the particles are aggregated together. The particles are fully filled with material, however compared to cases explained before, the inner structure is not totally homogeneous. In this case, the copper precursor has not totally reacted leaving small crystals of rouaite ($Cu_2(NO_3)(OH)_3$) and ammonium nitrate ($(NH_4)(NO_3)$) embedded into an amorphous titanium oxide matrix. These are the intermediate species that are formed at these temperatures as in the case of the production of pure copper oxide. These were identified by XRD as can be seen in the pattern in **Figure 79**. The average crystallite size of rouaite in these particles is 27.2 ± 2.6 nm while the average crystallite size of ammonium nitrate is 33.9 ± 11.5 nm. They form as a result of the partial thermal decomposition and the reaction between copper nitrate, the copper containing precursor, and ammonia, the partner reactant. The average particle size of

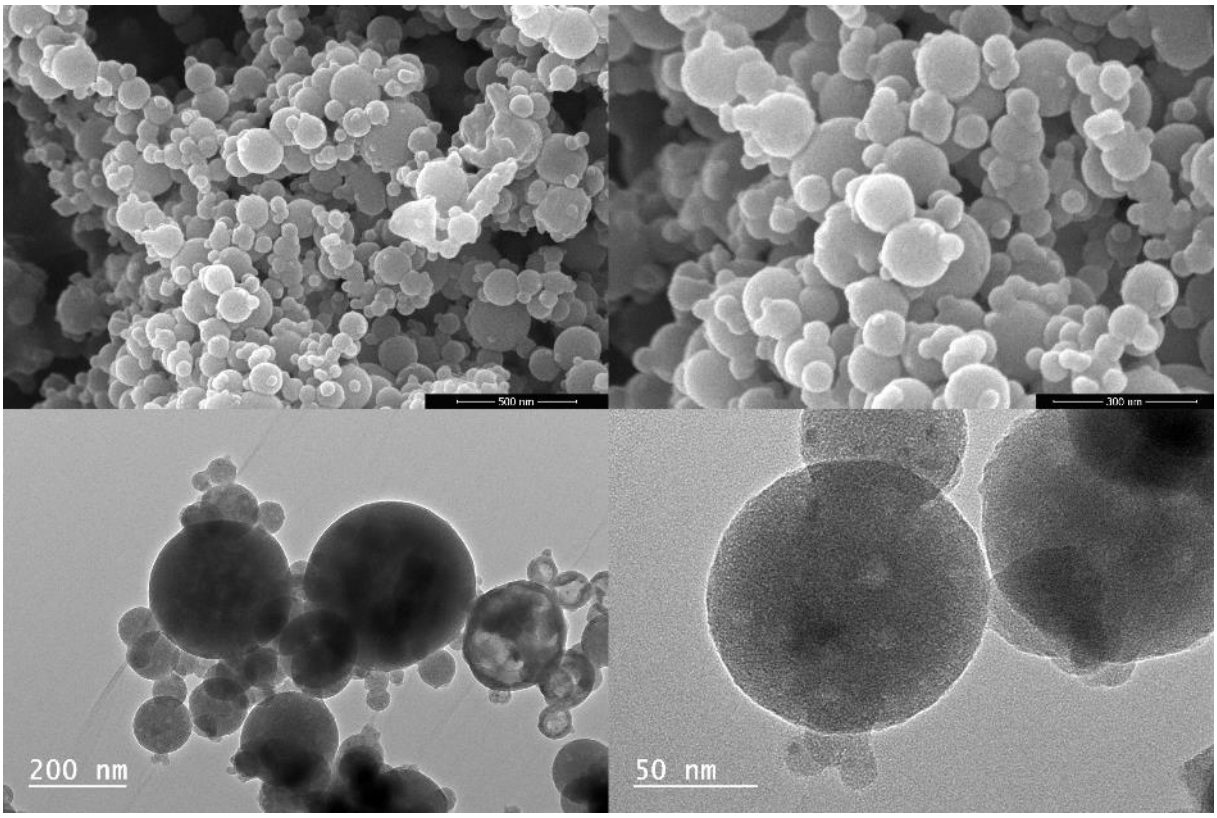

Figure 8. *SEM images of raw copper/titanium precursor mixture.*

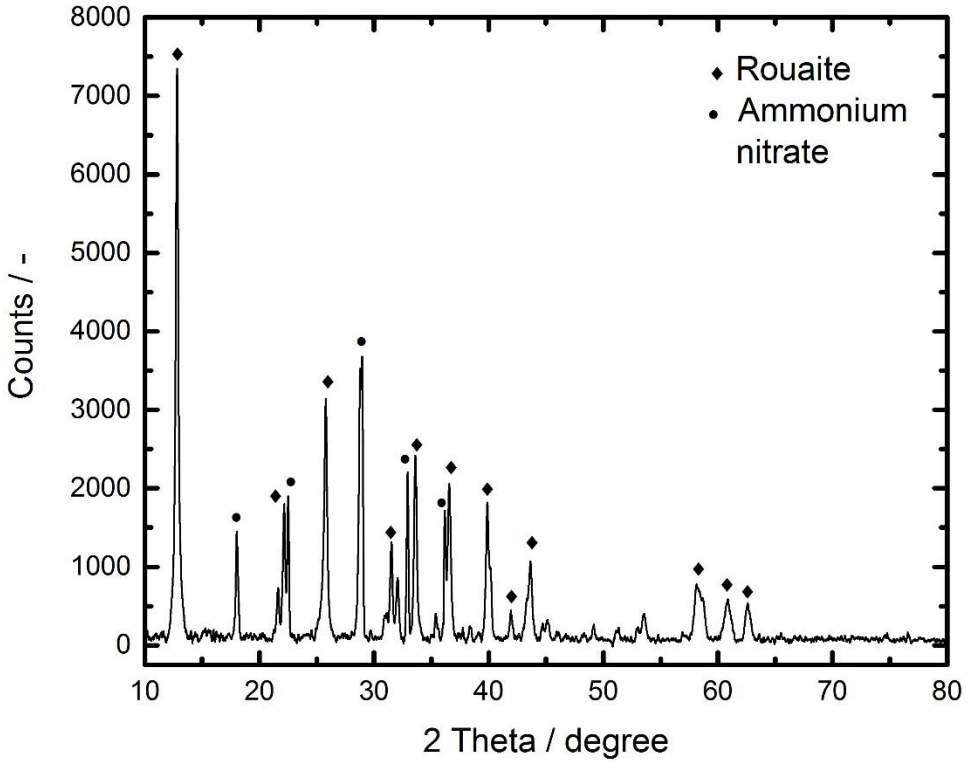

Figure 9. *XRD pattern of raw copper/titanium precursor mixture.*

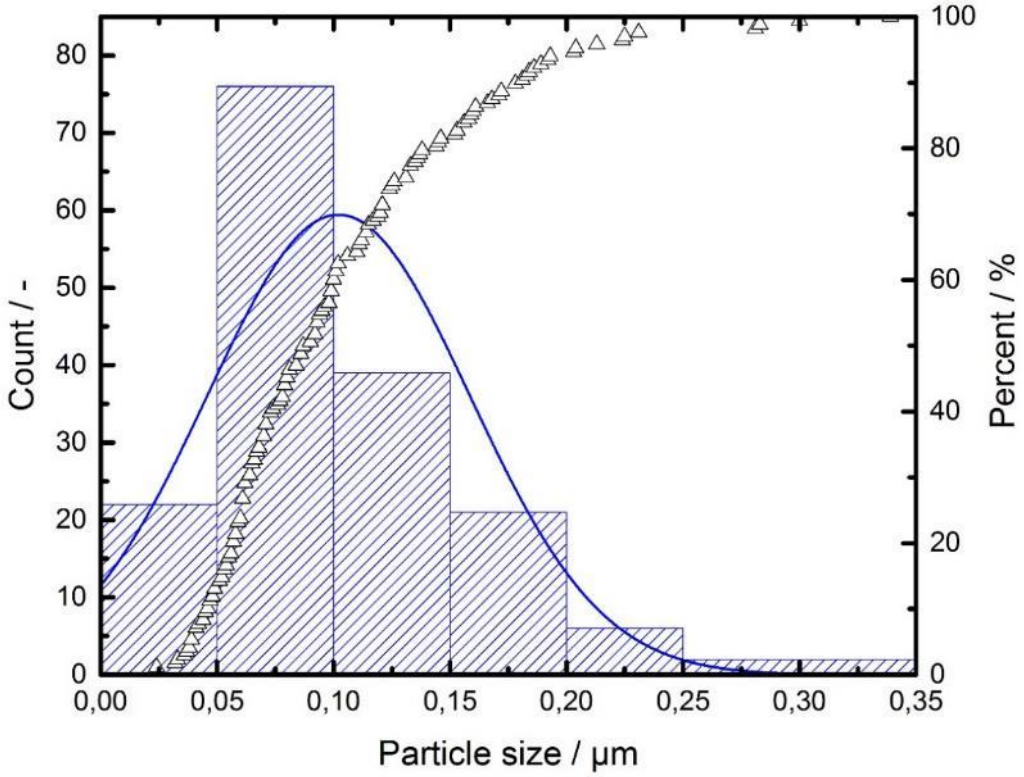

Figure 80. *Histogram and cumulative particle size distribution for copper/titanium precursor mixture.*

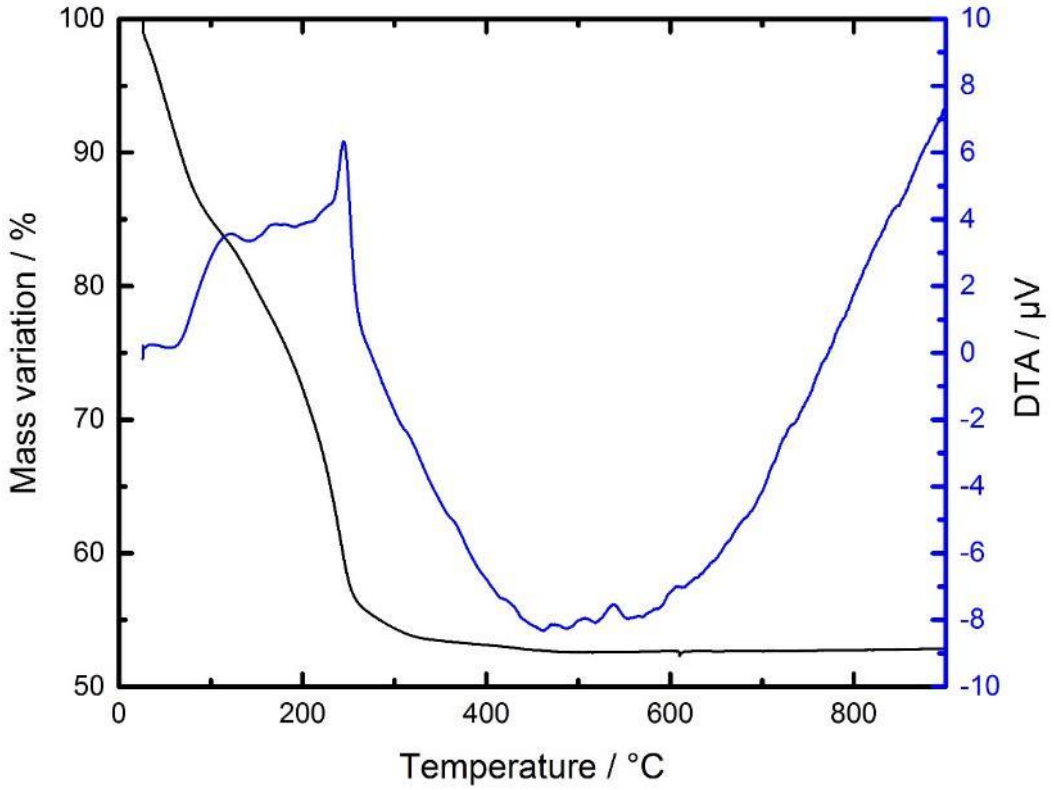

Figure 81. *Thermogravimetric analysis of raw copper/titanium precursor mixture.*

this material is 102.1 ± 56.4 nm. The majority of the particles (~80 %) can be found under 150 nm as can be seen in **Figure** . The average particle size is in the same range than the other materials prepared by SFS. The size distribution however is closer to the one for the bismuth titanate materials than those of pure materials.

Figure shows the TGA curve of the untreated powder. The powder presents a weight loss of 15% which corresponds to the loss of water and organic molecules coming from the reaction medium. This is followed by the thermal decomposition of ammonium nitrate ($(NH_4)(NO_3)$). An endothermic peak at 140°C can be identified, which corresponds to a phase change of ammonium nitrate.[221] At around 210°C, which presents a slight exothermic peak, water and nitrous oxide are the resulting products of the decomposition.[221] This high decomposition temperature can be explained by the intimate mixture of copper and ammonium nitrate in the particles. The material of the particles shows a certain similarity to copper phase-stabilized ammonium nitrate (Cu-PSAN) which is more stable than the pure ammonium nitrate.[221] Then the decomposition of copper hydroxide nitrate at 245°C corresponds to the stronger exothermic peak.[222] Here an amorphous network of copper oxide and titanium oxide is formed. At 300°C the weight loss stabilizes and reaches a plateau indicating that the

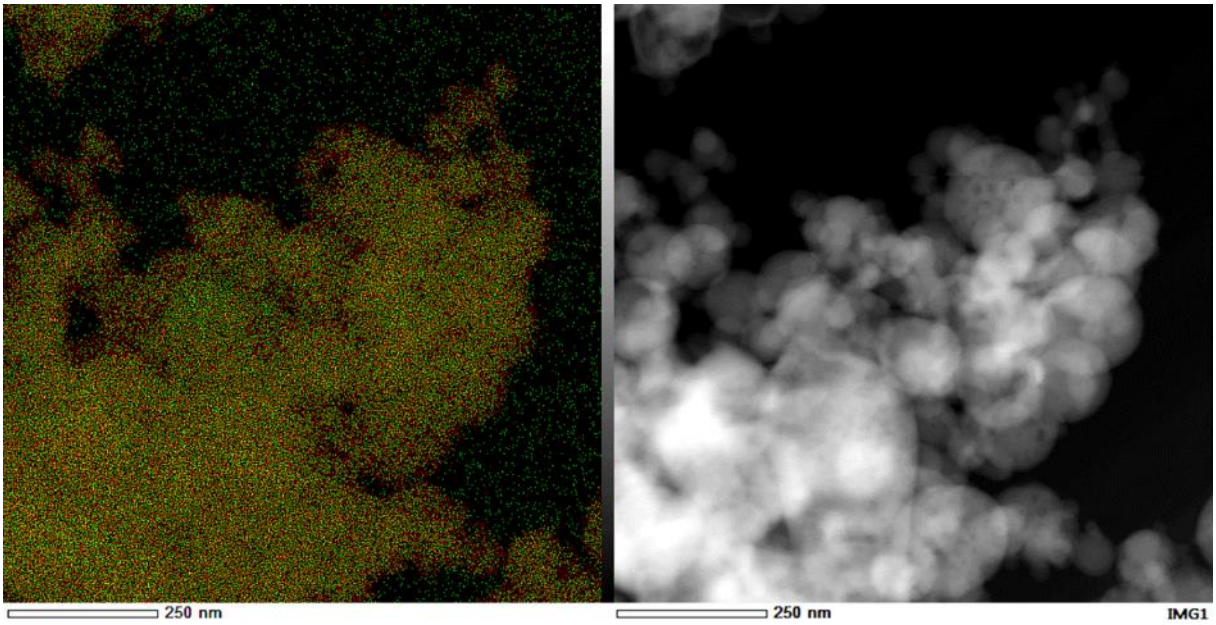

Figure 82. *EDX image of particles of copper/titanium precursor mixture (copper in green and titanium in red).*

material is thermally stable. The amorphous material will reorganize and form separated crystal phases at 540°C which can identified as the exothermic peak without mass variation.

All the particles present both elements, titanium and copper, distributed at molecular scale as can be seen in **Figure** . Nevertheless, some regions present a higher concentration of copper than others. This is owing to the incomplete reaction of the precursor. As the precursor is not totally decomposed, it forms crystallites where the copper concentration is higher. Thus, in these regions the copper does not mix because it part of the crystal structure of the precursor.

6.2. Properties of CuO/TiO_2 mixture calcined at 400°C

After calcining the particles at 400°C they maintain a spherical morphology, but slightly fuse together as highlights **Figure** . The calcined powder has a fine and loose texture with a change in color from clear blue to brownish-yellow as shown in **Figure** . The formation of a crystal structure changes the light absorption range and therefore changes the color when compared to the material obtained at 600°C.

The particles calcined at this temperature are still amorphous. At this temperature the crystallization and the reorganization of the matter did not take place. This is why the particles are highly porous. This porosity is originated by the exit of the organic molecules that remained trapped into the metal containing phases. The exit of the organic remainings and the adsorbed water happened before the network consolidated at higher temperatures. This led to a high surface area value of 125.3 $m^2 g^{-1}$.

As the elements did not change their relative positions, the degree of mixture of these maintained during the calcination. The homogeneous mixture of both copper and

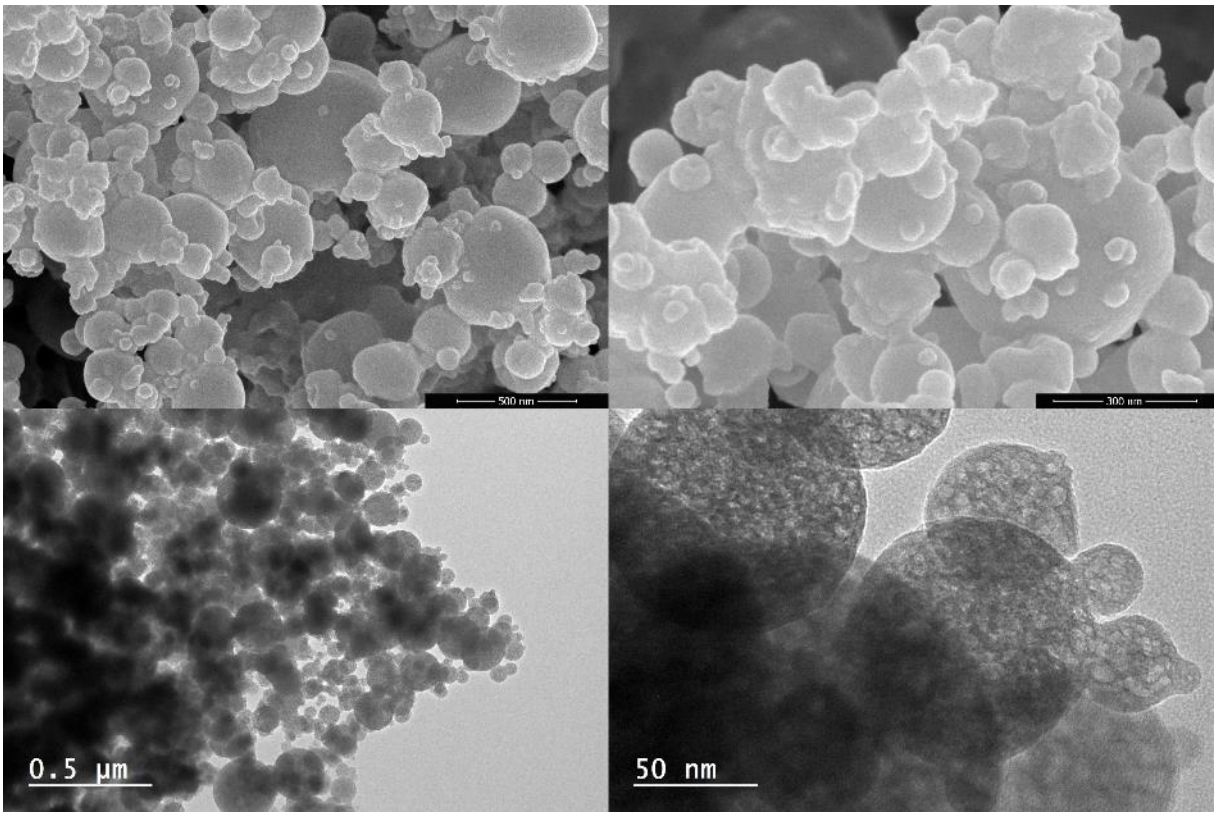

Figure 83. *SEM images of particles of copper/titanium oxide mixture calcined at 400°C.*

Figure 84. *Photography of copper/titanium oxide mixture calcined at (A) 400°C and (B) 600°C.*

titanium can be seen in **Figure** .

The average size of particles after calcination is 114.8 ± 61.5 nm which is slightly higher than the value for the raw material but in the usual range for materials prepared by SFS. The vast majority of the particles are smaller than 163 nm, as 80% of the cumulative counting of the particles are below this value. The particles can mainly

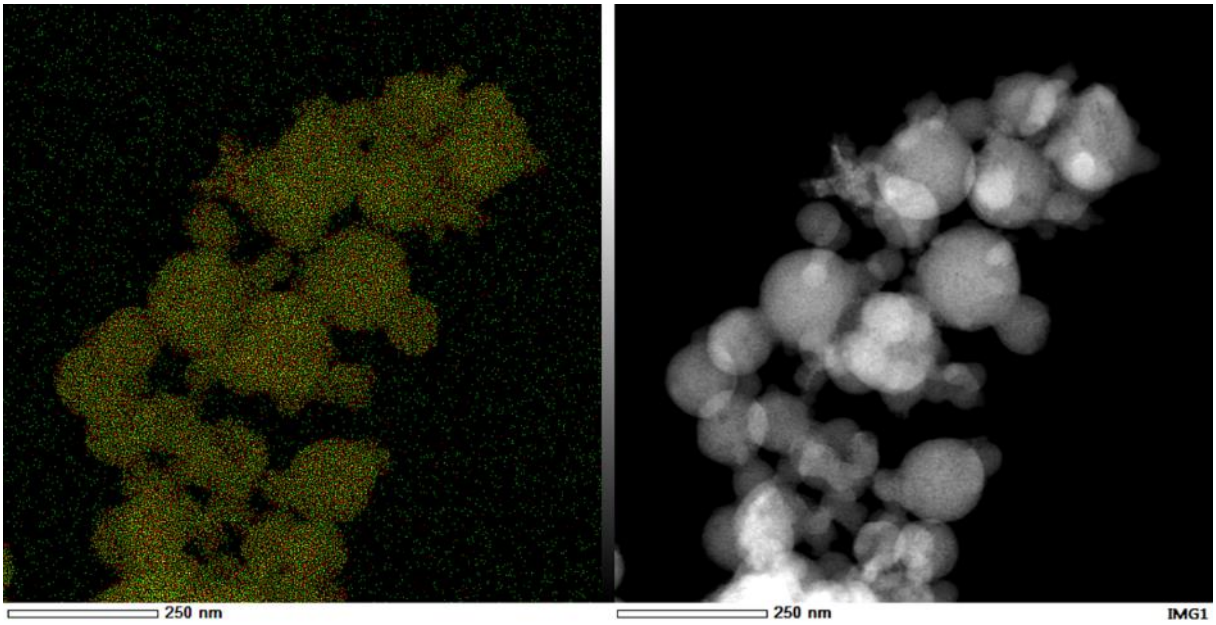

Figure 85. *EDX image of particles of copper/titanium oxide mixture (copper in green and titanium in red).*

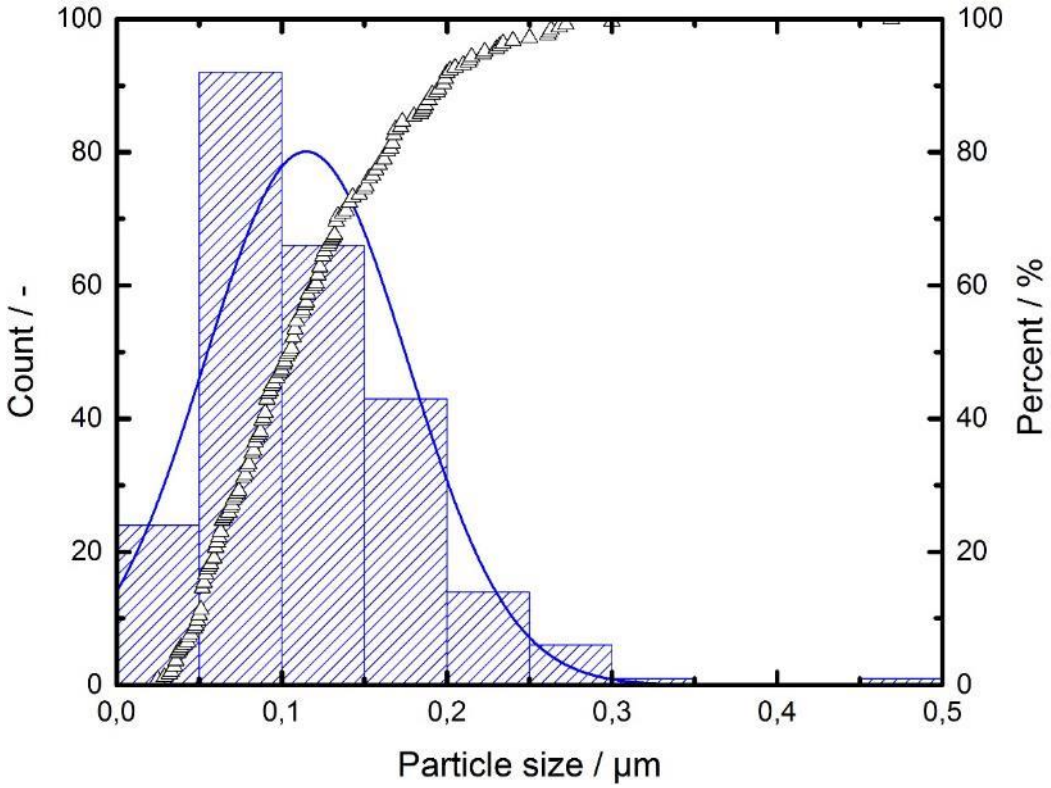

Figure 86. *Histogram and cumulative particle size distribution for copper/titanium oxide mixture calcined at 400°C.*

be found between 50 and 200 nm as shown in **Figure** .

The density of this mixture was measured by helium pycnometry. The measured density of this composite is 4.2 ± 0.1 g cm^{-3}. This value is lower than the theoretical value calculated, which is 4.8 g cm^{-3}. This value was obtained by taking into account a 1:1 ratio of titanium oxide (anatase) and copper oxide and by dividing their molar masses (80 g mol^{-1} for TiO_2 and 79.5 g mol^{-1} for CuO) by the volume occupied by the oxides by mol (20.25 cm^3 mol^{-1} for TiO_2 and 12.60 cm^3 mol^{-1}). This lower density value can be explained by internal porosity originated during the calcination by voids left in the material matrix from the organic remainings. The porosity of this material 12.5%.

Taking into account the SSA of this material and the density measured by the pycnometry, the surface porosity of this material was calculated to be 6.2%. Thus, the inner porosity can be calculated as the difference of the total porosity of the material minus porosity of the material surface. The inner porosity of the material is 6.3% which represents approximately half of the porosity of the material.

6.3. Properties of CuO/TiO_2 mixture calcined at 600°C

The powder produces at 600°C has a fine and loose appearance with a red-brownish colour as can be seen in **Figure** . The particles of this powder maintain a spherical appearance but specially the smaller particles lost their identity and are fused together. This is the consequence of the restructuration of the titanium oxide and copper oxide present which ultimately led to the crystallization with the segregation of the different phases. The dimensions of the crystallites and the inner structure of the particles of copper/titanium oxide mixture are shown in **Figure** . As can be seen, the porous inner and outer structure is totally lost in comparison to the material calcined at 400°C. This is a result of the calcination at higher temperature which led to the crystallization and reorganization of the material and therefore the loss of any existing structure beforehand.

The crystallization of the matter led to a polycrystalline structure of titanium oxide in two different phases, anatase and rutile, and copper (II) oxide. The presence of both anatase and rutile in this material can be explained by the anatase to rutile transition (ART) as seen before. In this case the transition from one phase to the other is also

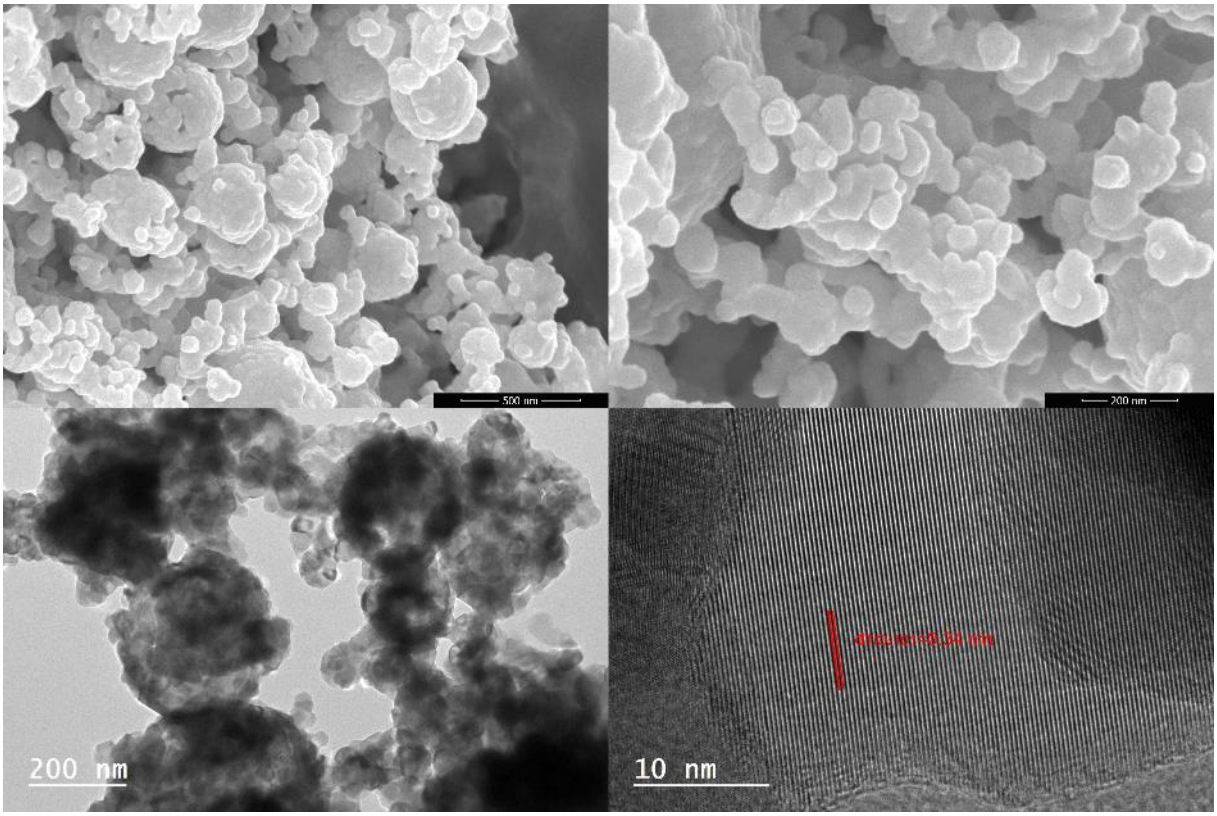

Figure 87. *SEM (above) and TEM (below) images of particles of copper/titanium oxide mixture calcined at 600°C.*

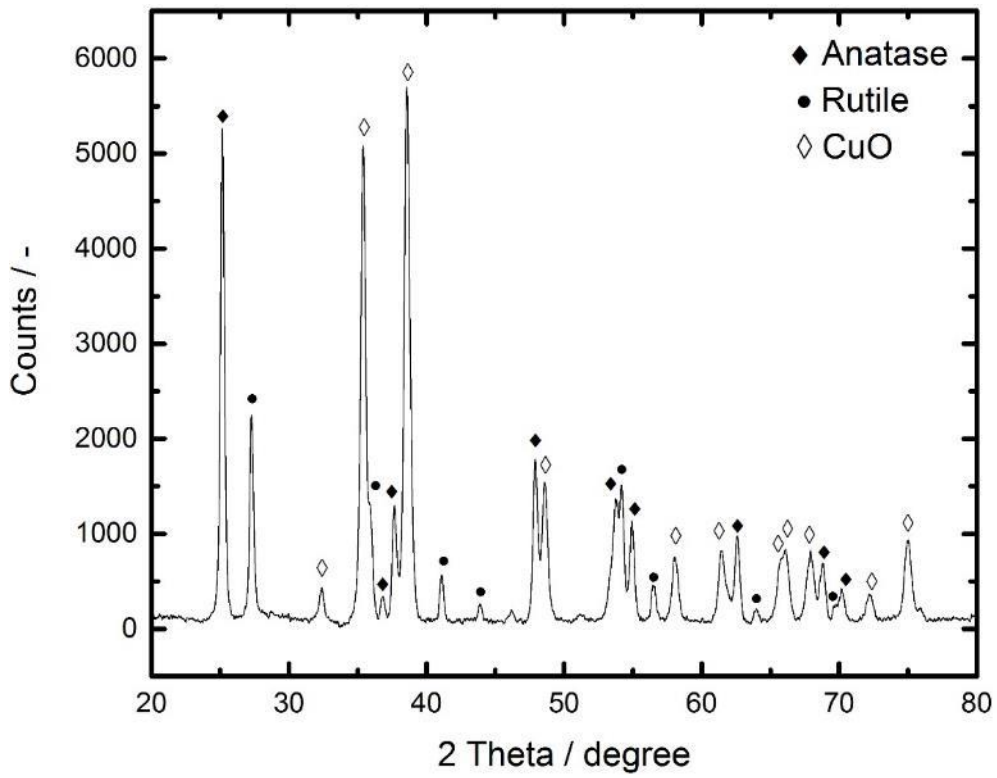

Figure 10. *XRD pattern of copper/titanium oxide mixture calcined at 600°C.*

influenced by the presence of "relative impurities" as in the case of bismuth titanate. Additionally, the anatase phase present did not form a new crystal structure with the copper oxide and therefore did not impede the transformation into rutile. The transition ratio has been calculated using Spurr and Myers method specifically modified for titanium oxide, which bases the calculi on the areas under the peak ratio of the rutile (110) peak and the anatase (101) peak. The empirically determined formula is as follows:[223 224]

$$f = \frac{1}{1 + 0.884 \frac{A_A}{A_R}} \tag{49}$$

Where f is the anatase to rutile weight ratio, A_R is the area under the curve for rutile and A_A is the area under the curve for anatase. Using **Eq. ()** the value for the ratio is 30.1% of anatase that transformed into rutile. The average crystallite size of the three phases was calculated using Scherrer's equation basing on the XRD pattern. The average crystallite size is 20.6 ± 2.6 nm for anatase, 24.1 ± 1.5 nm for rutile and 17.9 ± 1.6 nm for copper oxide. The average crystallite size of rutile is bigger than the average crystallite size of anatase because the average critical size for crystallites of rutile is bigger than the average critical size of the primary particles of the anatase

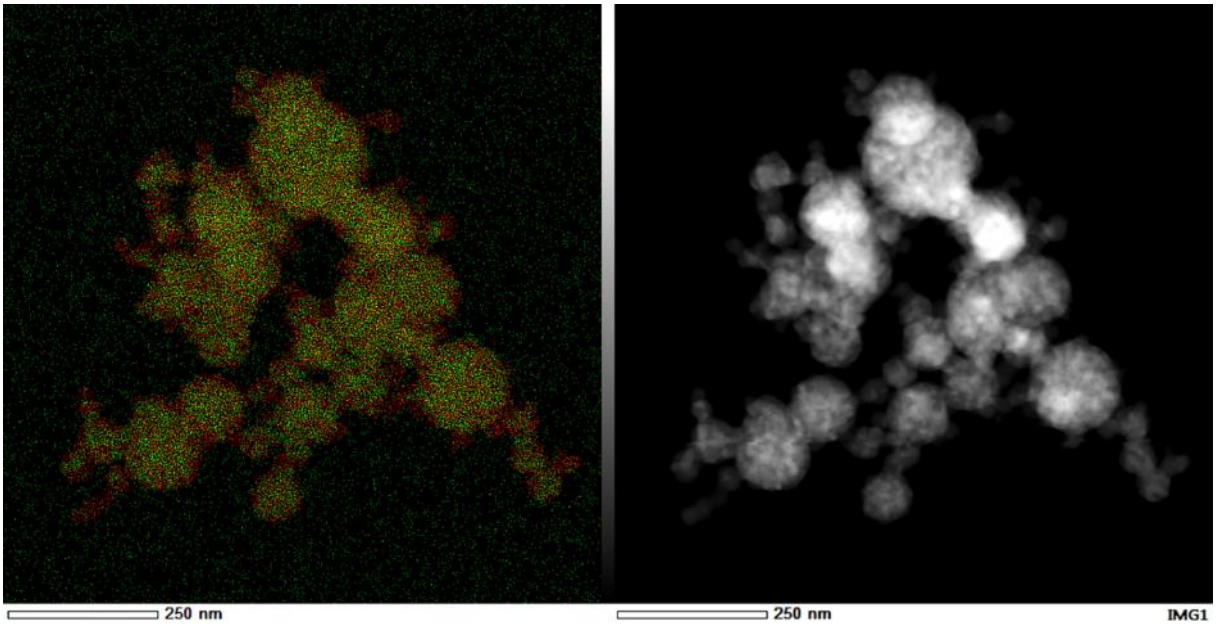

Figure 11. *EDX image of particles of copper/titanium oxide mixture (copper in green and titanium in red).*

polymorph.[225]

EDX images in **Figure 89** show the distribution in the particles of both elements, copper and titanium. It can be seen that the degree of intimate mixture between the oxides is maintained in most of the extension of the particles, mainly in the inner part of the bigger particles. However, the smaller particles and the outer shell of the particles is primary made of titanium oxide. As seen before, the amorphous material calcined at 400°C shows a perfectly homogeneous mixture, this means that the segregation and concentration of the copper oxide in the inner part of the particles is produced during the calcination. As the copper oxide was found all along the particles, the relative contraction of the elements to form the crystal structure left the titanium oxide in the outer part.

The average particle size of this nanomaterial is 217.1 ± 71.1 nm, which is the double in comparison to the raw particles. The particles have mainly sizes ranging between 100 and 300 nm as can be seen in **Figure** . There seem to exist two populations of particles, one around 175 nm and one around 275 nm. The introduction of CuO into the TiO_2 system leads to grain boundary complexions. These affect strongly the grain boundary properties of titanium oxide. The sintering and densification temperature of the material is lowered by several hundred degrees.[226] Therefore, when the crystallization takes place during the thermal treatment, the nanocrystals of copper

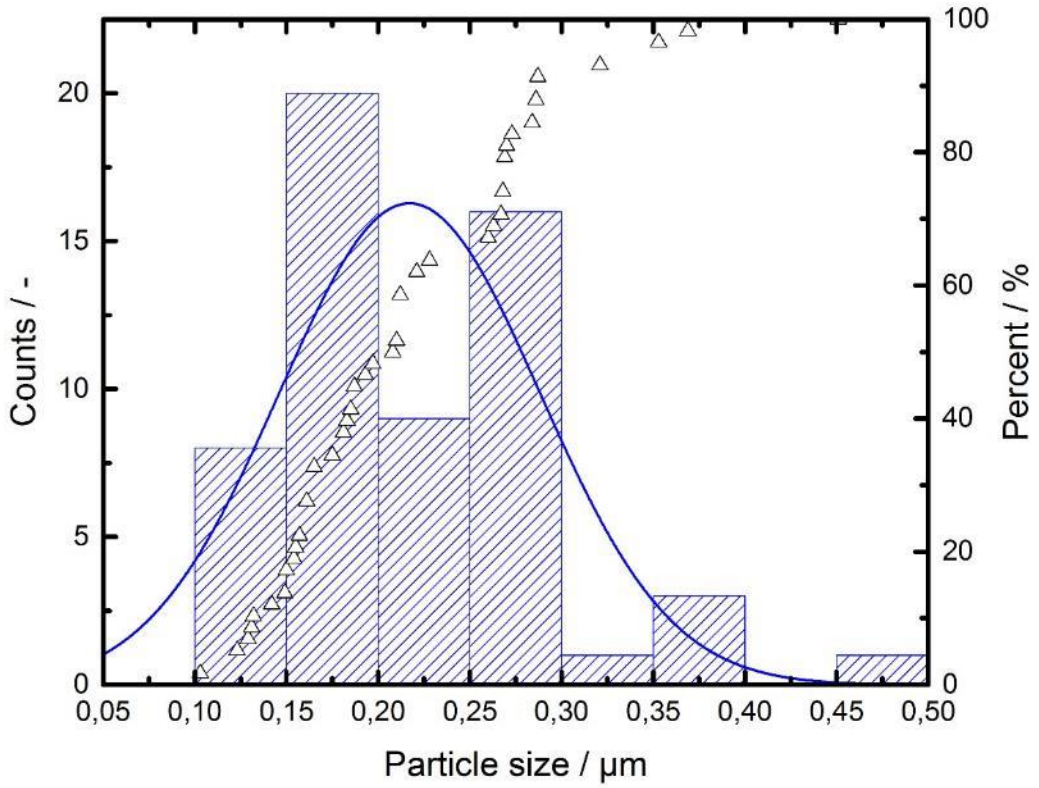

Figure 90. *Histogram and cumulative particle size distribution for copper/titanium oxide mixture calcined at 600°C.*

oxide form very small copper oxide domains. The small size of these particles has a strong influence on the melting temperature.[227] Both effects lead to a diffusion of copper oxide by capillarity trough the titanium oxide matrix, which is thermally speaking more stable. The liquid copper oxide then coalesces into bigger domains and solidifies when a critical mass is reached, ultimately leading to a segregation of the phases.

The FTIR analysis curve of the raw and calcined materials can be seen in **Figure** . A strong signal at ~3200 cm^{-1} of the raw material corresponds to the hydroxide of the copper nitrate hydroxide, this signal loses significantly in intensity in the case of the 400°C calcined material and is totally lost for the 600°C calcined material. This is owing to the high surface area of the former calcined one, there adsorbed species like water are trapped which is not the case for the latter low surface area material. Both calcined materials show no important peaks which indicates that all the organic material was successfully removed by the thermal treatment.

The density of this mixture was measured by helium pycnometry. The measured density of this composite is 4.9 ± 0.2 g cm^{-3}. This value is slightly higher than the

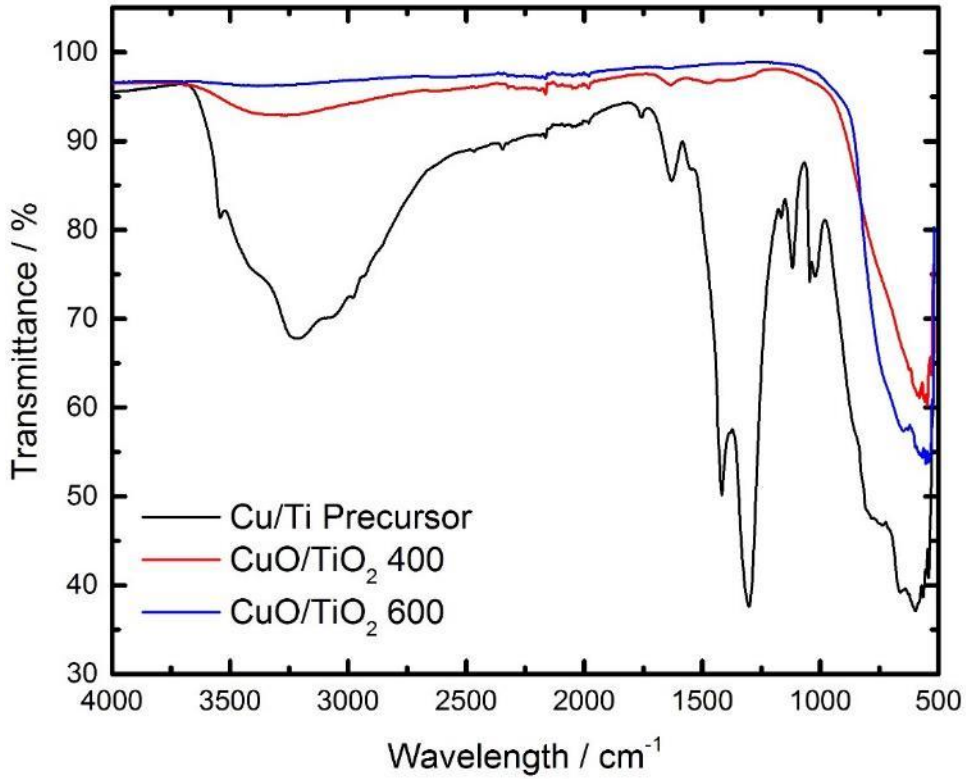

Figure 91. *FTIR spectra of raw copper/titanium precursor and calcined copper/titanium oxide mixture.*

theoretical value calculated by taking into account a 1:1 ratio of titanium oxide (anatase and rutile) and copper oxide which is 4.88 g cm^{-3}. However, taking into account the variation of the measurement it reaches the theoretical value and therefore it can be

Figure 92. *Comparison of the apparent densities of the pure copper oxide/titanium oxide mixtures at macroscale (CT600 left and CT400 right).*

said that the particles are fully dense and in agreement with other measurements. The appeareance and apparent density of the pure oxides can be seen in **Figure** .

7. Conclusions and perspectives

The synthesis temperature of the SFS process is defined by the temperature of the nozzle. The temperature used for the syntheses is found between 155-160 °C. The particles resulting from these synthesis conditions are generally in the range of submicron sized and adopt the morphology of the droplet. The physical and chemical properties of the solution (pH, solute concentration, surface tension, nature of the precursor and solvent) has a strong influence in the final particle morphology and size.

The process temperature is enough to partially decompose the precursors (TTIP, $AgNO_3$, $Bi(NO_3)_3$ and $Cu(NO_3)_2$) used for the synthesis. The materials produced are mixed with organic species, which result as byproducts of the reaction as well as the solvent, and chemical water. Furthermore, this temperature is not enough to transform the compounds directly into oxides. Therefore, the materials produced form an amorphous matrix.

Therefore, a thermal post-process treatment is necessary to anneal the particles. This removes the byproducts and induces the crystallization of the oxides. However, it also leads to the sintering of the particles. This restructuration of the mater lowers the specific surface area of the particles.

The research performed showed that it is possible to produce submicrometric pristine oxides (TiO_2, CuO), modified oxides ($Ag@TiO_2$), mixed oxides (bismuth titanates) and oxide mixtures (CuO/TiO_2). It was possible to produce the composites with a high homogeneity and a mixture degree at molecular scale. The production of the composites led to the formation of nanometric domains of pure oxides which strongly influenced their properties (melting temperature). Phases made of bismuth oxide and titanium oxide were produced which are normally not stable at the synthesis conditions (temperature and relative molar ratio). This illustrates the fact that SFS is an out-of-equilibrium process, which can be used to synthesize metastable phases.

USE OF THE PREPARED OXIDES IN PYROTECHNIC COMPOSITIONS

1. Glossary

SFS: Spray Flash Synthesis

TGA: Thermogravimetric Analysis

HPLC: High-Performance Liquid Chromatography

DSC: Differential Scanning Calorimetry

ESD: Electrostatic Discharge

SEM: Scanning Electron Microscopy

XRD: X-Ray Diffraction

PMMA: Poly(Methyl Methacrylate)

TMD: Theoretical Maximal Density

2. Introduction

Thermites are pyrotechnic compositions made of a solid fuel and oxidant. The fuel is a metal powder whose oxidation releases an important amount of energy. The oxidant is a metallic oxide or salt. One of the most used fuels is aluminium because of its thermal stability and low cost. The first use of these compositions was proposed by Goldschmidt process for welding the railway tracks together.[228]

The energetic composites known as nanothermites are prepared from components having nanometric (< 100 nm) or sometimes submicrometric (100 – 1000 nm) particles sizes. The miniaturization of the reactants has a dramatic influence on the reaction behaviour, leading to higher sensitivity to ignition and to electrostatic discharge but also to extremely high propagation velocities of the flame front in loose powders (up to 2500 m/s in nAl/nBi_2O_3).[52]

The oxides to prepare the aluminothermic compositions described in this chapter, titanium oxide and copper oxide, are known as oxidants with totally opposite reaction behaviours and characteristics in the pyrotechnical area. The initial candidates as oxidants for these compositions were bismuth oxide and titanium oxide. However, owing to technical difficulties to produce enough amount of these mixed oxides, the oxide mixture of CuO/TiO_2 was proposed to be studied. Titanium oxide is relatively stable, both thermally and chemically speaking, therefore it is used as weak oxidizer in pyrotechnical compositions. On the other side of the spectrum is copper oxide, known as a very reactive compound which releases a great amount of energy. Both oxides were intimately mixed thanks to the SFS system producing a unique composite which was analysed from the pyrotechnical point of view. Furthermore, it was used for the production of nanothermites with different fuel (Al) to oxidizer proportions.

3. Preparation and characterization of nanothermites from mixed oxides

3.1. Determining the composition of nanothermite mixtures

The mixed oxide of CuO and TiO_2, prepared by SFS, was used as oxidizer for the production of nanothermites. To understand the energetic properties of the mixed oxides, nanothermites with different fuel to oxidizer ratios, equivalence ratios (φ), were prepared. The equivalence ratio is defined as follows:

$$\varphi = \frac{\left({}^{F}/_{O}\right)_{A}}{\left({}^{F}/_{O}\right)_{St}} \tag{50}$$

Where, F represents the fuel, in this case nano-Aluminium, O represents the oxidizer, in this study CuO/TiO_2 and the subscripts in the equation are indicative for the actual (A) and the stoichiometric (St) ratios. This means that for values of φ below 1 the mixture is fuel lean, for values of φ equal to 1 the mixture is stoichiometric and for values above 1 the mixture is fuel rich.[229] [230]

For the calculi of the stoichiometric equivalence ratio the relative amount of metallic aluminium compared to aluminium that is present in the form of alumina (Al_2O_3). The oxide of aluminium appears as shells surrounding the particles, which is formed during the synthesis through controlled oxidation.[231] The mixed oxides were counted as separated elements in the reaction mechanism. The global reaction is as follows:

$$2Al + TiO_2 + CuO \rightarrow Al_2O_3 + Ti + Cu \tag{51}$$

3.2. Characterization of aluminium nanopowder

Thermogravimetric analysis (TGA) was carried out onto the nano-aluminium powder to calculate the percentage of aluminium oxide.[232 233] This forms surrounding the nano-aluminium particles as a result of the oxidation performed in the synthesis process. This Al to Al_2O_3 ratio of the aluminium nanoparticles decreases when the size of particle decreases. The nano aluminium used is Al QNA (Intrinsiq Materials Inc.) of around 100 nm in size and a specific surface area of 23.7 m^2 g^{-1}. The TGA curve of this material is shown in **Figure** . The pure aluminium is oxidized by the gaseous oxygen as follows:

$$2\,\mathrm{Al} + {}^{3}/_{2}\ O_2 \rightarrow Al_2O_3 \qquad (52)$$

The process starts with a weight loss up to 240°C which is ascribed to trapped species adsorbed at the surface like water, hydroxide and carbon dioxide. The oxidation of the aluminium then takes place by two competing mechanisms. The migration of aluminium through the amorphous oxide shell, which leads to the oxidation at the surface of the particles, happens in parallel to the diffusion of oxygen in the opposite sense, which in the other hand produces an oxidation in the inside of the particles. At around 500°C the amorphous oxide shell starts to crystallize, this phenomenon seems to benefit the oxygen diffusion which seems to be the predominant oxidation mechanism once the shell is totally crystallized. This is what happens at the pseudo-plateau leading to a slowing down of the oxidation rate and therefore of the mass variation. Above the pseudo-plateau the aluminium inside of the particles starts to melt. From this point on, the number of “steps” that can be identified in the curve depend on the size of the particles. The aluminium in the inside of the particles melts, increasing its volume and as consequence stress forces appear on the shell. This leads to cracks and leaks in the shell through which the aluminium will escape and oxidize, closing the gap. Therefore, if the particle exceeds a certain size, the pressure of the melted core soon drops as the new formed shell is thicker, leaving an un-oxidized aluminium core. This would lead to a third step, which is not the case for the aluminium used to carry out the research. The aluminium diffusion through the alumina shell is predominant in this phase until all the aluminium is oxidized.[234]

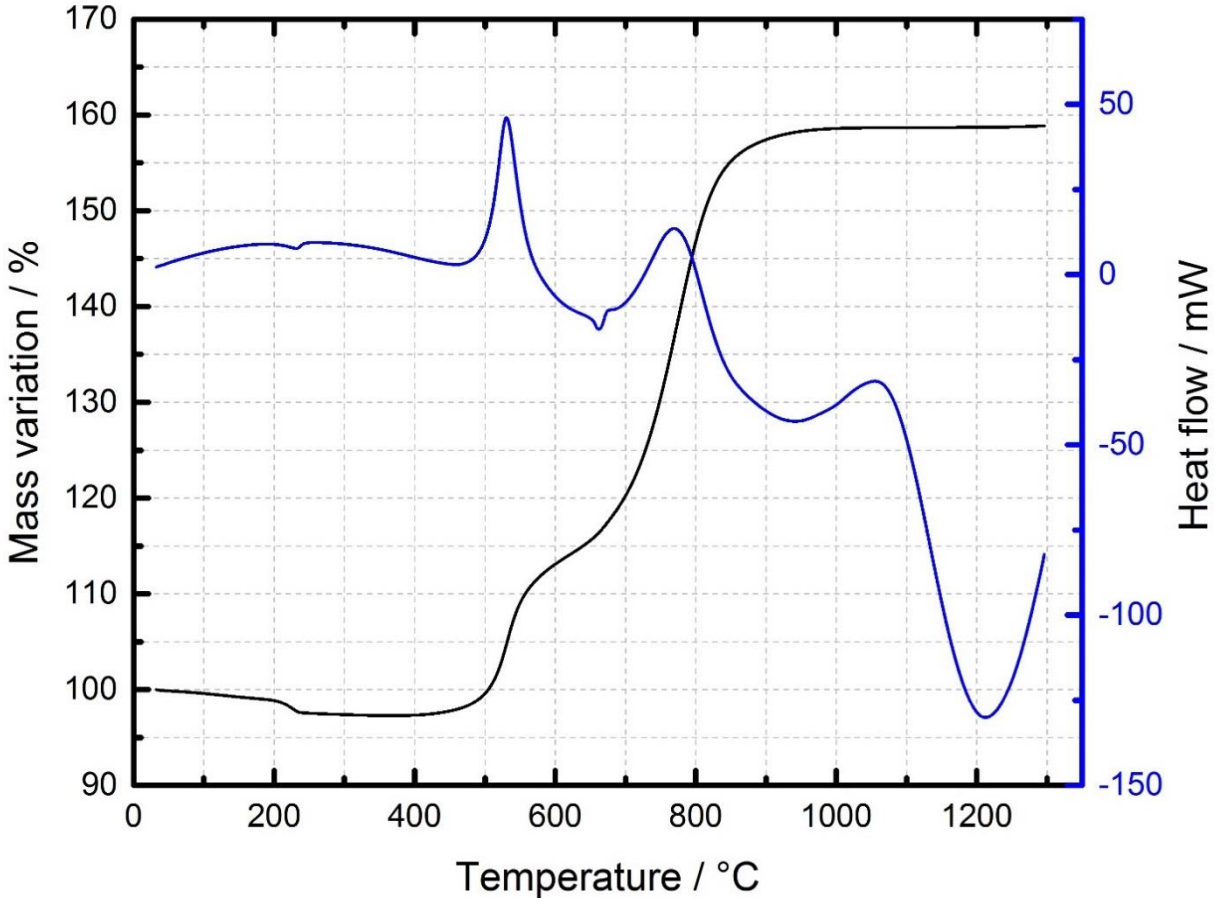

Figure 93. *TGA and DTA curves of nano-aluminium powder obtained at 5°C/min and 100 mL/min of Ar/O_2 (98%/2%).*

Basing on the mass of Al_2O_3 compared to the initial mass of Al, the percentages calculated were 68.1 % of metallic Al and 31.9 % of Al_2O_3.

3.3. Preparation of nanothermite mixtures

All the mixtures were prepared by adding the nano-aluminium either in stoichiometric ratio, φ=1, or with 40% excess of fuel, φ=1.4, to the corresponding quantities of mixed oxides. Additionally, to understand the influence of surface and crystallinity on the pyrotechnically properties, the mixed oxides calcined at two different temperatures (400°C and at 600°C) were used giving four different nanothermite compositions. The amount used are shown in the **Table 12**.

The preparation of the nanothermites, using the mixed oxides produced by SFS, was always done following the same procedure. Al and CuO/TiO_2 dry powders are mechanically mixed in a 100 mL flask by means of a vortex mixer operating at 2500 rpm for 1 min. Afterwards 20 mL of acetonitrile (CH_3CN, HPLC grade from Honeywell) per gram of thermite are added to the powder.

Acetonitrile is used as liquid dispersing medium owing to its polarity (ε_r=36.64) which helps to break the agglomerates and therefore enables the homogenization of the solid mixture.[235] The components form a suspension by sonication through an ultrasonic bath for 10 min. The liquid phase is forced to evaporation in a rotatory evaporator by the heat provided by a water bath set at 80°C while the flask turns at 90 rpm. The system is put under vacuum. The vacuum is achieved by lowering the pressure inside of the system until ~250 mbar gradually to avoid boiling of the liquid. At this point the

Nanothermite composition	**φ**	$\boldsymbol{Cont._{nAl}}$ **(wt. %)**	$\boldsymbol{Cont._{CuO/TiO_2}}$ **(wt. %)**	**Abbreviation**
$CuOTiO_2$/n-Al 400°C φ=1	1.0	32	68	CT410
$CuOTiO_2$/n-Al 600°C φ=1				CT610
$CuOTiO_2$/n-Al 400°C φ=1.4	1.4	40	60	CT414
$CuOTiO_2$/n-Al 600°C φ=1.4				CT614

Table 12. *Mixing table of the prepared nanothermites; φ: fuel equivalence ratio;* $\boldsymbol{Cont._{nAl}}$*: n-Al content and* $\boldsymbol{Cont._{CuO/TiO_2}}$ *: CuO/TiO_2 content.*

vacuum is further

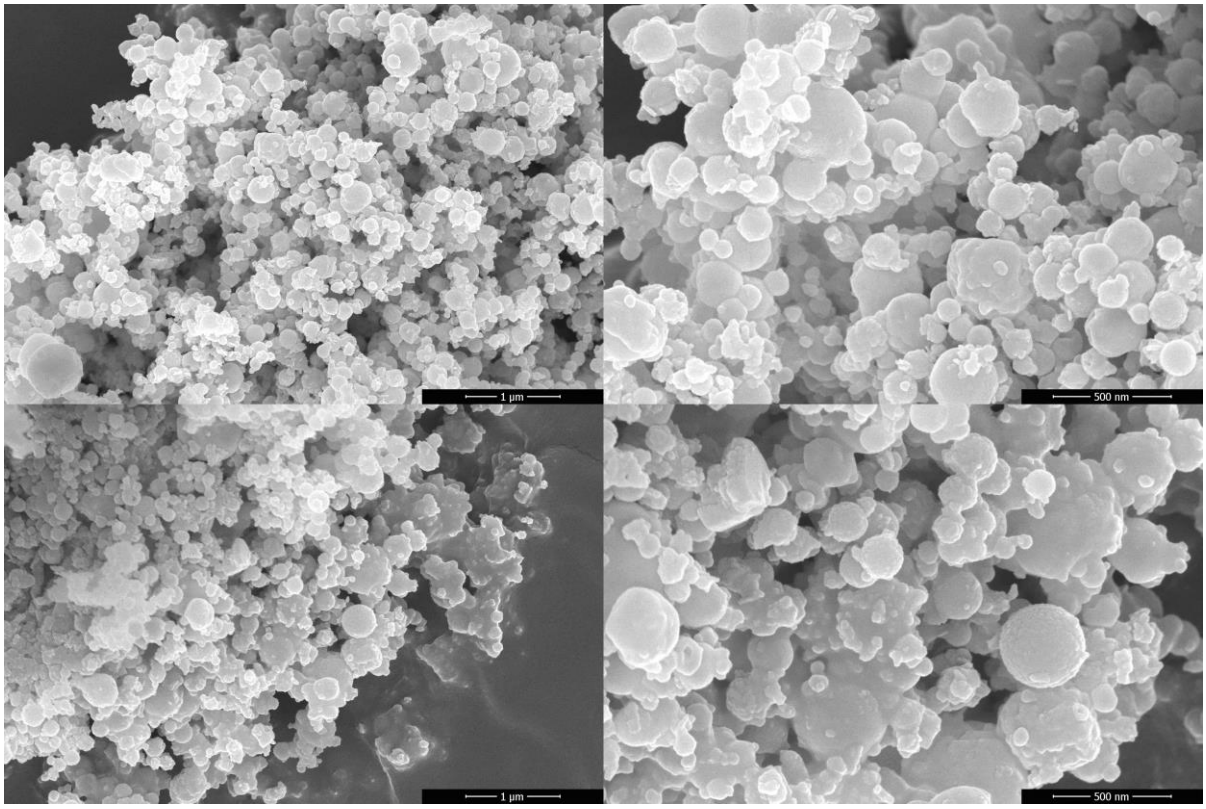

Figure 94. *SEM images of nanothermite composite: Upper images CT410 and lower images CT414.*

increased but at a lower rate. This is done until no substantial liquid recovery can be identified. The liquid is then removed from the system and the sample is left under vacuum under the same conditions for additional 20 min. The drying process is an important step to avoid any acetonitrile remaining in the powder, as this could lead to the production of hydrogen cyanide (HCN), which is extremely hazardous for the health, as a subproduct during the combustion reaction. The dry powder is recovered and the large macroscopic aggregates that formed during the evaporation are crushed. This step enhances the homogeneity of the powder and therefore lessens the erratic behaviour in the subsequent use. Afterwards it is stored in special conductive recipients for explosives which are specifically designed for this purpose.

The composites CT410 and CT414 can be seen in **Figure** while the composites CT610 and CT614 can be seen in **Figure** . It can be seen that the particles of both consitutents have approximately the same size and have a spherical morphology. For both fuel rich compositions, CT414 and CT614, the particles seem to be more strongly and fused together in comparison to the stoichiometric composites, CT410 and CT610. The aluminium in excess has an agglomerating effect on the particles that make up

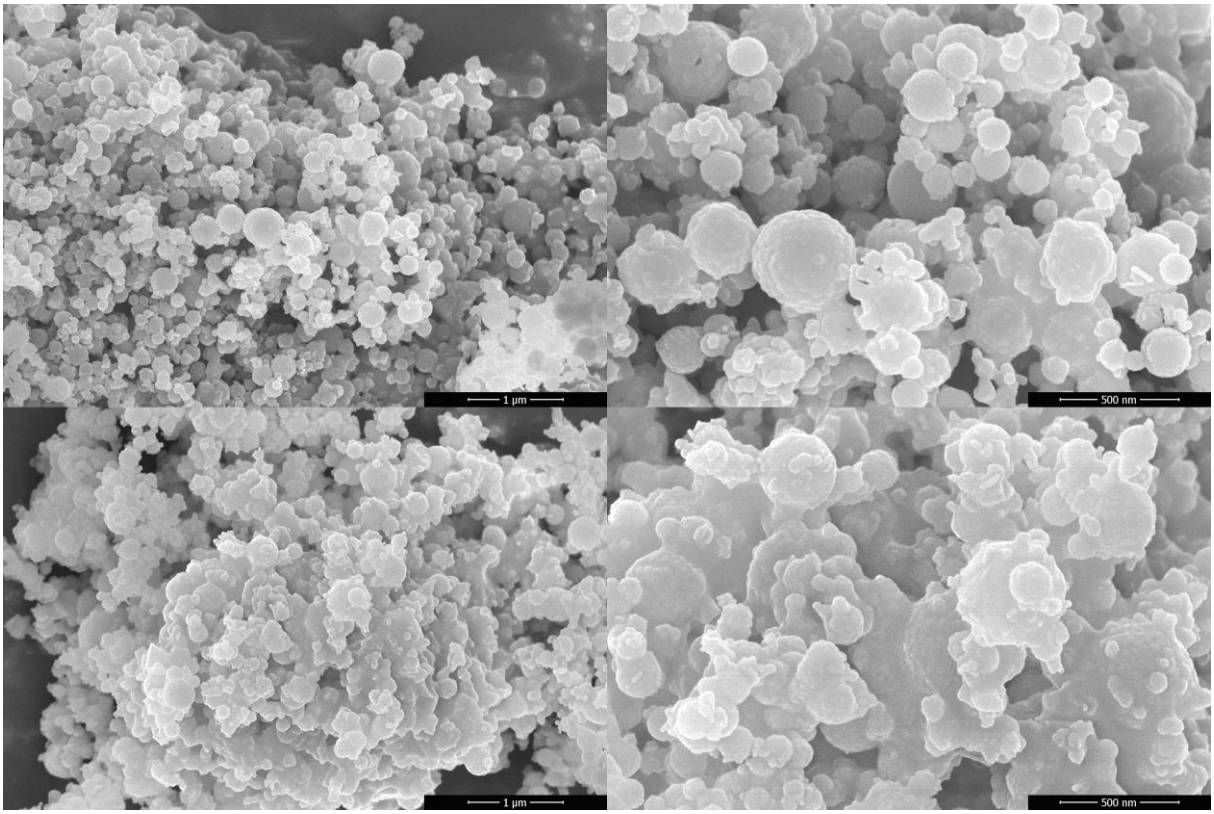

Figure 95. *SEM images of nanothermite composite: Upper images CT610 and lower images CT614.*

the compostion, this leads to regions where mater is in closer contact. The smaller spherical particles (~100 nm) are the aluminum particles, while the bigger ones (~200 nm) are the CuO/TiO_2 particles. It can be seen that both compounds are well mixed and dispersed.

3.4. Thermal analysis of the nanothermite mixtures

The thermal behaviour of the prepared nanothermites was measured by differential scanning calorimetry (DSC). All samples were analysed with the same conditions, for this the samples were placed into sealed crucibles (details in Chapter II). The results can be seen in **Figure** . All samples show thermal stability up to 150°C. Both nanothermites CT410 and CT414 show an exothermic peak between 240°C and 250°C. This energy release is produced by the reaction of water and aluminium. The water is trapped into the mixed oxides owing to its high specific surface area (125 m^2 g^{-1}). It desorbs upon heating process and reacts with the surrounding aluminium particles. This oxidation process is an exothermic reaction. The amount of aluminium that reacts by this process can be calculated by taking into account the quantity of energy generated by the reaction and the reaction enthalpy of the oxidation.[236] Aluminium can react fully to aluminium oxide (Al_2O_3), gibbsite ($Al(OH)_3$) or böhmite (AlO(OH)) depending on the water conversion efficiency.[237]

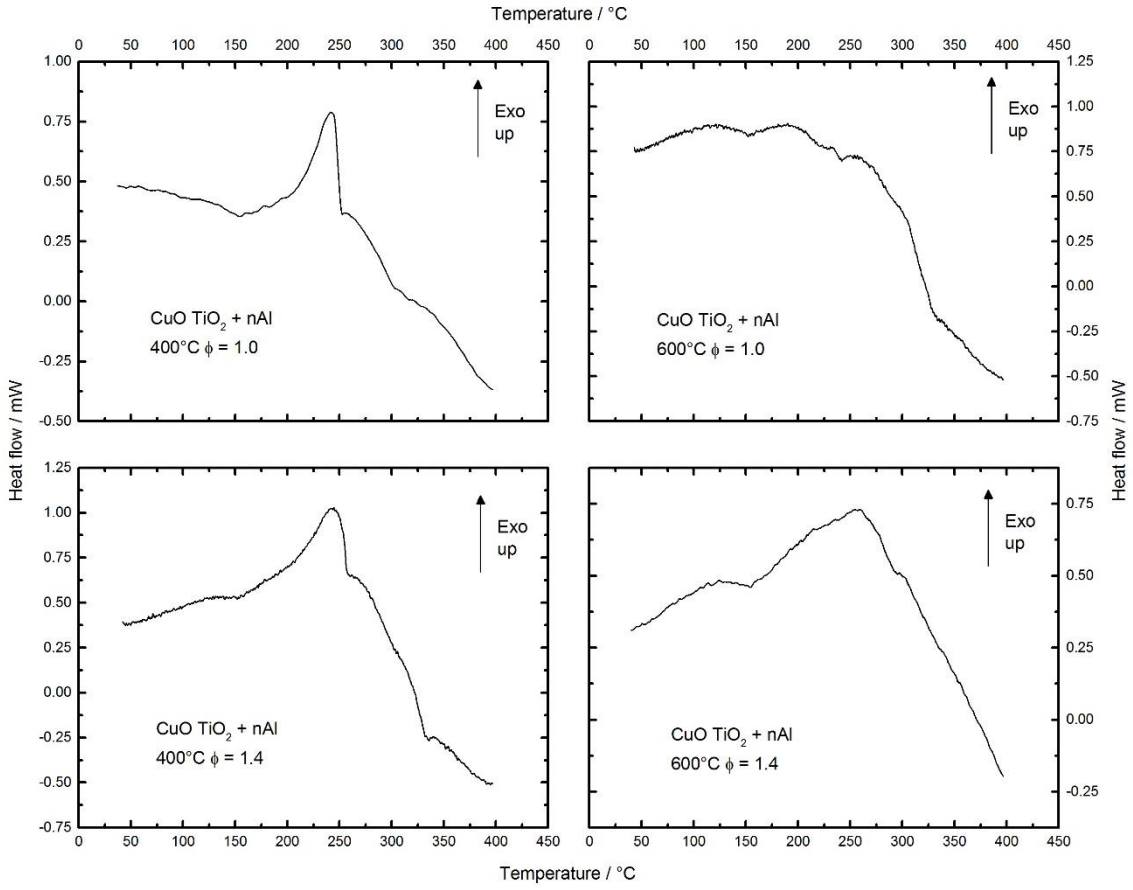

Figure 96. *DSC curves of the nanothermites prepared by the mixed oxides. The analysis was performed with a heating rate of 5°C* min^{-1} *and 50 mL of nitrogen flow.*

The exothermic peak of CT410 (**Figure**) equals to a heat release of 146.4 J/g. Taking into account the mass of the sample (1 mg) and the energy that is liberated by the reaction shown in **Eq. ()** (14734.68 J/g of aluminium), the amount of used water for this reaction is 0.015 mg.[238] This corresponds to 1.5 wt.% of the total mass of the sample.

$$2\ \mathrm{Al} + 3\ H_2O \ \rightarrow\ Al_2O_3 + \ 3\ H_2 \qquad (53)$$

Taking into account the mass variation recorded by the TGA device (**Figure**) at low temperatures (< 450°C), the water that was consumed for the reaction is smaller than the total amount of water adsorbed on the oxides. This means that the vast majority of the water does not react with the aluminium. The water vapour reacts, at this temperatures, with the aluminium close to the Al/Al_2O_3 interface. This reinforces the oxide layer and passivizes the particles against a deeper oxidation. This would explain why only a part of water reacted with the aluminium.

Following the same calculi, the energy released corresponding to the exothermic peak of CT414 (**Figure**) is 166.2 J/g. Analogously, the water used for this reaction is

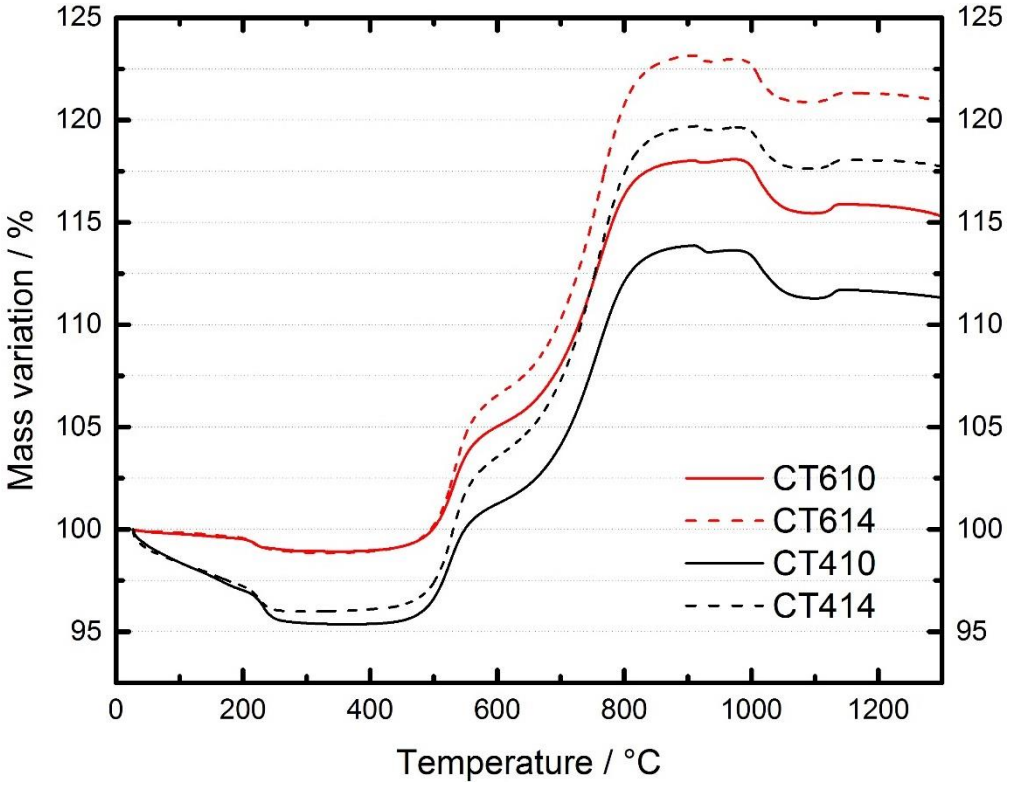

Figure 97. *TGA curve of nanothermites obtained at 5°C min^{-1} and 100 mL min^{-1} of Ar/O_2 (98%/2%).*

0.017 mg. The relative amount of water reacted increases with quantity of aluminium

present in the sample. A higher amount of aluminium implies a higher surface that is in contact with water. Therefore, more water is needed to create the passivation layer.

The desorbed water comes mainly from the oxide surface. However, the CT610 and CT614 nanocomposites have a very low surface area. In this cases slight exothermic hills at ~250°C can be identified. This is a consequence of the water adsorbed on the aluminium ($S_{BET/Al}$=23.7 m^2 g^{-1}). The sample CT610 is the one who contains less aluminium, and therefore less adsorbed water. This is why the oxidation phenomenon is less marked. From a pyrotechnical point of view, all the nanothermites prepared meet the thermal stability requirements for safe handle and use.

Figure shows the TG analysis curves of the nanothermites prepared with the mixed

Nanothermite composition	Al content (wt. %)	Al_2O_3 content (wt. %)
CT410	64.2	35.8
CT414	66.4	33.6
CT610	66.5	33.5
CT614	68.1	31.9
Pure nAl	68.1	31.9

Table 13. *Mass percentages of Al and Al_2O_3 in the Al nanopowder in the nanothermite compositions and in the pristine n-Al.*

oxides. It can be observed that the powders react following the same oxidation mechanism as the pure aluminium particles at the same temperatures up to 900°C. The nanothermites CT410 and CT414 have a much more pronounced initial weight loss compared to the nanothermites CT610 and CT614. As CT410 and CT6414 have higher surface area they absorb more volatile species, mainly water, and therefore when the samples are, calcined that weight loss is higher. The mass gain of pure aluminium powder is proportionally (~ 60%) higher than the one observed in nanothermites. The content of aluminium in the energetic materials is lower because it is mixed with the oxides, which do not react with oxygen and therefore do not contribute to the mass gain of the nanothermite sample.

The composition of aluminium nanopowder in the different composites can be seen in **Table** . The oxidizers, which are gaseous free oxygen and the oxide mixtures, compete to interact with available aluminium in the sample. Nevertheless, the oxidation by

gaseous oxygen produces a mass variation (external addition) while the oxidation by the solid oxides implies no mass variation. The aluminium content of the aluminium nanopowder is inferior in the CT410 sample in comparison with the aluminium content in the pure aluminium. This indicates that a small part of the nanoaluminium present in the sample reacts with the oxide mixture instead with the gaseous oxygen upon slow heating. If we compare the same phenomenon for the CT 414 sample, it can be seen that the aluminium content of the aluminium nanopowder is higher but still below the value for pure aluminium. This means that less aluminium reacts with the oxides and more reacts with the oxygen in gas form when the samples are heated slowly. This seems to be logical, as when the proportion of aluminium to oxide diminishes, less aluminium is in contact with the oxide and therefore more of it will react with the gaseous oxygen.

A similar behaviour is shown by CT610 and CT614. In the case of CT610, the aluminium content of the aluminium nanopowder is also smaller than the content of the pure aluminium, which indicates that a part of the aluminium is oxidised by the oxide upon slow heating. However, this is not true for the CT614 sample, in which the content of aluminium in the aluminium nanopowder equals the content of the pure aluminium. This implies that in this sample all the aluminium is oxidized by the gaseous oxygen like it happens for the pure fuel. In a similar way, it also means that the more aluminium present in the sample, the more it will react with the free gas when the samples are heated up slowly.

Comparing the aluminium content of the aluminium nanopowder of the samples calcined at 400°C to the content of the samples calcined at 600°C, it can be observed that the aluminium of the samples calcined at higher temperatures has a higher tendency to react with the gaseous oxygen instead of reacting with the solid oxides, which indicates that they are less reactive.

Sample	Initial mass (mg)	Amount of CuO (mg)	Weight if all Cu_2O (mg)	Mass change (wt. %)	Weight if all Cu (mg)	Mass change (wt. %)	Actual mass change (wt. %)
CT410	10.59	3.58	3.22	3.40	2.86	6.79	2.64
CT414	10.62	3.18	2.86	3.01	2.54	6.01	2.02
CT610	10.19	3.44	3.10	3.40	2.75	6.79	2.11
CT614	9.47	2.83	2.55	3.01	2.26	6.01	2.35

Table 14. *Mass variation of composites at temperatures above 900°C.*

Table highlights the mass variations of the composites at high temperatures. Starting at ~900°C, when the aluminium is fully oxidized to alumina, the samples present a mass variation. A small weight loss can be identified for all samples at ~925°C. This mass loss can only be explained by oxygen exiting the system as the aluminium cannot be oxidized further. The oxygen comes from the thermal decomposition of CuO into Cu_2O.

Then a slight mass increase can be identified at ~960°C. CuO (T_{fus}: 1446°C) has a higher melting point compared to Cu_2O (T_{fus}: 1235°C), these values are strongly reduced when the particles are of nanometric size.[202] Thus, the nanometric Cu_2O that is formed melts. The liquid Cu_2O reacts with the alumina layer of the aluminium nanoparticles. This composite has a spinel structure and is known as copper aluminate ($CuO{\cdot}Al_2O_3$).[239] To be able to form this structure, the copper(I) oxide is oxidized into copper(II) oxide, which would explain the mass gain. When the available alumina is depleted the thermal decomposition of copper(II) oxide into copper(I) oxide continues, which explains the mass loss (2-3 wt. %).

Finally, the weight increase at ~1150°C for all the nanothermite composites is explained by the formation of the spinel copper aluminate, but in this case with the alumina of the sample holders. **Figure** shows the sample holders after the TGA measurement, which are made of aluminium oxide. It can be observed that the sampler holders show a coloration which comes from the migration of copper oxide into the aluminium oxide.

Figure 98. *TGA sample holders after analysis of the nanothermites.*

3.5. Measurement of the sensitivity thresholds

The sensitivity to impact, friction and electrostatic discharge (ESD) of the nanothermite compositions were measured before performing any other experiment. This information was crucial to further work with the materials and manipulate them while meeting the security requirements. Moreover, the identification of these thresholds was also essential to understand the interactions between the fuel and the oxidizer. The results are presented in **Table** .

Nanothermite composition	Impact (J)	Friction (N)	ESD (mJ)
CT410	>100	>360	10.82
CT414	>100	>360	0.72
CT610	>100	216	<0.14
CT614	>100	>360	<0.14
nCuO nAl (ϕ=1.4)	90	7	<0.14

Table 15. *Sensitivity thresholds for the studied nanothermites.*

The sensitivity values of the materials were measured with different equipment depending on the stress studied. If the value of the impact sensitivity is lower than 2 J the material is considered to be sensitive. The threshold considered is 80 N for the friction sensitivity. It is considered to be thermally speaking stable if it does not react up to 100°C. If the compositions meet these requirements the materials can be handled and transported on public roads.[240] And a higher quantity of material can be produced and used at the same time.

All nanothermites are less insensitive to impact (>100 J) compared to the nanothermite made of pure nanometric copper oxide and nano aluminium powder. These nanopowders have a high interparticle porosity, which means that they have a proportionally high volume filled with air because the particles are very loosely packed (TMD < 10%). Therefore, when the impact is produced by the fall hammer, the interparticle air is compressed adiabatically. The heat released during this process is quickly dissipated into the surrounding particles. The thermal conductivity of aluminium nanopowder is higher than the one of air, but far smaller than the one of bulk aluminium. The thermal conductivity of the aluminium nanopowder increases when it

Pure compounds	TMD (%)	Nanothermites	TMD (%)	Calculated TMD (%)	Porosity (%)
nAl	7.15	**CT410**	6.35	6.07	93.65
CT400	5.55	**CT414**	7.55	6.19	92.45
CT600	7.46	**CT610**	9.32	7.36	90.68
		CT614	8.72	7.34	91.28

Table 16. *Theoretical maximal density of pure compounds and composites.*

is pressed. The closer the nanoparticles are to each other, the less space between particles is free to be filled by air, and the thermal conductivity of the nanopowder becomes closer to the one of the bulk material. The thermal conductivity of bulk aluminium is one order of magnitude higher than the thermal conductivities of bulk copper oxide and titanium oxide. Thus, the thermal conductivity of the mixture is ruled by the one of the aluminium. Therefore, when the hammer falls the thermal conductivity raises sharply, which favours the dissipation of heat in the whole mass of the sample. The particles are of mineral nature as consequence they are not sensitive to a moderate thermal stress. This explains the low sensitivity to impact of the nanothermites. The Al/CuO nanothermite is more sensitive to impact than the CT mixtures because the reaction propagation, when the reaction is started by a strong stress, is impeded by the presence of the titanium oxide.

With exception of the composition CT610, all the nanothermites present also an insensitivity to friction stimuli as their values are higher than 360 N. Nanopowders are much smaller in size than the roughness of the ceramic elements which are used in the testing device for the friction sensitivity tests. Therefore, the nanoparticles act as lubricant during the test, which renders them insensitive. Conversely, if the energetic compositions are well mixed at nanoscale, the reaction can spread easily through the sample because at local scale the elements are in contact in stoichiometric proportion. As can be seen in **Table** , the measured theoretical maximal densities (TMD) of the samples are higher than the values that the composites should have if the powders had not interaction among each other. This means that there is an agglomeration of the particles after mixing which increases their apparent density. The biggest difference can be found in the CT610 sampler, indicating that the particles of aluminium and oxide are more strongly agglomerated. This agglomeration puts the particles into close contact, meaning there is a higher probability that the reaction can spread

through and make the whole sample react, which leads to a higher sensitivity to this stress. Nonetheless, compared to the copper oxide nanothermite, all the composites produced are much less sensitive to friction. This is owing to the inhibiting effect of titanium oxide. When the reactions start locally and tries to spread through the material, it is quickly stopped by the titanium oxide particles which are evenly mixed in all directions of the sample and absorb heat without reacting.

The values of ignition by ESD for nanothermites are usual, as a high amount of energy is transmitted to the nanoparticles in a very short time (high power stress) owing to the nature of the test. As a rule, the energetic compositions containing fine metallic powders are sensitive to ESD. The sensitivity to ESD of pure aluminium under air was measured (1.42 mJ) and found to be higher than the one of the nanothermites prepared. This means that there is a sensitization of the aluminium by the presence of the oxides. The oxidation of the aluminium is more probable in close contact to the oxides than with the free air. These values obtained for these composites are in the usual range for nanothermites.[241 242]

3.6. Determining the explosion heat by calorimetric experiments

The explosion heat, of the different prepared formulations, were measured by a bomb calorimeter. The results can be seen in **Table** .

Nanothermite composition	Reaction energy (J g^{-1})
CT410	3188
CT414	3740
CT610	3538
CT614	3444

Table 17. *Results of calorimetric analysis of the nanothermites.*

All the thermite reactions show a higher reaction energy output than the one obtained by the theoretical calculation of the pure oxidizer-fuel reactions. Basing on data found in literature, the reaction energy of Al with TiO_2 is 1528 J g^{-1} while for the reaction of Al with CuO the energy is 4076J g^{-1}. If both constituents would react in equal proportions with pure aluminium, the theoretical energy released would be 2802 J g^{-1}. In the case of compositions prepared from aluminium nanopowders, the value would be even lower owing to the presence of alumina (~29 wt.% in Al nanopowder). Thus, it can be seen that the energy released by the reactions is higher that the theoretical value.[53]

By using X-Ray diffraction analysis the different crystalline phases that were formed by the reaction could be identified. Titanium(I) oxide is present in all the XRD patterns as highlights **Figure** . The appearance of this species indicates that the titanium(IV) oxide was not fully reduced into Ti^0 but into Ti^{II} (TiO). The presence of titanium monoxide indicates that it was not totally reduced. Therefore, there is an excess of fuel, as the proportions of the composites were calculated considering the complete reduction of titanium oxide. This excess in fuel available enables the reaction between the in-situ reduced metallic copper and the aluminium to form an alloy. This alloy is formed by the intermetallic reaction which liberates additional energy (451.87 J g^{-1}).

The heat released by the nanothermite CT410 is relatively low (3188J g^{-1}) compared to the other composites. In this composite, the peaks corresponding to metallic copper are very well defined and much more intense than the other species present. The absence of peaks associated to other copper containing compounds indicates that copper oxide was fully reduced to copper. The intensity of the peaks associated to

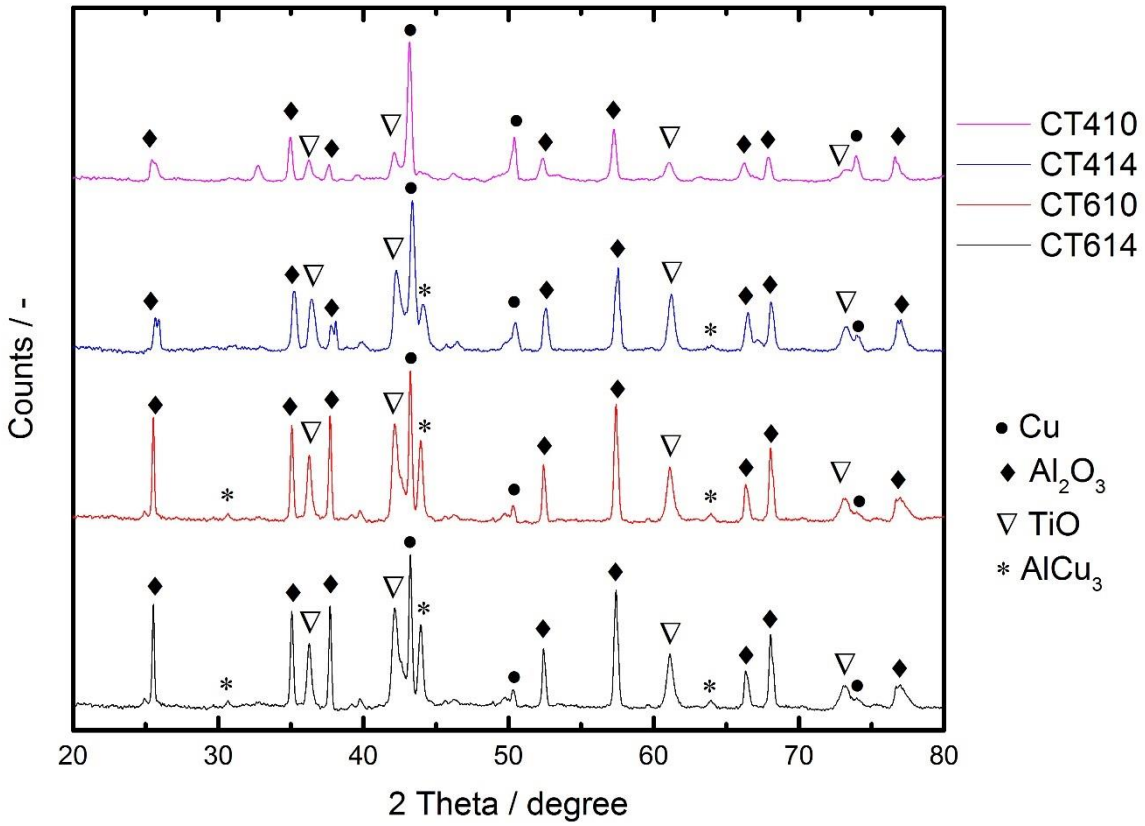

Figure 99. *XRD patterns of the residues obtained after the bomb calorimetry tests.*

titanium monoxide and aluminium oxide in relation to the copper peaks are less important for CT410 in comparison to the relative intensity of these peaks in the other cases. Additionally, no peaks associated to the intermetallic alloy can be found in the XRD pattern, which indicates that the reaction did not take place. This would also explain why the combustion heat released by this compound is lower than the other composites. The absence of the intermetallic compound, indicates that all the aluminium was fully oxidised, instead of partly reacting with the metallic copper present, this shows that the reactant are in optimal proportions.

The nanothermite CT414 was the composite which released the highest amount of energy (3740J g^{-1}). In this case the peaks for TiO and Al_2O_3 are more important than for CT410, which points out that both titanium monoxide and aluminium oxide have a higher crystallinity degree. This is a consequence of the higher energy released during the reaction which led to a better crystallization of the products. The higher energy liberated comes from higher proportion of aluminium which reacts not only with the water adsorbed on the surface but also by intermetallic route.

The CT610 and CT614 composites have very similar XRD patterns, both for the position of the peaks present as well as for their relative intensity of these. They also have very close values to the liberated combustion heat. The oxides of both composites have a very low surface area (11.98 $m^2 g^{-1}$). In consequence, the amount of adsorbed species on the surface is negligible, which means that little to no aluminium was oxidised by this species. On the other hand, the peaks for the alloy, the titanium monoxide and the aluminium oxide gained in intensity in comparison to CT410 and CT414. This can be explained by the lack of adsorbed species, which would mean that a higher proportion of aluminium is available for the intermetallic reaction with copper. This leads to an increase in the intensity of the peaks associated to this alloy. Therefore, the energetic contribution of this reaction to the total combustion energy released by the system is higher.[53]

3.7. Study of the combustion by tests in tubes

The combustion of the nanothermites was tested in transparent PMMA tubes. This experiment gave information regarding the combustion nature and the behavior of the material during the reaction. The density of the nanothermite loose powder has to be steady along all the tube to have a regular combustion propagation. For this purpose, during the filling of the tubes the weight was measured at different heights. This leads to the calculation of the apparent density along the tubes and in addition offered the possibility to verify its constancy (**Figure**).

Three tubes were prepared for each composition. It can be seen that the density of the different tubes is constant along the height. Additionally, all the lines, for a given composition, are close together forming clearly defined groups. This indicates that the densities are similar along the tubes and among tubes for each composition. From these lines the apparent density can be calculated as shown in **Table** .

The tubes prepared with composites calcined at 400°C (CT410 and CT414) show a lower apparent density than those prepared with the composites calcined at 600°C (CT610 and CT614).

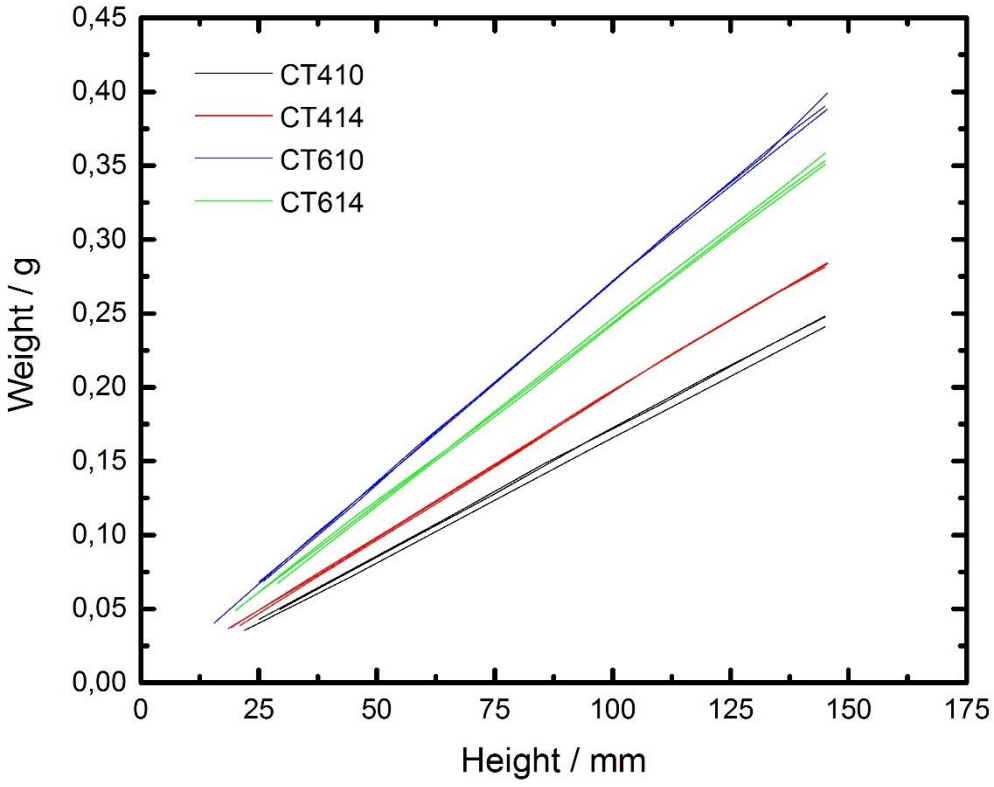

Figure 100. *Weight of the aluminothermic compositions along the height of the tubes.*

Nanothermite composition	d_a (g cm^{-3})	ρ_{ox} (g cm^{-3})	d_{true} (g cm^{-3})	TMD (%)	Porosity (%)
CT410	0.239	4.21	3.76	6.35	93.65
CT414	0.277		3.67	7.55	92.45
CT610	0.382	4.87	4.10	9.32	90.68
CT614	0.344		3.94	8.72	91.28

Table 18. *Average density of the nanothermites in the prepared combustion tubes; d_a: apparent density in tubes; ρ_{ox}: density of the oxides; d_{true}: true density of the composites.*

The maximal density of the composite that could be attained by the material was calculated basing on the mass ratios of the composite and the corresponding densities. The percentages of theoretical maximal density (TMD) of the CT410 and CT414 tubes is lower than those of the CT610 and CT614 tubes. This means that the oxide particles and the aluminium particles are more loosely packed in the first two cases. The packaging of the mixtures is affected by the porosity of the oxidant and by the interactions between fuel and oxidant particles.

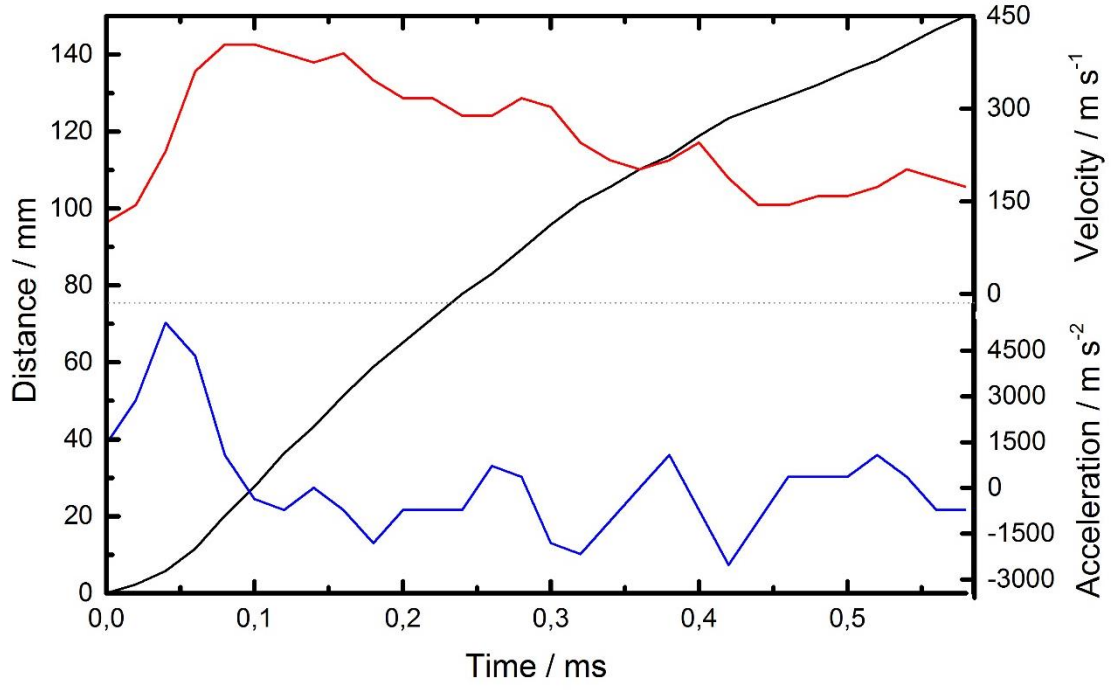

Figure 101. *Combustion propagation inside of the tube for the nanothermite CT410.*

The propagation of the combustion front in the tube for the CT410 sample is represented in **Figure** (black curve). The first 4 mm of the tube are filled with the CuO/nAl ignition composition. Then the combustion reaches the CT410 composition

and ignites it. The combustion accelerates strongly to up ~5400 m s^{-2} until the maximal velocity is reached of 400 m s^{-1}. The acceleration of the beginning of the test is an indication of how sensitive the material is to ignition by a thermal stress. From this point on it starts to decelerate. The deceleration rate, once reached the reaction plateau, is of -470 m s^{-2} with a standard deviation of 999 m s^{-2}. The deviation indicates the stability of the reaction, in this case quite unstable. It continues at this rate until it reaches the end of the composition at a speed of 170 m s^{-1}. The front propagation speeds reached are characteristic for a deflagration. This composition reaches the highest maximal speed of all the composites, which seems to be in accordance with the TMD, as it has the lowest value. In addition, it is the composite whose TMD value is the closest to the calculated TMD, indicating that this composite is the less agglomerated one. This promotes the convection of the generated combustion gases, which explains the highest speed attained. The free space between the reactants and the particles facilitates the convection of the hot reaction gases that are formed in situ. The combustion reaches the end of the tube without stopping, which means that the reaction is self-sustaining.

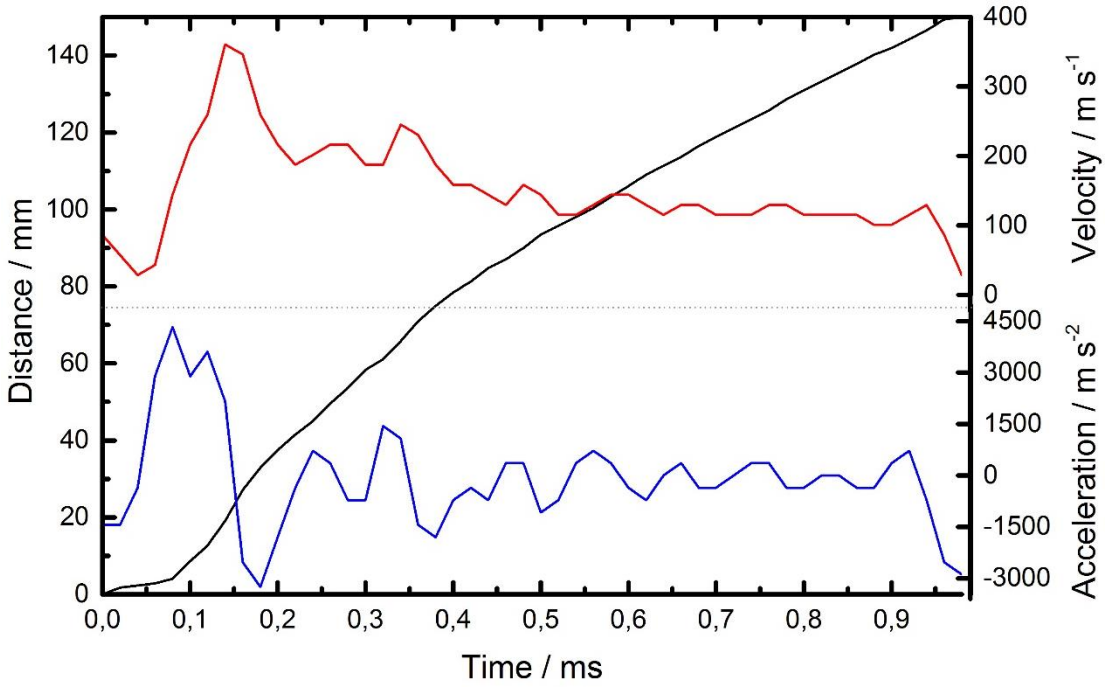

Figure 12. *Combustion propagation inside of the tube for the nanothermite CT414.*

Figure 10 shows the deflagration profile of the tube filled with the CT414 composite. After the ignition composition, the reaction accelerates strongly at up to 4325 m s^{-2} until the maximal speed of 360 m s^{-1} is reached. This material reacts with a slower

acceleration than the CT410, it is therefore less sensitive to ignition. This reduced sensitivity arises from the excess of aluminium and the higher aggregation of the particles. The reaction is slightly more stable in terms of velocity. The reaction decelerates in a slower rate (-126 ± 681 m s^{-2}) than the CT410 composite. The combustion propagation is more stable than in CT410 composition owing to the higher density of the energy produced by the combustion of CT414. CT414 is denser (9.32 % TMD) and releases a higher explosion heat than CT410.

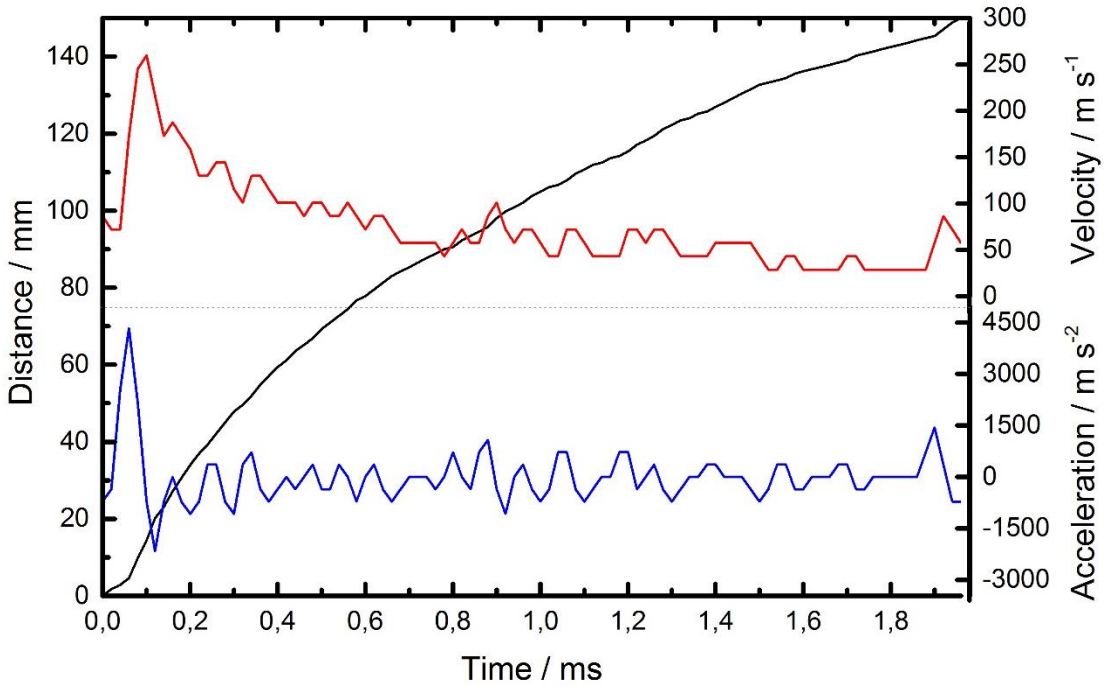

Figure 2. *Combustion propagation inside of the tube for the nanothermite CT610.*

The combustion of the composite CT610 is a deflagration all along the tube (**Figure 103**). This energetic mixture reaches a maximal speed of 260 m s^{-1} after accelerating at 4325 m s^{-2}. In this material, the proportion of fuel to oxidiser is close to the ideal case. However, the aggregation degree of the particles makes them less prone to react, which is reflected in the acceleration value and therefore the sensitivity to ignition. The combustion decelerates (-53 ± 481 m s^{-2}) until reaching approximately 50 m s^{-1}, from where it stays at a constant reaction speed. The combustion is decelerating reaction that is self-sustaining as it reached the end of the tube. This composite is the one with the highest density (9.32 % of the TMD). It is also the composition with biggest difference between the measured density and the calculated value. This indicates that the particles in this composition are more closely packed and agglomerated. This is reflected in the acceleration profile, whose variations are less important than those

observed for CT410 and CT414 compositions. For the CT410 and CT414 compositions, the adsorbed water molecules are decomposed during the reaction. The presence of adsorbed species makes the reaction more irregular because there are several reactions taking place at the same time. In the oxides calcined at 600°C, there is only the aluminothermic reaction. The absence of adsorbed species makes the reaction more homogeneous.

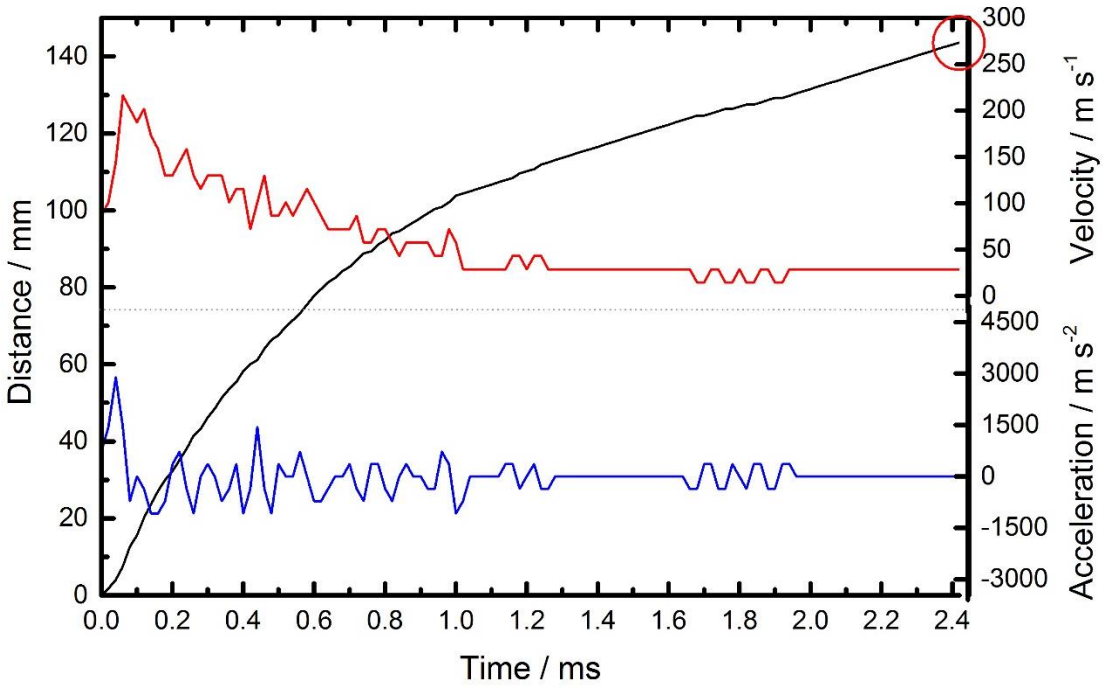

Figure 3. *Combustion propagation inside of the tube for the nanothermite CT610.*

The deflagration of the CT614 composite is the slowest of them all (**Figure 104**). This composite reaches a maximal velocity of 215 m s^{-1}. It shows also the smallest acceleration rate (2885 m s^{-2}). This material presents both an excess of aluminium and a high degree of aggregation of the particles. This results in a relatively low initial acceleration rate, which would render this material the less sensitive to ignition by thermal stress. This composite has a smaller density (8.72 % of the TMD) than the CT610 nanothermite. This composition reacts in a decelerating regime (-45 ± 381 m s^{-2}) that stop at the end, which indicates that the reaction is not self-sustaining (**Figure 104**, red circle). Both high surface area (125.32 m^2 g^{-1}) oxides produce compositions that react faster than those prepared from the composite with low surface area (11.98 m^2 g^{-1}). The adsorbed species (water) react with the surrounding aluminium, boosting the reaction, but at the same time making it more irregular.[243] [244] This phenomenon does not take place in the CT610 and CT614

composites. They react at slower rates but also at more stable velocities. The absence of adsorbed species avoids reactions parallel to the oxidation. This makes the system less complex, which explains why the reaction is more stable.

4. Conclusions

The copper/titanium oxide mixture was successfully used as oxidant for the production of nanothermites using aluminum as fuel. Oxides calcined at different temperatures were used to produce different nanothermite compositions. These presented differences in sensitivity, combustion heat and flame front propagation velocity.

The introduction of titanium had an important role in making the composites less sensitive to extern stress in comparison to the composite prepared from Al and CuO nanopowders, specially to impact and friction. The mixture of different oxides at such intimate degrees opens a new domain of tailored nanothermites where the pyrotechnical properties can be adjusted.

The surface of the oxides was a key factor which changed the reaction between the oxidant and the fuel. The oxides with high surface area harbored more adsorbed species, like water, which take part in the reaction of the composite. The gases released by the combustion spread though the composite by convection. They heat the surrounding particles, ensuring the propagation of the combustion. In addition, the use of oxides with high surface area leads to nanothermites with higher porosity (less agglomerated powder). The higher free space between the particles favors the convection of the combustion gases. Therefore, an overall enhancement of the reaction speed can be appreciated in comparison to the composites prepared with the oxides with low surface area. However, considering the flame front propagation velocity in the composites, it would be interesting to produce composites with a lower titanium proportion. The aim would be produce an energetic composite with low sensitivity but with combustion characteristics closer to the nCuO/nAl nanothermite.

The SFS systems opens the opportunity to produce a wide variety of different oxidants using different metallic oxides and salts varying their proportions. The use of two or more oxides, where each compound contributes for different aspects of the nanothermite is possible thanks to this process.

As future perspective, it would be interesting to study new compositions to create state of the art material. Furthermore the SFS process could be used to prepare directly nanothermites by the simultaneous synthesis and mixture of their components.

USE OF PREPARED OXIDES IN PHOTOCATALYSIS

1. Glossary

SFS: Spray Flash Synthesis

UV-Vis: Ultra Violet – Visible range

NIR: Near Infrared range

SSA: Specific Surface Area

SPR: Surface Plasmon Resonance

2. Introduction

In 1964, Kato *et al.* published their work using a TiO_2 suspension to photocatalytically oxidise tetralin.[7] The milestone in this domain however was the work of Fujishima and Honda in 1972.[8] They achieved the first production of hydrogen by photocatalysis of water. The first water-splitting was performed on titanium oxide electrode connected to a platinum electrode. Later on in 1980 and 1981, several studies revealed that it was possible to produce H_2 from methanol, sugar, proteins and materials originating from the biomass.[245] [22] [246] The production of hydrogen from water and methanol is an attractive energy production route with a closed carbon cycle.[22] [19] [20] It becomes interesting when the methanol source is of renewable origin.[18] The production of energy using hydrogen as fuel is a promising and studied way for clean and sustainable energy production.[21]

The photoreforming of methanol was already reported in 1978 by Domka *et al.* using an iron-chromium catalyst.[247] In 1980, Kawai *et al.* were able to produce hydrogen using titanium oxide and modified (Pt, Pd, RuO_2) titanium oxide as photocatalyst.[22]

This chapter reports the comparative study of the photocatalytic activity of different materials prepared by SFS towards H_2 production from methanol photoreforming. The inherent photocatalytic characteristics of the materials were analysed by UV-Vis spectroscopy. The efficiency of these materials as photocatalysts for the photoreforming of methanol (CH_3OH) was compared.

3. Photocatalytic properties of the synthetized materials

3.1. Unmodified titanium oxide

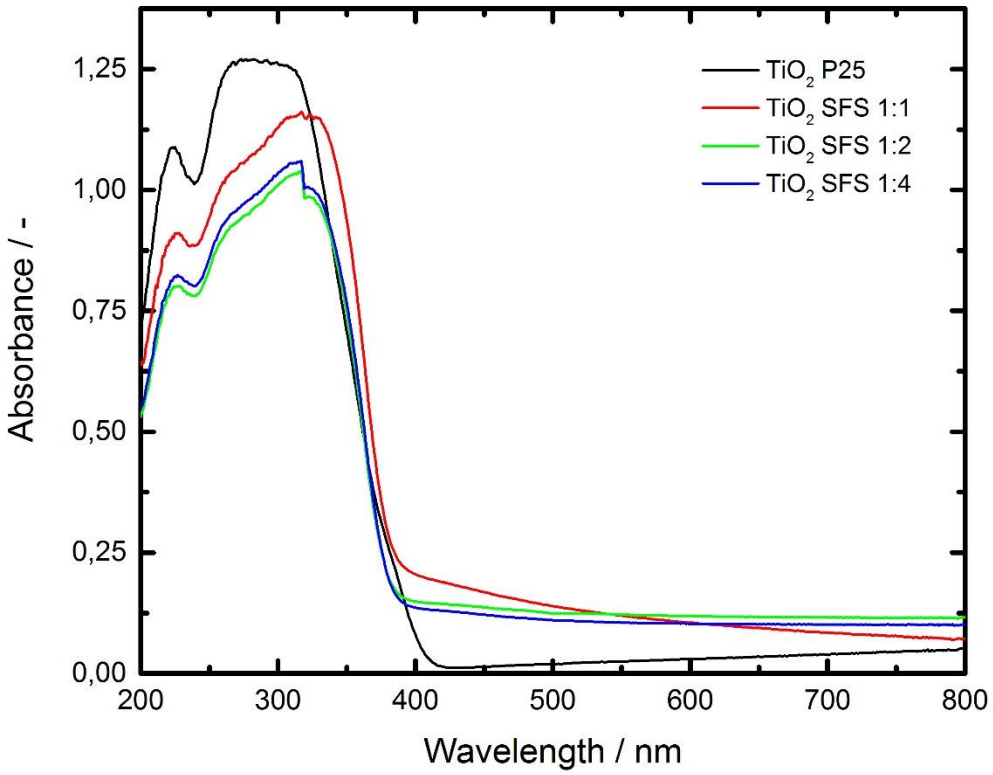

Figure 105. *UV-Vis absorbance spectra of unmodified titanium oxide prepared by SFS.*

The photocatalytic properties of the synthetized titanium oxide powders prepared by SFS were studied for three different water to titanium molar ratios 1:1, 1.2 and 1:4. The optical properties of the materials in terms of UV-Vis absorbance is compared to the commercial sample of TiO_2 P25 (Evonik), composed of *ca.* 80% anatase and 20% rutile phases. As can be seen in ***Figure*** , the absorbance of the P25 shows a tail in the beginning of visible light region. This is consequence of the 20% of rutile (lower band gap of *ca.* 3.0 eV) that is present in the reference sample. One can observe that the samples prepared by SFS exhibit an additional contribution shifted to higher visible light wavelengths, the largest contribution being observed for the 1:1 molar ratio. This additional visible light absorbance contribution could be the result of carbon-based residues incompletely removed during the moderate temperature calcination step. Furthermore, the materials prepared by SFS are submicrometric sized particles (110-160 nm; Chapter III) of pure anatase with a crystallite size of ~26 nm, which could explain diffusion behaviour at higher wavelengths. In comparison, the reference

material (P25) is made of nanometric sized (~90 nm) particles of 85% anatase and 15% of rutile with a crystallite size of around 21 nm.

The analysis of the materials by UV-Vis spectroscopy is fundamental for the calculation of the band gap. For this, the Kubelka-Munk function was applied on the absorbance spectra data. Afterwards, using the Tauc equation for indirect transition semiconductors (case of TiO_2) the bandgap can be calculated for the different materials.[248]

The Tauc relation is as follows:

$$\alpha h\nu = A\left(h\nu - E_g\right)^{\frac{1}{2}} \quad (54)$$

Where A is a constant, E_g is the optical band-gap energy, h is Planck's constant and ν is the incident frequency. By plotting $(\alpha h\nu)^2$ *vs.* $h\nu$, the intersection between the horizontal line and the prolongation of the curve equals to the value of the energy band gap.

The calculated band-gap for the materials can be seen in *Table* . The values calculated are equal to the theoretical band gap of pure anatase (3.2 eV) which is in accordance with the prepared material.[249]

Material	Band gap (eV)
TiO_2 SFS 1-1	3.20
TiO_2 SFS 1-2	3.20
TiO_2 SFS 1-4	3.20
TiO_2 P25 [250]	3.15

Table 19. *Band gap of pure titanium.*

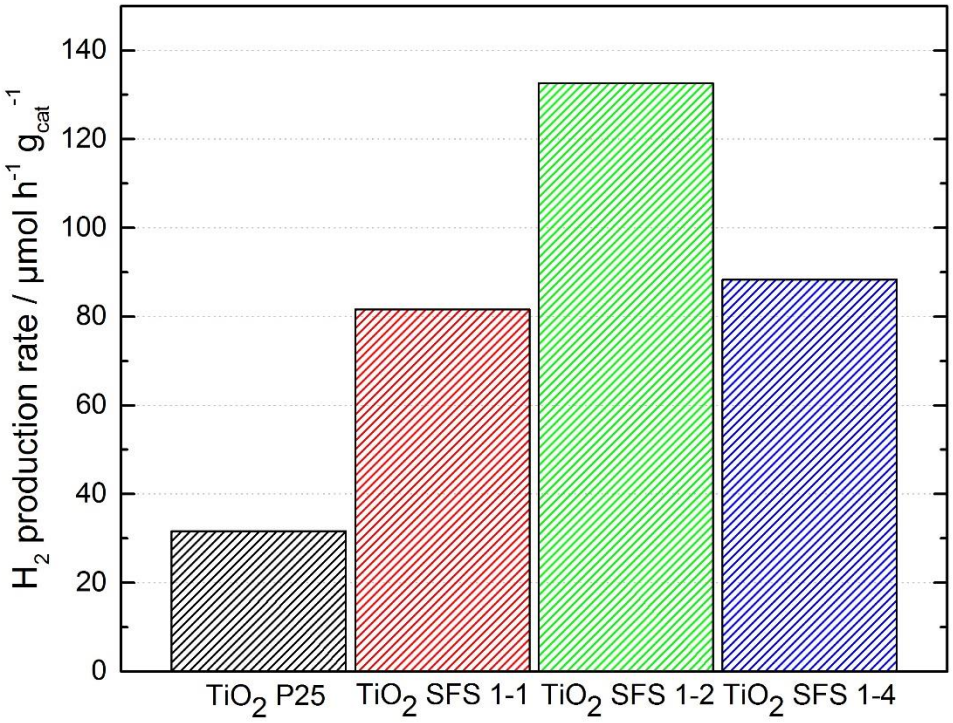

Figure 106. *Hydrogen production by methanol photoreforming using SFS prepared TiO_2 in comparison to reference P25 (experimental conditions detailed in Chapter II: 6).*

These materials were used in the setup (details in Chapter II: 6) prepared for the methanol photoreforming. The production rate once reached the reaction plateau after 60 min of irradiation can be seen in **Figure** . The average production rates of the different materials based on the experiments can be seen in **Table** . The materials prepared by SFS present, despite lower surface area and lower surface/volume ratio, a higher hydrogen production rate than the reference material. In addition, generally, the time needed for the interfacial charge transfer (especially for e^-) is much longer for larger particles thus enhancing the probability of recombination of the charge carriers.[15]

Material	Hydrogen production rate (µmol h^{-1} g_{cat}^{-1})	SSA (m^2 g^{-1})	Particle size (nm)	Cristallite size (nm)
TiO_2 SFS 1-1	81.36 ± 16.55	14.18	152	31.5
TiO_2 SFS 1-2	133.38 ± 11.01	14.18	138	22.4
TiO_2 SFS 1-4	88.75 ± 22.06	14.55	133	27.9
TiO_2 P25	35.98 ± 26.06	55 [251]	90 [252]	21

Table 20. *Hydrogen production rate.*

For particles, bigger than ~20 nm, the surface recombination regime becomes less important than the volume recombination regime. However, one may suppose that the SFS-prepared photocatalysts are subjected to better charge trapping phenomena, due to larger structure defects or to the presence of surface residues.[106]

The quantum yield of the photocatalytic reaction was calculated basing on the hydrogen production rates obtained before, the ratio between the quantity of hydrogen produced by incident photon (Chapter I – 4.1.1.) as well as the photon flux of the lamp. The photon flux of the lamp was measured with a ILT900-R spectroradiometer giving a value of 0.43 mol h^{-1}. This data were used to calculate the apparent quantum yield from the following the equation:[253 254]

$$\varphi H_2 = 3 * \left(\frac{molecules\ of\ H_2\ generated}{number\ of\ absorbed\ photons} \right) * 100 \qquad (55)$$

Here the number of hydrogen molecules generated during the reaction corresponds to two times the number of electrons generated during the reaction and the number of absorbed photons is equal to the number of incident photons during the reaction corrected by the absorbance of the material. This can be applied as the absorption spectra of titania is well known and therefore the diffusion of the particles can be eliminated from the absorption measurement.

The apparent quantum yield of the materials prepared by SFS is up to four times higher than for the reference (**Table)**. This may result from the higher production rate of the materials or from more efficient use of absorbed photons of the as-prepared samples.

Material	φH₂ (%)
TiO_2 SFS 1-1	0.00387
TiO_2 SFS 1-2	0.00633
TiO_2 SFS 1-4	0.00421
TiO_2 P25	0.00149

Table 21. *Quantum yield of methanol photoreforming using SFS prepared TiO_2 in comparison to reference P25.*

3.2. Silver modified titanium oxide

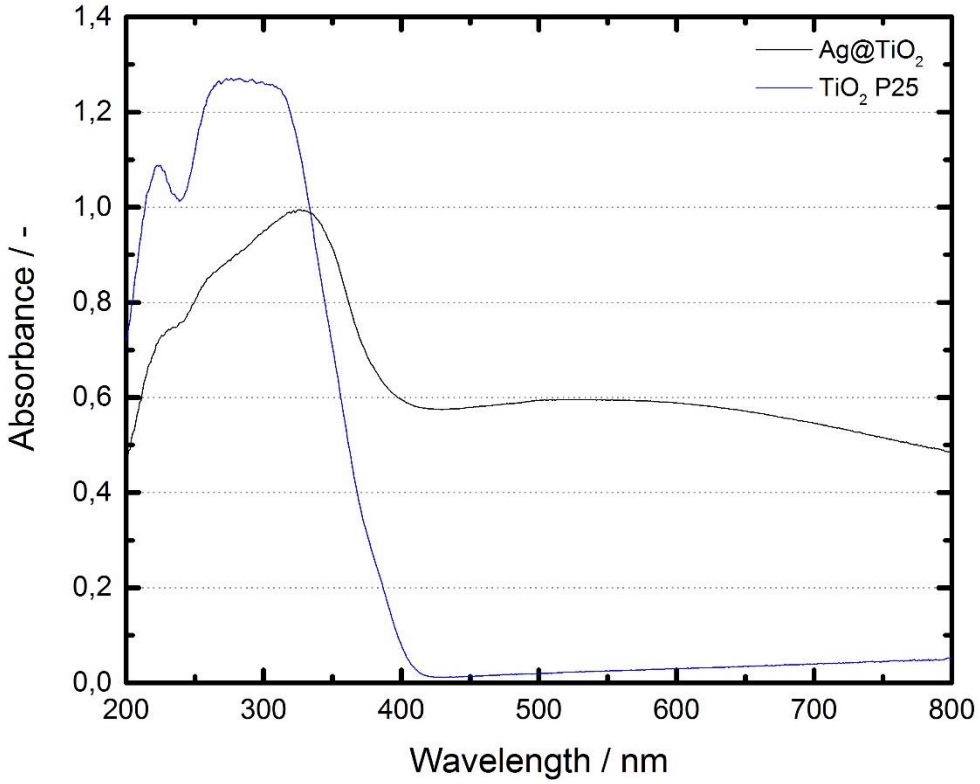

Figure 107. *UV-Vis absorbance spectra of silver-modified titanium oxide prepared by SFS.*

The photocatalytic properties of the silver-modified titanium oxide powder prepared by SFS was studied. The optical properties of the material in terms of UV-Vis absorbance is compared to the commercial sample of TiO_2 P25 (Evonik) as can be seen in **Figure** . In comparison to the reference, the titania modified with silver shows a large and additional contribution in the visible spectrum, plus a red shift of the absorbance of TiO_2. These observations might be attributed to Surface Plasmon Resonance (SPR) of silver nanoparticles or to the formation of Ag_xO surface species.

Based on the absorbance spectroscopy, the band gap of these materials could be calculated by using the Kubelka-Munk function and afterwards the Tauc equation as shown before. This resulted in a calculated band gap for this material of 2.8 eV which is lower than the pristine anatase (3.2 eV) prepared by SFS and lower than the band gap of P25 (3.1 eV).

This material was used as photocatalyst for the methanol photoreforming. The production rate once reached the reaction plateau after 100 min of irradiation can be seen in **Figure** . The average production rate, when the production plateau is

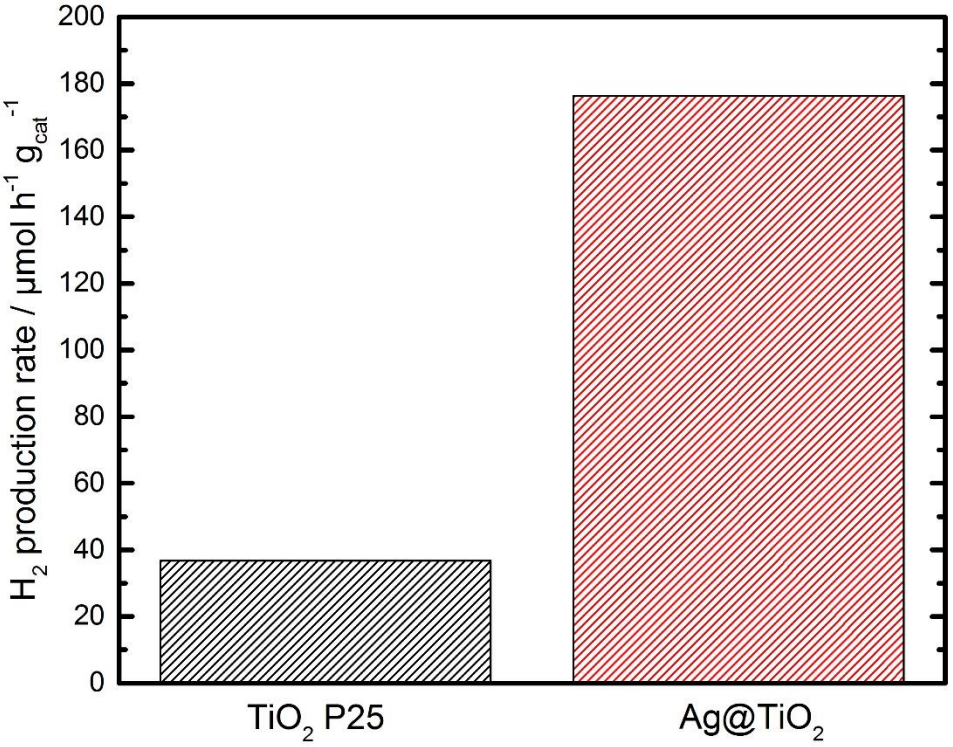

Figure 108. *Hydrogen production by photoreformation using silver loaded TiO_2 in comparison to reference P25 (experimental conditions detailed in Chapter II: 6).*

reached, is of 176. 37 ± 32.71 µmol h^{-1} g_{cat}^{-1}. The production rate (details in Chapter II: 6) of this material is not only higher than the reference material (P25) but also higher than the pristine TiO_2 prepared by the same method. The presence of silver nanoparticles that may lead to SPR properties could explain enhanced photons absorption thanks to local field enhancement or to hot electron injection into the conduction band of TiO_2. In addition, the presence of surface Ag_XO domains in close contact with TiO_2 can lead to the formation of beneficial heterojunctions. Furtermore, the silver particles, which are mainly found on the surface of the titania spheres, can act as charge carrier traps thus reducing the recombination probability and increasing the overall photocatalytic performance.[22 106]

Additionally, the quantum yield of the reaction was calculated for this material. The φH_2 for the silver loaded titania is 0.00570 % which is 3.8 times higher than the reference yield. The higher light absorption owing to the absorbance redshift allows a higher amount of charge carriers available for the catalytic reaction. This phenomenon in addition to the presence of silver on the surface to lower the surface recombination rate and acting as active reaction site may explain why this material has a higher production rate and a more efficient use of the absorbed photons.

3.3. Bismuth titanates

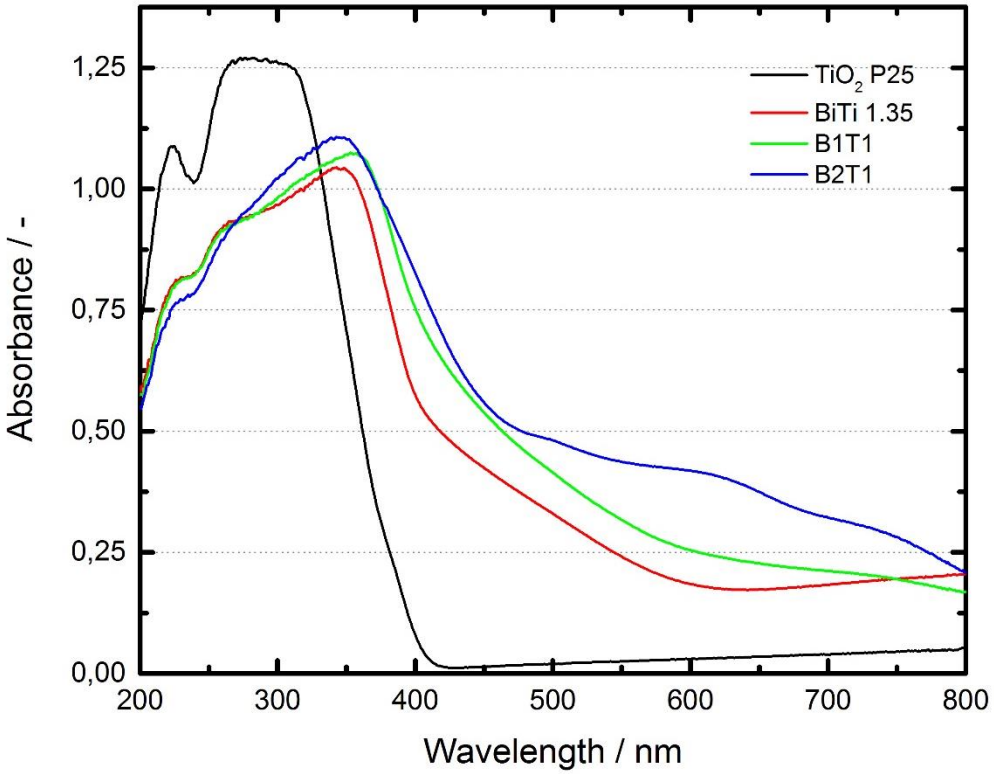

Figure 109. *UV-Vis absorbance spectra of bismuth titanates prepared by SFS.*

The photocatalytic response of the three bismuth titanates materials produced by SFS were studied by UV-Vis spectroscopy and compared to the one of pure titania P25 (**Figure**). The materials show the presence of additional contributions exhibiting large Vis-NIR absorption properties that could be attributed to the presence of bismuth titanates structures. As highlighted by the curves, the materials show an increase in the absorbance when the bismuth content in the materials increases. Therefore, the higher Bi/Ti ratio produces a redshift in the absorption characteristics of the materials.

Material	Band gap (eV)
BiTi 1.35	2.87
B1T1	2.72
B2T1	2.48

Table 22. *Band gap of bismuth titanates powders.*

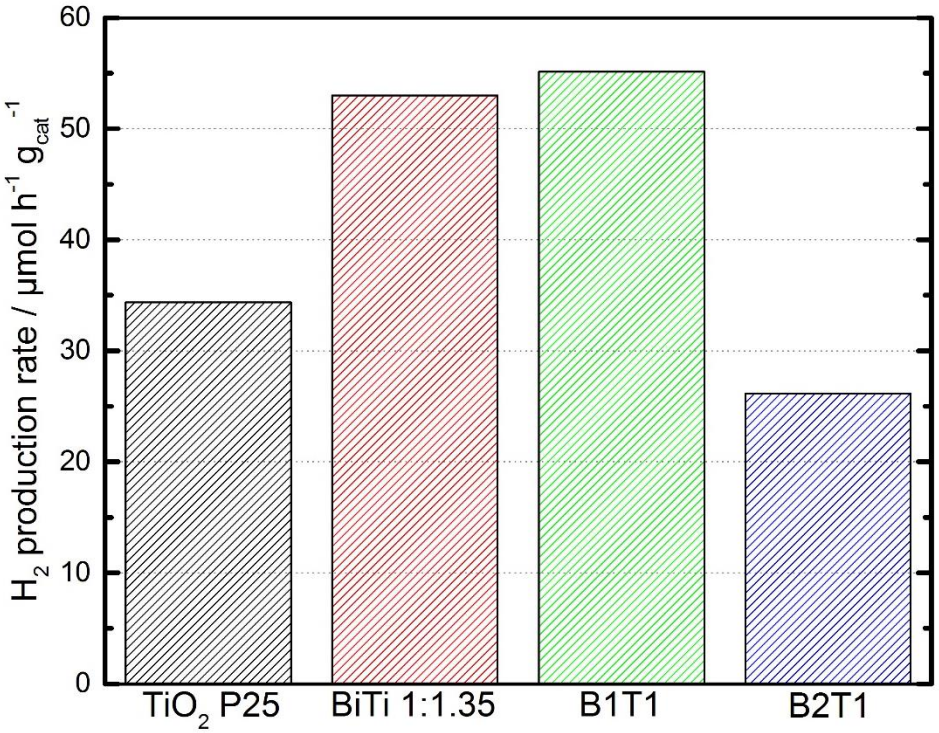

Figure 110. *Hydrogen production by photoreformation using bismuth titanates in comparison to reference P25 (experimental conditions detailed in Chapter II: 6).*

Based on the absorbance spectroscopy, the band gap of these materials could be calculated. By using the Kubelka-Munk function and afterwards the Tauc equation the calculated band gap can be seen in **Table** . The band gaps of the bismuth titanates nanomaterials are lower than the band gap of pure titanium. The lower band gap is determined by the 3d orbitals of titanium which provide the conduction band and the 2p orbitals which supply the valence band. Bismuth (cationic) modification of the structure of TiO_2 may lead to the introduction of intermediate states below the conduction band, that could explain the lowering of the band gap. The band gap of 2.6 eV is obtained for the case of the B1T1 ($Bi_2Ti_2O_7$) material. The material with a higher content of titanium, *i.e.,* BiTi 1.35 ($Bi_2Ti_2O_7$ + TiO_2) presents a wider band gap owing to the influence of the titanium oxide which is in the material. The decrease in the band gap with the increase of the Bi/Ti ratio comes from the $6s^2$ electrons of bismuth, there are responsible for the inert pair effect in Bi.[255] As consequence, these materials are able to absorb less energetic radiation in comparison to pristine titania.

Figure shows the production of the different bismuth titanates powders used as catalysts for the photoreforming of methanol when the production plateau is reached after 60 min of irradiation. The bismuth titanates B1T1 and BiTi 1.35 react in a similar manner compared to the reference material. However, the material with a higher

Material	Hydrogen production (µmol h^{-1} g_{cat}^{-1})
BiTi 1.35	54.86 ± 11.74
B1T1	53.83 ± 11.60
B2T1	26.17 ± 7.01
TiO_2 P25	35.98 ± 26.06

Table 23. *Hydrogen production in photoreformation setup.*

bismuth content, *i.e.* B2T1 has a lower hydrogen production than all the other materials. In this case the hydrogen production values are highlighted in **Table** . The main difference between B1T1 and BiTi 1.35 is the presence of an excess of titania in the form of rutile for the BiTi 1.35 which seems to increase slightly the production rate. The relatively low production rate comes from one of the main drawbacks of bismuth titanate for photocatalytic applications. This is the high charge carrier recombination rate, often dealt with by introducing metals like for example Fe or Pt.[256 257] The low production rate of B2T1 shows that titanium oxide is the photocatalyst which is aided by bismuth oxide. So even though the material is able to absorb more energy from the visible and NIR region, the contact between the reactants and the titania molecules needs to be ensured.

The quantum yield for these materials was calculated as described before (**Table)**. The quantum yield of the bismuth materials is up to two times higher than the reference material. This is a consequence of the higher absorption of the materials in the visible region, but also to the formation of the heterojunction with TiO_2 domains leading to enhanced charge separation. This leads to a higher efficiency in the use of the absorbed photons.

Material	φH_2 (%)
BiTi 1.35	0.00231
B1T1	0.00223
B2T1	0.00109
TiO_2 P25	0.00149

Table 24. *Quantum yield and relative proportions.*

3.4. Copper oxide / titanium oxide mixture

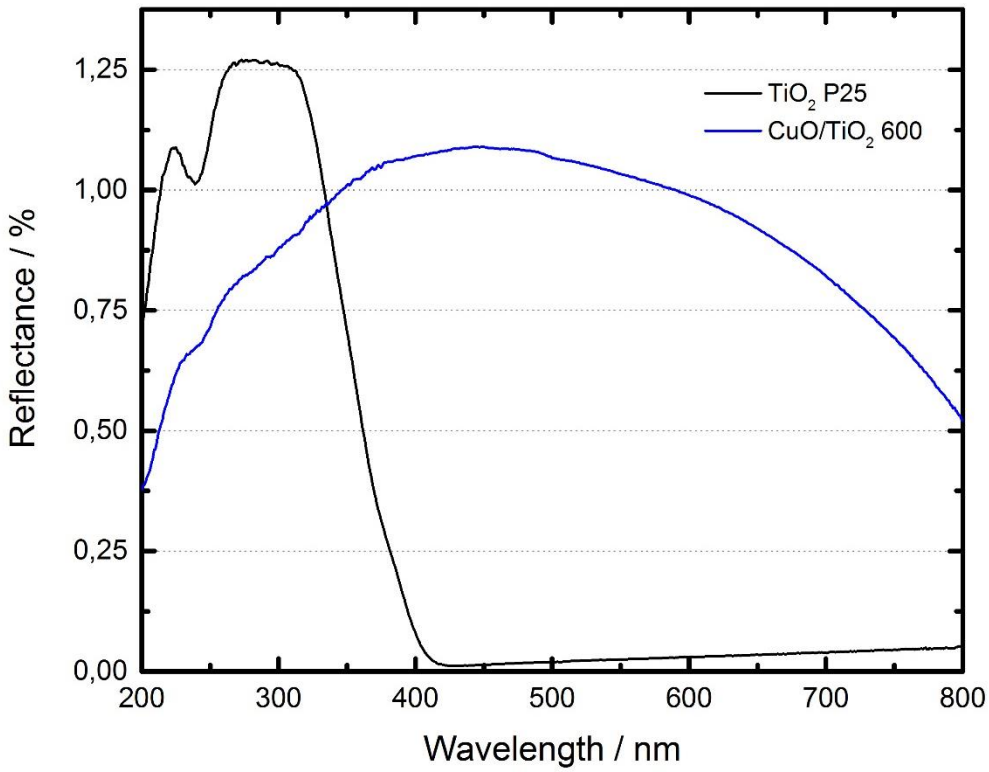

Figure 111. *UV-Vis absorbance spectra of copper/titanium mixture prepared by SFS.*

The photocatalytic properties of the copper oxide and titanium oxide mixture in form of powder prepared by SFS was studied. The optical properties of the material to UV-Vis irradiation are compared to the commercial sample of TiO_2 P25 (Evonik) as can be seen in **Figure** . This material absorbs at very high rates all along the NIR and the visible spectra. The introduction of CuO, which absorbs mainly in the visible region, helps to increase the overall absorption efficiency. In addition, the presence of SPR effects issued from Cu nanoparticles must not be excluded.

Based on the reflectance spectroscopy results, the band gap of this material was calculated. After applying the Kubelka-Munk function followed by the Tauc equation the calculated band gap of the composite copper/titanium material is 1.26 eV which is around a third of the band gap of pure anatase. It must be mentioned here that the presence of Cu_xO and Cu-Ti mixed phases cannot be excluded.

This material was used as photocatalyst for the photoreforming reaction of methanol under simulated solar light irradiation. The hydrogen production rate of the copper/titanium oxide mixture along the photocatalytic experiment can be seen in **Figure** . The production rate once the plateau is reached for this material is

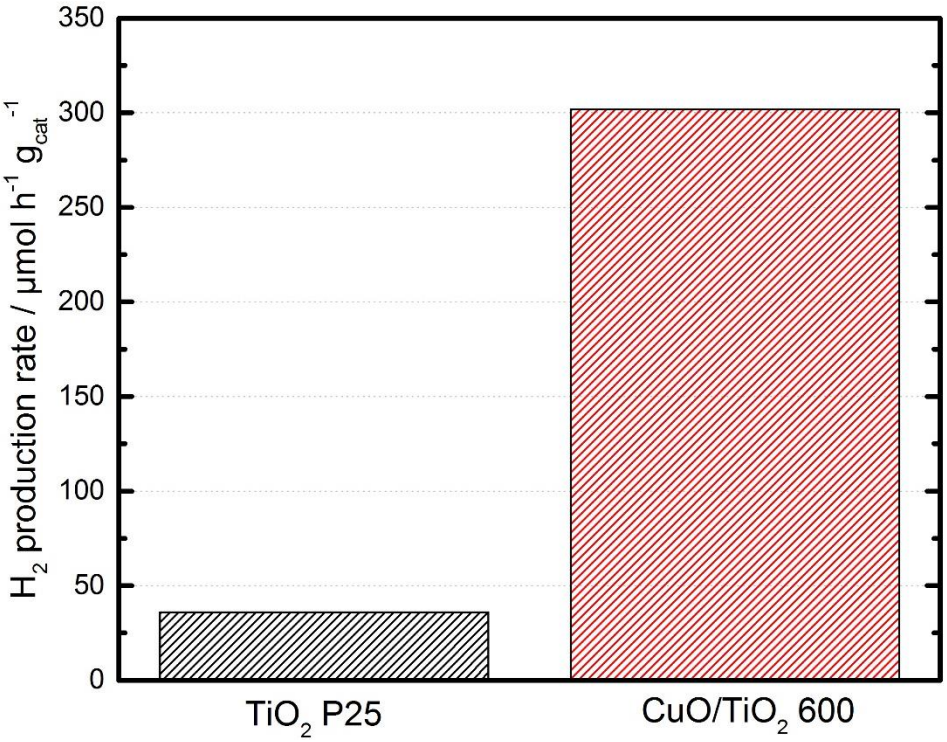

Figure 112. *Hydrogen production by photoreformation using copper/titanium oxide mixture.*

301.79 ± 58.53 µmol h^{-1} g_{cat}^{-1}. This is the highest production rate reached for the different kind of materials that were synthetized by SFS. The high photocatalytic activity of this material is owing to the intimate contact of the different Ti-, Cu- or Cu-Ti based phases probably leading to the formation of beneficial heterojunctions between different semiconductive materials, allowing increased charge separation properties but also to the ability of Cu_xO phases to absorb visible light photons. In this case one can underline that copper could also act as co-catalyst for methanol photoreforming reactions. The overall activity is enhanced because excited electrons are photogenerated in the conduction bands of both oxides resulting in an accumulation of electrons in excess in the conduction band of CuO.[258] The introduction of copper oxide to the titanium oxide network is beneficial for the charge separation during the photocatalytic reaction and acts as a water reduction site.[57 259 260]

With these results, the quantum yield of the reaction using this composite material could be calculated. The φH_2 for the copper/titanium oxide mixture is 0.01252 % which is 8.4 times higher than the reference yield. Taking into account the higher production rate and the more efficient use of absorbed photons and of the resulting photogenerated charges it is logical that the quantum yield is higher than the reference material.

4. Conclusions and perspectives

The materials prepared by SFS were successfully used as photocatalysts in a setup prepared for methanol photoreforming for the production of H_2 with the addition of silver nanoparticles. The performance was compared to a commercial reference sample of nanosized TiO_2 (Evonik P25).

The modification of these particles with silver increased the production rate thanks to the silver/silver oxide particles acting as active sites and enhancing the charge carrier separation.

Bismuth titanates with different bismuth to titanium ratios showed a higher performance in comparison to the reference material (TiO_2 P25). The introduction of bismuth produces a redshift due mainly to the presence bismuth titanates phases.

The oxide mixture of copper and titanium was the material with the highest production rate from all the materials presented. The absorption spectrum of this material shows that it is able to absorb on a very broad domain of wavelengths. Additionally, copper acts as co-catalyst and as accumulator for photoexcited electrons. Furthermore, copper oxide phases help charge carrier separation thanks to the formation of heterojunctions. These phenomena explain the high production rate of this material.

All the materials produced by SFS presented a higher quantum yield than the reference material, indicating that they were more efficient considering visible light absorption and/or increasing charge carriers separation.

The efficiency and potential applications of nanomaterials strongly depend on the synthesis method. The SFS process is a production technique which provides an interesting alternative for the preparation of photocatalytic materials. It enables the study of different materials and its mixtures.

CONCLUSION

The aim of this thesis was to develop a new synthesis process able to produce submicrometric materials with unique properties, the Spray Flash Synthesis (SFS). The objective included to synthesize oxide powders made of mixed metallic elements with a unique degree of homogeneity.

The analysis of the nanomaterial synthesis methods showed that they are generally batch syntheses which involve very complex reaction mechanisms. In comparison to these “classical” synthesis routes, the SFS process produces the material in a similar way to the sol-gel method. Nevertheless, owing to the nature of the synthesis, the reaction is stopped before the formation of the gel can take place, which makes the produced particles so singular.

The materials prepared by SFS are powders made of submicron sized particles (150-200 nm). The spherical particles adopt the morphology of the droplets of the spray during the synthesis. The production temperature was not high enough to fully decompose the precursor. In the case of TTIP, the titanium oxide precursor, only two of the four isopropyl ligands are hydrolysed. In the case of copper, the SFS process led to a transformation of the coordination sphere of the Cu atom. The study of the formation mechanism suggests that the reaction takes mainly place in the chamber of the system taking into account the reaction kinetics. In all the cases, intermediate compounds formed which were mixed with organic by-products of the reaction creating an amorphous matrix. The materials needed to be thermally treated post-process to remove the organic residues and to crystallize the materials. During this process, the external porosity of the particles is lost and they slightly sinter together. An internal porosity is formed as a consequence of the removal of volatile species and crystallization of the oxide. The particles of the materials maintained a submicrometric size after the calcination. The only exception is pristine copper oxide which formed porous micrometric aggregates.

It was demonstrated that the thermal decomposition degree of the precursor increases with the increase of the temperature. This was the case for copper oxide, for which different intermediate compounds were produced depending on the synthesis temperature. The synthesis of titanium oxide modified with silver was studied by SFS process and by classical solvothermal synthesis. The nanostructuration of the silver particles in the materials produced by SFS, lowered strongly their melting point. In

addition, it was shown that the SFS process is able to produce particles with narrower size distributions and more homogeneous morphologies and elements distributions. The research on bismuth oxide and titanium oxide showed that there are different kind of phases that can be produced with these elements depending on the relative proportions. The morphology of the particles and their size distribution are affected by the surface tension of the solution, which influences the droplet collision behaviour during the synthesis. When calcined, the elements can suffer segregation when the proportion is not stoichiometric. As in the case of silver, the formation of nanometric domains of bismuth oxide strongly influenced its melting temperature. Copper oxide and titanium oxide do not form a mixed oxide. Instead a very intimate mixture of these compounds was produced. The presence of copper oxide during the calcination had influence in the anatase to rutile transformation, in this case titanium oxide was present both as anatase and rutile.

The use of CuO/TiO_2 as oxidiser for pyrotechnical compositions demonstrated that the adsorbed species (water) react with aluminium changing the reaction mechanism. When reaching high temperatures at a slow heating rate, copper oxide decomposes and a spinel between copper oxide and alumina is formed. The introduction of titanium oxide has a great effect in desensitizing to impact and friction the nanothermites in comparison to a pure copper oxide nanothermite. However, it also reduces strongly the flame front propagation velocity. The mixing of the Al nanopowder with the oxides makes it more sensitive to ESD. It is shown that the heat released by the aluminothermic reaction is higher than the theoretical value calculated for the ideal aluminothermic mixture. The analysis of the residues of the reaction revealed that copper oxide reacts more easily with the aluminium than titanium oxide and that titanium oxide does not fully react, leaving titanium monoxide. It was also found out that copper reacts with aluminium to form an alloy ($AlCu_3$), which increases the energy released.

The materials produced by SFS achieved a higher production rate and higher quantum yield for the methanol photoreformation than commercial titanium oxide. The exception are the bismuth titanates which had production rate and quantum yield similar to the reference sample (TiO_2 P25). The introduction of elements like silver, bismuth oxide or copper oxide lowers the band gap of the materials and acts as charge carrier separator. The best material was the CuO/TiO_2 which had a band gap of 1.3 eV. The production

rate and quantum yield attained by this material are 8.3 times higher and 8.4 times higher than the reference, respectively.

The SFS system opens the opportunity to produce a wide variety of different metallic oxides and salts with tailored proportions at submicrometric sizes for all kind of different application fields. A promising idea in the pyrotechnical field is to produce composites with low sensitivity and high-performance combustion characteristics by playing on the ratios of the different elements. It would be also very interesting to produce nanothermites directly with the SFS system, which would consist in synthesizing and mixing the nanothermite components in a single step. The photocatalytic efficiency and potential applications of nanomaterials depends strongly on the synthesis method. This is why the intimate mixture degree attained by the SFS along with the size distribution of these particles produce high performing materials for the photocatalysis.

The SFS process has a wide spectrum of applications, as it could produce submicron composites for many industrial applications, such as pigments, magnetic materials or catalysts. Submicron materials are also very often used in the energy storage field, as Li-ion batteries or potassium-ion batteries (PIB) anodes. They are also demanded in the biomedical fields for implant applications, or for the production of far infrared (FIR) rectennas.

BIBLIOGRAPHY

1. Baur, W. H., Über die verfeinerung der kristallstrukturbestimmung einiger vertreter des rutiltyps: TiO2, SnO2, GeO2 und MgF2. *Acta Crystallographica* **1956,** *9* (6), 515-520.
2. Greenwood, N. N.; Earnshaw, A., *Chemistry of the Elements*. Elsevier: 2012.
3. Swamy, V.; Holbig, E.; Dubrovinsky, L. S.; Prakapenka, V.; Muddle, B. C., Mechanical properties of bulk and nanoscale TiO2 phases. *Journal of Physics and Chemistry of Solids* **2008,** *69* (9), 2332-2335.
4. Zhang, H.; Banfield, J. F., Understanding polymorphic phase transformation behavior during growth of nanocrystalline aggregates: insights from TiO2. *The Journal of Physical Chemistry B* **2000,** *104* (15), 3481-3487.
5. Zhang, W.; Zhu, Z.; Cheng, C. Y., A literature review of titanium metallurgical processes. *Hydrometallurgy* **2011,** *108* (3-4), 177-188.
6. Ellsworth, D. K.; Verhulst, D., Titanium nanoparticles move to the marketplace. **2000**.
7. Kato, S.-i.; Masuo, F., Titanium dioxide-photocatalyzed oxidation. I. *Titanium dioxide photocatalyzed liquid phase oxidation of tetralin, Kogyo Kagaku Zasshi* **1964,** *67*, 1136-1140.
8. Fujishima, A.; Honda, K., Electrochemical photolysis of water at a semiconductor electrode. *nature* **1972,** *238* (5358), 37.
9. Fujishima, A.; Rao, T. N.; Tryk, D. A., Titanium dioxide photocatalysis. *Journal of photochemistry and photobiology C: Photochemistry reviews* **2000,** *1* (1), 1-21.
10. Hoffmann, M. R.; Martin, S. T.; Choi, W.; Bahnemann, D. W., Environmental applications of semiconductor photocatalysis. *Chemical reviews* **1995,** *95* (1), 69-96.
11. Tee, S. Y.; Win, K. Y.; Teo, W. S.; Koh, L. D.; Liu, S.; Teng, C. P.; Han, M. Y., Recent progress in energy-driven water splitting. *Advanced science* **2017,** *4* (5), 1600337.
12. Szczepankiewicz, S. H.; Colussi, A.; Hoffmann, M. R., Infrared spectra of photoinduced species on hydroxylated titania surfaces. *The Journal of Physical Chemistry B* **2000,** *104* (42), 9842-9850.
13. Grätzel, M., Dye-sensitized solar cells. *Journal of photochemistry and photobiology C: Photochemistry Reviews* **2003,** *4* (2), 145-153.
14. Bai, Y.; Mora-Sero, I.; De Angelis, F.; Bisquert, J.; Wang, P., Titanium dioxide nanomaterials for photovoltaic applications. *Chemical reviews* **2014,** *114* (19), 10095-10130.
15. Asahi, R.; Taga, Y.; Mannstadt, W.; Freeman, A. J., Electronic and optical properties of anatase TiO 2. *Physical Review B* **2000,** *61* (11), 7459.
16. Scanlon, D. O.; Dunnill, C. W.; Buckeridge, J.; Shevlin, S. A.; Logsdail, A. J.; Woodley, S. M.; Catlow, C. R. A.; Powell, M. J.; Palgrave, R. G.; Parkin, I. P., Band alignment of rutile and anatase TiO 2. *Nature materials* **2013,** *12* (9), 798.
17. Maira, A.; Yeung, K.; Lee, C.; Yue, P.; Chan, C., Size effects in gas-phase photo-oxidation of trichloroethylene using nanometer-sized TiO2 catalysts. *Journal of Catalysis* **2000,** *192* (1), 185-196.
18. Goeppert, A.; Czaun, M.; Jones, J.-P.; Prakash, G. S.; Olah, G. A., Recycling of carbon dioxide to methanol and derived products–closing the loop. *Chemical Society Reviews* **2014,** *43* (23), 7995-8048.
19. Dias De Oliveira, M. E.; Vaughan, B. E.; Rykiel, E. J., Ethanol as fuel: energy, carbon dioxide balances, and ecological footprint. *BioScience* **2005,** *55* (7), 593-602.
20. Grasemann, M.; Laurenczy, G., Formic acid as a hydrogen source–recent developments and future trends. *Energy & Environmental Science* **2012,** *5* (8), 8171-8181.

21. Bowker, M., Photocatalytic hydrogen production and oxygenate photoreforming. *Catalysis letters* **2012,** *142* (8), 923-929.
22. Kawai, T.; Sakata, T., Photocatalytic hydrogen production from liquid methanol and water. *Journal of the Chemical Society, Chemical Communications* **1980,** (15), 694-695.
23. Ni, M.; Leung, M. K.; Leung, D. Y.; Sumathy, K., A review and recent developments in photocatalytic water-splitting using TiO2 for hydrogen production. *Renewable and Sustainable Energy Reviews* **2007,** *11* (3), 401-425.
24. Linsebigler, A. L.; Lu, G.; Yates Jr, J. T., Photocatalysis on TiO2 surfaces: principles, mechanisms, and selected results. *Chemical reviews* **1995,** *95* (3), 735-758.
25. Burda, C.; Lou, Y.; Chen, X.; Samia, A. C.; Stout, J.; Gole, J. L., Enhanced nitrogen doping in TiO2 nanoparticles. *Nano letters* **2003,** *3* (8), 1049-1051.
26. Wang, L. L.; Munir, Z.; Maximov, Y. M., Thermite reactions: their utilization in the synthesis and processing of materials. *Journal of Materials Science* **1993,** *28* (14), 3693-3708.
27. Puszynski, J., Processing and characterization of aluminum-based nanothermites. *Journal of Thermal Analysis and Calorimetry* **2009,** *96* (3), 677-685.
28. Boggs, T.; Zurn, D.; Cordes, H.; Covino, J., Combustion of ammonium perchlorate and various inorganic additives. *Journal of Propulsion and Power* **1988,** *4* (1), 27-40.
29. Reid, D. L.; Kreitz, K. R.; Stephens, M. A.; King, J. E.; Nachimuthu, P.; Petersen, E. L.; Seal, S., Development of highly active titania-based nanoparticles for energetic materials. *The Journal of Physical Chemistry C* **2011,** *115* (21), 10412-10418.
30. Dargar, S.; Groven, L.; Swiatkiewicz, J.; Puszynski, J., In situ densification of SHS composites from nanoreactants. *International Journal of Self-Propagating High-Temperature Synthesis* **2007,** *16* (3), 125-132.
31. Patnaik, P., *Handbook of inorganic chemicals*. McGraw-Hill New York: 2003; Vol. 529.
32. Eranna, G.; Joshi, B.; Runthala, D.; Gupta, R., Oxide materials for development of integrated gas sensors—a comprehensive review. *Critical Reviews in Solid State and Materials Sciences* **2004,** *29* (3-4), 111-188.
33. Kharton, V.; Marques, F.; Atkinson, A., Transport properties of solid oxide electrolyte ceramics: a brief review. *Solid State Ionics* **2004,** *174* (1-4), 135-149.
34. Shuk, P.; Wiemhöfer, H.-D.; Guth, U.; Göpel, W.; Greenblatt, M., Oxide ion conducting solid electrolytes based on Bi2O3. *Solid State Ionics* **1996,** *89* (3-4), 179-196.
35. Van Uitert, L.; Egerton, L., Bismuth titanate. A ferroelectric. *Journal of Applied Physics* **1961,** *32* (5), 959-959.
36. Cummins, S.; Cross, L., Electrical and optical properties of ferroelectric Bi4Ti3O12 single crystals. *Journal of Applied Physics* **1968,** *39* (5), 2268-2274.
37. Yang, X.; Qu, N.; Wang, H.; Huang, B.; Wei, J., A study of La-doped Bi2Ti2O7 nanocrystals prepared by chemical solution deposition technique. *Materials Letters* **2006,** *60* (23), 2886-2888.
38. Thiruramanathan, P.; Sharma, S. K.; Sankar, S.; Ganesh, R. S.; Marikani, A.; Kim, D. Y., Synthesis of bismuth titanate (BTO) nanopowder and fabrication of microstrip rectangular patch antenna. *Applied Physics A* **2016,** *122* (12), 1006.
39. Subbarao, E., Ferroelectricity in Bi 4 Ti 3 O 12 and its solid solutions. *Physical Review* **1961,** *122* (3), 804.

40. Yao, W. F.; Wang, H.; Xu, X. H.; Shang, S. X.; Hou, Y.; Zhang, Y.; Wang, M., Synthesis and photocatalytic property of bismuth titanate Bi4Ti3O12. *Materials Letters* **2003,** *57* (13-14), 1899-1902.
41. Meenakshi, P.; Selvaraj, M., Bismuth titanate as an infrared reflective pigment for cool roof coating. *Solar Energy Materials and Solar Cells* **2018,** *174*, 530-537.
42. Nogueira, A. E.; Longo, E.; Leite, E. R.; Camargo, E. R., Synthesis and photocatalytic properties of bismuth titanate with different structures via oxidant peroxo method (OPM). *Journal of colloid and interface science* **2014,** *415*, 89-94.
43. Santos, D.; Barbosa, L.; Silva, R.; Macedo, Z., Fabrication and Electrical Characterization of Translucent Bi12TiO20 Ceramics. *Advances in Condensed Matter Physics* **2013,** *2013*.
44. Yao, W. F.; Wang, H.; Xu, X. H.; Cheng, X. F.; Huang, J.; Shang, S. X.; Yang, X. N.; Wang, M., Photocatalytic property of bismuth titanate Bi12TiO20 crystals. *Applied Catalysis A: General* **2003,** *243* (1), 185-190.
45. Xu, S.; Shangguan, W.; Yuan, J.; Shi, J.; Chen, M., Photocatalytic properties of bismuth titanate Bi12TiO20 prepared by co-precipitation processing. *Materials Science and Engineering: B* **2007,** *137* (1-3), 108-111.
46. Zhu, X.; Zhang, J.; Chen, F., Study on visible light photocatalytic activity and mechanism of spherical Bi12TiO20 nanoparticles prepared by low-power hydrothermal method. *Applied Catalysis B: Environmental* **2011,** *102* (1-2), 316-322.
47. Sleight, A. W., Chemistry of high-temperature superconductors. *Science* **1988,** *242* (4885), 1519-1527.
48. Xu, J.; Ji, W.; Shen, Z.; Tang, S.; Ye, X.; Jia, D.; Xin, X., Preparation and characterization of CuO nanocrystals. *Journal of Solid State Chemistry* **1999,** *147* (2), 516-519.
49. Motoyoshi, R.; Oku, T.; Suzuki, A.; Kikuchi, K.; Kikuchi, S.; Jeyadevan, B.; Cuya, J., Fabrication and characterization of cuprous oxide: fullerene solar cells. *Synthetic metals* **2010,** *160* (11-12), 1219-1222.
50. Singh, J.; Kaur, G.; Rawat, M., A brief review on synthesis and characterization of copper oxide nanoparticles and its applications. *J. Bioelectron. Nanotechnol* **2016,** *1* (9).
51. Ren, G.; Hu, D.; Cheng, E. W.; Vargas-Reus, M. A.; Reip, P.; Allaker, R. P., Characterisation of copper oxide nanoparticles for antimicrobial applications. *International journal of antimicrobial agents* **2009,** *33* (6), 587-590.
52. Lafontaine, E.; Comet, M., *Nanothermites*. John Wiley & Sons: 2016.
53. Fischer, S.; Grubelich, M. In *A survey of combustible metals, thermites, and intermetallics for pyrotechnic applications*, 32nd Joint Propulsion Conference and Exhibit, 1996; p 3018.
54. Jian, G.; Liu, L.; Zachariah, M. R., Facile aerosol route to hollow CuO spheres and its superior performance as an oxidizer in nanoenergetic gas generators. *Advanced Functional Materials* **2013,** *23* (10), 1341-1346.
55. Muscetta, M.; Andreozzi, R.; Clarizia, L.; Di Somma, I.; Marotta, R., Hydrogen production through photoreforming processes over Cu2O/TiO2 composite materials: A mini-review. *International Journal of Hydrogen Energy* **2020**.
56. Chiang, K.; Amal, R.; Tran, T., Photocatalytic degradation of cyanide using titanium dioxide modified with copper oxide. *Advances in Environmental Research* **2002,** *6* (4), 471-485.
57. Bandara, J.; Udawatta, C.; Rajapakse, C., Highly stable CuO incorporated TiO 2 catalyst for photocatalytic hydrogen production from H2O. *Photochemical & photobiological sciences* **2005,** *4* (11), 857-861.

58. Kim, T. W.; Ha, H.-W.; Paek, M.-J.; Hyun, S.-H.; Choy, J.-H.; Hwang, S.-J., Unique phase transformation behavior and visible light photocatalytic activity of titanium oxide hybridized with copper oxide. *Journal of Materials Chemistry* **2010,** *20* (16), 3238-3245.
59. Matijevic, E., Production of monodispersed colloidal particles. *Annual Review of Materials Science* **1985,** *15* (1), 483-516.
60. Zaleska, A., Doped-TiO2: a review. *Recent patents on engineering* **2008,** *2* (3), 157-164.
61. Dambournet, D.; Belharouak, I.; Amine, K., Tailored preparation methods of TiO2 anatase, rutile, brookite: mechanism of formation and electrochemical properties. *Chemistry of materials* **2009,** *22* (3), 1173-1179.
62. Arnal, P.; Corriu, R. J.; Leclercq, D.; Mutin, P. H.; Vioux, A., A Solution Chemistry Study of Nonhydrolytic Sol− Gel Routes to Titania. *Chemistry of materials* **1997,** *9* (3), 694-698.
63. Müller, U., *Inorganic structural chemistry*. New York: 1993.
64. Cohen, H. J., Cyclic nitrilotriethylene triorganosilyl titanate (IV):'Mono-','di-'and 'trititanates'. *Journal of Organometallic Chemistry* **1966,** *5* (5), 413-419.
65. Bickmore, C. R.; Waldner, K. F.; Baranwal, R.; Hinklin, T.; Treadwell, D. R.; Laine, R. M., Ultrafine titania by flame spray pyrolysis of a titanatrane complex. *Journal of the European Ceramic Society* **1998,** *18* (4), 287-297.
66. Livage, J.; Henry, M.; Sanchez, C., Sol-gel chemistry of transition metal oxides. *Progress in solid state chemistry* **1988,** *18* (4), 259-341.
67. Rahtu, A.; Ritala, M., Reaction mechanism studies on titanium isopropoxide–water atomic layer deposition process. *Chemical Vapor Deposition* **2002,** *8* (1), 21-28.
68. Chemseddine, A.; Moritz, T., Nanostructuring titania: control over nanocrystal structure, size, shape, and organization. *European journal of inorganic chemistry* **1999,** *1999* (2), 235-245.
69. Sugimoto, T.; Okada, K.; Itoh, H., Synthetic of uniform spindle-type titania particles by the gel–sol method. Elsevier: 1997.
70. Kim, C.-S.; Moon, B. K.; Park, J.-H.; Choi, B.-C.; Seo, H.-J., Solvothermal synthesis of nanocrystalline TiO2 in toluene with surfactant. *Journal of Crystal Growth* **2003,** *257* (3-4), 309-315.
71. Zhang, Z.; Zhong, X.; Liu, S.; Li, D.; Han, M., Aminolysis route to monodisperse titania nanorods with tunable aspect ratio. *Angewandte Chemie International Edition* **2005,** *44* (22), 3466-3470.
72. Menzel, R.; Duerrbeck, A.; Liberti, E.; Yau, H. C.; McComb, D.; Shaffer, M. S., Determining the morphology and photocatalytic activity of two-dimensional anatase nanoplatelets using reagent stoichiometry. *Chemistry of Materials* **2013,** *25* (10), 2137-2145.
73. Jun, Y.-w.; Casula, M. F.; Sim, J.-H.; Kim, S. Y.; Cheon, J.; Alivisatos, A. P., Surfactant-assisted elimination of a high energy facet as a means of controlling the shapes of TiO2 nanocrystals. *Journal of the American Chemical Society* **2003,** *125* (51), 15981-15985.
74. Wang, C.-C.; Ying, J. Y., Sol− gel synthesis and hydrothermal processing of anatase and rutile titania nanocrystals. *Chemistry of materials* **1999,** *11* (11), 3113-3120.
75. Niederberger, M.; Garnweitner, G., Organic reaction pathways in the nonaqueous synthesis of metal oxide nanoparticles. *Chemistry–A European Journal* **2006,** *12* (28), 7282-7302.

76. Oskam, G.; Nellore, A.; Penn, R. L.; Searson, P. C., The growth kinetics of TiO2 nanoparticles from titanium (IV) alkoxide at high water/titanium ratio. *The Journal of Physical Chemistry B* **2003,** *107* (8), 1734-1738.
77. Gerasimova, L.; Maslova, M., Hydrothermal behavior of titanium (IV) sulfate solutions. *Russian Journal of Inorganic Chemistry* **2012,** *57* (3), 313-319.
78. Xie, R.-C.; Shang, J. K., Morphological control in solvothermal synthesis of titanium oxide. *Journal of materials science* **2007,** *42* (16), 6583-6589.
79. Xu, R.; Xu, Y., *Modern inorganic synthetic chemistry*. Elsevier: 2010.
80. Kim, C.-S.; Moon, B. K.; Park, J.-H.; Chung, S. T.; Son, S.-M., Synthesis of nanocrystalline TiO2 in toluene by a solvothermal route. *Journal of crystal growth* **2003,** *254* (3-4), 405-410.
81. Wen, B.-M.; Liu, C.-Y.; Liu, Y., Solvothermal synthesis of ultralong single-crystalline TiO 2 nanowires. *New journal of chemistry* **2005,** *29* (7), 969-971.
82. Kominami, H.; Kato, J.-i.; Takada, Y.; Doushi, Y.; Ohtani, B.; Nishimoto, S.-i.; Inoue, M.; Inui, T.; Kera, Y., Novel synthesis of microcrystalline titanium (IV) oxide having high thermal stability and ultra-high photocatalytic activity: thermal decomposition of titanium (IV) alkoxide in organic solvents. *Catalysis Letters* **1997,** *46* (3-4), 235-240.
83. Dastan, D.; Chaure, N.; Kartha, M., Surfactants assisted solvothermal derived titania nanoparticles: synthesis and simulation. *Journal of Materials Science: Materials in Electronics* **2017,** *28* (11), 7784-7796.
84. Seifried, S.; Winterer, M.; Hahn, H., Nanocrystalline titania films and particles by chemical vapor synthesis. *Chemical Vapor Deposition* **2000,** *6* (5), 239-244.
85. Ayllon, J.; Figueras, A.; Garelik, S.; Spirkova, L.; Durand, J.; Cot, L., Preparation of TiO2 powder using titanium tetraisopropoxide decomposition in a plasma enhanced chemical vapor deposition (PECVD) reactor. *Journal of materials science letters* **1999,** *18* (16), 1319-1321.
86. Gurav, A.; Kodas, T.; Pluym, T.; Xiong, Y., Aerosol processing of materials. *Aerosol science and technology* **1993,** *19* (4), 411-452.
87. Martin, P. M., *Handbook of deposition technologies for films and coatings: science, applications and technology*. William Andrew: 2009.
88. Wu, J.-J.; Yu, C.-C., Aligned TiO2 nanorods and nanowalls. *The Journal of Physical Chemistry B* **2004,** *108* (11), 3377-3379.
89. Jang, H. D.; Kim, S.-K., Controlled synthesis of titanium dioxide nanoparticles in a modified diffusion flame reactor. *Materials research bulletin* **2001,** *36* (3-4), 627-637.
90. Strobel, R.; Pratsinis, S. E., Flame aerosol synthesis of smart nanostructured materials. *Journal of Materials Chemistry* **2007,** *17* (45), 4743-4756.
91. Oh, S.-M.; Ishigaki, T., Preparation of pure rutile and anatase TiO2 nanopowders using RF thermal plasma. *Thin Solid Films* **2004,** *457* (1), 186-191.
92. Ilie, A. G.; Scarisoreanu, M.; Dutu, E.; Dumitrache, F.; Banici, A.-M.; Fleaca, C. T.; Vasile, E.; Mihailescu, I., Study of phase development and thermal stability in as synthesized TiO2 nanoparticles by laser pyrolysis: ethylene uptake and oxygen enrichment. *Applied Surface Science* **2018,** *427*, 798-806.
93. Blešić, M. D.; Šaponjić, Z.; Nedeljković, J.; Uskoković, D., TiO2 films prepared by ultrasonic spray pyrolysis of nanosize precursor. *Materials letters* **2002,** *54* (4), 298-302.
94. GmbH, E. R. E., Product information AEROXIDE® TiO2 P25. *www.aerosil.com* **2020**.
95. Adschiri, T.; Hakuta, Y.; Arai, K. J. I.; research, e. c., Hydrothermal synthesis of metal oxide fine particles at supercritical conditions. **2000,** *39* (12), 4901-4907.

96. Hakuta, Y.; Haganuma, T.; Sue, K.; Adschiri, T.; Arai, K. J. M. r. b., Continuous production of phosphor YAG: Tb nanoparticles by hydrothermal synthesis in supercritical water. **2003,** *38* (7), 1257-1265.
97. Desmoulins-Krawiec, S.; Aymonier, C.; Loppinet-Serani, A.; Weill, F.; Gorsse, S.; Etourneau, J.; Cansell, F. J. J. o. M. C., Synthesis of nanostructured materials in supercritical ammonia: nitrides, metals and oxides. **2004,** *14* (2), 228-232.
98. Karlsson, H. L.; Gustafsson, J.; Cronholm, P.; Möller, L., Size-dependent toxicity of metal oxide particles—a comparison between nano-and micrometer size. *Toxicology letters* **2009,** *188* (2), 112-118.
99. Norris, D. J.; Efros, A. L.; Erwin, S. C., Doped nanocrystals. *Science* **2008,** *319* (5871), 1776-1779.
100. Pearton, S.; Abernathy, C.; Overberg, M.; Thaler, G.; Norton, D.; Theodoropoulou, N.; Hebard, A.; Park, Y.; Ren, F.; Kim, J., Wide band gap ferromagnetic semiconductors and oxides. *Journal of Applied Physics* **2003,** *93* (1), 1-13.
101. Klimov, V. I.; Ivanov, S. A.; Nanda, J.; Achermann, M.; Bezel, I.; McGuire, J. A.; Piryatinski, A., Single-exciton optical gain in semiconductor nanocrystals. *Nature* **2007,** *447* (7143), 441-446.
102. Michalet, X.; Pinaud, F. F.; Bentolila, L. A.; Tsay, J. M.; Doose, S.; Li, J. J.; Sundaresan, G.; Wu, A.; Gambhir, S.; Weiss, S., Quantum dots for live cells, in vivo imaging, and diagnostics. *science* **2005,** *307* (5709), 538-544.
103. Gur, I.; Fromer, N. A.; Geier, M. L.; Alivisatos, A. P., Air-stable all-inorganic nanocrystal solar cells processed from solution. *Science* **2005,** *310* (5747), 462-465.
104. Mori, K.; Yamashita, H.; Anpo, M., Photocatalytic reduction of CO 2 with H2O on various titanium oxide photocatalysts. *Rsc Advances* **2012,** *2* (8), 3165-3172.
105. Bowker, M.; Morton, C.; Kennedy, J.; Bahruji, H.; Greves, J.; Jones, W.; Davies, P. R.; Brookes, C.; Wells, P.; Dimitratos, N., Hydrogen production by photoreforming of biofuels using Au, Pd and Au–Pd/TiO2 photocatalysts. *Journal of Catalysis* **2014,** *310*, 10-15.
106. Chiarello, G. L.; Selli, E.; Forni, L., Photocatalytic hydrogen production over flame spray pyrolysis-synthesised TiO2 and Au/TiO2. *Applied Catalysis B: Environmental* **2008,** *84* (1-2), 332-339.
107. Seery, M. K.; George, R.; Floris, P.; Pillai, S. C., Silver doped titanium dioxide nanomaterials for enhanced visible light photocatalysis. *Journal of Photochemistry and Photobiology A: Chemistry* **2007,** *189* (2-3), 258-263.
108. Deshmukh, S.; Dhokale, R.; Yadav, H.; Achary, S.; Delekar, S., Titania–supported silver nanoparticles: An efficient and reusable catalyst for reduction of 4-nitrophenol. *Applied surface science* **2013,** *273*, 676-683.
109. Turnbull, D., Formation of crystal nuclei in liquid metals. *Journal of Applied Physics* **1950,** *21* (10), 1022-1028.
110. Dalpian, G. M.; Chelikowsky, J. R., Self-purification in semiconductor nanocrystals. *Physical review letters* **2006,** *96* (22), 226802.
111. Erwin, S. C.; Zu, L.; Haftel, M. I.; Efros, A. L.; Kennedy, T. A.; Norris, D. J., Doping semiconductor nanocrystals. *Nature* **2005,** *436* (7047), 91-94.
112. Zhu, J.; Zheng, W.; He, B.; Zhang, J.; Anpo, M., Characterization of Fe–TiO2 photocatalysts synthesized by hydrothermal method and their photocatalytic reactivity for photodegradation of XRG dye diluted in water. *Journal of Molecular Catalysis A: Chemical* **2004,** *216* (1), 35-43.
113. Bessekhouad, Y.; Robert, D.; Weber, J.-V.; Chaoui, N., Effect of alkaline-doped TiO2 on photocatalytic efficiency. *Journal of Photochemistry and Photobiology A: Chemistry* **2004,** *167* (1), 49-57.

114. Colmenares, J.; Aramendia, M.; Marinas, A.; Marinas, J.; Urbano, F., Synthesis, characterization and photocatalytic activity of different metal-doped titania systems. *Applied Catalysis A: General* **2006,** *306*, 120-127.
115. Anpo, M., Use of visible light. Second-generation titanium oxide photocatalysts prepared by the application of an advanced metal ion-implantation method. *Pure and applied chemistry* **2000,** *72* (9), 1787-1792.
116. Yamashita, H.; Harada, M.; Misaka, J.; Takeuchi, M.; Ikeue, K.; Anpo, M., Degradation of propanol diluted in water under visible light irradiation using metal ion-implanted titanium dioxide photocatalysts. *Journal of Photochemistry and Photobiology A: Chemistry* **2002,** *148* (1-3), 257-261.
117. Cao, Y.; Yang, W.; Zhang, W.; Liu, G.; Yue, P., Improved photocatalytic activity of Sn 4+ doped TiO 2 nanoparticulate films prepared by plasma-enhanced chemical vapor deposition. *New Journal of Chemistry* **2004,** *28* (2), 218-222.
118. Gracia, F.; Holgado, J.; Caballero, A.; Gonzalez-Elipe, A., Structural, Optical, and Photoelectrochemical Properties of M n+− TiO2 Model Thin Film Photocatalysts. *The Journal of Physical Chemistry B* **2004,** *108* (45), 17466-17476.
119. Majimel, M.; Marre, S.; Garrido, E.; Aymonier, C. J. C. V. D., Supercritical fluid chemical deposition as an alternative process to CVD for the surface modification of materials. **2011,** *17* (10-12), 342-352.
120. Vamathevan, V.; Amal, R.; Beydoun, D.; Low, G.; McEvoy, S., Photocatalytic oxidation of organics in water using pure and silver-modified titanium dioxide particles. *Journal of Photochemistry and Photobiology A: Chemistry* **2002,** *148* (1-3), 233-245.
121. Lee, M. S.; Hong, S.-S.; Mohseni, M., Synthesis of photocatalytic nanosized TiO2–Ag particles with sol–gel method using reduction agent. *Journal of Molecular Catalysis A: Chemical* **2005,** *242* (1-2), 135-140.
122. Mogal, S. I.; Gandhi, V. G.; Mishra, M.; Tripathi, S.; Shripathi, T.; Joshi, P. A.; Shah, D. O., Single-step synthesis of silver-doped titanium dioxide: influence of silver on structural, textural, and photocatalytic properties. *Industrial & Engineering Chemistry Research* **2014,** *53* (14), 5749-5758.
123. Chang, C.-C.; Lin, C.-K.; Chan, C.-C.; Hsu, C.-S.; Chen, C.-Y., Photocatalytic properties of nanocrystalline TiO2 thin film with Ag additions. *Thin Solid Films* **2006,** *494* (1-2), 274-278.
124. Binitha, N.; Yaakob, Z.; Reshmi, M.; Sugunan, S.; Ambili, V.; Zetty, A., Preparation and characterization of nano silver-doped mesoporous titania photocatalysts for dye degradation. *Catalysis Today* **2009,** *147*, S76-S80.
125. Poroshkov, V.; Gurin, V., Surface structures on titanium dioxide electrodes after electrochemical silver deposition. *Surface science* **1995,** *331*, 1520-1525.
126. Tobaldi, D.; Piccirillo, C.; Pullar, R.; Gualtieri, A.; Seabra, M.; Castro, P.; Labrincha, J., Silver-modified nano-titania as an antibacterial agent and photocatalyst. *The Journal of Physical Chemistry C* **2014,** *118* (9), 4751-4766.
127. Martinez-Gutierrez, F.; Olive, P. L.; Banuelos, A.; Orrantia, E.; Nino, N.; Sanchez, E. M.; Ruiz, F.; Bach, H.; Av-Gay, Y., Synthesis, characterization, and evaluation of antimicrobial and cytotoxic effect of silver and titanium nanoparticles. *Nanomedicine: Nanotechnology, Biology and Medicine* **2010,** *6* (5), 681-688.
128. Juan, L.; Zhimin, Z.; Anchun, M.; Lei, L.; Jingchao, Z., Deposition of silver nanoparticles on titanium surface for antibacterial effect. *International journal of nanomedicine* **2010,** *5*, 261.
129. Awazu, K.; Fujimaki, M.; Rockstuhl, C.; Tominaga, J.; Murakami, H.; Ohki, Y.; Yoshida, N.; Watanabe, T., A plasmonic photocatalyst consisting of silver nanoparticles embedded in titanium dioxide. *Journal of the American Chemical Society* **2008,** *130* (5), 1676-1680.

130. Qiu, Y.; Liu, D.; Yang, J.; Yang, S., Controlled synthesis of bismuth oxide nanowires by an oxidative metal vapor transport deposition technique. *Advanced materials* **2006,** *18* (19), 2604-2608.
131. Raza, W.; Haque, M.; Muneer, M.; Harada, T.; Matsumura, M., Synthesis, characterization and photocatalytic performance of visible light induced bismuth oxide nanoparticle. *Journal of Alloys and Compounds* **2015,** *648*, 641-650.
132. Gattow, G., Die Polymorphie der Wismutoxyde. *Angewandte Chemie* **1963,** *75* (16-17), 799-799.
133. Malmros, G., The crystal structure of a-Bi2O3. *Acta Chemica Scandinavica* **1970,** *24*, 384Ā396.
134. MEDERNACH, J. W.; SNYDER, R. L., Powder diffraction patterns and structures of the bismuth oxides. *Journal of the American Ceramic Society* **1978,** *61* (11-12), 494-497.
135. Harwig, H., On the Structure of Bismuthsesquioxide: The α, β, γ, and δ-Phase. *Zeitschrift für anorganische und allgemeine Chemie* **1978,** *444* (1), 151-166.
136. Oniyama, E.; Wahlbeck, P., Phase Equilibria in the Bismuth− Oxygen System. *The Journal of Physical Chemistry B* **1998,** *102* (22), 4418-4425.
137. Krüger, J.; Winkler, P.; Lüderitz, E.; Lück, M.; Wolf, H. U., Bismuth, bismuth alloys, and bismuth compounds. *Ullmann's Encyclopedia of Industrial Chemistry* **2000**.
138. Grice, J. D., A solution to the crystal structures of bismutite and beyerite. *The Canadian Mineralogist* **2002,** *40* (2), 693-698.
139. Mark, H. F.; Kirk, R. E.; Othmer, D. F.; Grayson, M.; Eckroth, D., *Kirk-Othmer encyclopedia of chemical technology: Vol. 1*. John Wiley & Sons, Incorporated: 1978.
140. Mallahi, M.; Shokuhfar, A.; Vaezi, M.; Esmaeilirad, A.; Mazinani, V., Synthesis and characterization of bismuth oxide nanoparticles via sol-gel method.
141. Fruth, V.; Popa, M.; Berger, D.; Ramer, R.; Gartner, M.; Ciulei, A.; Zaharescu, M., Deposition and characterisation of bismuth oxide thin films. *Journal of the European Ceramic Society* **2005,** *25* (12), 2171-2174.
142. Chen, R.; Shen, Z.-R.; Wang, H.; Zhou, H.-J.; Liu, Y.-P.; Ding, D.-T.; Chen, T.-H., Fabrication of mesh-like bismuth oxide single crystalline nanoflakes and their visible light photocatalytic activity. *Journal of Alloys and Compounds* **2011,** *509* (5), 2588-2596.
143. Eberl, J.; Kisch, H., Visible light photo-oxidations in the presence of α-Bi 2 O 3. *Photochemical & Photobiological Sciences* **2008,** *7* (11), 1400-1406.
144. Martirosyan, K.; Wang, L.; Vicent, A.; Luss, D., Synthesis and performance of bismuth trioxide nanoparticles for high energy gas generator use. *Nanotechnology* **2009,** *20* (40), 405609.
145. Takeyama, T.; Takahashi, N.; Nakamura, T.; Itoh, S., Bi2O3 rods deposited under atmospheric pressure by means of halide CVD on c-sapphire. *Solid state communications* **2005,** *133* (12), 771-774.
146. Lin, G.; Tan, D.; Luo, F.; Chen, D.; Zhao, Q.; Qiu, J.; Xu, Z., Fabrication and photocatalytic property of α-Bi2O3 nanoparticles by femtosecond laser ablation in liquid. *Journal of Alloys and Compounds* **2010,** *507* (2), L43-L46.
147. Mädler, L.; Pratsinis, S. E., Bismuth oxide nanoparticles by flame spray pyrolysis. *Journal of the American Ceramic Society* **2002,** *85* (7), 1713-1718.
148. Rao, A. P.; Robin, A.; Komarneni, S., Bismuth titanate from nanocomposite and sol-gel processes. *Materials Letters* **1996,** *28* (4-6), 469-473.
149. Umabala, A.; Suresh, M.; Prasadarao, A., Bismuth titanate from coprecipitated stoichiometric hydroxide precursors. *Materials Letters* **2000,** *44* (3-4), 175-180.

150. Liu, W.; Xia, H.; Han, H.; Wang, X., Structural and dielectrical properties of bismuth titanate nanoparticles prepared by metalorganic decomposition method. *Journal of crystal growth* **2004,** *269* (2-4), 499-504.
151. Pookmanee, P.; Uriwilast, P.; Phanichpant, S., Hydrothermal synthesis of fine bismuth titanate powders. *Ceramics International* **2004,** *30* (7), 1913-1915.
152. Subohi, O.; Kumar, G.; Malik, M.; Kurchania, R., Dielectric properties of Bismuth Titanate (Bi4Ti3O12) synthesized using solution combustion route. *Physica B: Condensed Matter* **2012,** *407* (18), 3813-3817.
153. Khort, A.; Podbolotov, K., Effect of reductant type on phase composition and ferroelectric behavior of combustion-synthesized BaTiO 3 and Bi 4 Ti 3 O 12. *International Journal of Self-Propagating High-Temperature Synthesis* **2014,** *23* (2), 106-111.
154. Oliveira, R.; Cavalcante, L.; Sczancoski, J.; Aguiar, E.; Espinosa, J.; Varela, J. A.; Pizani, P.; Longo, E., Synthesis and photoluminescence behavior of Bi4Ti3O12 powders obtained by the complex polymerization method. *Journal of alloys and compounds* **2009,** *478* (1-2), 661-670.
155. Ren, J.; Liu, G.; Wang, Y.; Shi, Q., A novel method for the preparation of Bi2Ti2O7 pyrochlore. *Materials Letters* **2012,** *76*, 184-186.
156. Wang, S. W.; Wang, H.; Wu, X.; Shang, S.; Wang, M.; Li, Z.; Lu, W., Rapid thermal processing of Bi2Ti2O7 thin films grown by chemical solution decomposition. *Journal of crystal growth* **2001,** *224* (3-4), 323-326.
157. McInnes, A.; Sagu, J. S.; Wijayantha, K., Fabrication and photoelectrochemical studies of Bi2Ti2O7 pyrochlore thin films by aerosol assisted chemical vapour deposition. *Materials Letters* **2014,** *137*, 214-217.
158. Hector, A. L.; Wiggin, S. B., Synthesis and structural study of stoichiometric Bi2Ti2O7 pyrochlore. *Journal of Solid State Chemistry* **2004,** *177* (1), 139-145.
159. Hong, Z.-s.; Cao, Y.; Deng, J.-f., A convenient alcohothermal approach for low temperature synthesis of CuO nanoparticles. *Materials letters* **2002,** *52* (1-2), 34-38.
160. Darezereshki, E.; Bakhtiari, F., A novel technique to synthesis of tenorite (CuO) nanoparticles from low concentration CuSO4 solution. *Journal of Mining and Metallurgy B: Metallurgy* **2011,** *47* (1), 73-78.
161. Chang, Y.; Zeng, H. C., Controlled synthesis and self-assembly of single-crystalline CuO nanorods and nanoribbons. *Crystal growth & design* **2004,** *4* (2), 397-402.
162. Anandan, S.; Lee, G.-J.; Wu, J. J., Sonochemical synthesis of CuO nanostructures with different morphology. *Ultrasonics sonochemistry* **2012,** *19* (3), 682-686.
163. Saito, G.; Hosokai, S.; Tsubota, M.; Akiyama, T., Synthesis of copper/copper oxide nanoparticles by solution plasma. *Journal of applied physics* **2011,** *110* (2), 023302.
164. Krishnan, S.; Haseeb, A.; Johan, M. R., Synthesis and growth kinetics of spindly CuO nanocrystals via pulsed wire explosion in liquid medium. *Journal of nanoparticle research* **2013,** *15* (1), 1410.
165. Abboud, Y.; Saffaj, T.; Chagraoui, A.; El Bouari, A.; Brouzi, K.; Tanane, O.; Ihssane, B., Biosynthesis, characterization and antimicrobial activity of copper oxide nanoparticles (CONPs) produced using brown alga extract (Bifurcaria bifurcata). *Applied Nanoscience* **2014,** *4* (5), 571-576.
166. Dehestaniathar, S.; Khajelakzay, M.; Ramezani-Farani, M.; Ijadpanah-Saravi, H., Modified diatomite-supported CuO–TiO2 composite: Preparation, characterization and catalytic CO oxidation. *Journal of the Taiwan Institute of Chemical Engineers* **2016,** *58*, 252-258.

167. Luna, A. L.; Valenzuela, M. A.; Colbeau-Justin, C.; Vázquez, P.; Rodriguez, J. L.; Avendaño, J. R.; Alfaro, S.; Tirado, S.; Garduño, A.; José, M., Photocatalytic degradation of gallic acid over CuO–TiO2 composites under UV/Vis LEDs irradiation. *Applied Catalysis A: General* **2016,** *521*, 140-148.
168. Bharad, P. A.; Nikam, A. V.; Thomas, F.; Gopinath, C. S., CuOx-TiO2 Composites: Electronically Integrated Nanocomposites for Solar Hydrogen Generation. *ChemistrySelect* **2018,** *3* (43), 12022-12030.
169. Hu, Q.; Huang, J.; Li, G.; Chen, J.; Zhang, Z.; Deng, Z.; Jiang, Y.; Guo, W.; Cao, Y., Effective water splitting using CuOx/TiO2 composite films: role of Cu species and content in hydrogen generation. *Applied Surface Science* **2016,** *369*, 201-206.
170. Risse, B.; Schnell, F.; Spitzer, D., Synthesis and Desensitization of Nano-β-HMX. *Propellants, Explosives, Pyrotechnics* **2014,** *39* (3), 397-401.
171. Sève, A.; Pichot, V.; Schnell, F.; Spitzer, D., Trinitrotoluene nanostructuring by spray flash evaporation process. *Propellants, Explosives, Pyrotechnics* **2017,** *42* (9), 1051-1056.
172. Pessina, F.; Schnell, F.; Spitzer, D., Tunable continuous production of RDX from microns to nanoscale using polymeric additives. *Chemical Engineering Journal* **2016,** *291*, 12-19.
173. Guillevic, M.; Pichot, V.; Fioux, P.; Schnell, F.; Spitzer, D., Nanodiamond-based energetic core-shell composites: The route towards safer materials. *Diamond and Related Materials* **2019,** *93*, 150-158.
174. Hübner, J.; Pichot, V.; Lobry, E.; Deckert-Gaudig, T.; Deckert, V.; Spitzer, D., Formation Mechanism of Anisotropic RDX/TNT Core/Shell Nanoparticles and their Influence onto Nanodiamond Detonation Syntheses. **2020**.
175. Pichot, V.; Seve, A.; Berthe, J. E.; Schnell, F.; Spitzer, D., Study of the Elaboration of HMX and HMX Composites by the Spray Flash Evaporation Process. *Propellants, Explosives, Pyrotechnics* **2017,** *42* (12), 1418-1423.
176. Berthe, J. E.; Schnell, F.; Boehrer, Y.; Spitzer, D., Nanocrystallisation of Ammonium DiNitramide (ADN) by Spray Flash Evaporation (SFE). *Propellants, Explosives, Pyrotechnics* **2018,** *43* (6), 609-615.
177. Spitzer, D.; Risse, B.; Schnell, F.; Pichot, V.; Klaumünzer, M.; Schaefer, M., Continuous engineering of nano-cocrystals for medical and energetic applications. *Scientific reports* **2014,** *4*, 6575.
178. Risse, B.; Spitzer, D.; Hassler, D.; Schnell, F.; Comet, M.; Pichot, V.; Muhr, H., Continuous formation of submicron energetic particles by the flash-evaporation technique. *Chemical Engineering Journal* **2012,** *203*, 158-165.

179. Risse, B. Continuous crystallization of ultra-fine energetic particles by the Flash-Evaporation Process. Université de Lorraine, 2012.
180. Coats, A.; Redfern, J., Thermogravimetric analysis. A review. *Analyst* **1963,** *88* (1053), 906-924.
181. O'neill, M., The Analysis of a Temperature-Controlled Scanning Calorimeter. *Analytical chemistry* **1964,** *36* (7), 1238-1245.
182. Graves, P.; Gardiner, D., Practical raman spectroscopy. *Springer* **1989**.
183. Patterson, A., The Scherrer formula for X-ray particle size determination. *Physical review* **1939,** *56* (10), 978.
184. Brunauer, S.; Emmett, P. H.; Teller, E., Adsorption of gases in multimolecular layers. *Journal of the American chemical society* **1938,** *60* (2), 309-319.
185. Comet, M.; Martin, C.; Schnell, F.; Spitzer, D., Nanothermites: a short review. factsheet for experimenters, present and future challenges. *Propellants, Explosives, Pyrotechnics* **2019,** *44* (1), 18-36.

186. UN, E., Recommendations on the Transport of Dangerous Goods: Model Regulations - Twenty-first Revised Edition. *Model Regulations (21st Revised Edition - Vol. I & II)* **2019**
187. Greason, W. D., Electrostatic discharge characteristics for the human body and circuit packs. *Journal of Electrostatics* **2003,** *59* (3-4), 285-300.
188. Piercey, D. G.; Klapoetke, T. M., Nanoscale aluminum-metal oxide (thermite) reactions for application in energetic materials. *Central European Journal of Energetic Materials* **2010,** *7* (2), 115-129.
189. Son, S. F.; Asay, B.; Foley, T.; Yetter, R. A.; Wu, M.-H.; Risha, G. A., Combustion of nanoscale Al/MoO_3 thermite in microchannels. *Journal of Propulsion and Power* **2007,** *23* (4), 715-721.
190. Kubelka, P., Ein Beitrag zur Optik der Farbanstriche (Contribution to the optic of paint). *Zeitschrift fur technische Physik* **1931,** *12*, 593-601.
191. Davis, E.; Mott, N., Conduction in non-crystalline systems V. Conductivity, optical absorption and photoconductivity in amorphous semiconductors. *Philosophical Magazine* **1970,** *22* (179), 0903-0922.
192. Tauc, J., Optical properties and electronic structure of amorphous Ge and Si. *Materials Research Bulletin* **1968,** *3* (1), 37-46.
193. Huang, P. J.; Chang, H.; Yeh, C. T.; Tsai, C. W., Phase transformation of TiO2 monitored by Thermo-Raman spectroscopy with TGA/DTA. *Thermochimica Acta* **1997,** *297* (1-2), 85-92.
194. Moran, P. D.; Bowmaker, G. A.; Cooney, R. P.; Finnie, K. S.; Bartlett, J. R.; Woolfrey, J. L., Vibrational spectra and molecular association of titanium tetraisopropoxide. *Inorganic chemistry* **1998,** *37* (11), 2741-2748.
195. Masters, K., Spray drying handbook. *Spray drying handbook.* **1985**.
196. Vehring, R., Pharmaceutical particle engineering via spray drying. *Pharmaceutical research* **2008,** *25* (5), 999-1022.
197. Ogi, T.; Nandiyanto, A. B. D.; Okuyama, K., Nanostructuring strategies in functional fine-particle synthesis towards resource and energy saving applications. *Advanced Powder Technology* **2014,** *25* (1), 3-17.
198. Nandiyanto, A. B. D.; Okuyama, K., Progress in developing spray-drying methods for the production of controlled morphology particles: From the nanometer to submicrometer size ranges. *Advanced Powder Technology* **2011,** *22* (1), 1-19.
199. Hanaor, D. A.; Sorrell, C. C., Review of the anatase to rutile phase transformation. *Journal of Materials science* **2011,** *46* (4), 855-874.
200. Sing, K. S., Reporting physisorption data for gas/solid systems with special reference to the determination of surface area and porosity (Recommendations 1984). *Pure and applied chemistry* **1985,** *57* (4), 603-619.
201. Kingery, W. D.; Bowen, H. K.; Uhlmann, D. R., *Introduction to ceramics*. John wiley & sons: 1976; Vol. 17.
202. Haynes, W. M., *CRC handbook of chemistry and physics*. CRC press: 2014.
203. Parkhurst, W.; Dallek, S.; Larrick, B. *Thermogravimetric Analysis of Silver Oxide Mixtures*; NAVAL SURFACE WEAPONS CENTER SILVER SPRING MD: 1982.
204. Asoro, M.; Damiano, J.; Ferreira, P., Size effects on the melting temperature of silver nanoparticles: In-situ TEM observations. *Microscopy and Microanalysis* **2009,** *15* (S2), 706-707.
205. Kirshenbaum, A.; Cahill, J.; Grosse, A., The density of liquid silver from its melting point to its normal boiling point 2450 K. *Journal of Inorganic and Nuclear Chemistry* **1962,** *24* (3), 333-336.

206. Steacie, E. W. R.; Johnson, F., The solubility and rate of solution of oxygen in silver. *Proceedings of the Royal Society of London. Series A, Containing Papers of a Mathematical and Physical Character* **1926,** *112* (762), 542-558.
207. Ng, L. Y.; Mohammad, A. W.; Rohani, R.; Hairom, N. H. H., Development of a nanofiltration membrane for humic acid removal through the formation of polyelectrolyte multilayers that contain nanoparticles. *Desalination and Water Treatment* **2016,** *57* (17), 7627-7636.
208. Socrates, G., *Infrared and Raman characteristic group frequencies: tables and charts*. John Wiley & Sons: 2004.
209. Saito, K.; Yamada, T., Silver-Catalyzed CO_2 Fixation. *CO_2 as a Building Block in Organic Synthesis* **2020**, 397-436.
210. Taylor, T.; Dollimore, D.; Gamlen, G., Deaquation and denitration studies on copper nitrate trihydrate. *Thermochimica acta* **1986,** *103* (2), 333-340.
211. Permprasert, J.; Devahastin, S., Evaluation of the effects of some additives and pH on surface tension of aqueous solutions using a drop-weight method. *Journal of food engineering* **2005,** *70* (2), 219-226.
212. Gh. Macarovici, C.; Morar, G., Mixed Bismuth and Titanium Oxides obtained by thermolysis of hydroxide coprecipitates. *Zeitschrift für anorganische und allgemeine Chemie* **1972,** *393* (3), 275-283.
213. Li, P.; Jiang, C.; Wang, Q.; Zuojiao, K.; Zhang, Z.; Liu, J.; Wang, Y., Preparation and Characterization of $Bi_2Ti_2O_7$ Pyrochlore by Acetone Solvothermal Method. *Journal of nanoscience and nanotechnology* **2018,** *18* (12), 8360-8366.
214. Kargin, Y. F.; Ivicheva, S.; Volkov, V., Phase relations in the Bi_2O_3-TiO_2 system. *Russian Journal of Inorganic Chemistry* **2015,** *60* (5), 619-625.
215. Koçyiğit, S.; Gökmen, Ö.; Temel, S.; Aytimur, A.; Uslu, İ.; Bayari, S. H., Structural investigation of boron undoped and doped indium stabilized bismuth oxide nanoceramic powders. *Ceramics International* **2013,** *39* (7), 7767-7772.
216. Charalampous, G.; Hardalupas, Y., Collisions of droplets on spherical particles. *Physics of Fluids* **2017,** *29* (10), 103305.
217. Egerton, R.; Li, P.; Malac, M., Radiation damage in the TEM and SEM. *Micron* **2004,** *35* (6), 399-409.
218. Dorrian, J.; Newnham, R.; Smith, D.; Kay, M., Crystal structure of $Bi_4Ti_3O_{12}$. *Ferroelectrics* **1972,** *3* (1), 17-27.
219. Guenther, G. Size-dependent high-temperature behavior of Bismuth Oxide nanoparticles. Technische Universität, 2012.
220. Guenther, G.; Schierning, G.; Theissmann, R.; Kruk, R.; Schmechel, R.; Baehtz, C.; Prodi-Schwab, A., Formation of metallic indium-tin phase from indium-tin-oxide nanoparticles under reducing conditions and its influence on the electrical properties. *Journal of Applied Physics* **2008,** *104* (3), 034501.
221. Chaturvedi, S.; Dave, P. N., Review on thermal decomposition of ammonium nitrate. *Journal of Energetic Materials* **2013,** *31* (1), 1-26.
222. Liu, B., One-dimensional copper hydroxide nitrate nanorods and nanobelts for radiochemical applications. *Nanoscale* **2012,** *4* (22), 7194-7198.
223. Spurr, R. A.; Myers, H., Quantitative analysis of anatase-rutile mixtures with an X-ray diffractometer. *Analytical chemistry* **1957,** *29* (5), 760-762.
224. Gribb, A. A.; Banfield, J. F., Particle size effects on transformation kinetics and phase stability in nanocrystalline TiO_2. *American Mineralogist* **1997,** *82* (7-8), 717-728.
225. Kumar, K.-N. P., Growth of rutile crystallites during the initial stage of anatase-to-rutile transformation in pure titania and in titania-alumina nanocomposites. *Scripta Metallurgica et Materialia* **1995,** *32* (6), 873-877.

226. Ma, S.; Cantwell, P. R.; Pennycook, T. J.; Zhou, N.; Oxley, M. P.; Leonard, D. N.; Pennycook, S. J.; Luo, J.; Harmer, M. P., Grain boundary complexion transitions in WO3-and CuO-doped TiO2 bicrystals. *Acta materialia* **2013,** *61* (5), 1691-1704.

227. Ahmed, A.; Elvati, P.; Violi, A., Size-and phase-dependent structure of copper (II) oxide nanoparticles. *RSC Advances* **2015,** *5* (44), 35033-35041.

228. Goldschmidt, H., Verfahren zur Herstellung von Metallen oder Metalloiden oder Legierungen derselben. *Process for the production of metals or metalloids or alloys of the same'), Kaiserliches (German) Patent* **1895,** *96317*.

229. Pantoya, M. L.; Levitas, V. I.; Granier, J. J.; Henderson, J. B., Effect of bulk density on reaction propagation in nanothermites and micron thermites. *Journal of Propulsion and Power* **2009,** *25* (2), 465-470.

230. Pantoya, M. L.; Granier, J. J., Combustion behavior of highly energetic thermites: Nano versus micron composites. *Propellants, Explosives, Pyrotechnics: An International Journal Dealing with Scientific and Technological Aspects of Energetic Materials* **2005,** *30* (1), 53-62.

231. Mott, N., Oxidation of metals and the formation of protective films. *Nature* **1940,** *145* (3687), 996-1000.

232. Pesiri, D.; Aumann, C. E.; Bilger, L.; Booth, D.; Carpenter, R. D.; Dye, R.; O Neill, E.; Shelton, D.; Walter, K. C., Industrial scale nano-aluminum powder manufacturing. *Journal of Pyrotechnics* **2004**, 19-31.

233. Walter, K. C.; Pesiri, D. R.; Wilson, D. E., Manufacturing and performance of nanometric Al/MoO3 energetic materials. *Journal of Propulsion and Power* **2007,** *23* (4), 645-650.

234. Coulet, M.-V.; Rufino, B.; Esposito, P.-H.; Neisius, T.; Isnard, O.; Denoyel, R., Oxidation mechanism of aluminum nanopowders. *The Journal of Physical Chemistry C* **2015,** *119* (44), 25063-25070.

235. Le Houx, N. Synthèse d'oxyde de tungstène à tailles ultimes (inférieures à dix nanomètres) en vue de l'élaboration et de l'étude de la réactivité de composés nanothermites. Strasbourg, 2010.

236. Chung, S. W.; Guliants, E. A.; Bunker, C. E.; Jelliss, P. A.; Buckner, S. W., Size-dependent nanoparticle reaction enthalpy: oxidation of aluminum nanoparticles. *Journal of Physics and Chemistry of Solids* **2011,** *72* (6), 719-724.

237. Bunker, C. E.; Smith, M. J.; Fernando, K. S.; Harruff, B. A.; Lewis, W. K.; Gord, J. R.; Guliants, E. A.; Phelps, D. K., Spontaneous hydrogen generation from organic-capped Al nanoparticles and water. *ACS applied materials & interfaces* **2010,** *2* (1), 11-14.

238. Miller, P. L.; Navarro, A. *Hazardous Reactions of Aluminum Powder with Water in the Propellant, Explosive and Pyrotechnic (PEP) Industries*; Alliant Techsystems Inc Hopkins Mn: 1996.

239. Paulsson, H.; Rosén, E., A study of the formation of CuAl2O4 from CuO and Al2O3 by solid state reaction at 1000 C and 950 C. *Zeitschrift für anorganische und allgemeine Chemie* **1973,** *401* (2), 172-178.

240. Siegert, B.; Comet, M.; Spitzer, D., Safer energetic materials by a nanotechnological approach. *Nanoscale* **2011,** *3* (9), 3534-3544.

241. Roux, M.; Auzanneau, M.; Brassy, C., Electric spark and esd sensitivity of reactive solids (primary or secondary explosive, propellant, pyrotechnics) part one: Experimental results and reflection factors for sensitivity test optimization. *Propellants, explosives, pyrotechnics* **1993,** *18* (6), 317-324.

242. Kelly, D.; Beland, P.; Brousseau, P.; Petre, C. F., Electrostatic discharge sensitivity and resistivity measurements of Al nanothermites and their fuel and oxidant precursors. *Central European Journal of Energetic Materials* **2017,** *14*.
243. Sundaram, D. S.; Yang, V.; Connell Jr, T. L.; Risha, G. A.; Yetter, R. A., Flame propagation of nano/micron-sized aluminum particles and ice (ALICE) mixtures. *Proceedings of the Combustion Institute* **2013,** *34* (2), 2221-2228.
244. Risha, G.; Connell, T.; Yetter, R.; Yang, V.; Wood, T.; Pfeil, M.; Pourpoint, T.; Son, S. In *Aluminum-ice (ALICE) propellants for hydrogen generation and propulsion*, 45th AIAA/ASME/SAE/ASEE Joint Propulsion Conference & Exhibit, 2009; p 4877.

245. Kawai, T.; Sakata, T., Hydrogen evolution from water using solid carbon and light energy. *Nature* **1979,** *282* (5736), 283-284.
246. Sakata, T.; Kawai, T., Heterogeneous photocatalytic production of hydrogen and methane from ethanol and water. *Chemical Physics Letters* **1981,** *80* (2), 341-344.
247. Domka, F.; Łaniecki, M., Iron-chromium catalysts in the conversion of methanol with water vapor. *Reaction Kinetics and Catalysis Letters* **1978,** *8* (4), 507-513.
248. Tauc, J.; Grigorovici, R.; Vancu, A., Optical properties and electronic structure of amorphous germanium. *physica status solidi (b)* **1966,** *15* (2), 627-637.
249. Reddy, K. M.; Manorama, S. V.; Reddy, A. R., Bandgap studies on anatase titanium dioxide nanoparticles. *Materials Chemistry and Physics* **2003,** *78* (1), 239-245.
250. Tayade, R. J.; Kulkarni, R. G.; Jasra, R. V., Photocatalytic degradation of aqueous nitrobenzene by nanocrystalline TiO_2. *Industrial & engineering chemistry research* **2006,** *45* (3), 922-927.
251. Oros-Ruiz, S.; Zanella, R.; Prado, B., Photocatalytic degradation of trimethoprim by metallic nanoparticles supported on TiO_2-P25. *Journal of hazardous materials* **2013,** *263*, 28-35.
252. Zhang, Z.; Wang, C.-C.; Zakaria, R.; Ying, J. Y., Role of particle size in nanocrystalline TiO_2-based photocatalysts. *The Journal of Physical Chemistry B* **1998,** *102* (52), 10871-10878.
253. Williams, A. T. R.; Winfield, S. A.; Miller, J. N., Relative fluorescence quantum yields using a computer-controlled luminescence spectrometer. *Analyst* **1983,** *108* (1290), 1067-1071.
254. Wong, K.-L.; Bünzli, J.-C. G.; Tanner, P. A., Quantum yield and brightness. *Journal of Luminescence* **2020**, 117256.
255. Gupta, S.; De Leon, L.; Subramanian, V. R., Mn-modified $Bi_2Ti_2O_7$ photocatalysts: bandgap engineered multifunctional photocatalysts for hydrogen generation. *Physical Chemistry Chemical Physics* **2014,** *16* (25), 12719-12727.
256. Khanal, V.; Ragsdale, W.; Gupta, S.; Subramanian, V. R., Insights into the photoactivity of iron modified bismuth titanate (Fe_BTO) nanoparticles. *Catalysis Today* **2018,** *300*, 81-88.
257. Ragsdale, W. C. Iron Modified Bismuth Titanate Pyrochlore Photocatalysts for Environmental Remediation and Solar Fuel Production. 2016.
258. Jin, Z.; Zhang, X.; Li, Y.; Li, S.; Lu, G., 5.1% Apparent quantum efficiency for stable hydrogen generation over eosin-sensitized CuO/TiO_2 photocatalyst under visible light irradiation. *Catalysis Communications* **2007,** *8* (8), 1267-1273.
259. Xu, S.; Sun, D. D., Significant improvement of photocatalytic hydrogen generation rate over TiO_2 with deposited CuO. *International Journal of Hydrogen Energy* **2009,** *34* (15), 6096-6104.
260. Ohtani, B.; Iwai, K.; Nishimoto, S.-i.; Sato, S., Role of platinum deposits on titanium (IV) oxide particles: structural and kinetic analyses of photocatalytic reaction

in aqueous alcohol and amino acid solutions. *The Journal of Physical Chemistry B* **1997,** *101* (17), 3349-3359.

Denis Horst PRÜSSING

Synthèse par nébulisation flash de spray d'oxydes purs, de mélanges d'oxydes et d'oxydes mixtes – Applications photocatalytiques et pyrotechniques

Résumé

L'objectif de la thèse est d'obtenir des "briques" d'oxydes mixtes de taille submicronique pour des applications pyrotechniques et photocatalytiques. Le procédé de synthèse par nébulisation flash de spray (procédé SFS) a été utilisé pour synthétiser des oxydes métalliques simples et mixtes. Les recherches ont principalement porté sur la synthèse d'oxydes de titane (TiO_2), de cuivre (CuO) et de bismuth (Bi_2O_3) de taille submicronique et ainsi que de mélanges de ces oxydes.

La première étape du travail de thèse a consisté à adapter l'appareil de SFS à la production d'oxyde de titane. La première modification a consisté à améliorer le contrôle des débits des solutions contenant les précurseurs, en introduisant des vannes de précision afin de maintenir constante la proportion des précurseurs dans la solution nébulisée. Le mélange des précurseurs, l'eau et le tétraisopropoxyde de titane (TTIP), est effectué avant la pulvérisation. Différents rapports eau/TTIP ont été étudiés: sous-stoechiométrique (1:1), stoechiométrique (1:2) et super-stoechiométrique (1:4). Les matériaux obtenus ont une morphologie sphérique. Ces matériaux ont été calcinés pour donner des particules sphériques submicrométriques composées d'anatase. L'introduction d'un métal (Ag) dans l'oxyde de titane a été étudiée. Le matériau est constitué de particules sphériques submicrométriques d'oxyde de titane à la surface desquelles sont réparties des particules d'argent nanométriques. Le traitement thermique, modifie la morphologie des particules d'argent en polyèdres de forme allongées. Sur la base des paramètres de production de l'oxyde de titane, la synthèse d'oxydes mixtes de bismuth et de titane a été réalisée. Trois systèmes différents de bismuth et de titane ont été proposés. La première expérience a donné un mélange de titanate de bismuth avec un excès d'oxyde de titane. La structure cristalline a été identifiée comme du titanate de bismuth (Bi2Ti2O7) et du rutile pour l'excès d'oxyde de titane. En ajustant le rapport Bi/Ti, le titanate de bismuth (Bi2Ti2O7) pur a été produit. En augmentant la proportion de bismuth, du titanate de bismuth pur (Bi4Ti3O12) a également été synthétisé. Dans une autre série d'expériences, de l'oxyde de cuivre pur a été produit par le système SFS. Les particules présentent une forme moins homogène et régulière que les poudres à base de titane. Dans une étape suivante, des particules de cuivre et d'oxyde de titane ont été produites par le système SFS.

Certains de ces matériaux ont été utilisés dans des applications pyrotechniques et photocatalytiques. La taille et la forme de ces particules ainsi que le degré de mélange inégalé des différents éléments composant ces matériaux leur donne des propriétés uniques en leur genre et ouvre la voie à de nombreuses applications dans différents domaines.

Mots-clefs: Synthesis, spray, submicronisation, oxyde métalliques, pyrotechnie, photocatalyse

Denis Horst PRÜSSING

Synthèse par nébulisation flash de spray d'oxydes purs, de mélanges d'oxydes et d'oxydes mixtes – Applications photocatalytiques et pyrotechniques

Résumé en anglais

The objective of the thesis is to obtain submicron-sized mixed oxide "bricks" for pyrotechnic and photocatalytic applications. The spray flash synthesis (SFS) process has been used to synthesize simple and mixed metal oxides. Research has focused on the synthesis of submicron-sized titanium (TiO_2), copper (CuO) and bismuth (Bi_2O_3) oxides and mixtures of these oxides.

The first stage of the thesis work consisted in adapting the FSS apparatus to the production of titanium oxide. The first modification consisted in improving the control of the flow rates of the solutions containing the precursors, by introducing precision valves in order to maintain constant the proportion of precursors in the nebulised solution. Mixing of the precursors, water and titanium tetraisopropoxide (TTIP), is carried out prior to spraying. Different water/TTIP ratios have been studied: sub-stoichiometric (1:1), stoichiometric (1:2) and super-stoichiometric (1:4). The materials obtained have a spherical morphology. These materials were calcined to give submicrometric spherical particles composed of anatase. The introduction of a metal (Ag) into titanium oxide was studied. The material consists of submicrometric spherical titanium oxide particles with nanometric silver particles distributed on the surface. Heat treatment changes the morphology of the silver particles into elongated polyhedra. Based on the production parameters of titanium oxide, the synthesis of mixed oxides of bismuth and titanium was carried out. Three different systems of bismuth and titanium were proposed. The first experiment resulted in a mixture of bismuth titanate with an excess of titanium oxide. The crystal structure was identified as bismuth titanate (Bi2Ti2O7) and rutile for the excess titanium oxide. By adjusting the Bi/Ti ratio, pure bismuth titanate (Bi2Ti2O7) was produced. By increasing the proportion of bismuth, pure bismuth titanate (Bi4Ti3O12) was also synthesized. In another series of experiments, pure copper oxide was produced by the SFS system. The particles have a less homogeneous and regular shape than titanium-based powders. In a further step, copper and titanium oxide particles were produced by the SFS system.

Some of these materials have been used in pyrotechnic and photocatalytic applications. The size and shape of these particles as well as the unequalled degree of mixing of the different elements composing these materials gives them unique properties and opens the way to numerous applications in different fields.

Keywords: Synthesis, spray, submicronization, metal oxides, pyrotechnics, photocatalysis